CATALYST ELECTRODE DEVELOPMENT FROM ONE-DIMENSIONAL PLATINUM SILVER-BASED ALLOY NANOSTRUCTURES FOR PROTON EXCHANGE MEMBRANE FUEL CELLS

By

Elok Fidiani

A thesis submitted to the

University of Birmingham

For the degree of

Doctor of Philosophy

Centre for Doctoral Training in Fuel Cells and their Fuels

School of Chemical Engineering

College of Engineering and Physical Sciences

University of Birmingham

September 2020

ABSTRACT

The primary research activity on proton exchange membrane fuel cells (PEMFCs) is still directed to reduce the system cost by using a low Pt catalyst loading while maintaining high power performance and durability. The development of advanced catalyst designs usually focuses on shape-controlled nanostructures and alloying to form bimetallic or multimetallic compositions. They have been demonstrated as effective strategies to boost the catalyst activities toward the sluggish oxygen reduction reaction (ORR) at the cathodes in PEMFCs. However, most of the advanced catalyst nanostructures with the superior catalytic activities are limited to half-cell electrochemical measurement in liquid electrolytes, and there is a big challenge to fully transferring the performance to electrodes in operating fuel cells.

Such a challenge motivates this PhD research to develop high power performance and durable catalyst electrodes from one-dimensional (1D) Pt-based alloy nanostructures for PEMFC application, advancing our previous achievements on 1D Pt nanostructure array gas diffusion electrodes (GDEs). The alloying of Pt with Ag is investigated to construct a cost-effective AgPt nanorod catalyst, based on the close lattice constant between Ag and Pt to minimise the atomic segregation and sustain catalyst stability. The influence mechanisms of the reaction process are systematically explored on the growth, crystal structure and morphology of 1D AgPt nanostructures considering their catalytic performance recorded in the membrane electrode assembly (MEA) test in single PEMFCs.

Firstly, a scalable preparation method is established for growing AgPt NRs on carbon support utilising formic acid reduction approach. Ultrafine single-crystal AgPt NRs with an average diameter of 3-4 nm and length of ~15 nm are obtained by controlling the ion reduction process to induce the nucleation and growth of Pt and Ag along the <111> direction. The optimal Ag_1Pt_1 NR/C catalyst shows 1.22 and 1.51-fold higher power density and mass activity, respectively than commercial Pt/C nanoparticles (NPs) as cathode catalysts in PEMFCs. After the accelerated degradation test (ADT), severe Ag redeposition is observed at the interface between the cathode and polymer electrolyte membrane.

The introduction of Au is therefore proceeded to improve the stability of AgPt NR/C forming Au-AgPt NR/C. The integration of 5 at% Au effects the metal ion reduction procedure, leading to the formation of longer NRs of up to ~20 nm and a high ratio of Pt depositing on the surface. Consequently, these improvements bring about 7% increase in the electrochemical surface area (ECSA) of the catalyst, and 1.15- and 1.70-fold higher ORR activity compared to AgPt NR/C and Pt/C, respectively. The stabilisation effect of the Au alloying is evaluated in PEMFCs, and even better stability is demonstrated than Pt NR/C.

The understanding and experience obtained from controlling the ion reduction process to grow AgPt NRs are transferred to fabricate GDE by growing AgPt NR arrays directly on GDLs. A different alloying mechanism between Ag and Pt is found for the NR growth on the GDL from that on the carbon support, ascribed to the inert GDL surface and moderate reaction temperature of 40 °C. The alloying turns less harmonised when the Ag content more than 10 at% as this leads to the formation of a Ag metal phase. Au is then introduced to construct Au-AgPt NR GDE, and its alloying effect is probed. It is found that the integration of Au plays a game-changing role in the NR structure, leading to self-rearrangement atomic deposition and improving Pt placement on the NR surface. The Au-AgPt NR GDE shows a higher peak power density of 0.61 W cm^{-2} than those of the Pt NR and Pt/C GDEs with ~20 wt% more of Pt loading and a less performance decline after the ADT.

ACKNOWLEDGEMENT

I thought it would be impossible to pursue a PhD after getting married and having a baby. But, this thesis has proven myself wrong. Therefore, I am sincerely thankful to my whole family, especially my little son and my husband, for being supportive of my decision. This past four year has been a roller coaster journey of being a PhD student and full-time mom. However, I feel grateful that my son has always been there with me going through every situation.

I sincerely express my gratitude to my primary supervisor, Shangfeng Du, for kindly welcoming me into his research group and guiding me throughout my PhD. Thanks for the outstanding supervision to always directing me on the right track of my research and generously cooperate with my situation. I may be a bit slow and made several mistakes, particularly at the beginning of my PhD. Still, he always patiently monitors my progress and gives me valuable feedback to improve my knowledge and skills, especially in writing. I would not be able to reach this point without his excellent supervision. I sincerely wish the best for his works and future.

I owe many thanks to Pete for welcoming me since the first day I entered the lab and introducing me to the practical electrochemistry. Thanks to his patient for assisting me using most of the equipment at the beginning of my PhD, helping me to get a better understanding about fuel cells through his unique perspective and valuable discussions during my PhD. Thanks to my labmates: Huixin, Yang, Yichang, Pushpa, Abby, Ruba, Alan, Kun, Min, Liam, Ahmad, and Satish for sharing the space and happy memory in G5 and G6 with me, and offering a help sometimes to keep an eye to my experiment, especially when there was an urgency regarding my parental duty. And many thanks to the whole of fuel cell group particularly Neil Rees for giving me the advice for my work during big group meeting and year-2 assessment, Ahmad El-Kharouf for the SEM training and giving access to use it, Arthur

Majewski for training me and giving me access to use TGA, Aimee the one introducing me to ICP-MS, Lina, Nisa, Lois, James, Daniel, Laura, Sam, Miguel, Chris, Naser, Eridei, Bhargav, Abu, Abdul, Abiola, Melisa, Hal, Oujen for being part of my journey. I wish the best for all of you.

My deepest acknowledgement for Prof. Hanshan Dong for being my second supervisor and allowing me to use the active screen plasma to treat my samples. My gratitude for Lynn Draper and John Hopper for assisting me regarding the school administrative requirements, Chyntol for helping me to cope with the technical issues in G5 and G6, Ellaine for giving me access to Biochemical Engineering and assisting me in using centrifuges. I also would like to thanks to Jie Chan for training me and giving me the access to use XRD, and the members of centre electron microscopy the University of Birmingham, especially Paul and Theresa for their technical support during me working with TEM. Many thanks to Gnani for analysing my samples with HR-TEM and STEM-EDX.

I owe great thanks to Indonesia endowment fund for education (LPDP) for sponsoring my PhD. I am thankful for being an awardee of one of the most prestigious Indonesian government scholarship. I would also like to express my acknowledgement to all the member and staff of FTIS Unpar, especially Department of Physics, for giving me a chance to pursue my PhD and the support during my study.

Finally, to all those who contribute to my PhD work and this thesis, I sincerely express my gratitude.

LIST OF PUBLICATIONS

Peer-reviewed Journal Paper

1. **E. Fidiani**, G. Thirunavukkarasu, Y. Li, Y.-L. Chiu, S. Du, Ultrathin AgPt Alloy Nanorods as Low-cost Oxygen Reduction Reaction Electrocatalysts in Proton Exchange Membrane Fuel Cells, J. Mater. Chem. A. 8 (2020) 11874–11883, doi.org/10.1039/D0TA02748K.
2. **E. Fidiani**, G. Thirunavukkarasu, Y. Li, Y.-L. Chiu, S. Du, Au Integrated AgPt Nanorods for Oxygen Reduction Reaction in Proton Exchange Membrane Fuel Cells, *Submitted to Journal Material Chemistry A. Under reviewing.*
3. **E. Fidiani**, G. Thirunavukkarasu, Y.-L. Chiu, S. Du, Au-AgPt Nanorod Array Gas Diffusion Electrodes for Proton Exchange Membrane Fuel Cells, *Under preparation.*
4. **E. Fidiani**, Y. Li, P Mardle, S. Du, Pt Nanotubes with Highly Porous Walls from Ag Nanowire Templates for Oxygen Reduction Reaction Applications, *Under preparation.*

Conference Presentation

1. 18th International Conference on Sustainable Energy Technologies – SET 2019, 20th – 22nd August 2019, Kuala Lumpur, Malaysia; ***Oral Presentation*** “Performance and Stability of One-Dimensional AgPt Alloy Nanostructure Electrocatalysts towards Oxygen Reduction Reaction in Proton Exchange Membrane Fuel Cells” *(peer-reviewed)*
2. 23rd EFCF Conference in Low-Temperature Fuel Cells, Electrolysers & H_2 Processing, Lucerne, Switzerland, 2nd-5th July 2019; ***Poster Presentation*** “One-Dimensional AgPt based Alloy Nanorod Catalysts for Proton Exchange Membrane Fuel Cells” *(peer-reviewed)*
3. The 5th International Symposium on Hydrogen Energy, Renewable Energy and Materials, Bangkok, Thailand, 13-14th June 2019: ***Oral Presentation*** “One-Dimensional AgPt Alloy Nanorods As Oxygen Reduction reaction Electrocatalysts for Proton Exchange Membrane Fuel Cells”

4. H_2FC Supergen Research Conference 2018, Birmingham, UK, 18-19th December 2018: ***Oral Presentation*** "Facile Synthesis of Bimetalic AgPt Alloy Nanorods for Proton Exchange Membrane Fuel Cells"
5. 14th International Hydrogen and Fuel Cell Conference, Birmingham, UK, 13th March 2018; ***Poster presentation*** "One-Dimensional Pt Nanotube Electrocatalysts from Ag Nanowire template for Proton Exchange Membrane Fuel Cells"
6. Energy from Waste and Waste to Energy, Birmingham, UK, 20th-21st July 2017; ***Poster Presentation*** "Development of One-Dimensional Nanostructure AgPt Nanowires for Proton Exchange Membrane Fuel Cells"
7. UK Chem Eng Day 2017, Birmingham, UK, 27-28th March 2017; ***Poster presentation*** "Facile Synthesis Ultrathin Ag Nanowires trough Solution-Phase Chemical Approach"

TABLE OF CONTENTS

LIST OF FIGURES

LIST OF TABLES

ABBREVIATIONS AND SYMBOLS

0D	Zero-dimensional
1D	One-dimensional
3D	Three-dimensional
ADT	Accelerated degradation test
AEFC	Alkaline electrolyte fuel cell
AQLI	Air quality life index
BEV	Battery electric vehicle
CCM	Catalyst coated membrane
CTAB	Cetyltrimethylammonium bromide
CV	Cyclic voltammetry
DFT	Density functional theory
DMF	N,N-dimethyl formamide
DMFC	Direct Methanol Fuel cell
DoE	U.S Department of Energy
E	Potential
ECSA	Electrochemical surface area

EDX	Energy-dispersive X-ray spectroscopy
EIS	Electrochemical impedance spectroscopy
F	Faraday’s constant
FCC	Face-centred cubic
ΔG	The change in Gibbs free energy
GDE	Gas diffusion electrode
GDL	Gas diffusion layer
H_{des}	Hydrogen desorption
HFCV	Hydrogen fuel cell vehicle
HNCN	Hollow nanochain-like network
HOR	Hydrogen oxidation reaction
HR-TEM	High resolution transmission electron microscopy
HSC	High surface-area carbon
i	Current density
I	Current
ICP-MS	Inductively coupled plasma-mass spectroscopy
I_k	Kinetic current
I_m	Mass activity
IPA	Isopropyl alcohol

I_s	Specific activity
JM	Johnson Matthey
MEA	Membrane electrode assembly
MPL	Microporous layer
n	Number of electrons transferred
NO_2	Nitrogen dioxide
NP	Nanoparticle
NR	Nanorod
NT	Nanotube
NW	Nanowire
O_2	Oxygen
OAm	Oleylamine
OCV	Open circuit voltage
ORR	Oxygen reduction reaction
P	Power density
PEM	Proton exchange membrane
PEMFC	Proton exchange membrane fuel cell
PGM	Platinum group metals
PSA	Perfluorocarbon sulfonic acid

Pt/C	Commercial catalyst (TKK)
PTFE	Polytetrafluoroethylene
PVP	Polyvinylpyrrolidone
R_{CT}	Charge transfer resistance
R_{Ω}	Ohmic resistance
RDE	Rotating disk electrode
RHE	Reversible hydrogen electrode
SEM	Scanning electron microscopy
SRP	Standard reduction potential
SOFC	Solid oxide fuel cell
STEM	Scanning transmission electron microscopy
TEM	Transmission electron microscopy
TGA	Thermo-gravimetric analysis
XPS	X-ray photoelectron spectroscopy
XRD	X-ray diffraction

Chapter 1

Introduction

1.1 Introduction

The energy demand in the transportation sector increases steadily with rapid global population and economic growth. It leads to the rise of issues linked to the fossil fuel combustion, which releases a large number of pollutants such as carbon monoxide (CO), nitrogen dioxide (NO_2), sulphur dioxide (SO_2), ground-level ozone and greenhouse gases such as carbon dioxide (CO_2), etc. Apart from the arising environmental problem caused by the greenhouse effect, the health issue is also a major concern, particularly in highly populated areas. Jakarta, as one of the biggest and most populated cities in South East Asia, has been struggling with the pollution issues, where about 70% of pollutants are released from transportation vehicles [1]. According to Air Quality Life Index (AQLI), the worsening daily air quality in Jakarta has long reached unhealthy stages because of the high level of toxicity, shortening average life span [2–4]. It is believed that such description also represents the major condition of densely populated cities worldwide, which requires a practical solution to cope with the world's clean energy crisis. Finally, the world leaders in the Paris Climate Change Conference 2015 came to an agreement to limit the global temperature increases below 2 °C from the pre-industrial level [5]. To meet such an ambitious target, massive investment and serious actions are required.

In response to the challenge, hydrogen and fuel cell technologies offer an efficient clean energy conversion to assist the transition to a low-carbon economy. Currently, many types of fuel cells have been successfully developed including proton exchange membrane fuel cells (PEMFCs), alkaline electrolyte fuel cells (AEFCs), direct methanol fuel cells (DMFCs), solid oxide fuel cells (SOFCs), etc. [6]. Basically, they function in a similar way but with different types of electrolytes encompassing a wide range of applications. In the transportation sector, PEMFCs arise as an ideal solution for vehicle fleets empowering the hydrogen fuel cell vehicle (HFCV). They efficiently convert hydrogen directly into electric energy by a clean mechanism. Electric energy, water and heat are the final product from the PEMFC, making it as an attractive choice for the next-generation power generator, mainly for transportation and stationary due to their low operational temperature, high power density and easy start-up and shut-down [7].

Electrification of the energy network utilising battery electric vehicle (BEV) has also been demonstrated as an efficient alternative to eliminate the pollutants with more competitive price than of HFCV [8]. However, the HFCV provides a shorter refuelling time and longer driving range compared to the BEV. Therefore, the utilisation of PEMFCs is best directed for the heavy-duty transport requiring greater longevity such as buses, trucks and train [9]. With the increasing manufacturing volume of HFCV, it can reduce the operating cost inducing the more prevalent replacement for the conventional gasoline vehicles [10].

1.2 Proton Exchange Membrane Fuel Cells (PEMFCs)

Schematically, the single PEMFC consists of several parts, as shown in Figure 1.1 [11]. The PEM at the heart of the stack is commonly materialised from perfluorocarbon sulfonic acid (PSA) ionomer, which acts as the electrolyte for proton mobilisation. It possesses good mechanical strength and chemical resistance. The catalyst layers located at both sides of the PEM work as the anode and cathode, which are mainly consisted of Pt nanoparticles (NPs) on the support material, e.g. carbon black (Pt/C), coated with proton conducting ionomer to facilitate the ion transport. The catalyst layer can be made by spraying or painting catalyst ink onto a gas diffusion layer (GDL) as a gas diffusion electrode (GDE), or directly onto the PEM, also known as the catalyst coated membrane (CCM). These parts: PEM, catalyst layers and GDLs are the main components to fabricate a membrane electrode assembly (MEA). Gaskets are placed between the MEA and flow field plate to prevent gas leaks. They also function to manage the compression in the MEA. The flow-field plate is commonly made of high electrically conductive material (e.g. stainless steel or graphite) with a pattern channel to flow the gas over the electrodes. In the end, the current collector plates are settled to provide the structural support and connect the cell to the external circuits (i.e. electrical and heat wires).

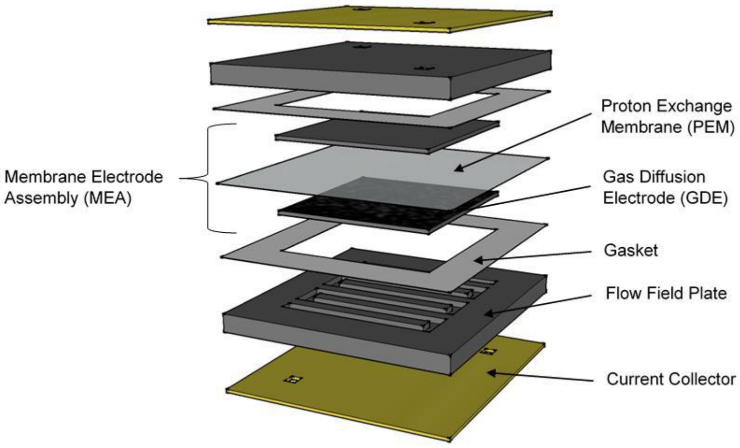

Figure 1.1 Schematic illustration of single PEMFC composition [11].

In PEMFC operation, hydrogen and air/oxygen gases are supplied to the anode and cathode, respectively (Figure 1.2). At the anode side, hydrogen is oxidised into positive charge (proton) and negative charge (electron), also known as hydrogen oxidation reaction (HOR), which is shown in Equation 1.1. While protons migrate to the cathode through the PEM, electrons are conducted through an external electrical circuit, producing an electrical current. At the cathode, the incoming oxygen gas is reduced, also known as oxygen reduction reaction (ORR), where oxygen, protons and electrons are combined to form water and produce heat during the process (Equation 1.2) [6,12]. The ORR at the cathode side is slower of up to six – order of magnitude than the HOR as it involves the cleavage of the oxygen bond followed by the multi-step electron and proton transfer to form water [13]. Hence, catalysts are crucial to optimise the kinetic reaction at the cathode and will be the focus of this thesis.

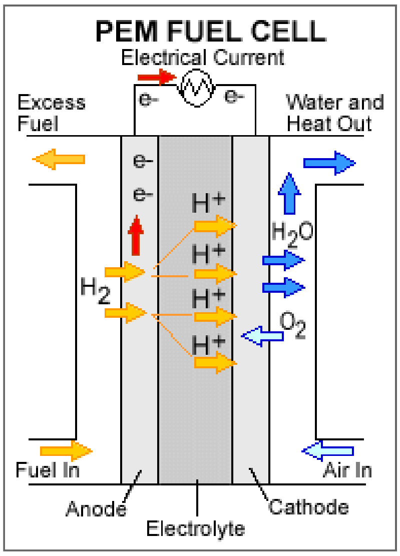

Figure 1.2 The schematic of basic PEMFC operating principle [12].

Anode: $$2H_2 \rightarrow 4H^+ + 4e^- \quad \text{(Eq. 1.1)}$$

Cathode: $$O_2 + 4H^+ + 4e^- \rightarrow 2H_2O \quad \text{(Eq. 1.2)}$$

Overall: $$2H_2 + O_2 \rightarrow 2H_2O \quad \text{(Eq. 1.3)}$$

Pt-based catalyst is commercially used to catalyse both HOR and ORR in PEMFC [14]. Typically, carbon black nanoparticles (NPs) with the size between 20-40 nm is employed to deposit Pt catalyst. Due to a slower ORR kinetic rate, a higher Pt loading is commonly applied at the cathode. The catalyst layer where the ORR takes place is ideally described as Pt/C particles coated in a network hydrated ionomer with the effective gas transport provided by the gaseous pores within the microscopic structure (Figure 1.3). Such a feature can effectively facilitate the oxygen transport trough the void, while proton and electron can travel via ionomer and conductive solid, respectively [15]. The water formed should be effectively removed from the electrode as it potentially blocks the oxygen access throughout the catalyst layer. It is believed that a good catalyst distribution is key to optimise the electrochemical surface area and improve the fuel cell performance.

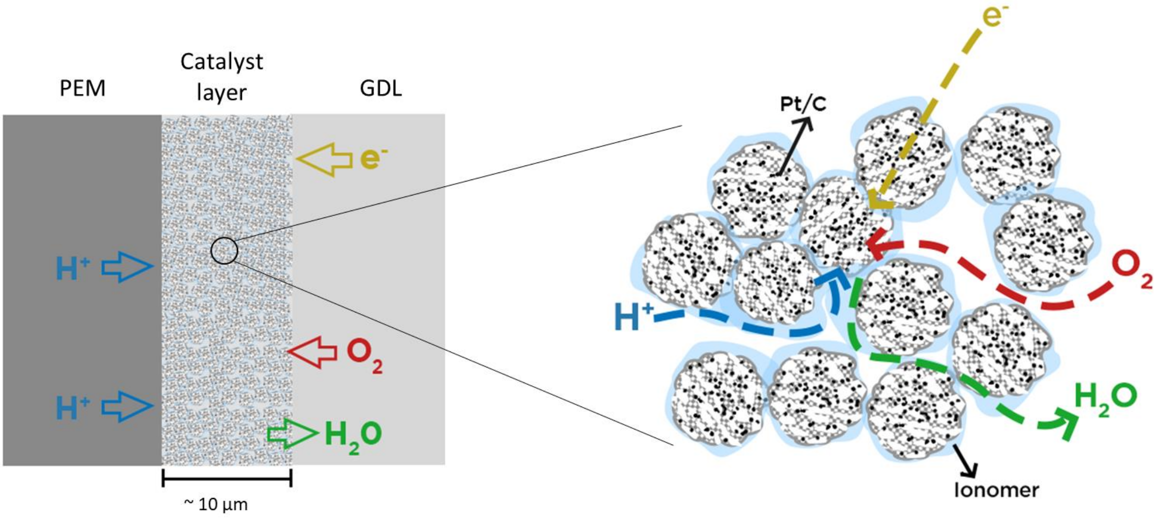

Figure 1.3 The schematic structure of the cathode catalyst layer

Thermodynamically, by presuming the overall reaction (Equation 1.3) is spontaneous, the theoretical electric work done is equivalent to the Gibbs free energy released (ΔG) as below:

$$\Delta G = -nFE \qquad \text{(Eq. 1.4)}$$

Where n is the number of electrons involved in the reaction. Referring to Equation 1.3, n value is 2 by assuming that two electrons are released from each molecule of hydrogen to form one molecule of water. F is the Faraday's constant (96485 C mol^{-1}), and E is a reversible voltage. The Gibbs free energy value is not constant, and it depends on the change of temperature and the state. At the standard reaction condition of 25 °C with water formed at the liquid state and the pressure of 1 atm, the value of ΔG is -237.2 kJ mol^{-1}, giving a potential (E) of 1.23 V. However, the practical potential obtained is lower due to irreversible losses as presented in a typical polarisation curve in Figure 1.4.

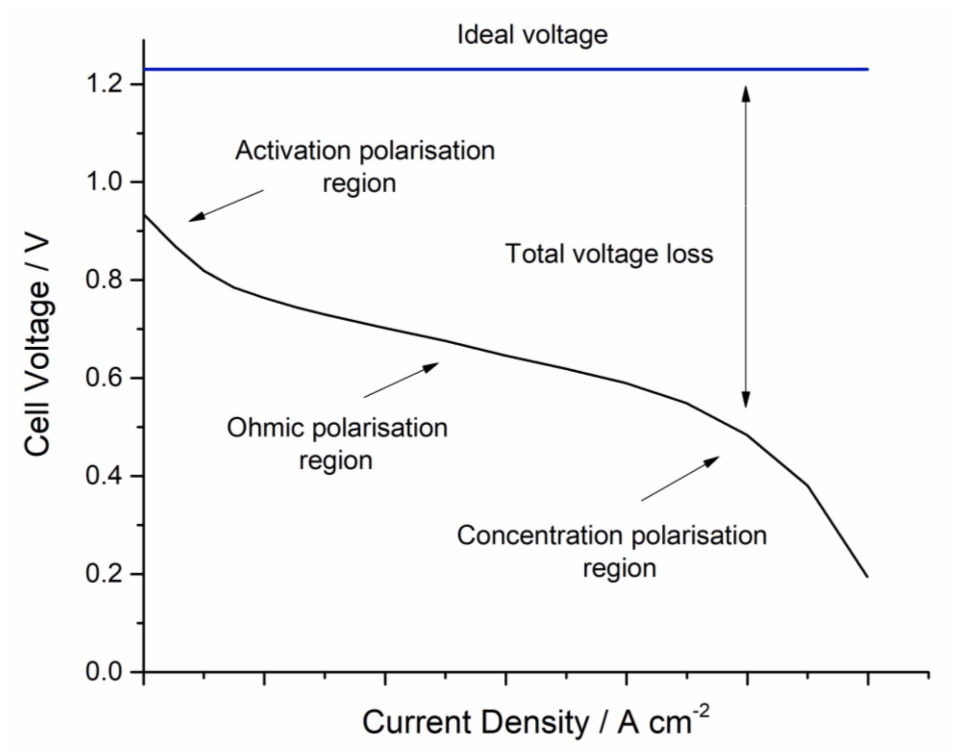

Figure 1.4 Typical potential losses for a PEMFC presented as the polarisation curve.

The open-circuit voltage (OCV) at a given operational condition (i.e. temperature, state and pressure) is approximately equal to the theoretical potential. However, there are always some losses attributed to the kinetics of the electrochemical reactions (i.e. HOR and ORR) because of the large activation energy barriers. This type of losses occurs at the high potential region at both anode and cathode, also known as the activation losses. The oxidation of impurities from the catalysts and gas crossover also contribute to the major loss at the activation region, which is mainly induced by the permeation of hydrogen through the membrane (hydrogen crossover) [16]. The Ohmic losses are proportional to the current density and commonly associated with the proton transport across the membrane, electrodes and interconnections. Hence, potential losses can be interpreted following Ohm’s law. At the large current region, the losses are referred to mass transfer resistance, which commonly observed as a sudden voltage drop. The increasing current density causes a higher consumption of reactants, thus leading to potential loss when the diffusion rate to the catalyst surface cannot sufficiently balance the consumption rate [15]. This type of current is also known as a limiting current, which determines the maximum current that can be reached in operational PEMFC condition.

1.3 Current progress and challenges

A broad range of PEMFC applications has reached the commercial markets mainly in portable power and automotive sectors, including buses and passenger cars [17]. Although the heavy-duty vehicles have a higher potential for expanding PEMFC commercialisation, the development of passenger cars has also grown rapidly since the launched of Toyota Mirai in 2014, offering more competitive features in the markets [14,18]. In some cities in Europe and Japan, PEMFCs have already been deployed for public transport vehicles [19,20]. According to the trend, public demand on the HFCVs is expected to keep rising in the future. However, HFCVs are still considered too expensive to compete with the conventional diesel or gasoline vehicles, and their availability is still limited only in few countries because of additional infrastructure requirements [21]. Increasing PEMFC demand in the market should allow a cheap manufacturing process through scalable production [10]. However, the material cost of Pt-based catalysts is less sensitive to the manufacturing volume making PEMFCs less affordable.

The intensive research and development in past decades have been focussed on improving the catalytic performance of the electrodes towards ORR and minimising Pt usage. The hybridisation of Pt with affordable earth-abundant transitional metals (e.g. Co and Ni) has gained lots of attention to incorporate the catalyst cost and activity. In 2016, Kongkanand et al. reviewed the substantial progress to reduce the Pt loading that effectively suppressed the state-of-the-art anode and cathode loading to 0.05 and 0.2 mg_{Pt} cm^{-2}, respectively [22]. The commercial PtCo NP catalysts on high surface-area carbon (HSC) support has successfully reduced the Pt amount by 7% at the cathode, and an improved power density of up to 46% has also been realised [23]. Despite that the total Pt catalyst loading has now been reduced to 0.125 mg_{Pt} cm^{-2} in some advanced researches, it still contributes a high proportion (~ 40%) of the manufacturing cost of the PEMFC stack, and requires further reduction to penetrate HFCVs in the market expeditiously.

The improvement of catalytic performance is directly integrated with the catalyst cost as it leads to a minimised Pt loading. However, catalyst stability is another challenge. In fact, it is key to maintaining fuel cell durability against degradation because of highly acidic and oxidative cathode environment during PEMFC operation. Despite the fact that Pt is considered as a stable metal, its dissolution under acidic operating condition has been observed as the main degradation mechanism along with the corrosion of the carbon support [24]. In addition, the determination of PtCo/C as the new standard PEMFC catalyst potentially arises another issue relating to the susceptibility of transitional metal toward leaching in the acidic environment [25]. The hybrid PtCo structure also induces a higher degree of segregation because of the lattice mismatch between both metals, leading to Co depletion and severe potential loss [26,27]. Therefore, putting a targeted Pt content reduction should carefully consider the stability of the substituted metal.

The major breakthroughs to improve catalyst stability include the de-alloying method, metal doping and total leaching of the transitional metals [28–31]. Many of them demonstrated significant stability improvement surpassing the DoE target 2020 of maintaining the initial activity loss of less than 40% after the life test [12]. However, most of these achievements are based on the ex-situ half-cell electrochemical measurement by using the rotating disc electrode (RDE) technique in liquid electrolytes, which cannot guarantee the same outcome as in the PEMFC operation [32]. For transportation application, the development of Pt group metals (PGM) catalysts should focus on achieving durability performance of above 5.000 hours, including also 5.000 cycles of the start-up and shut-down condition, which commonly accelerates the degradation mechanisms [12]. Therefore, testing conditions that emulate real operation in a vehicle is important in the true evaluation of catalyst stability.

1.4 Research strategies and objectives

Pt-based catalysts are still the focus to cope with the high overpotential induced by the sluggish ORR kinetic in the cathode in PEMFCs. Ideally, the catalyst possessing lower surface energy, defect-free crystal plane and preferential exposure of active sites such as a single-crystal one-dimensional (1D) nanostructure is a promising candidate with enhanced catalytic activities and minimised dissolution [33–35]. Utilising highly active and stable 1D nanostructures, the works in our group have been long focussed on developing a facile method to fabricate high-performance GDEs from 1D Pt-based nanostructure (e.g. nanowire (NW) and nanorod (NR)) arrays grown directly on GDLs. The monolayer array of single-crystal Pt NWs (diameter of ~4 nm and length of up to 120 nm) offers high porosity within the catalyst layer for improved mass transport performance. The direct catalyst deposition on the GDL surface also eliminates the requirement of the carbon support, thus minimising the degradation mechanism caused by the carbon corrosion.

These promising features motivate the advanced development of 1D Pt hybrid nanostructure GDEs, which has been the focus of this PhD work. The strategies include the alloying of Ag as a second metal possessing a much lower cost and close lattice constant to Pt to improve catalyst activities and mitigate the segregation issues to maintain stability [36]. The introduction of a third alloy metal (Au) to control the growth of the AgPt NRs and further improve their stability is also studied. The research objectives of this PhD work are listed below:

1. To develop a scalable synthesis method for carbon-supported AgPt NR (AgPt NR/C) catalysts using the formic acid reduction method, and to understand the enhanced effects of Ag and Pt towards the NR structure and catalytic properties.
2. To establish influence mechanisms of the atomic ratio of Ag and Pt with AgPt NR/C catalysts on their catalytic performance as cathode catalysts toward ORR in PEMFCs.
3. To study synergy effects of alloying Au with the AgPt NR/C catalysts toward their structure, catalytic activities and stability towards ORR in fuel cell operation.
4. To transfer the synthesis approaches and knowledge obtained in objectives 1 and 3 to develop GDEs from the AgPt and Au-AgPt NR arrays grown on GDL, and evaluate their catalytic performance and durability as cathodes in PEMFCs.

1.5 Thesis overview

An overview of the PEMFC technology is introduced in **Chapter 1,** including the basic principle and performance evaluation with a typical polarisation curve. The status and potential challenges are covered following the research strategy that guides the main motivation of this work.

The literature study is presented in **Chapter 2**, covering details of the ORR mechanism and the latest development in ORR catalysts. The stability issues are overviewed and discussed, highlighting the development of 1D nanostructure-based catalysts. This chapter further assesses the advanced development of support-free 1D Pt nanostructure electrodes as a promising feature to achieve high power performance and durability in PEMFC applications. A brief overview of the recent progress preparing 1D Pt hybrid catalysts is finally included to guide the advanced development of noble metal hybridisation into 1D nanostructures.

In **Chapter 3**, the experimental details to prepare all catalysts (i.e. 1D Pt NRs, AgPt NRs and Au-AgPt NRs) and GDEs are comprehensively described, as well as the evaluation techniques for physical characterisations and electrochemical analysis approaches in the MEA test.

Hybridisation and deposition of 1D AgPt NRs on carbon support (AgPt NR/C) using the formic acid reduction method are extensively explored in **Chapter 4**, covering the physical characterisation results to evaluate the growth mechanisms, and effects of the atomic ratio and heat treatment. The catalytic performance of 1D AgPt NR/C is evaluated as the cathode catalyst towards ORR in the MEA test, alongside their stability during the accelerated degradation test (ADT).

The introduction of Au forming multimetallic 1D Au-AgPt NR/C catalysts is explicitly presented in **Chapter 5,** corresponding to the morphology control of 1D nanostructures and atomic arrangement. The effects of the Au content on the catalytic activities and stability towards ORR are further investigated to obtain the ideal catalytic composition.

In **Chapter 6,** the growth method from Chapter 4 is adopted to grow AgPt NRs on GDLs to fabricate support-free 1D nanostructure array GDEs. The reaction conditions are studied, including the interval reduction time and atomic ratio to find an ideal parameter set considering power performance of the AgPt NR GDEs as cathodes in PEMFCs. Finally, 2 at% of Au is integrated to achieve highly durable Au-AgPt NR GDEs adapting the approach developed in Chapter 5. The power performance of the GDEs is evaluated in conjunction with the ADT in the MEA test.

All the findings obtained in this thesis are summarised in **Chapter 7**, further enclosing the overview of the PhD work and potential advanced development in the future.

Chapter 2

Literature Review

In this chapter, fundamental oxygen reduction reaction (ORR) principles are first discussed explicitly, including deriving factors of the ORR kinetic activities. The state-of-the-art ORR catalysts are then briefly reviewed, focusing on recent achievements in improving catalytic activities and durability in operating proton exchange membrane fuel cells (PEMFCs). The stability issues are further discussed considering the functional links between their morphology and durability, specifically toward the development of one-dimensional (1D) nanostructure-based catalysts. Furthermore, a broad overview of the advanced achievement of support-free 1D Pt nanostructure electrodes is also covered. The progress in improving the intrinsic activities of 1D Pt nanostructures toward ORR via alloying is highlighted, emphasising the development of Pt-noble metal catalysts to minimise the element segregation for enhanced durability. The purpose is to extend the advances in highly active 1D Pt hybrid nanostructures to the electrode level and validate their real power performance in PEMFCs, which is the main motivation of this PhD project.

2.1 Oxygen Reduction Reaction (ORR) in PEMFCs

ORR is an essential process of electrochemical energy conversion in fuel cells. The detailed mechanisms are very complicated because the multi-electron reaction involves many intermediates, which mainly depends on the nature of the catalyst material and pH environment of the electrolyte used for measurement [37,38]. The simplified scheme of ORR pathways in the acidic media is presented in Figure 2.1 [39,40]. Following a 4-electron pathway, oxygen (O_2) is reduced electrocatalytically on the catalyst surface with protons and electrons to produce water (H_2O) directly. In a series mechanism, hydrogen peroxide (H_2O_2) is formed through a 2-electron process, followed by a further reduction to produce H_2O. In PEMFCs, the ORR process with the direct 4-electron pathway is highly preferred, because the series mechanism through H_2O_2 reduces half-fold efficiency of energy conversion. Furthermore, the decomposition of H_2O_2 leads to the formation of radicals, which potentially interfere with chemical bonds of the electrolyte ionomer, causing further membrane degradation [41].

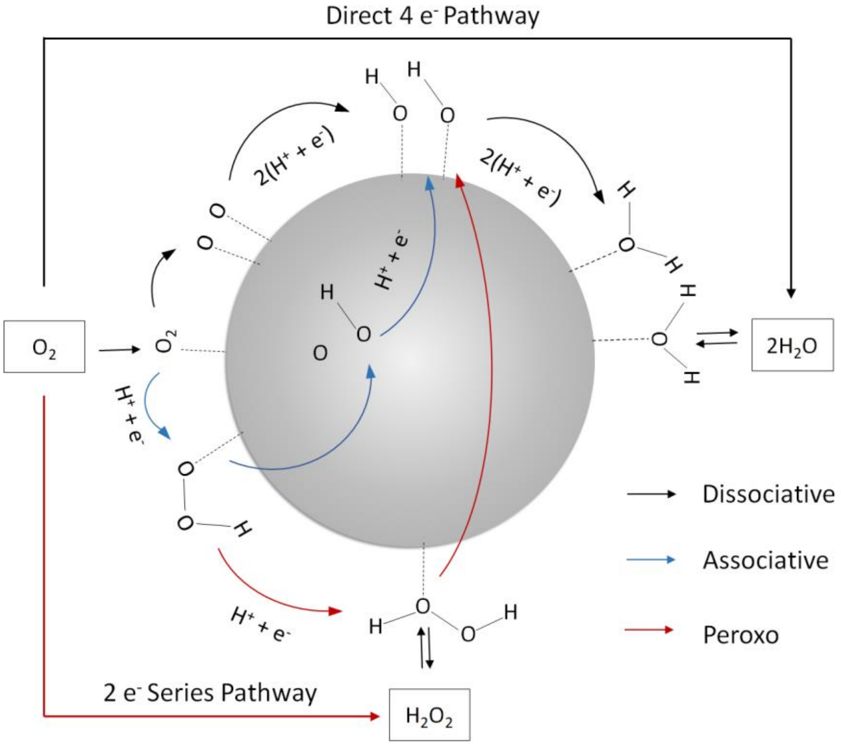

Figure 2.1 The simplified scheme of ORR pathways on catalyst surface in the acidic media.

The specific ORR principles, including dissociative, associative and peroxo mechanisms, have been proposed by Katsounaros et al. [40]. Although the detailed ORR processes are still under debate, it is widely accepted that the ORR mechanism involves O_2 adsorption and bonding cleavage, and multi-step electron and proton transfer, as shown in Figure 2.1. With the dissociative mechanism, breaking of the O-O bond occurs spontaneously after adsorption of O_2* (where * refers to adsorption on catalytic sites of the catalyst surface) generating O* intermediates, followed by successive reduction to form OH* and then H_2O*. Meanwhile, through the associative pathway, OOH* intermediate is firstly formed after adsorption of O_2*. Then, cleavage of the O-O bond leads to the formation of O* and OH* species, which are further reduced to H_2O*. The peroxo pathway is also called the second associative pathway because of the same process with the initial mechanism. However, in this pathway, HOOH* is formed prior to the O-O bond cleavage. From these mechanisms, it is clear that the adsorption behaviour of O_2 and intermediates formed during the process (O*, OH* and OOH*) determines the ORR kinetic rate, which depends on the catalyst thus defining its activities [42,43]. The rate of proton or electron transfer to dissociate O_2 is limited if the catalyst surface binds those species weakly. In contrast, too strong adsorption of the intermediates renders a limiting rate of final product desorption, which also potentially blocks active sites on the catalyst surface. Therefore, it is important to identify those catalyst materials owning moderate binding energy toward the O-containing species to achieve optimum ORR activities.

Using density functional theory (DFT) numerical simulation, Nørskov et al. described the relationship between the O bond strength on different metal surfaces and their ORR activities based on Sabatier principle, presented as a volcano plot in Figure 2.2a [43]. Accordingly, Pt shows a remarkable activity positioned at the closest to the volcano peak due to its efficiency to bind the O-containing species moderately compared to other metals on the (111) crystal facet. The metals with more positive oxygen binding energy (ΔE_O) than Pt such as Au and Ag possess a less stable attraction toward oxygen, while, most of the potential metals with more negative ΔE_O tend to attach oxygen too firmly (Figure 2.2a). It also explains why Pt has been employed as the standard ORR catalyst in PEMFCs [44]. Comparing different crystal facets, Marković et al. observed a better ORR activity on Pt (111) compared to Pt (100) [45]. Later, it was explained by Viswanathan et al. using the DFT that the Pt (100) facet tended to attract O intermediates too strongly leading to less favourable for the ORR process compared to Pt (111) as shown in Figure 2.2 b [46]. However, the DFT also showed that Pt (111) still bound oxygen a little too strongly. Hence, reducing the binding affinity of the O-containing species on Pt (111) surface has been considered as a potential strategy to boost the kinetic activity of Pt-based catalysts [47].

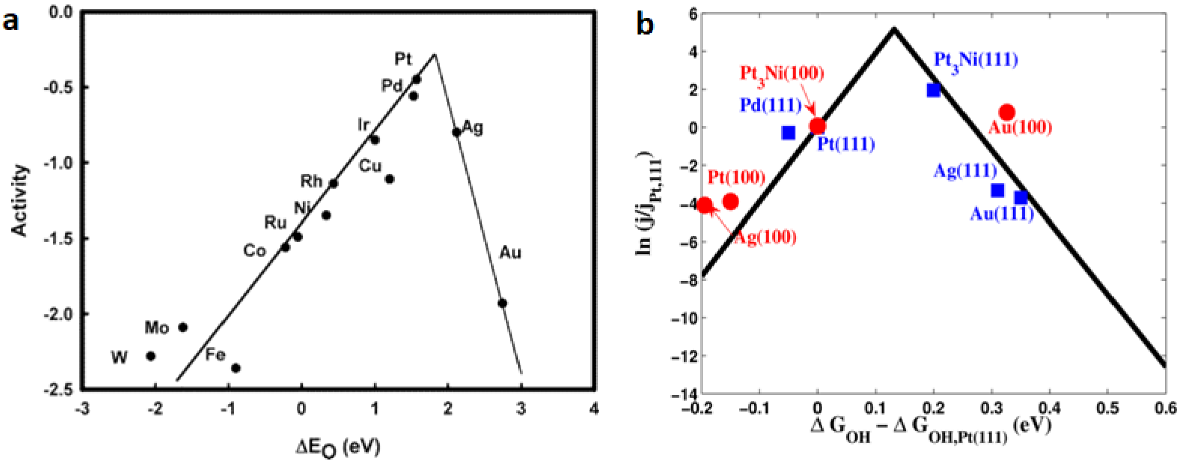

Figure 2.2 Volcano plot of the ORR activity as a function of the oxygen-binding energy on **(a)** the (111) crystal facet of metal catalysts [43], and **(b)** comparison on (100) and (111) crystal facets [46].

To date, shape-controlled nanostructures have been intensively explored to improve ORR activities of the Pt-based catalysts [48,49]. As shown in Figure 2.2 (b), the ORR activity of Pt (111) increases closer to the volcano peak after its integration with Ni (Pt_3Ni) indicating a change of the Pt catalytic activity rendered by the alloying [46]. The integration of Pt with other metals modifies not only the physical structure of Pt but also its electronic property induced by shifts of the Pt d-band centre [47,50–52]. According to Ruban et al., the integration of two metals owning different lattice constants results in a shift of the d-band centre due to adjustment of the d-band filling caused by lattice strain [53]. The d-band state represents d-type orbitals occupied by electrons, which is expected to determine the interaction on the metal surface of the adsorbates such as O and other intermediates. A direct correlation between the d-band state and catalytic activities is more complex for catalysts in operating PEMFCs [54]. However, it is still considered as an effective parameter to define the ORR kinetics on the catalyst surface, and as useful guidance for the rational design of highly active ORR catalysts.

2.2 The state-of-the-art ORR catalysts for PEMFCs

Practically, the ORR activity metric refers to the intrinsic activity normalised to the catalyst electrochemical surface area (μA cm^{-2}) named as specific activity, or the activity quantified per unit of mass (A mg^{-1}) also known as mass activity. The trend from previous studies shows that an increase of the catalyst size is followed by increasing specific activity, while a low mass activity is commonly observed for the catalyst of above 4 nm [55–58]. The change of the particle size potentially modifies the surface orientation, such as a higher proportion of Pt (111) is induced by a larger catalyst size, leading to a higher specific activity [59]. However, to reach an optimum balance of both ORR parameters, tailoring Pt nanoparticles (NPs) between 3-4 nm is regarded as the ideal catalyst size.

Currently, platinum group metals (PGM) are still the most practical catalyst materials applied for commercial PEMFCs in the anode and cathode. The recent development of ORR catalysts applies carbon black-supported Pt NPs (Pt/C, size of 3-5 nm) as the benchmark catalyst, which is primarily attributed to enhancing their catalytic activities and reducing the Pt loading in practical applications [22,60]. The improved ORR activities for hybrid catalysts Pt-M, such as Co [32,61–63], Ni [28,64–66], Fe [67–69], Pd [70–73], Au [74–76], Ag [77–79], Cu [80–83],Y [84,85], Pb [86,87] ,etc, have been widely reported in the literature. The eminence of the Pt hybridisation with other metals is mainly related to the surface property modification, which is caused by the change of the Pt-Pt bond distance and bonding interaction between Pt and the hybrid metals [53,88,89]. These phenomena lead to a shift of the Pt d-band centre and changing its electronic property, which has been discussed above in Section 2.1.

Stamencovic and co-workers demonstrated a specific activity trend with the Pt-transition metal catalysts following an order of Pt < Pt_3Ti < Pt_3Fe < Pt_3Ni < Pt_3Co [90]. The improvement factor of an annealed Pt_3Co catalysts is up to 5 times than of monometallic Pt, which is originated from an optimum d-band shift to effectively modify the electronic structure on Pt surface [12]. In another work, they achieved a 90-fold higher specific activity than Pt/C through a tailored $Pt_3Ni(111)$ catalyst [65]. It was presumed that the unique electronic structure and atomic arrangement of $Pt_3Ni(111)$ were the main factors rendering the high catalytic activity. These works derived a crucial impact on the following development of Pt alloy-based catalysts in the past decade. To date, the advanced design of Pt alloy nanostructures has been considered as a new baseline for the second generation ORR catalysts [91]. It is also worth noticing that the mass activity is intensively proportional to the economic cost related to the catalyst usage, serving a more reliable metric for a practical perspective. For this reason, the hybridisation of Pt with transition metals, especially Co and Ni, has attracted the most attention considering the advantage of reducing the Pt loading with much cheaper transitional metals.

The advanced catalyst architectures, which have been reported with significantly improved ORR activities, are presented in Figure 2.3a [92]. The major breakthrough has been achieved from the 1D nanostructure of ultrafine jagged Pt nanowires (NWs). It was reported with an extraordinary mass activity of 13.6 A mg^{-1} at 0.9 V vs reversible hydrogen electrode (RHE) (52-fold higher than Pt/C), which has been the highest for ORR catalysts up to now [31]. The boosted ORR activity was attributed to a rhombic structure on the NW surface rendering a weakening Pt-O bond, enhancing the kinetic activity on the Pt surface. The rhombic structure was obtained through electrochemical dealloying of PtNi alloy NWs. After a complete Ni leaching, the re-forming Pt NWs with the jagged surface was generated owning a smaller diameter of 2.2 nm as shown by transmission electron microscope (TEM) and high-resolution TEM (HR-TEM) images (Figure 2.3c-d). The structure demonstrates the effectiveness of extending the electrochemical surface area (ECSA) and mass activity at the same time. The stability test was performed using an accelerated degradation test (ADT) with 6000 potential sweeping cycles between 0.6 - 1.0 V vs RHE in O_2-saturated 0.1 M $HClO_4$. The ADT confirmed the outstanding stability of the jagged Pt NWs, showing only ~7% ECSA loss, whereas Pt/C exhibited much more significant ECSA loss of up to ~30%.

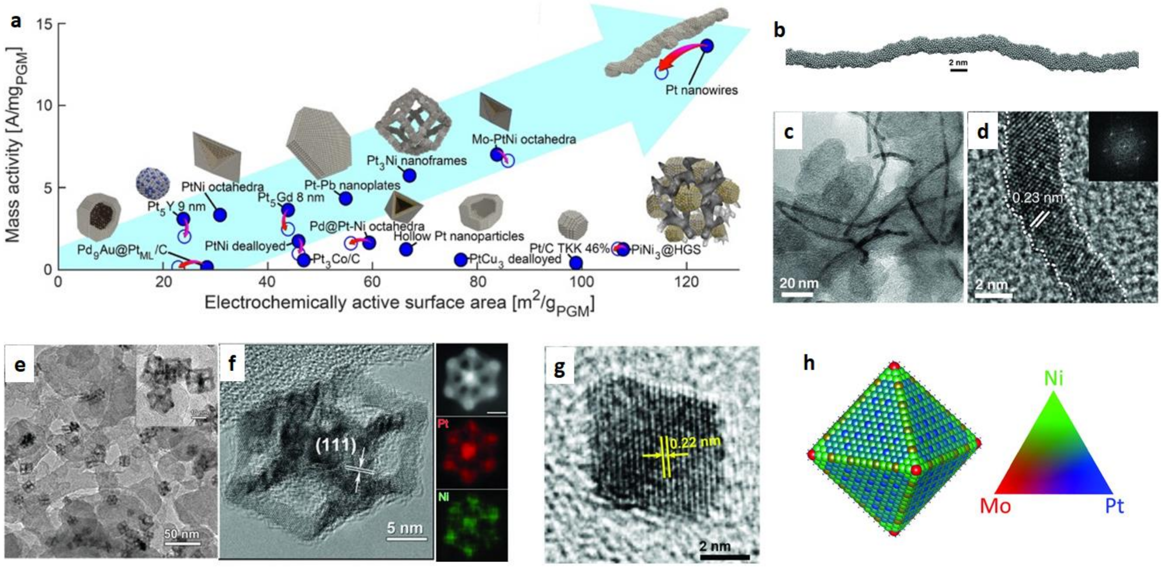

Figure 2.3 (a) Recent advanced development of ORR catalysts as a function of electrochemical surface area (ECSA) and mass activity at 0.9 V vs RHE based on the RDE measurement [92]. **(b)** Illustration, **(c)** TEM and **(d)** HR-TEM images of ultrafine jagged Pt NWs [31]. **(e)** TEM and **(f)** HR-TEM with STEM-EDX mapping images of Pt_3Ni nanoframes [28] and **(g)** HR-TEM image of Mo doped Pt_3Ni octahedra with **(h)** theoretical simulation representing atomic arrangements of Mo-Pt_3Ni octahedral [29].

Another expanded highly active $Pt_3Ni(111)$ catalyst is shape-controlled, and third metal-doped Mo-Pt_3Ni octahedra (Figure 2.3g-h) [29]. The ORR activity obtained of 6.98 A mg^{-1} at 0.9 V vs RHE is lower than that of the jagged Pt NWs, but, it served a better enhancement of up 73-fold than of commercial Pt/C catalysts. Chen et al. demonstrated a de-alloying method to construct a Pt_3Ni nanoframe catalyst with a Pt-skin (Figure 2.3e-f) [28]. The open structure is an advanced design to extend the high-surface-to-volume ratio of the catalyst and making it more accessible for electrochemical reactions. As a result, an extraordinary mass activity of 5.7 A mg_{pt}^{-1} was achieved. Both shape-controlled architectures (octahedra and nanoframe) based on Pt_3Ni catalysts showed remarkable stability after the accelerated degradation test

(ADT) in 0.1 M $HClO_4$ electrolyte. After 8000 potential sweeping cycles between 0.6 – 1.1 V vs RHE, Mo doped Pt_3Ni octahedral exhibited 5.5 % loss of its initial ORR activity, which was much lower compared to more than 50% of undoped Pt_3Ni [29]. While negligible activity loss was claimed by Pt_3Ni nanoframes compared to 40% loss of commercial Pt/C after 10.000 cycles of potential sweeping between 0.6-1.0 V vs RHE [28].

Those impressive achievements in catalyst activities were all recorded in ex-situ half-cell electrochemical measurement using the rotating disk electrode (RDE) technique in liquid electrolytes. There is still a huge challenge for a full projection of these superior activities of shape-controlled catalysts to practical fuel cell electrodes. The measured ORR activity using the RDE technique is usually much higher than that obtained in the membrane electrode assembly (MEA) test in single PEMFCs [60]. For instance, Liu and co-workers reported an escalated mass activity of 12.36 A mg_{pt}^{-1} for Pt-Co NPs catalysts using the RDE measurement, but only 1.77 A mg_{pt}^{-1} achieved in the MEA test [32]. In the RDE measurement, an extremely thin catalyst layer is employed, and the liquid electrolyte can easily penetrate the catalyst surface or even into pores inside, thus renders less concern to the mass transfer resistances. In practical fuel cell electrodes in the MEA test, reaching into a pore of less than ~20 nm is a challenge for ionomer because of its large size, limiting proton and oxygen transport through the catalyst layer [93]. As a consequence, it potentially induces an immense voltage loss at a high current density region as observed from the preliminary MEA test of the Pt_3Ni nanoframe catalysts [94]. Pam et al. reported the realisation of the advanced shape-controlled Pt-based catalysts into the MEA test in H_2/O_2 and H_2/Air (Figure 2.4) [95]. Utilising the ultra-low Pt loading, most of the shape-controlled Pt hybrid catalysts generated a higher mass activity than of commercial Pt/C measured at 0.9 V (Figure 2.4a). However, only a few of them outdo the performance of Pt/C catalyst at the fuel cell operational voltage of 0.6 V under H_2/Air feeds (Figure 2.4b).

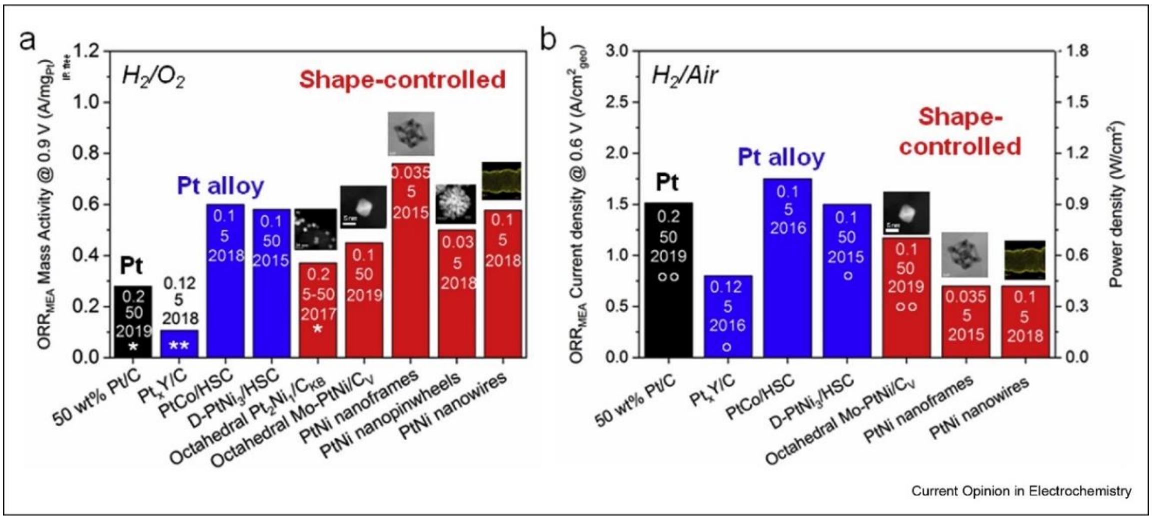

Current Opinion in Electrochemistry

Figure 2.4 Compared the catalytic activity of the advanced Pt-based ORR catalysts: **(a)** mass activities measured at 0.9 V_{Cell} in MEAs under H_2/O_2 feeding single fuel cells, and **(b)** power densities and current densities recorded at 0.6 V in single fuel cell MEAs under H_2/air feeds [95].

Poor stability is another big challenge for ORR catalysts, which is attributed to the harsh operating conditions in PEMFCs, high operation temperature and a wide range of operation current. Large potential fluctuation during start-up and shut down can accelerate the cell degradation induced by the partial air exposure at the anode side raising the interfacial voltage difference of up to 1.44 V. Even for potential sweeping conducted at a slightly higher range of 0.6-1.26 V vs RHE in the RDE measurement, the octahedral Mo-PtNi/C catalyst exhibited a severe degradation with an activity loss of 78% after only 1000 cycles, compared to only 5.5 % loss after 8000 cycles between 0.6 – 1.1 V vs RHE [29]. A big issue with the PtCo and PtNi alloy catalysts is their unstable composition, induced by segregation of the alloyed transitional metals. Electrode from the ultrafine jagged Pt NW may be less interfered with the durability issue advantaging from its 1D nanostructure feature which can offer a better resistance toward agglomeration and Ostwald ripening [31]. Nevertheless, the serious difficulty with scalable production of these highly active catalysts is still a hindrance to bringing them to the MEA level. Currently, Toyota Mirai utilises PtCo/C catalysts, which achieved excellent catalytic activities in the latest commercial fuel cell vehicles (Figure 2.4) [14]. However, the fuel cell durability is still a big challenge that yet to be solved in order to meet the DoE 2020 target of minimising the activity loss of less than 40% in practical condition [12].

The durability issues in PEMFCs are mostly linked to the degradation of several components in fuel cell stack, including the catalyst NPs, carbon support, ionomer, membrane, gas diffusion layer (GDL) and bipolar plates. According to Borup et al., the deterioration of the MEA causes the major degradation of PEMFCs [41]. Such an issue is mainly directed to the electrocatalyst stability at the cathode aggravated by the high voltage in fuel cell operation and acidic environment. Referring to commercial PtCo/C catalysts, the stability is primarily ascribed to (i) dissolution of the NPs [96–98], (ii) corrosion of the carbon support [99–101], and (iii) segregation of metal alloy [26,27,102].

Degradation mechanisms may be minimised for monometallic Pt NP catalysts as it is less concerned with atomic segregation. However, Meier et al. discovered the domination of Pt NPs dissolution toward stability [24]. Atomic dissolution is a critical problem, which has been long observed in a highly corrosive and oxidising environment, and it is mostly derived by the catalyst size and surface coordination [98]. The trends in stability observation confirm the susceptibility of smaller NPs toward dissolution and agglomeration, which is potentially related to their high surface energy [103]. Holby et al. explained the significant increase of Gibbs-Thomson energy within the small NPs of 2-3 nm inducing a significant susceptibility towards atomic dissolution, and leading to a drastic decrease of the surface area under PEMFCs operation condition [104]. Further intensive studies have revealed the dependency of size effect of NPs towards Pt/Pt-M dissolution in PEMFCs [58,105–108]. Hence, determining the critical size of the ORR catalyst above 3 nm should be considered to minimise the stability issues. Furthermore, a certain Pt surface facet tends to attract more O species than other facets to increase the formation of Pt oxide, which accelerates Pt dissolution [109]. Markovic and co-workers also revealed the relation of Pt surface crystal facet coordination towards stability following order of Pt (111) > Pt (100) > Pt (110) [110]. The high-coordination site shows a better resistance against dissolution, suggesting better stability for the catalyst with a lower number of defects. In agreement, Chung et al. observed starker atomic dissolution from the low-coordination sites of Pt catalysts, leading to the formation of larger defects, and decreasing electrochemical durability [111].

Further development of ORR catalysts should consider these factors rendering the stability issues. It is agreed that ORR is the structure-sensitive mechanism, for which the reactions occurring on the catalyst surface are driven by the nature of the composed material and surface crystal facets. These outcomes rationalise the importance of controlling the surface structure, together with the shape and size of nanostructures to achieve highly active and stable catalysts. The catalyst stability plays a significant role in fuel cell durability. If these main propositions triggering NP susceptibility in PEMFC condition are subdued, the further advanced engineering of Pt hybridisation can be realised.

2.3 1D Pt-based nanostructure catalysts

Asymmetric single-crystal 1D Pt-based nanostructures (e.g. NWs and nanorods (NRs)) are the ideal morphology to overcome the drawbacks of 0D NP catalysts, specifically toward the dissolution and Ostwald ripening [33]. The typical growth into one direction enables the exposure of some specific crystal facets with limited lattice boundary and exhibits lower surface energy compared to their 0D counterparts, as well as a fewer defect surface [34]. Thus, the enhanced catalytic activities and stability are expected from single-crystal 1D nanostructure catalysts. Additionally, a catalyst layer built from 1D nanostructures offers high porosity which is an advantage to promote mass transport performance in PEMFC operation. Lu et al. has reviewed and highlighted the promising progress of the 1D Pt-based nanostructures as highly active and durable electrocatalyst design toward ORR for PEMFCs [35]. Yet, to meet the high standard requirements for practical application, the fabrication procedure needs to consider the extension of the active sites, enhancement of intrinsic activities and scalable production.

The 1D ultrafine jagged Pt NW is considered as the most promising feature for an ORR catalyst, attracting lots of intention for current research development [31]. It provides a significant enlarged ECSA, which is commonly a drawback for single crystal 1D Pt-based nanostructure catalysts. However, scaling up synthesis of 1D jagged Pt NWs transferable to MEA fabrication remains a huge challenge until now. The methods utilised organic solvent oleylamine (OAm), and several advanced steps of product separation and Ni leaching. Such a method may be a hindrance to maintain high-quality materials in scale-up production. Whereas, a large amount of catalysts of up to gram scale is required for practical usage in fuel cell stacks [112].

Several approaches have also been introduced to extend the number of catalyst active sites of 1D Pt-based nanostructures. Song et al. employed cetyltrimethylammonium bromide (CTAB) as a soft template to synthesise ultra-thin Pt NWs [113]. With a smaller diameter of 2.2 nm, Pt NWs achieved a slightly larger ECSA of 32.4 $m^2\ g_{Pt}^{-1}$, intensifying an effective approach to extend the number of Pt active sites by reducing the NW size. Koenigsman et al. presented the size-dependent catalytic activity of 1D Pt nanostructures by controlling the diameter of Pt NWs [114]. The solution-based synthesis was employed using sodium borohydride ($NaBH_4$) as the reducing agent with a mixture of N,N-dimethyl formamide (DMF) and toluene. The acid wash treatment was then applied to exfoliate Pt NWs, reducing the diameter to ~1.3 nm. The measurement in 0.1 M $HClO_4$ recorded a specific activity of 1.45 mA cm^{-2}, which is 3- and 7-fold higher than that of non-acid treated Pt NWs and 0D Pt/C, respectively. Apparently, the acid wash effectively dissolved amorphous Pt, thus optimising the active surface exposure and minimising the defect sites, which profoundly enhanced the kinetic activity of the NW surface.

A comparative study was also conducted and confirmed the sensitivity of the ORR activity toward the diameter and surface morphology of Pt NWs, as shown in Figure 2.5c [115].

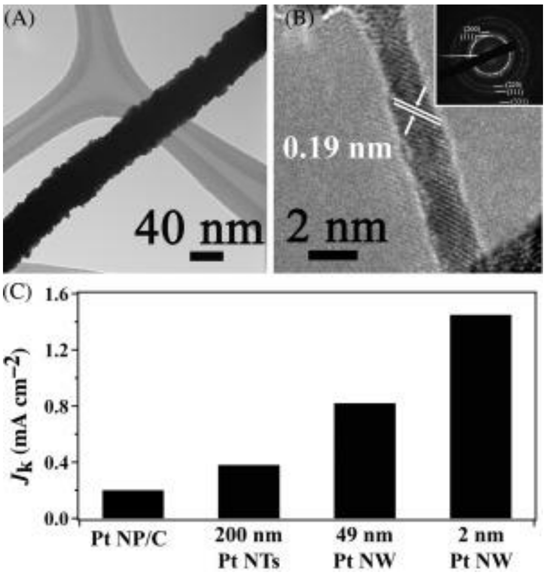

Figure 2.5 TEM images of Pt NWs with an average diameter of **(a)** 49 nm and **(b)** 2 nm. **(c)** The specific ORR activity measured at 0.9 V as a function of the size of 1D Pt nanostructures as a comparison with commercial Pt/C catalysts [115].

Apart from controlling diameter to achieve Pt NWs with a high ECSA to improve their ORR catalytic activities, a biometric synthesis method was developed by Ruan et al. assisting the formation of a network structure with 2 nm Pt NWs having twin planes [116]. The ultrafine 1D morphology and multiple-twinned structure contributed to extended ORR active sites leading to increased ECSA of 80.36 m^2 g^{-1}, which was even higher than 77.77 m^2 g^{-1} of the commercial Pt/C catalyst (20 wt% Pt on Vulcan XC72R carbon support, Johnson Matthey (JM)). A 58.2% higher mass activity than that of Pt/C was recorded in half-cell measurement in 0.1 M $HClO_4$. Despite a higher degree of defect sites, the Pt NW network structure showed remarkable stability after 6000 cycles of ADT, with ECSA losing less than 15% compared to 56.7% of Pt/C.

From these results, it is agreed that small size and preferential exposure of highly active surface facets offer an improved ORR activity through the extension of the catalyst active site number.

However, the catalytic performance and stability of these 1D catalysts have not been evaluated in operating PEMFCs, which may exhibit a different behaviour as that in the half-cell measurement [50,117]. For practical application in fuel cells, scalable synthesis and rational design should be the main intention. The utilisation of template method proposes a facile diameter and length adjustment approach by controlling the templates. The exploration of templates, such as porous alumina membrane, anodic aluminium oxide film, pores of a track-etched polycarbonate, etc. demonstrated the advantage of the template method to obtain ordered uniform 1D nanostructures [118–121]. Nevertheless, the scalability of template approaches is limited due to the complication of template removal. The usage of surfactant, e.g. toluene, OAm and polyvinylpyrrolidone (PVP), should also be taken into consideration, as it requires an extra sophisticated step to remove them from the catalyst surface. Otherwise, the remaining contaminants potentially interfere with the catalytic activities in operating fuel cells [122–124].

Sun et al. demonstrated a surfactant-free method for growing Pt NWs by employing a slow reaction approach using a weak reducing agent, formic acid [125]. The reduced Pt ions initially generated Pt seeds possessing very high surface energy, and some of them form agglomerates. Under a very slow Pt reduction rate at room temperature, the accretion continued with preferential crystal growth along the <111> direction. After 16 hours it formed a flower-like structure constructed from single-crystal Pt NWs with a diameter of ~ 4 nm. This method was successfully transferred onto Vulcan XC72 carbon to prepare Pt NW/C catalysts as presented by scanning electron microscope (SEM) and TEM images (Figure 2.6a-c) [126]. The growth density was regulated by changing the mass ratio of Pt precursor and carbon support, while the reaction time contributed to control the length of Pt NWs. The evaluation as the cathode catalysts in the MEA test under H_2/O_2 showed enhanced power performance compared to the state-of-the-art 0D Pt/C (Figure 2.7d), which was attributed to the large aspect ratio of Pt NWs improving O_2 diffusion toward Pt surface. Although the bulk feature of the anisotropic 1D nanostructure led to a lower surface area of $22.1\ m^2\ g_{Pt}^{-1}$ compared to $43.3\ m^2\ g_{Pt}^{-1}$ of Pt/C (Figure 2.6e), Pt NW/C catalysts still showed a 50% higher mass activity and 3-fold larger specific activity compared to 0D Pt/C. The ADT was conducted using the ex-situ half-cell measurement in $0.5\ \mathrm{M}\ H_2SO_4$. The results showed that after 4000 potential sweeping cycles Pt NW/C exhibited less ECSA loss of 40%, which was much lower compared to 67.5% of Pt/C (Figure 2.6f-g) [127]. These outcomes intensify that the morphology change from 0D to 1D gains a large enhancement on the catalytic activities and stability. The smooth atomic surface and preferential exposure of highly active crystal facets facilitate a fast ORR kinetic on the Pt surface and increase the resistance against dissolution and Ostwald ripening.

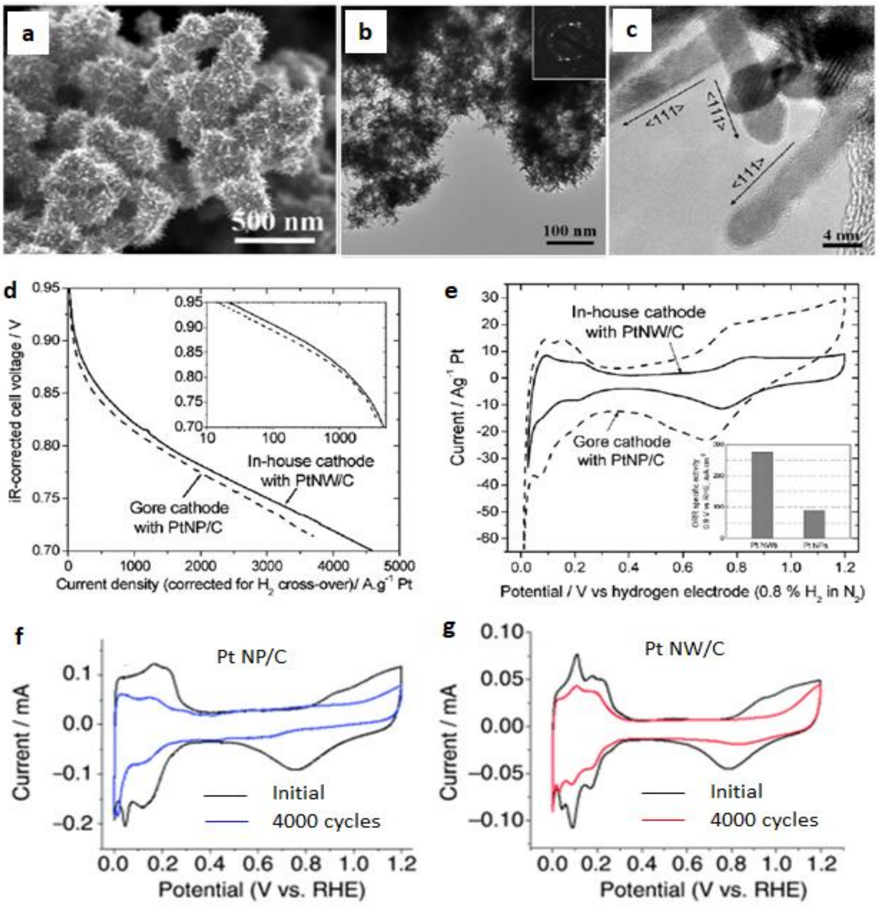

Figure 2.6 (a) SEM and **(b-c)** TEM images of Pt NWs grown on the carbon support. **(d)** Comparison of cathode polarisation curves of the as-prepared Pt NW/C and Pt NP/C catalysts, **(e)** corresponding CV (inset: comparison of the ORR specific activity) [126]. CV curves of **(f)** Pt NP/C and **(g)** Pt NW/C before and after 4000 potential cycles of ADT [127].

To date, the formic acid reduction method is still considered as one of the most practical approaches for scale-up preparation of Pt NWs. It can be achieved at room temperature without using any template or surfactant in aqueous solution. Adapting this method [126], Li et al. fabricated 50 cm^2 MEA utilising the as-prepared Pt NW/C as the cathode catalyst with a Pt loading of 0.4 mg$_{pt}$ cm^{-2} [128]. Single-cell test in H_2/Air showed 5% higher power performance than that from commercial Pt/C catalysts. Pt NW/C has also been employed as the cathode catalyst to construct 1.5-kW PEMFC stack consisting of 15 individual MEAs with an active area of 250 cm^2 [129]. The compared power density after 420 hours dynamic drive cycle test showed degradation rates of 14.4% and 17.9% for the as-prepared Pt NW/C and commercial Pt/C, respectively (Figure 2.7a-b). TEM images showed the minimum change of Pt NW structure before and after the durability test (Figure 2.7c-d) compared to 0D Pt/C catalysts with severely increased particle size. It further demonstrates the superiority of 1D nanostructures towards the degradation mechanisms in fuel cell operating conditions. A small power performance loss of Pt NWs was mainly attributed to the degradation of Pt/C catalysts at the anode. The regression of electrode structure may also contribute to the power decline originated from the less optimised contact between ionomer and Pt NWs [130]. Nevertheless, these achievements further encourage the advanced development of 1D Pt-based nanostructures, e.g. evolving the concept of support-free Pt-based NWs, which have been demonstrated as an ultimate approach to improve catalyst durability [127,131–133].

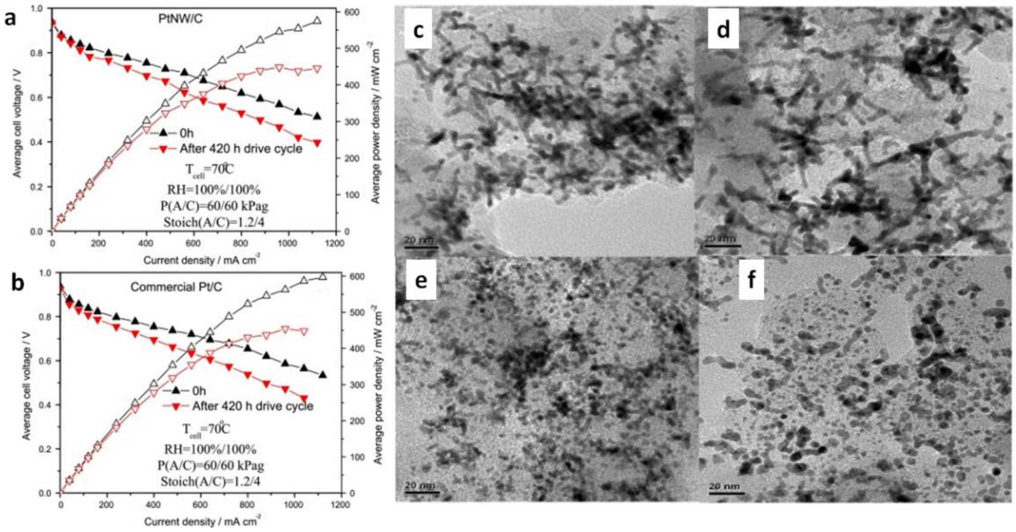

Figure 2.7 Polarisation and power density curves of the fuel cell with **(a)** Pt NW/C, **(b)** commercial Pt/C as the cathode catalyst. TEM images of **(c-d)** Pt NW/C and **(e-f)** commercial Pt/C before and after 420 hours durability test, respectively [129].

2.4 1D Pt nanostructure gas diffusion electrodes

Schematically, the degradation mechanism can be effectively minimised by eliminating the carbon support using a self-supported catalyst layer (Figure 2.8a) [127]. Carbon black is commonly used as the catalyst support in PEMFCs. It provides good conductivity and large surface area for better catalyst dispersion and distribution. Its porous structure is also an advantage for facilitating oxygen mass transfer through the catalyst layer in fuel cell operation [134]. However, under the acidic condition and high oxygen concentration at the cathode, the oxidation of carbon is thermodynamically possible in operating PEMFCs at a potential range of 0.6-1.0 V, and can be worsened at some certain conditions of restart and shutdown, which can dramatically accelerate carbon corrosion [135,136]. Consequently, it degenerates the detachment of metal catalysts, promoting aggregation and decreasing ECSA [96,137,138]. Such condition also compromises the electronic conductivity resulting in a decreased intrinsic activity for the metal catalyst attached to carbon support [138]. Therefore, eliminating carbon support can be a potential solution to improve durability.

A simple approach to growing support-free Pt NWs onto carbon paper without catalyst support material was introduced by Sun et al. via self-assembled single-crystal NWs forming 3D nanoflowers (Figure 2.8b-e) [125]. Adopting a similar approach using the formic acid reduction method, our group successfully grew single-crystal Pt NW arrays on GDLs [139]. GDLs are the main component constructing the MEA to support the catalyst layer. Thus a GDL with Pt NWs can be directly used as a gas diffusion electrode (GDE) for PEMFCs. Monolayer array of Pt NWs with a diameter of ~4 nm and length of ~ 120 nm constructs a three-dimensional (3D) ordered catalyst layer on the GDL surface. With a low Pt loading of 0.4 mg cm^{-2}, the Pt NW GDE recorded 25% higher peak power density than that with a commercial Pt/C cathode (E-TEK ELAT^{TM} GDE LT120EW, Pt loading 0.5 mg cm^{-2}, 25 cm^2 MEA tested under H_2/air). The thin catalyst layer with the high aspect ratio Pt NWs and open structure facilitates gas transport to reach the catalyst surface and reduces oxygen transfer resistance, thus leading to improve power performance.

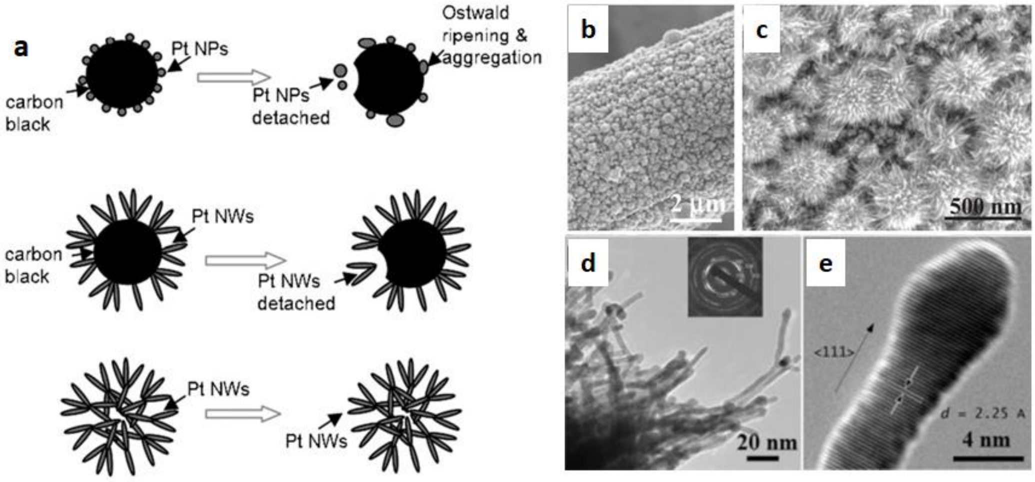

Figure 2.8 (a) Schematic of morphology changes that occur in different Pt structure during accelerated electrochemical cycling [127]. **(b-c)** SEM and **(d-e)** TEM images of Pt NWs grown on carbon fibres within carbon paper [125].

The power performance of Pt NW GDEs is highly dependent on the Pt amount deposited on the GDL. According to our observation, the trend with the increase of the Pt loading was followed by an increasing open-circuit voltage (OCV) and power output with an optimum loading of ca. 0.5 mg_{pt} cm^{-2} [140]. A higher loading resulted in a drastic voltage loss at the larger current density region caused by the arising mass transfer resistance. It was attributed to severe agglomerated NWs as observed from the GDE with a high Pt loading of 1.0 mg_{pt} cm^{-2}. The inert nature of the GDL surface provides a limited number of nucleation sites inducing the large aggregates and minimising the Pt utilisation ratio. It suggests the importance of controlling the Pt NW density and distribution to achieve high power performance electrodes.

GDLs are made of carbon fibre-based substrate with a top carbon sphere-based microporous layer (MPL). They are coated with superhydrophobic polytetrafluoroethylene (PTFE) to prevent water flooding during fuel cell operation [141]. This feature makes their surface very difficult to be wetted in aqueous solution as that in the formic acid reduction process, thus limiting the nuclei cites and finally forming many large Pt NW agglomerates decreasing the catalyst utilisation ratio. The distribution of Pt NWs has been successfully improved through controlling the reaction temperature of the growth process on the GDL [142]. The study revealed the effectiveness of applying a moderate reaction temperature of 40 °C to reduce the water contact angle and improve the wettability on the hydrophobic GDL surface. Increasing temperature also induced a faster reaction rate. As a result, it boosted the nucleation site number on the GDL surface and minimised the formation of large Pt NW agglomerates (Figure 2.9a). The MEA test with the Pt NW GDE as the cathode confirmed an improved power performance (Figure 2.9b), and nearly double mass activity compared to a commercial Pt/C GDE (TKK). Furthermore, the durability of the Pt NW GDE was evaluated through in-situ 2000 potential cycles, exhibiting a lower ECSA loss of 48% than 67% of the Pt/C GDE (Figure 2.9c).

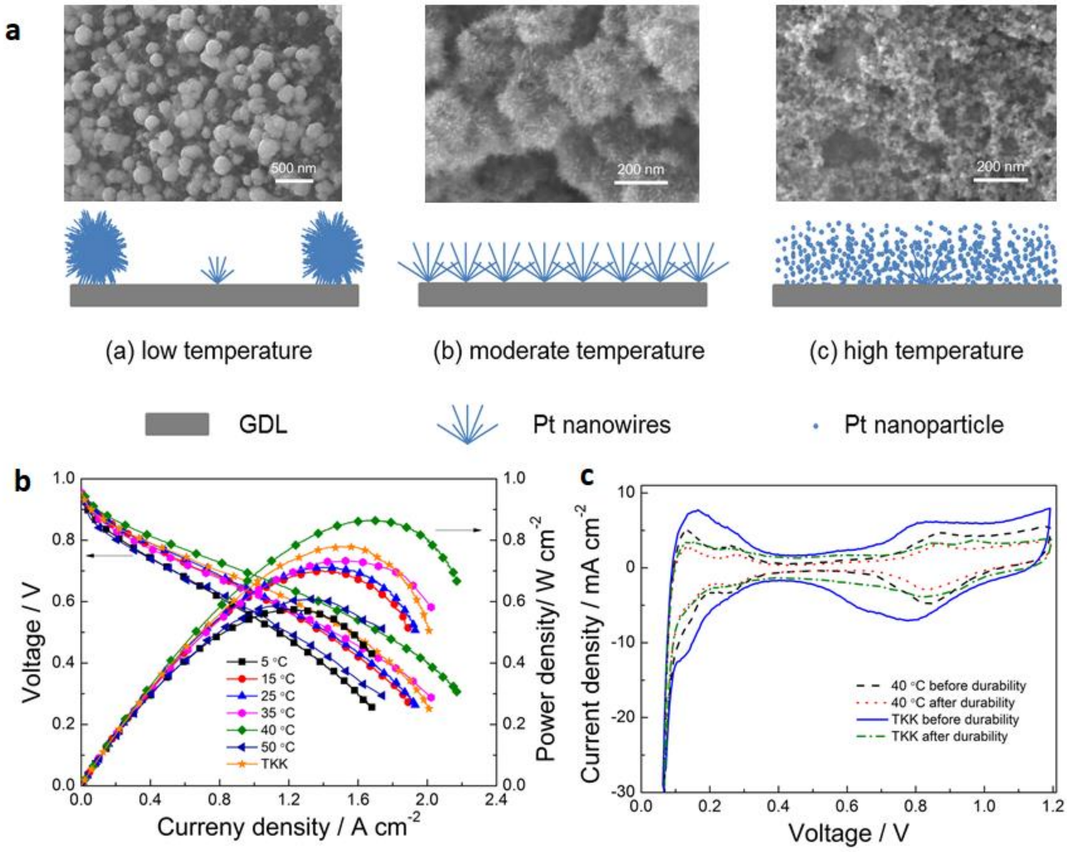

Figure 2.9 (a) Schematic growth of Pt nanostructures on GDL at different reaction temperatures, with **(b)** corresponding polarisation and power density curves and **(c)** CVs of PtNW GDEs grown at 40 °C before and after the ADT in comparison to Pt/C (TKK) [142].

Active screen plasma treatment has also been employed as an effective method to improve the dispersion and distribution of Pt NWs on GDLs at relatively low temperature [143]. Plasma nitriding led to a large number of defects and provided the GDL surface with more functional groups. The increased surface activity enabled a good contact of the GDL surface with the mediating reaction solution. It promoted the uniform nucleation of Pt and the formation of ultrafine and long Pt NWs resulting in an enlarged ECSA.

The later work in our group demonstrated the introduction of Pd nanoseeds on the GDL surface and their influences on the morphology and distribution of Pt NW arrays [70]. Mixing Pd and Pt precursors ($PdCl_2$ and H_2PtCl_6) in formic acid solution rendered a faster reduction of Pd to form nanoseeds on the GDL surface. The seeding effect was observed with a much lower Pd content of ca. 5 at%, leading to more uniform growth of 1D nanostructures forming PtPd nanodendrites on the GDL. Such structure provided a larger ECSA and smaller mass transfer resistance than that of the Pt NW GDE. Another seeding method using a thin Pt/C NP (0.005 mg_{Pt} cm^{-2}) layer as a matrix to control Pt NW growth was demonstrated by Sui et al. [144]. Pt seeds facilitated deposition of the reduced Pt atoms rendering more uniform Pt NWs, but an excessive amount of Pt NPs resulted in reduced length and crystallinity. Despite the recorded current density at 0.6 V was 5% lower than a commercial Pt/C GDE, the significantly enhanced mass current of 89.56 A g_{pt}^{-1} was obtained, which is 2.1-fold higher than that of the Pt/C GDE. Other works by using a carbon matrix for optimising the growth of Pt NWs have also been demonstrated [145,146]. Through these works, it is agreed that the uniformity of catalyst deposition and distribution are the main factors determining the electrode power performance in PEMFCs.

These studies demonstrated a promising development of support-free 1D Pt-based nanostructure electrodes with improved power performance and durability. A further development to improve ORR activities with a lower Pt loading can attain a closer stage to the commercial level. The enhancement of intrinsic activities through hybridisation of Pt NWs to build NW array GDEs is a promising approach to improve ORR kinetic and further minimise Pt loading in PEMFCs, which will be further explored in this thesis.

2.5 Toward the development of 1D Pt-based hybrid nanostructure electrodes

The synthesis of bimetallic and multimetallic metal alloy 1D nanostructures with excellent stability is another challenge. The different nature of each metal such as the surface energy, atomic size and lattice constant render segregation and deformation of 1D nanostructures during fuel cell operation. However, the alloying of the second metal is considered as an effective strategy to boost the catalyst intrinsic activity and reduce Pt loading, thus the research on 1D Pt-based alloy nanostructures has also attracted many efforts. As demonstrated by Zhang and co-workers, the alloying with Co through a soft surfactant template method enhanced the mass activity of Pt NW/C catalysts by 20% to 1.5-fold higher than the Pt/C catalyst (40 wt% Pt/C, JM HiSpec 4000) [147]. After a stability test of 3.000 potential cycles between 0.6 and 1.15 V vs RHE, PtCo NW/C showed only an ECSA loss of 14.7% compared to 35% of the Pt/C catalyst.

The degradation is commonly more pronounce for Pt hybrid catalysts induced by poor stability of the transition metals, which are oxidised spontaneously at low pH, and suffer from leaching under electrochemical reaction in acidic conditions [148]. Like the Pt alloy NPs, the leaching of transitional metals is also a challenge for 1D catalysts. Sun and co-workers adopted an organic-phase synthesis method using 1-octadecene (ODE) and OAm as reducing agent to synthesise ultrafine FePt and CoPt alloy NWs with a diameter of ~2.5 nm [149]. A post-treatment was conducted with acetic acid to dissolve most of the alloyed transition metals, remaining only ~20% of Fe and less than 10% of Co. It resulted in improved ORR activities for $Fe_{20}Pt_{80}$ NWs compared to Co_8Pt_{92} NWs and commercial Pt/C. After 4000 potential cycles, a decreased Fe ratio was observed, suggesting the leaching of Fe, although TEM analysis still showed very little NW morphology change before and after the durability test. Jiang et al. demonstrated the advanced structuring of multimetallic PtCoNi NW catalysts through a solvothermal approach utilising glucose as the reducing agent [150]. The method privileged a high crystallinity surface and sub-nanometer size 1D nanostructure with a diameter of ~ 1 nm. The catalyst exhibited an improved ORR mass activity of 4.20 A mg^{-1}, which was 4-, 1.4- and 32.3-fold higher than that of Pt NW, PtNi NW and commercial Pt/C catalysts, respectively. After 30.000 cycles ADT in 0.1 M $HClO_4$, PtCoNi NW catalyst exhibited 27.6% ECSA loss, which was attributed to the dissolution of transition metal as confirmed by EDX analysis presenting a decreased atomic ratio of Ni and Co of up to 40%. During the MEA test, the transition metals leached out potentially contaminates polymer electrolyte membrane, accelerating the cell degradation and significant performance loss [151].

The stability issues with the bimetallic nanostructures originate from the atomic mismatch and different surface energies between two metals, thus tending to segregate at some certain conditions such as during the ORR process [152]. The DFT showed Pt surface segregation on PtNi, which was rendered by lower surface energy and much smaller atomic size of Ni than those of Pt. The trend on the surface segregation and stability toward ORR suggested the highly unstable structure of bimetallic Pt with 3d elements such as Fe, Co, Ni and Cu due to the lattice mismatch, inducing a high degree of atomic dissolution [36]. The structuring of more ordered intermetallic Pt-M alloy with transition metals through high-temperature annealing has been shown as a practical approach to minimise the segregation and improve stability [61,153]. However, applying such treatment is a challenge for most shape-controlled alloy catalysts, such as due to the susceptibility of ultrafine 1D Pt-based nanostructures toward the heat treatment, annealing at a temperature above 200 °C causes sintering and tunes NWs into agglomerated NPs [149,154]. The DFT predicted better stability of Pt integration with 4d and 5d elements compared to 3d transition metals and showed the least segregation with Ag and Au ascribed to the similar lattice spacing to Pt [36].

2.5.1 Hybridisation of Pt-Ag nanostructures

The interaction of bimetallic Pt and Ag exhibits weaker adsorption of OH species than that on pure Pt surface [155,156], hence inducing more facile desorption of the intermediates and accelerating the ORR kinetic through the four-electron pathway. Highly conductive Ag is also an advantage to alleviate the electron transfer, thus minimising the impedance that induces voltage losses in PEMFCs [157]. Additionally, the similar lattice constant facilitates the growth of bimetallic Pt-M alloy with simple control of the atomic arrangement into a specific shape [158].

The morphology and catalytic activity of bimetallic PtAg hybrid nanostructures are highly derived by the atomic ratio of Pt and Ag [77,156,159–161]. An optimal atomic ratio in tailoring 20 nm hollow Pt-skin $Pt_{68}Ag_{32}$ NPs (Figure 2.10a) resulted to an upgraded mass activity of 0.438 A mg_{pt}^{-1} (3-fold higher than Pt/C) measured in 0.1 M $HClO_4$ electrolyte using the RDE technique [79]. Employing citrate reduction in colloidal Ag solution, Feng et al. demonstrated the change of core-shell PtAg NP structures into porous PtAg NPs with an increasing Pt atomic ratio [156]. A comparable mass activity to commercial Pt/C was obtained with Pt_1Ag_2 NPs toward ORR in 0.5 M H_2SO_4, while it showed 1.4-fold higher mass activity in 0.5 M KOH than that of Pt/C. These outcomes reasonably relate to the superiority of Ag, possessing high catalytic activity, especially in alkaline media showing a similar ORR kinetic and reaction mechanism to Pt [162]. Therefore, the development of Ag-based catalysts gains more attention for alkaline fuel cells and is less popular in the acidic media compared to 3d elements. At a low pH environment (i.e. in PEMFCs) the activity and stability of bulk Ag is an issue, which limits the oxygen reduction via a two-electron pathway on the surface of Ag (111). Thus additional strategies need to be considered to overcome this drawback in preparing AgPt bimetallic catalysts [163].

Wang et al. demonstrated a one-pot successive co-reduction method to synthesise 3D porous PtAg hollow nanochain-like network (HNCN) structure (Figure 2.10b) [159]. Based on the Koutecky–Levich analysis, the direct oxygen reduction through the 4-electron pathway dominated the ORR process on all the PtAg HNCN catalysts with various atomic ratios. The highest mass activity of 2.5-times enhancement versus commercial Pt/C was achieved at an atomic ratio of $Pt_{75}Ag_{25}$. The excellent stability of $Pt_{75}Ag_{25}$ was confirmed maintaining its specific activity of above 70% better than Pt/C of below 50%, which is originated from the 3D self-supported feature to prevent Ostwald ripening and minimise carbon corrosion. In fuel cell operation, the integration of Pt and Ag in the form of Ag@Pt core-shell NPs exhibited better stability compared to that of Pt/C, and a peak power density of 0.47 W cm^{-2} (30% higher than Pt/C) was achieved at an Ag and Pt atomic ratio of 1:3 [77].

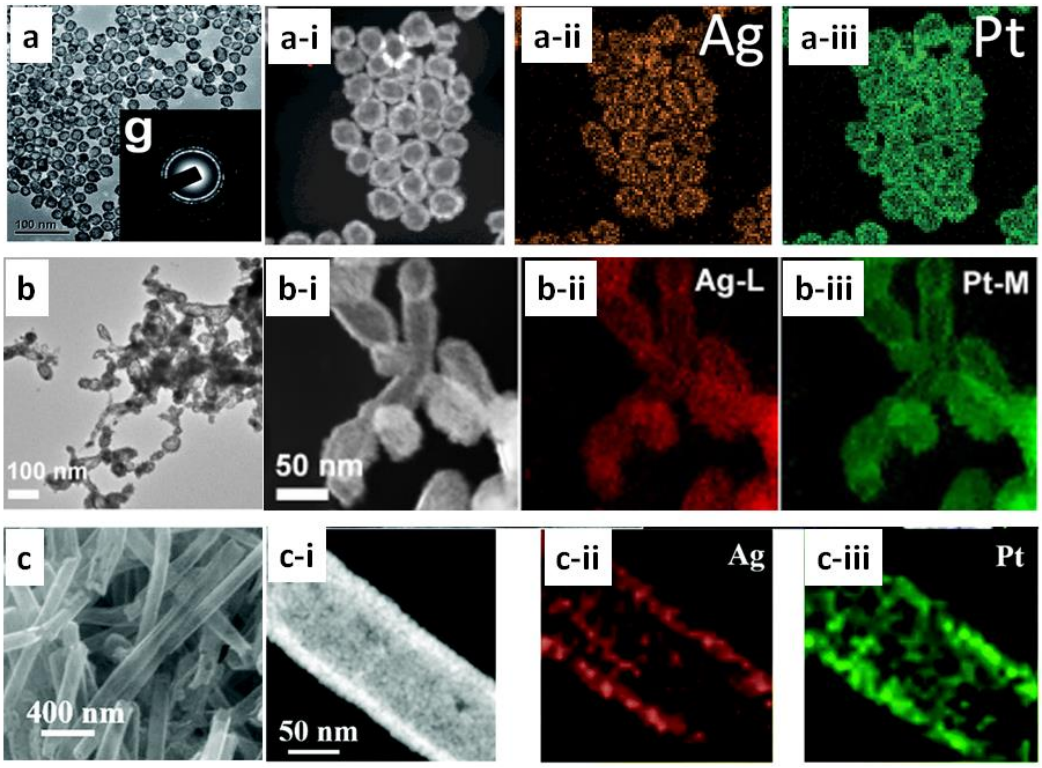

Figure 2.10 TEM images and EDX mapping of porous PtAg catalysts **(a)** hollow porous Ag-Pt@Pt NPs [79], **(b)** 3D PtAg HNCN structure [159] and **(c)** porous 1D bimetallic PtAg-4 NTs [164].

Zhang et al. transformed the porous 1D PtAg structure into 1D PtAg nanotube (NT) with a diameter of ~100 nm via a galvanic replacement method (Figure 2.10c) [164]. The increasing Pt ratio to Ag resulted in higher porosity and thinner wall of NTs of ca. 5 nm obtained for PtAg-4 NTs (with the surface and bulk Pt:Ag atomic ratio of 5:3 and 1:1, respectively). The DFT model on PtAg-4 NTs (111) predicted a downshift of the d-band centre resulting from the compressive strain of Pt and Ag. As a consequence, it weakened the binding energy of O species on the catalyst surface and boosted the ORR kinetic, hence positioning PtAg-4 NTs (111) closer to the peak of the volcano plot. In agreement with the theoretical study, a mass activity of 0.688 A $mg_{Pt}^{-1}$was recorded for PtAg-4 NTs/C using the RDE measurement in 0.1 M $HClO_4$ electrolyte (4.3-fold higher than commercial Pt/C), which has been the highest among the porous PtAg structures. After 10.000 potential cycles, no obvious degradation was observed. The same rigid morphology presented by TEM analysis before and after the cycling test also indicated excellent stability of 1D PtAg-4 NTs. It was believed that the combination of 1D geometry, thin wall thickness and a good ratio of Pt-Ag alloy structure established the unique less vulnerable structure toward aggregation and dissolution.

The advancement of PtAg-based catalysts has been explored through structure modification such as nanocrystal [165,166], interfacial alloy [167], smaller NPs on mesoporous graphene [168], dendritic nanostructures [160], and even integration with Pd forming 1D PdPt NTs and Pt/Ag-Pd NTs [131,133]. Among these nanostructures, the 1D bimetallic PtAg NT catalyst is reported possessing the highest ORR activity [164]. However, transferring such a structure to practical electrodes will be a challenge considering the requirement of enormous Ag NWs as the sacrificial template, which is less beneficial for economic reasons. Additionally, the large amount of PVP used as the capping agent in the synthesis process also interferes with catalytic performance when trapped inside the MEA [122]. Therefore, the development of a facile approach for the preparation of ultrafine 1D PtAg nanostructures with a clear catalyst surface is required to potentially advance the superiority of Pt-Ag alloy structures transferable to practical electrodes. This is achieved in this PhD research, and the details are demonstrated in Chapter 4.

2.5.2 Au integrated 1D Pt-based nanostructures

Referring to the DFT prediction of less metal segregation between Pt and 4d or 5d metal elements, Au is considered as the next ideal option because of its stability [36]. Au is well known as a highly stable metal in the acidic environment and proven offering the stabilisation effect to Pt and transition metals toward ORR [30,169–171]. For instance, the stabilisation of Pt NPs with Au was reported suppressing the ECSA loss to only 4%, which was much lower compared to 46% of Pt/C after 30.000 potential cycles [30]. Other studies have also shown the integration with Au effectively prevented surface segregation and improved stability [169–171].

In the form of bimetallic 1D PtAu nanostructures, Chang et al. modified a hydrothermal method to regulate the dominated (111) surface facet of ultrathin PtAu NWs featuring parallel-bundled Boerdijk–Coxeter helix type of structure (Figure 2.11) [172]. The study found that the atomic balance between Pt and Au was the key to reach an optimal ORR activity and stability due to the ligand effect of Pt neighbouring with Au. A higher Au content led to lower Pt active site exposure and a less d-band shift from the fermi level, hence decreasing the ORR kinetic activity on the surface. While too low the Au atomic ratio (e.g. ~10%) provided less effect to modify the Pt lattice structure. With a composition of $Pt_{76}Au_{24}$, an enhanced mass activity was obtained showing 1.9-, 2- and 2.8-fold higher than that of Pt NWs, $Pt_{76}Au_{24}$ NPs and commercial Pt/C, respectively. These further demonstrate the enhancement effect by alloying with Au, and better accessibility of the helix NW structure than NPs. Furthermore, excellent stability was demonstrated for the PtAu NWs. After an ADT with 10.000 potential sweeping cycles, the catalyst only showed a degradation rate of ~7% from its initial ECSA and ~6% in mass activity.

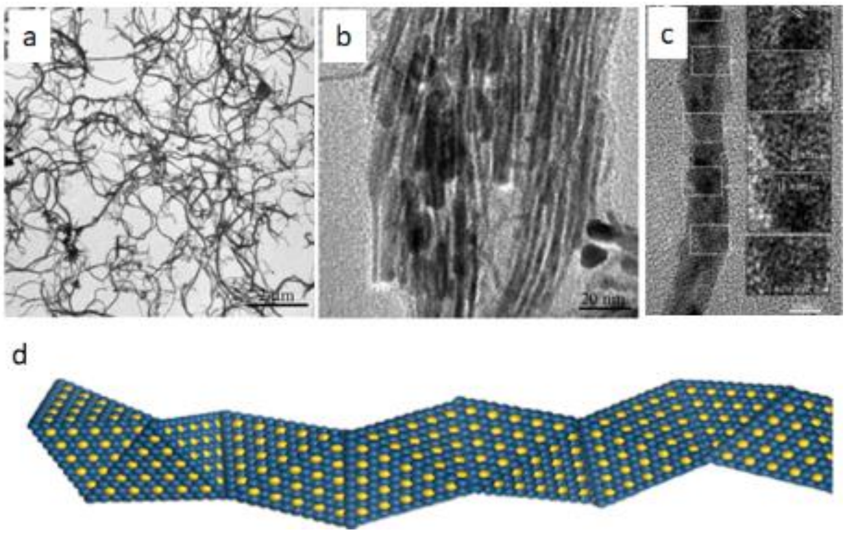

Figure 2.11 (a-c) TEM images of $Pt_{72}Au_{28}$ NWs and **(d)** the corresponding model illustration of 1D nanostructure featuring parallel-bundled Boerdijk–Coxeter helix type of structure [172].

Working with a less complex and more approachable method to obtain 1D PtAu nanostructures, Liu et al. synthesised PtAu core-shell nanorods (NRs) with Pt- and PtAu-shell via the formic acid reduction method [173]. A similar diameter and length were observed by TEM analysis for both catalysts. However, PtAu NRs with the Pt-shell exhibited a higher ECSA compared to the one with the PtAu-shell, indicating a reduced number of active sites with the Au attachment. PtAu NRs with the Pt-shell exhibited 1.4-fold higher mass activity than that one with the PtAu-shell, whereas both catalysts showed similar stability after a test with 1200 potential cycles. Therefore, it can be concluded that the stabilisation of Au was still preserved by placing it beneath the surface compared with the PtAu alloying [30]. Park et al., showed that CO treatment at 150 °C was able to tune the arrangement of Pt and Au, inducing Pt surface enrichment and a higher ORR activity [174]. These studies revealed the less attractive Au surface in promoting the ORR activities. Hence, the placement of Au under the Pt skin layer has been considered as an effective approach to improve stability of the core materials (e.g. Ni, Co, Fe, Pd) toward ORR [69,75,76,175–177].

Tan et al. prepared Au/Pt NWs and Au/Pt_3Ni NWs using Au NWs with a diameter of ~10 nm as the template [178]. Normalised to Pt loading, 2.4- and 5.1-fold mass activities were obtained for Au/Pt NWs and Au/Pt_3Ni NWs compared to Pt/C, respectively. A comparable ECSA loss after 5000 potential cycles was observed for Au/Pt NWs (~7%) and Au/Pt_3Ni NWs (~10%), which were much smaller compared to 37.9% of Pt/C. 2.5 nm FePtAu NW core with a 0.8 nm FePt shell has been successfully prepared using a seed-mediated growth method [179]. The alloying of Au into the core effectively improved the ORR activity and durability of FePt NWs. The NWs showed ignorable activity decrease after 5.000 potential cycles in 0.1 M $HClO_4$, indicating very little agglomeration or dissolution occurred to change the catalyst structure. A similar stabilisation effect to the FePt core was also obtained with the alloying of Pd, which further confirmed the DFT analysis of excellent stability of Pt alloying with 4d and 5d elements [36]. However, Pd is less electropositive compared to Au, thus the exposure of Pd is more vulnerable toward ORR than that of Au [179,180].

The improvement of Au alloying to Pt catalysts can be concluded as below: (i) the presence of Au provides a stabilisation effect through electronic structure modification on Pt-based catalysts, thus preventing the oxide formation on Pt surface. (ii) The charge transfer effect induced by a small number of Au atoms potentially reduces the formation of unstable high-energy Pt sites, improving its stability under ORR condition; and finally (iii) Au also stabilises the catalyst by weakening the binding of oxygen species on the catalyst surface, suppressing the segregation of the alloyed metals and Pt.

However, the stability of 1D Pt-based nanostructures with the Au surface layer could be different. Using the formic acid reduction method, Liang et al. synthesised core-shell 1D Pt@M (M=Au, Ag or Pd, Pt:M = 3:1) nanostructures [74]. Three types of NRs before and after the stability test are shown in Figure 2.12, together with their ORR activities measured by the RDE technique in O_2-saturated 0.5 M $HClO_4$. Both DFT calculation and experimental results demonstrated the highest ORR activity of the Pt@Au NR catalyst. A similar result indicating the more active PtAu NR surface than that of PtPd NRs was also reported toward ORR in the acid electrolyte in a previous study [181]. The ADT demonstrated better stability of PtAg NRs, exhibiting a much lower mass activity loss of 8.9% than 23.7% of PtAu NRs (Figure 2.12h).

However, no details have been provided to explore the mechanisms for the better stability of PtAg NRs. The further study of alloying Au into 1D AgPt nanostructures is presented in Chapter 5 and 6 of this PhD thesis.

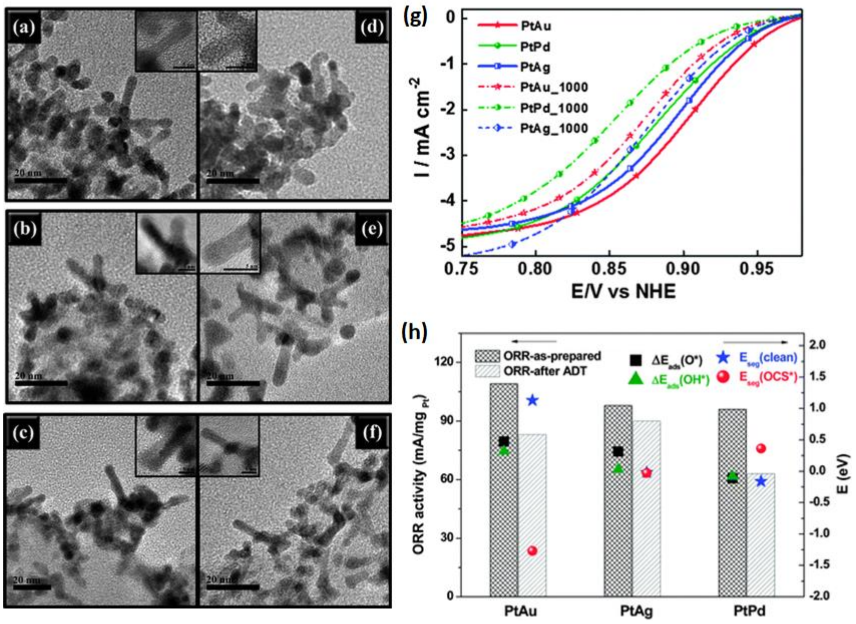

Figure 2.12 TEM images of nanorod morphology before and after 1000 cycles of ADT: **(a)** and **(d)** PtAu, **(b)** and **(e)** PtPd, **(c)** and **(f)** PtAg. **(g)** The linear sweep voltammetry (LSV) curves before and after the ADT, and **(h)** the corresponding ORR activities from the experiments and DFT calculation for the measured Pt-M alloys [74].

2.6 Summary & Perspective

Through the intensive development of ORR catalysts toward successful commercialisation, Pt-based alloy NPs have attracted the most attention for practical application in PEMFCs. Hybridisation has been the ultimate strategy to reduce the utilisation of scarce Pt and successfully established as the new baseline of the-state-of-the-art ORR catalysts possessing a high catalytic activity. However, catalyst stability is still a major challenge to maintain long-term performance without activity loss. The dissolution of NPs is identified as the main reason for the electrode decline along with corrosion of carbon support and segregation of bimetallic

Pt-alloy. The dissolution of NPs could be minimised through shape-controlled strategies to construct the catalyst possessing lower surface energy, defect-free plane and preferential exposure of active sites such as 1D nanostructures.

Recent achievements in tailoring 1D Pt-based nanostructures have demonstrate good efficiency in suppressing the atomic dissolution and preventing the catalyst coalescence. They offer improved activities and high resistance against degradation for good durability at the same time. Concluding from various works, the translation of Pt NWs to practical catalyst electrodes in fuel cells has been successfully realised through a facile self-assembly formic acid reduction method and is further advanced for growing Pt NW arrays on GDLs to fabricate 3D ordered support-free electrodes. This unique support-free 1D NW array structure is considered as the ideal electrode feature to resolve issues of carbon corrosion and mass transfer resistance attributing to its high porosity and the thin catalyst layer. The recent development of 1D Pt NW-based GDEs has been focused on optimising the uniformity of Pt deposition and distribution as these are the main factors determining electrode power performance in PEMFCs. Further development of GDEs with hybridisation 1D Pt-based NWs is a promising approach to enhance ORR performance and reduce Pt loading at the same time.

If hybridisation is considered as an effective approach to improve the intrinsic activity of the monometallic Pt-based catalyst, the alloying with additional metals should also contemplate the segregation issue to achieve excellent stability. The numerical studies suggested alloying with the additional metals having a close lattice constant to Pt such as Au and Ag to mitigate the segregation and promote stability. Hence, the alloying of noble metals is often applied to stabilise the transition metal toward depletion. In the form of 1D nanostructures, the integration of Pt-Ag and Pt-Au forming bimetallic or even multimetallic hybrid catalysts have shown improved activities and durability toward ORR. However, the performance reported for most of these catalysts remain in the half-cell measurement in liquid electrolytes, which cannot guarantee high power performance in real conditions in operating PEMFCs because of the mass transport issue.

Future works should emphasise the catalyst evaluation in operating PEMFCs to move forward the promising cultivation of 1D Pt-alloy nanostructures as ORR catalysts. The fuel cell electrode fabrication requires a large amount of catalyst material, which is often a hindrance for the advanced shape-controlled nanostructures of bimetallic and multimetallic catalysts due to the complication steps for scalable production. Therefore, the facile method and fundamental concept to construct 1D Pt-alloy nanostructures should be further highlighted prior to transferring them to practical electrode fabrication. For these reasons, the deposition and self-assembly of 1D AgPt catalysts on carbon support in acidic solution are investigated in this study (Chapter 4) considering their catalytic performance in the single-cell test. Through understanding the parameters deriving the reduction and growth mechanisms of the metal ions, it rather extenuates highly scalable synthesis and translation of such mechanisms on other support media. The controlled alloying of Au to form multimetallic 1D Au-AgPt nanostructures is explicitly discussed in Chapter 5, including its influence on the catalyst activity and stability in operating PEMFCs. Finally, the development of support-free 1D AgPt-based nanostructure electrodes is further explored via direct growing AgPt NRs on GDLs in Chapter 6. The work is also advanced to Au-AgPt NR GDEs achieving high power performance and durable electrodes for PEMFCs.

Chapter 3

Materials & Method

This chapter introduces the materials used for this PhD research. The detailed experimental steps of the catalyst synthesis and gas diffusion electrode (GDE) fabrication are presented, including the methodology for physical characterisation techniques. The procedures of the membrane electrode assembly (MEA) preparation and tests in single fuel cells are outlined, including the accelerated degradation test (ADT) to evaluate the electrode stability.

3.1 Catalyst Preparation and GDE fabrication

3.1.1 Growing Pt and AgPt NRs on Carbon

Pt nanorods supported on carbon (Pt NR/C) - 50 mg carbon black XC-72R (Fuel Cell Store, USA) was dispersed in 100 mL H_2O (deionised to 18 MΩ cm using a Millipore water system, Milli-Q, Germany) using bath sonication (Ultrawave 300H, 35 W, UK). 1.5 mL H_2PtCl_6 (8 wt% in H_2O, Sigma Aldrich, UK) in 100 mL H_2O was added subsequently to the carbon suspension, followed by adding 10 mL HCOOH (Sigma Aldrich, UK) dropwise under sonication over 10 minutes. The solution was then stirred for 96 hours at room temperature to finish the reaction. The obtained catalyst was washed with H_2O for three times and then ethanol (Fisher Scientific, UK) using a centrifuge (Sigma 3K30, UK) with the speed of 15,000 rpm for 15 minutes followed by drying in the oven at 60 °C for 2 hours.

AgPt nanorods supported on carbon (AgPt NR/C) – The integration of Pt NR/C with Ag was conducted by adjusting the metal ratio of Pt and Ag while keeping the total metal loading constant. For a typical synthesis of Ag_1Pt_1 NR/C (atomic ratio of Ag:Pt = 1:1), the reaction step was intended to replace 50 at% of Pt with Ag. The same dispersion of carbon black (50 mg in 100 mL H_2O) was mixed with 1 mL H_2PtCl_6 (8 wt% in H_2O) in 50 mL H_2O, followed by adding 10 mL HCOOH dropwise under sonication for 10 minutes. After 5 hours of stirring at room temperature, 2 mL 0.1 mol L^{-1} $AgNO_3$ (Sigma Aldrich, UK) in 50 mL H_2O was added.

The stirring was then continued at room temperature for a total duration of 96 hours to finish the reaction. The chemical reactions are shown below:

$H_2PtCl_6 + 2HCOOH \rightarrow Pt^0 + 6Cl^- + 6H^+ + 2CO_2$ (Eq. 3.4)

$2AgNO_3 + HCOOH \rightarrow 2Ag^0 + 2NO_3^- + 2H^+ + CO_2$ (Eq. 3.2)

Regardless of close standard reduction potential (SRP) of Pt and Ag ions ($[PtCl_4^-/Pt^0] = 0.75$ V, and $[Ag+/Ag^0] = 0.79$ V), Pt ions take more steps to be reduced and form Pt^0, inducing a slower Pt reducing kinetic rate. The difference of the kinetic behaviour between both metal ions is a challenge to form 1D AgPt alloy, which will be explored in details in Chapter 4. The same methods of washing and drying as those for Pt NR/C were applied, followed by a heating step for all AgPt alloy catalysts to improve the catalyst properties further. The heat treatment was conducted between 120 and 200 °C for 2 hours under 60 mL min^{-1} of 4% H_2/Ar within a quartz tube in a tube furnace (Vecstar Ltd., UK).

3.1.2 Synthesis of Au integrated AgPt NR/C

The integration of Au was applied to the Ag_1Pt_1 NR/C catalyst, keeping the total metal loading constant. For the synthesis of 5 at% Au integrated AgPt NR/C A catalyst (Au-AgPt NR/C A), 1 mL of H_2PtCl_6 (8 wt% in H_2O) in 50 mL water was added into 100 mL water containing 50 mg carbon black. 10 mL HCOOH was subsequently added dropwise under sonication for 10 minutes. 1 mL 0.025 mol L^{-1} $HAuCl_4$ (Sigma Aldrich, UK) was then added under stirring. The stirring was continued at room temperature for ca. 5 hours and then 1.7 mL 0.1 mol L^{-1} $AgNO_3$ in 50 mL water was added. The reaction was kept under stirring for 96 hours at room temperature. The final product was then washed with water and ethanol, followed by drying in the oven (60 °C, 2h).

The atomic arrangement was controlled through the insertion of Au ions along with the growth of AgPt NR, which will be comprehensively evaluated in Chapter 5. Finally, the varied Au loading was applied by changing the concentration of Au and Ag precursors, while keeping Pt and the total metal loading constant.

3.1.3 Growing of Pt NR and AgPt NR on Gas diffusion layer (GDL)

Pt NR GDE (0.4 mg$_{pt}$ cm^2) – A piece of 5 x 5 cm^2 Sigracet 39 BC carbon paper gas diffusion layer (GDL, Fuel Cell Store, USA) was rinsed with H_2O and IPA (Fisher Scientific, UK), followed by soaking in H_2O for 10 minutes. The GDL was then placed in a square petri dish (5 x 5 cm^2) and immersed in 16.5 mL H_2O. 255 µL H_2PtCl_6 (8 wt% in H_2O) and 830 µL HCOOH were then added followed by bath sonication for one minute. The petri dish was then covered with a lid and stored in an oven at 40 °C for 72 hours to get Pt NR GDE. The Pt NR GDE was then washed with H_2O and IPA, followed by drying at 40 °C for 2 hours.

AgPt NR GDE (0.4 mg$_{AgPt}$ cm^2) – To grow AgPt NRs on GDL, the same procedure to prepare Pt NR GDE was conducted. However, due to the addition of Ag ions, the Pt precursor concentration was adjusted to keep the total metal loading of 0.4 mg$_{AgPt}$ cm^{-2}. To fabricate Ag_3Pt_7 GDE (atomic ratio of Ag:Pt = 3:7), the washed GDL was immersed in 16.5 mL H_2O, and then 200 µL of H_2PtCl_6 (8 wt% in H_2O) and 830 µL HCOOH were added followed by storing it at 40 °C. 185 µL of 0.1 mol L^{-1} $AgNO_3$ was added after a fixed time, and then, the reaction was continued for a total duration of 72 hours. The as-prepared Ag_3Pt_7 NR GDE was then washed and neutralised with H_2O and IPA, followed by drying at 40 °C.

The growth and formation of 1D AgPt alloy nanostructure on GDL are explicitly explained in Chapter 6. A crucial parameter such as interval time of mixing both Ag and Pt precursors was varied. The influence of the varied atomic ratio of Ag and Pt towards structure, morphology and catalytic activity was also investigated to optimise the catalytic properties of AgPt NR GDE. The fabrication steps are shown in Figure 3.1, and the characterisations were consistently taken from the same piece of AgPt NR GDE, as described in Figure 3.2.

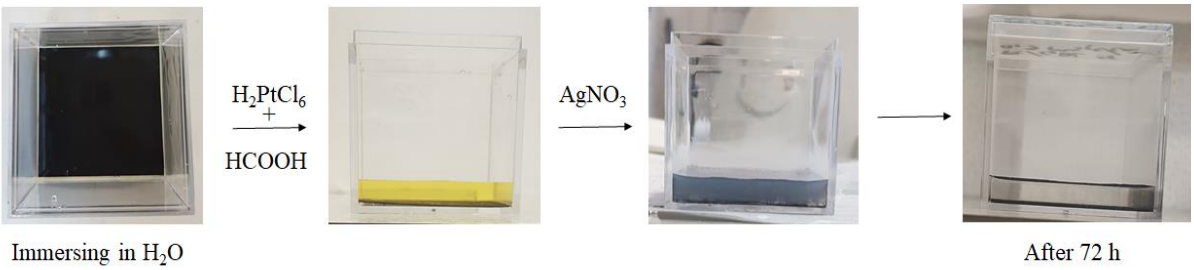

Figure 3.1 Experiment steps for growing AgPt NRs on GDLs.

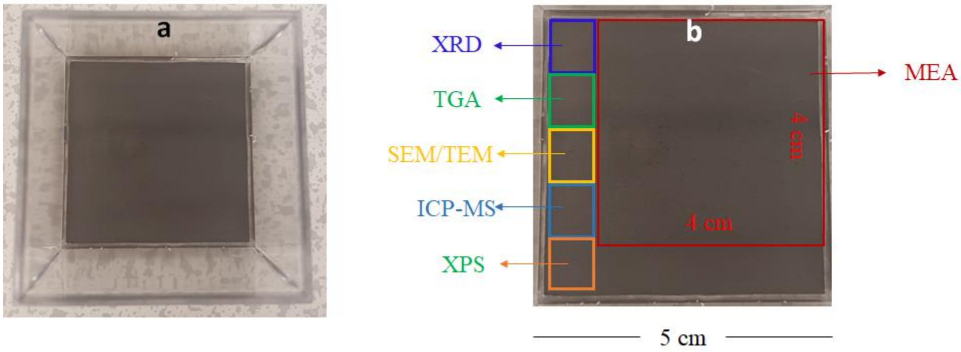

Figure 3.2 One as-prepared AgPt NR GDE (a) after washing step in petri dish and (b) after drying ready for further characterisations.

Au-AgPt NR GDE (0.4 $mg_{Au\text{-}AgPt}$ cm^2) – ~2 at% of Au integration was adjusted trough the fabrication of Ag_3Pt_7 NR GDE by keeping Pt and total metal loading constant. A piece of 5 x 5 cm^2 Sigracet 39 BC GDL was immersed in 16.5 mL H_2O, and then 200 µL H_2PtCl_6 (8 wt% in H_2O) and 830 µL HCOOH were added followed by bath sonication for 1 minute. 60 µL 0.025 mol L^{-1} $HAuCl_4$ was added dropwise during the sonication period. The petri dish was then covered with a lid, followed by storing at 40°C. After ca. 3 hours, 162 µL 0.1 mol L^{-1} $AgNO_3$ was added. The reaction was continued for a total duration of 72 hours. The as-prepared Au-AgPt NR GDE was then washed with H_2O and IPA, followed by drying at 40 °C for 2 hours. The overview of a preliminary study on Au integrated AgPt GDEs is presented in Chapter 6.

3.2 Physical Characterisation

3.2.1 Scanning Electron Microscopy - Energy-Dispersive X-ray Spectroscopy (SEM-EDX)

SEM-EDX (Hitachi TM3030 with an accelerated voltage of 15 kV) was used to obtain the surface structure and structure, and estimate the atomic ratio of Ag and Pt in the alloy AgPt catalysts. For quantitative EDX mapping, each sample was taken at least three different spots for scanning of 150 seconds/spot. For sample preparation of the carbon-supported catalysts, a small amount of catalyst powder (~ 1 mg) was dispersed onto carbon tape. Similarly, a small piece of the sample was cut from GDEs and then placed it onto carbon tape followed by loading it into the sample holder.

3.2.2 Transmission Electron Microscopy (TEM)

TEM analysis was conducted using JEOL 1400 TEM with an accelerated voltage of 80 kV. And for certain samples, a high-resolution transmission electron microscope (HR-TEM, Talos F200X, operated at 200 kV) equipped with Super-X EDS system with four silicon drift detectors (SDDs) (Bruker, USA) was used to obtain the crystallinity and elemental mapping of NRs. For sample preparation, a small amount of catalyst (powder and GDEs) was dispersed in the ethanol by bath sonication for ca. 2 minutes. The suspension was then pipetted onto a TEM grid (Formvar films-Copper, Agar Scientific, UK) followed by drying in the air for up to 15 minutes. For HR-TEM samples, the drying was conducted of up to 1 hour, followed by storing it in a vacuum for overnight to minimise the contamination.

3.2.3 Thermo-gravimetric analysis (TGA)

To determine the metal loading of the catalysts, Thermo-gravimetric analysis (TGA, NETZSCH TG209F1, Germany) was conducted between 20-900 °C under 40 mL min^{-1} airflow with the heating rate of 10 °C min^{-1}. For every measurement, ca. 7-10 mg of sample powder (for carbon-based catalysts) or a 1x1 cm^2 GDE was loaded into a crucible. The metal loading was determined from the final mass of the residue.

3.2.4 Inductively coupled plasma – mass spectrometry (ICP-MS)

ICP-MS was conducted to measure the element loading (Pt, Ag and Au) in the catalyst. For sample preparation, 2-3 mg of sample powder (for carbon-based catalysts) or a piece 1x1 cm^2 GDEs were dissolved in 10 mL of aqua Regia solution by sonicating them on bath at 80-90 °C for 2 hours. In 100 mL of the aqua Regia solution contains 18.9 mL of HCl (37%) and 6.6 mL HNO_3 (70%) both purchased from Sigma Aldrich, UK. The samples were allowed to cool down, and then 20 mL of H_2O was added at ca. 30 minutes before the measurement. The testing vial filled with 10 mL of filtered sample (using 0.22 µm filter syringe) was loaded into The ICP-MS device (Perkin Elmer Nexion 300X, USA) with a plasma strength of 1500 W. The result shows the concentration of the metal element in ppm.

3.2.5 X-Ray Diffraction (XRD)

For the carbon-supported catalysts, 3-4 mg of sample powders were dispersed onto scotch tape with the area of ca. 1 cm^2, or cutting 1x1 cm^2 of GDE samples, followed by sticking them onto sample holders. The samples were loaded into D8 Auto-sampler Bruker XRD (USA), equipped with a Cu Kα X-Ray source (λ = 0.15418 nm) operated at 40 kV and 40 mA. The XRD patterns were scanned between a 2θ range from 5 to 90° with a step size of 0.02° and dwell time of 0.2 seconds.

3.2.6 X-ray photoelectron spectroscopy (XPS)

For XPS sample preparation, Si wafer with a thickness of 0.4 mm was cut 0.5x0.5 cm^2 layered with the double tape to deposit the sample. For carbon supported catalysts, ~1 mg of sample powder was dispersed on it. Otherwise, the same size of a GDE sample was cut and placed on the Si wafer. A Thermo Fisher Scientific NEXSA spectrometer with a micro-focused monochromatic Al Kα source (1486.6 eV) and power of 72 W was used to analyse the surface composition and oxidation state of the catalysts. The XPS data analysis was processed using the CasaXPS software (version: 2.3.18PR1.0) and sample charging corrected using the C 1s peak at 284.8 eV as reference.

3.3 Fabrication of Membrane Electrode Assemblies (MEAs)

GDEs made from carbon-supported catalysts - The catalyst ink for the cathode was made of 0.5 mL IPA, 45.7 µL of 10 wt% Nafion dispersion (D1021, Ion Power Inc., USA) and the catalyst powder required for a Pt loading of 0.2 mg_{Pt} cm^{-2}. A sonication probe (A Sonics Vibra-CellTM VCX130, Sonics & Material Inc., USA) was used at a power amplitude of 20% for 10 minutes to obtain a fine dispersion of the catalyst ink. The ink was then painted onto 4 × 4 cm^2 Sigracet 39 BC GDL and then left to dry for 2 hours at 35°C.

Pt NR and Pt-alloy NR GDEs - The ionomer solution with a Nafion loading of ca. 0.4 mg cm^{-2} was applied to coat the cathode GDEs. The solution was made of 62.5 µL of 10wt% Nafion and 0.2 mL of IPA mixed together using a sonication bath for 5 minutes. The coated GDE was then dried at 35°C for 2 hours.

The MEA was fabricated by assembling the as-prepared cathode, commercial gas diffusion electrode (GDEs, 0.2 mg_{Pt} cm^{-2}, Fuel Cell Store, USA) as the anode and 6 × 6 cm^2 Nafion®™ 212 membrane using hot-press under a 4.9 MPa at 135 °C for 2 minutes. The MEA was allowed to cool down at room temperature before testing in PEMFCs.

3.4 MEA test in Single Fuel Cells

The MEA was loaded into Biologic-PaxiTech FCT-50S PEM fuel cell test rig (France) with polytetrafluoroethylene (PTFE, 254 µm in thickness) gaskets used at both the anode and cathode sides (Figure 3.3). The in-situ MEA test encompasses the polarisation curves and electrochemical impedance spectroscopy (EIS) to understand the catalytic activities of the tested catalysts in operational PEMFC. The mass and specific activities were measured along with cyclic voltammetry (CV) generated using EZStat-Pro (NuVant Systems) integrated to the PEM device. The general protocol of in-situ testing is described below:

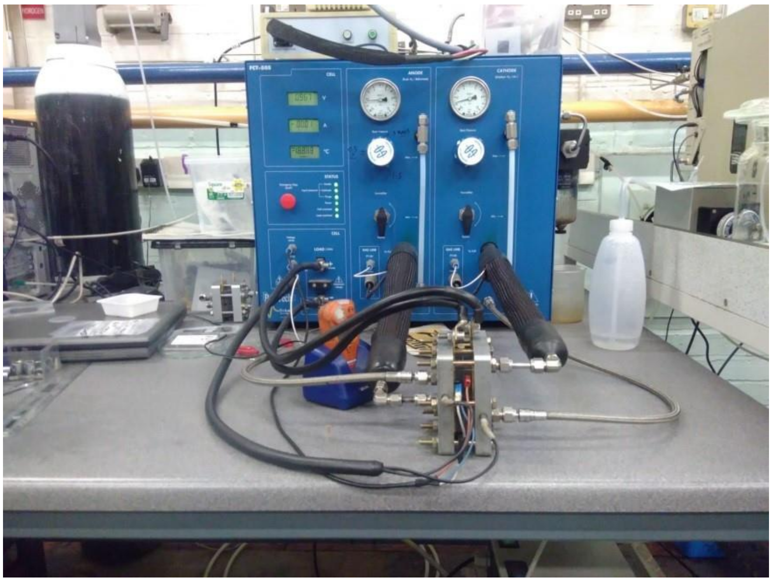

Figure 3.3 Biologic-PaxiTech FCT-50S PEM fuel cell test rig

Polarisation curves (H_2/Air) - Prior testing, the membrane hydration was carried on by holding the voltage at 0.6 V for about 12 hours or until reaching a stable current. The procedure was conducted under fully humidified H_2/Air at 80 °C and stoichiometric ratios of 1.3/1.5 with an absolute pressure of 1.5/1.5 bar at the anode and cathode, respectively. The cell break-in procedure followed the EU harmonised protocol by cycling the voltage between 0.4 and 0.8 V for ca. 1 hour, as shown in Figure 3.4a [182]. This step was intended to activate the catalysts further. Adapting the EU test protocol, polarisation curves were recorded between 0 – 2.0 A cm^{-2} at 80 °C and fully humidified H_2/Air and stoichiometric ratios of 1.3/1.5 with an absolute pressure of 2.5/2.3 bar, respectively. The quick scan was first run with a step size of 0.02 and 0.1 A cm^{-2} between 0.0 – 0.1 and 0.1 – 2.0 A cm^{-2}, respectively. Followed by backward scan from 2.0 – 0.1 and 0.1 – 0.0 A cm^{-2} with a step size of 0.1 (150 sec holding) and 0.02 A cm^{-2} (90 sec holding), respectively, (Figure 3.4b). The recorded stable potentials and current outputs from each stepping point of the backward scan were averaged to obtain the polarisation curve, as presented in Figure 3.4c. The standard deviations of each measurement were taken into consideration together with the repeated scans for the same sample to divine the error bars. EIS analysis was then conducted at 30 mA cm^{-2}, 0.65 V and 0.5 V with the amplitude of 72 mA, 10 mV and 10 mV, respectively, in the frequency range of 10 kHz – 0.1 Hz.

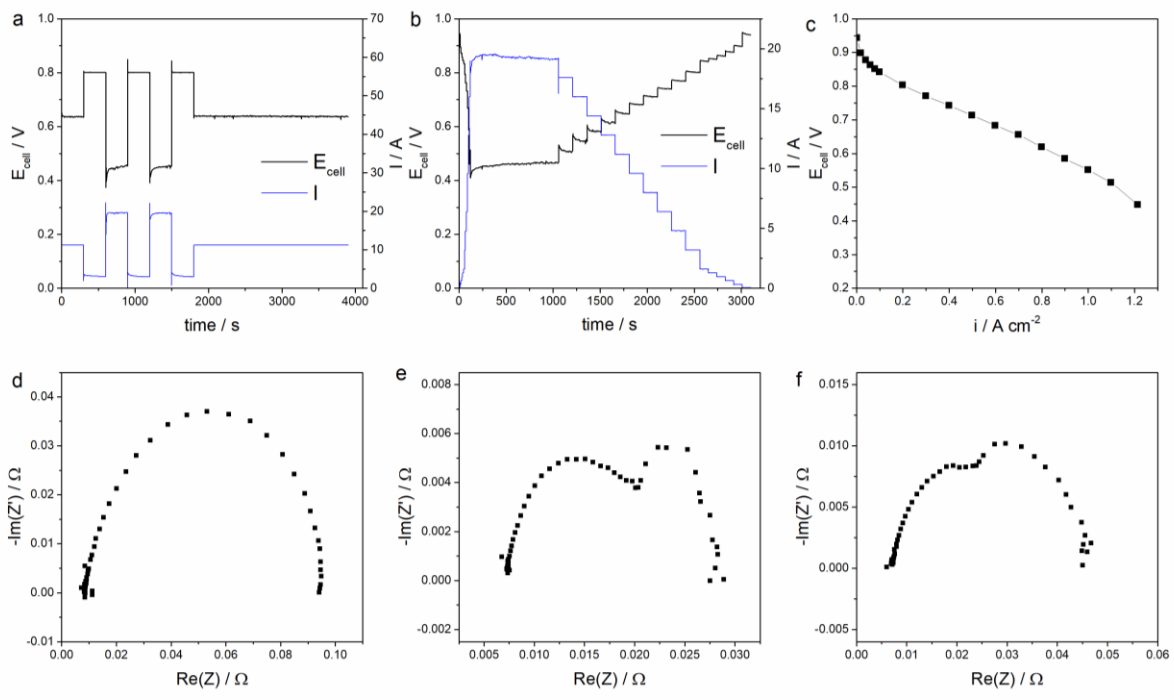

Figure 3.4 The steps of MEA testing in H2/Air: (a) the cell break-in procedure, (b) the acquisition data from the first and second scans, which is further proceeded to obtain (c) the polarisation curve. Nyquist plots of the EIS measurements at (d) 30 mA cm^{-2} (amplitude of 72 mA) (e) 0.65 V (amplitude of 10 mV) and (f) 0.5 V (amplitude of 10 mV).

The typical Nyquist plots acquired by EIS measurements are presented in Figure 3.4d-f. A single semi-circle loop (Figure 3.4d) represents the loss induced by the interfacial kinetic of the electrochemical process, which commonly occurs at a low current density region [183]. The intercept of the arc with the real axis at high and low-frequency corresponds to the internal ohmic (R_{Ω}) and charge transfer resistance (R_{CT}), respectively. Two impedance arcs are commonly obtained at medium and high current density (Figure 3.4e-f). In this type of EIS spectra, the charge transfer resistance is shown by the first semi-circle end (medium-frequency), and the second arc (low-frequency) reflects the loss caused by mass transfer resistance. In this work, the potentio EIS were recorded at a fixed potential to analyse the impedance at medium and high current density. This method was intended to anticipate the huge voltage drop before reaching a high current density region. Hence, fixing the voltage (e.g. at 0.5 V) is considered as an effective method to obtain the impedance spectra corresponding to mass transfer resistance.

Polarisation curves (H_2/O_2) - This test was performed to evaluate the mass activity of catalysts in practical electrodes in fuel cell operation. Carried on from the previous step, the gas flow connected to cathode was then switched to O_2, and the condition was changed following the DoE (U.S. Department of Energy) protocols to 2.0/9.5 stoichiometric ratio with an absolute pressure of 1.5/1.5 bar for H_2/O_2, respectively, [12]. The temperature was kept the same at 80 °C with fully humidified H_2/O_2. The same procedure of cell break-in and obtaining polarisation curve as of in H_2/Air was applied, including the EIS analysis at the low current density of 30 mA cm^{-2} with the amplitude of 72 mA in the frequency range of 10 kHz – 0.1 Hz. The O_2 polarisation curve (Figure 3.5a) was then corrected with the internal ohmic resistance determined from the intercept of the arc with the real axis at high-frequency range (R_Ω) (Figure 3.5b) and hydrogen crossover current density (i_{Hcross}) (Figure 3.5c), following the method described by Gasteiger et al. [184]. Both generated values of R_Ω and i_{Hcross} were then included to obtain the corrected voltage and current density (blue curve in Figure 3.5a). The measured current at 0.9 V from the corrected polarisation curve was then applied to calculate the specific and mass activities (Equation 3.3 and 3.4).

Cyclic voltammetry (H_2/N_2) - The integrated EZstat-Pro system was then connected to the single-cell test hardware, and the cathode gas was switched to N_2. The cell condition was maintained the same as the previous test in H_2/O_2. Before running the CV, N_2 purging was conducted while holding at 0.6 V for at least 1 hour to reach the saturation. 6 quick CV scans were then run for cleaning purpose at a scan rate of 50 mV s^{-1} from 0.05 – 1.2 V vs. RHE, followed by 3 CVs with a slower scan rate of 20 mV s^{-1}. The last CV from the slow scan (Figure 3.5d) was used to determine the catalyst electrochemical surface area (ECSA). The hydrogen crossover current density (i_{Hcross}) was then obtained by holding at 0.5 V for at least 30 minutes under H_2/N_2 feeds (Figure 3.5c).

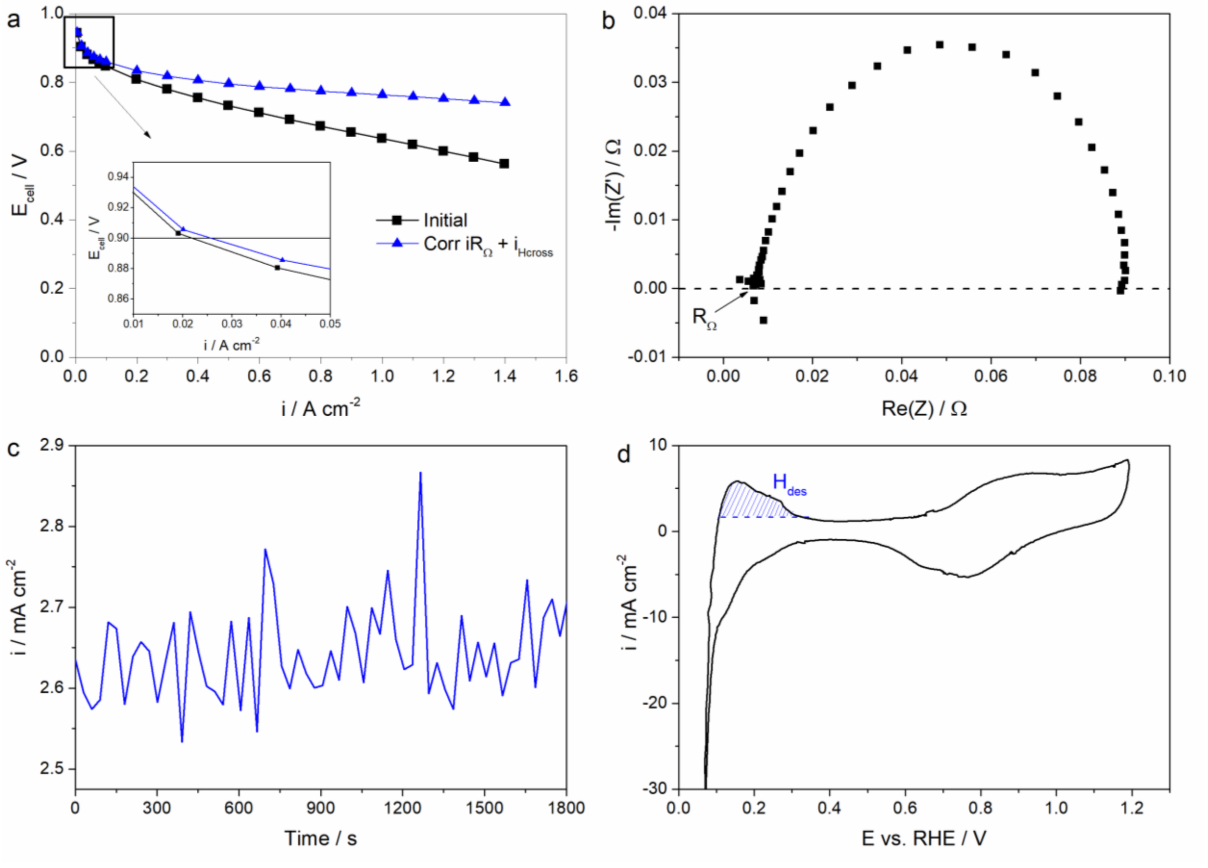

Figure 3.5 (a) Polarisation curves obtained in H_2/O_2 with the internal resistance and H_2 crossover correction. (b) The corresponding EIS measured at 30 mA cm^{-2} with the amplitude of 72 mA in the frequency range of 10 kHz – 0.1 Hz, (c) H_2 - crossover current density of the MEA and (d) cyclic voltammetry (CV).

The charge associated with the electrochemical process (Q_{Hdes} / C) was measured from the H_{des} region (Figure 3.5d) converted to a current vs. time plot [185]. By applying the conversion factor of 210 µC cm^{-2}, which corresponds to the charge required to reduce hydrogen atoms on a polycrystalline Pt surface, the absolute surface area ($Area\ /\ cm^2$) was then calculated following Equation 3.1:

$$Area = \frac{Q_{Hdes}}{210\ \mu C\ cm^{-2}} \qquad \text{Eq. 3.1}$$

Normalised to Pt loading used at the cathode (m_{Pt} / *mg*), the *ECSA* / m^2 g^{-1} was then obtained based on the calculation below:

$$ECSA = \frac{Area}{m_{Pt}} \qquad \text{Eq. 3.2}$$

The kinetic current (I_k / *A*) measured at 0.9 V from the corrected polarisation curve in Figure 3.5a was then applied to obtain specific activity (I_s / $\mu A\ cm^{-2}$) and mass activity (I_m / $A\ mg_{Pt}^{-1}$) based on the following equations:

$$I_s = \frac{I_k\ (@\ 0.9\ V)}{Area} \qquad \text{Eq. 3.3}$$

$$I_m = \frac{I_k\ (@\ 0.9\ V)}{m_{Pt}} \qquad \text{Eq. 3.4}$$

Accelerated Degradation Test (ADT) – The ADT was conducted by applying the same condition as of the previous step in H_2/N_2, then running 5000 potential cycles from 0.6 – 1.2 V vs. RHE with a scan rate of 100 mV s^{-1} (Figure 3.6). The CVs were then recorded, followed by polarisation curves in H_2/Air to compare the ECSA and power performance loss due to the ADT.

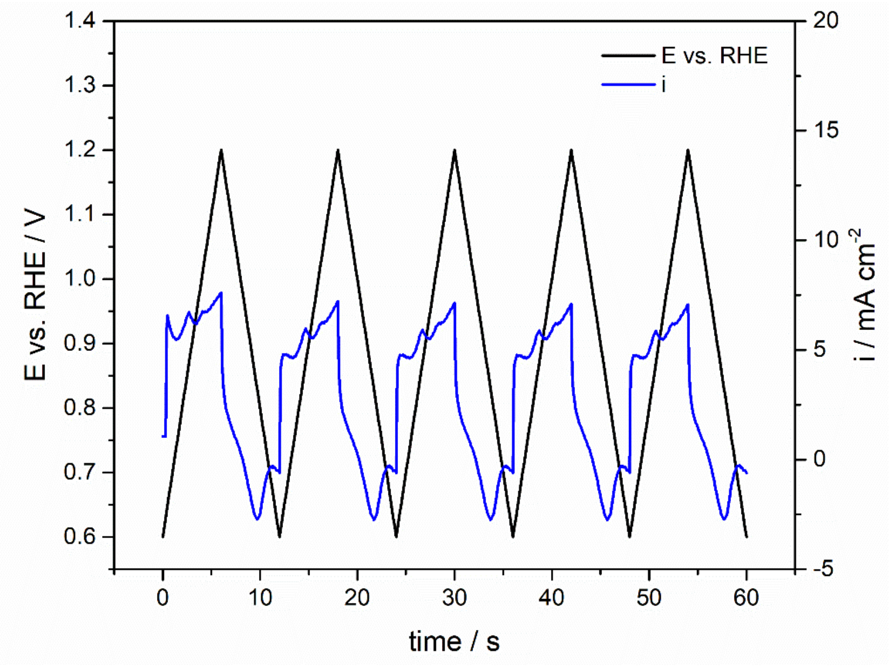

Figure 3.6 The potential cycling and current density recorded during the ADT.

Chapter 4

Carbon Supported AgPt nanorods as Electrocatalysts for Oxygen Reduction Reaction

---

This chapter is based on the publication:

E. Fidiani, G. Thirunavukkarasu, Y. Li, Y.-L. Chiu, S. Du, Ultrathin AgPt Alloy Nanorods as Low-cost Oxygen Reduction Reaction Electrocatalysts in Proton Exchange Membrane Fuel Cells, J. Mater. Chem. A. 8 (2020) 11874–11883,

doi.org/10.1039/D0TA02748K

In this chapter, the mechanism of the formic acid reduction method to grow the hybrid one-dimensional (1D) AgPt nanostructures on carbon support is explored. They are evaluated as cathode catalysts in proton exchange membrane fuel cells (PEMFCs). The effects of varied Ag to Pt atomic ratio toward 1D morphology and structure are investigated, in regard to the power performance in operating PEMFCs. The functionalisation step of post heat treatment is further demonstrated to enhance the catalytic activities of 1D AgPt nanostructures. A brief discussion regarding the stability of AgPt alloy catalyst is also enclosed based on the accelerated degradation test (ADT) in membrane electrode assemblies (MEAs).

4.1 Introduction

The alloying with Ag can be a potentially promising approach for the development of cost-effective Pt hybrid catalysts to achieve high catalytic activities and a good match between both atomic structures to preserve the atomic segregation. The PtAg-based catalysts have been explored in Chapter 2, resuming the attractive alloy feature for highly active and durable oxygen reduction reaction (ORR) catalysts. The most noticeable 1D PtAg NTs showed an enhanced mass activity of up to 4.3-fold higher than the state-of-the-art Pt/C in RDE measurement, advantaging a larger number of the active sites to facilitate the ORR [164]. However, such achievement is less reliable for real application as catalyst electrodes in PEMFCs, because of the following factors: (i) Scalable synthesis is a hindrance for MEA fabrication due to the requirement of the immense amount of Ag NWs as the sacrificial template, which is also less favourable for the low-cost purpose. (ii) Mass transfer issues often arise with the porous structure limiting by the ionomer pathway to reach the inner tube [93]. Such case is less presentable in half-cell measurement using the RDE technique in a liquid electrolyte. This behaviour is similar to the remained polyvinylpyrrolidone (PVP) (used as a surfactant in synthesis) as it may be washed out in the liquid electrolyte during the electrochemical measurement process but can be trapped inside MEAs thus interfering the power performance of PEMFCs [122]. Further development of 1D AgPt alloy nanostructure should further consider minimising the usage of capping agent and rational morphology with a simple fabrication method for high-scale production.

Designing a facile method to synthesise 1D AgPt alloy ORR catalysts highly transferable to fuel cells is the main goal of this chapter. The formic acid reduction method has been reported as an effective approach to obtain the formation of 1D Pt-based nanostructures. It utilises a slow reaction rate assisting a self-assembly growth into <111> crystal direction at room temperature [125,186]. A close standard reduction potential (SRP) of Pt and Ag metal salts ($[PtCl_4^{2-}/Pt^0] = 0.75$ V and $[Ag^+/Ag^0] = 0.79$ V) is an advantage to obtain a simultaneous reduction process in acidic media. In addition, a close lattice constant of Pt and Ag induces more feasible alloy formation at relatively low temperature [79]. Thus, the formic acid reduction method was adjusted to derive the nucleation and growth of both Pt and Ag on carbon support by adopting a slow reaction to configure 1D Pt nanostructure. Room temperature is applied as it has been reported as an ideal condition for generating 1D Pt nanostructure with a high crystallinity in this reduction process [125,127].

4.2 Growth of 1D AgPt nanorods

The schematic reaction mechanisms for the preparation of AgPt nanorods (NRs) using the formic acid reduction method are illustrated in Figure 4.1a. The dehydration of formic acid in aqueous solution produces formate anion acting to reduce Pt salts. However, there are several possible mechanisms for assisting the growth to generate 1D nanostructure. The first pathway suggested the high attraction of formate anion on the Pt surface other than (111) facets [187]. Consequently, the reduced Pt tend to nucleate on the less covered Pt surface resulting in the growth along the <111> direction. The other studies proposed the poisoning effect by CO released from dehydration of formic acid on the Pt surface [188,189]. However, Pt (111) facets are less sensitive toward CO poisoning, which leads to the growth mechanism into forming 1D Pt nanostructures. Both possible routes show a similar trend of the less favourable Pt (111) surface interaction toward formic acid intermediates. Hence, the reaction mechanisms assist the growth of reduced Pt along the <111> direction and prohibit growth in other directions forming 1D nanostructures following the illustration in Scheme 1 (Figure 4.1a). A transmission electron microscope (TEM) image of the Pt NRs supported on carbon support is shown in Figure 4.1b. At the same solution condition, the reduction process of Ag ions into Ag metal is expected due to a close SRP of both metal ions. Compared to Pt, Ag surface conducts less ability to adsorb the dissociated formic acid species limiting its ability to control the growth of Ag seeds into a specific 1D direction. Finally, large Ag NPs are generated, which is shown in Scheme 2 and Figure 4.1c.

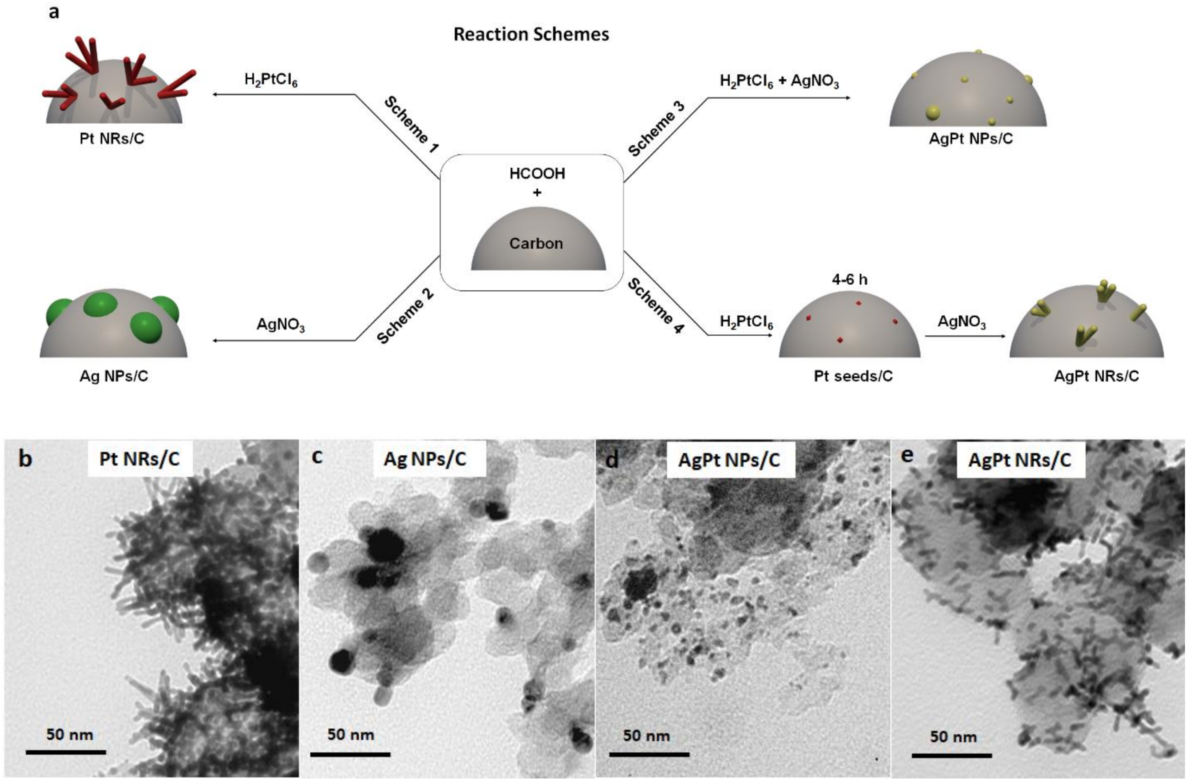

Figure 4.1 (a) The reaction schemes of Pt and Ag growth on supported carbon black conducted at room temperature with a total reaction duration of 96 hours. **(b-e)** TEM images of the catalysts obtained from the reactions shown in Schemes 1-4 in **(a)**.

In the presence of both Ag and Pt metal salts, the interval time of mixing both precursors is crucial to derive the shaping of 1D alloy nanostructures. For instance, the reduction of Ag and Pt ions together leads to the formation of AgPt NPs (Scheme 3 and the TEM image in Figure 4.1d). Despite a close SRP of Ag and Pt precursors, the reduction of Ag^+ occurs more spontaneously compared to the two steps reduction of Pt ions (Pt^{4+} and Pt^{2+}). Hence, a faster reduction rate of Ag ions induces the domination of Ag seeds at the early stage of the reaction. To facilitate the formation of 1D AgPt alloy nanostructure, the whole chemical reaction still needs to be dominated by Pt reduction. It is necessary for Pt to be reduced at first to form crystal seeds to mediate the epitaxial growth of both metals into a specific direction, followed by adding Ag after a controlled duration of Pt reduction of ca. 5 hours. In this case, the early reduction of Pt ions allows the formation of Pt seeds introducing the shape and size-controlled effect for further reduction, finally achieving 1D AgPt nanostructure with an average diameter of 3-4 nm and length of ~15 nm (Scheme 4 and the TEM image in Figure 4.1e, for Ag_1Pt_1 NR/C with an atomic ratio of Ag:Pt = 1:1,). Shorter NRs obtained from the bimetallic catalyst of Ag_1Pt_1 NR/C compared to Pt NR/C indicates the change of kinetic reaction by replacing 50 at% of Pt with Ag, which further confirms the major role of Pt to derive the formation of 1D morphology in the acidic media [125].

4.2 Optimisation of Ag-Pt Atomic Ratio

Through the literature study in Chapter 2, the atomic ratio is crucial to optimise the catalytic properties of Pt-Ag alloys as ORR catalysts. In this section, the atomic ratio is studied to obtain the ideal bimetallic AgPt alloy catalyst composition, and the total metal loading is fixed to carbon support. Figure 4.2 shows the TEM images of AgPt NR/C catalysts with different Ag and Pt ratios. The introduction of Ag changes the morphology of the 1D Pt alloy structure as it reduces the length of the 1D catalyst nanostructures. Shorter NRs are obtained with the increasing Ag content, intensifying the accelerated reaction rate with the less concentration of Pt ions. In the end, a much lower Pt ratio (Ag:Pt = 2:1) results in the domination of NPs formed on a carbon support, as shown in Figure 4.2d.

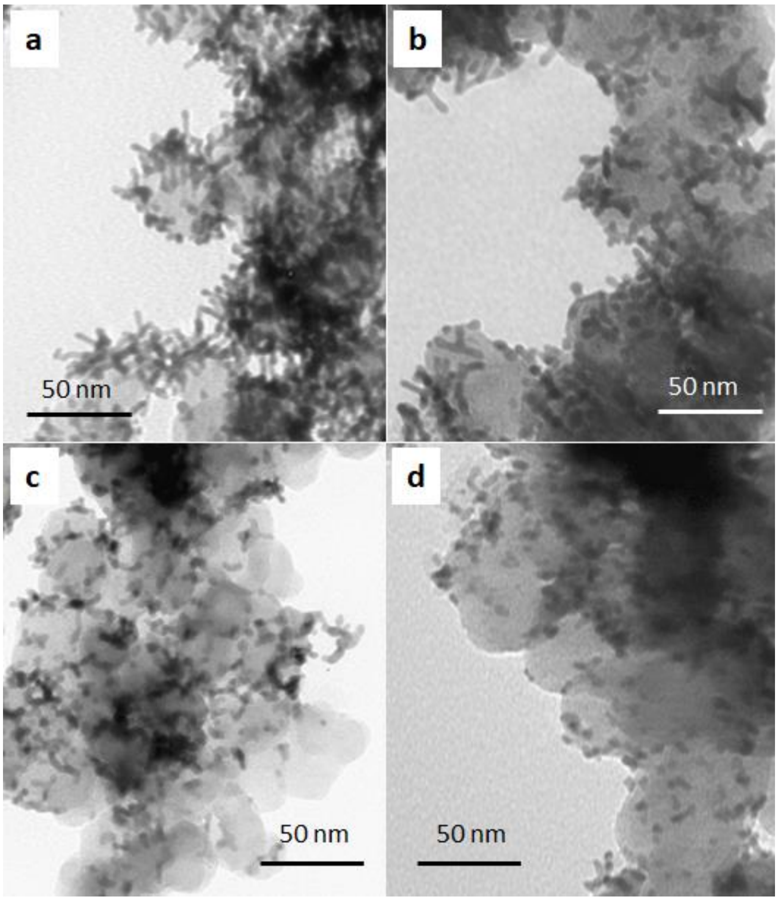

Figure 4.2 TEM images of the AgPt NR/C catalysts with different atomic ratios of Ag to Pt: **(a)** Ag_1Pt_4 NR/C, **(b)** Ag_1Pt_2 NR/C, **(c)** Ag_1Pt_1 NR/C, and **(d)** Ag_2Pt_1 NR/C.

The energy-dispersive X-ray spectroscopy (EDX) spectra (Figure 4.3) and inductively coupled plasma-mass spectroscopy (ICP-MS) analysis were both performed to determine the elemental contents of the catalysts with various Ag and Pt ratios. The results are listed in Table 4.1, along with the thermogravimetric analysis (TGA) data, showing a good consistency with the expected metal ratios deposited on carbon.

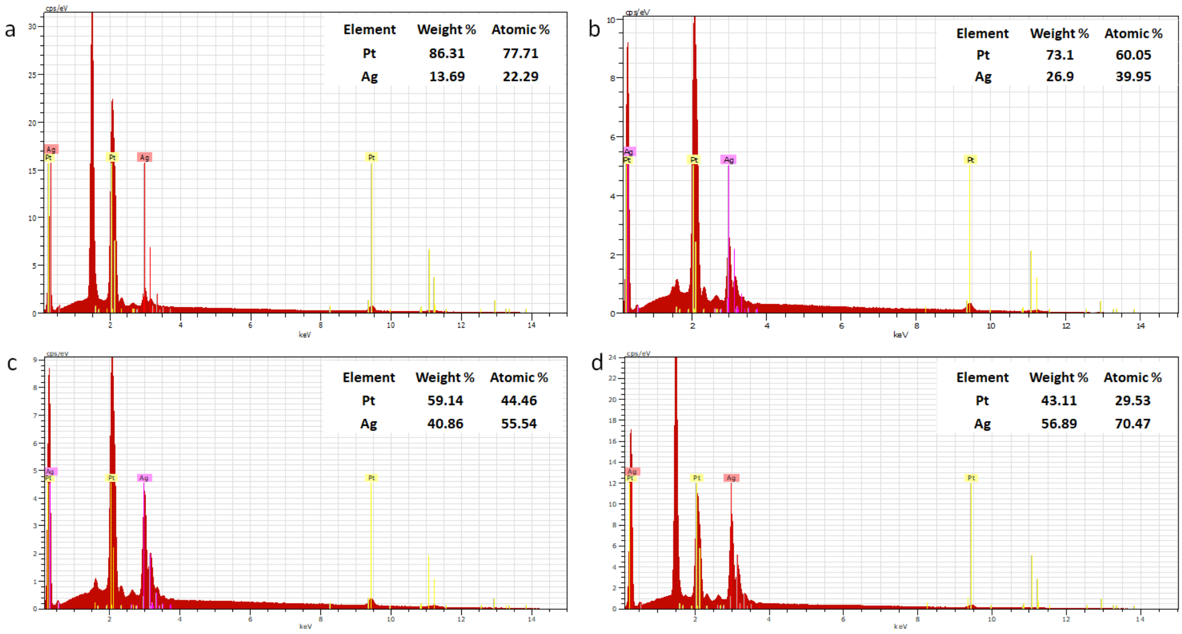

Figure 4.3 EDX spectrum of **(a)** Ag_1Pt_4 NR/C, **(b)** Ag_1Pt_2 NR/C, **(c)** Ag_1Pt_1 NR/C and **(d)** Ag_2Pt_1 NR/C

Table 4.1 The metal residue generated by TGA and the corresponding metal content measured by ICP-MS and EDX.

Catalysts	TGA (metal loading / wt%)	ICP-MS / wt%		ICP-MS / at%		EDX / at%	
		Ag	Pt	Ag	Pt	Ag	Pt
Pt NR/C	58.20	0	100	0	100	0	100
Ag_1Pt_4 NR/C	61.20	11.53	88.47	19.07	80.93	22.29	77.71
Ag_1Pt_2 NR/C	62.04	21.16	78.84	32.67	67.32	39.95	60.05
Ag_1Pt_1 NR/C	60.98	32.23	67.77	46.23	53.77	55.54	44.46
Ag_2Pt_1 NR/C	63.22	52.82	47.18	66.94	33.06	70.47	29.53

A typical NR for the Ag_1Pt_4 NR/C catalyst is shown by high-resolution (HR) TEM analysis (Figure 4.4a). The image indicates the single-crystal feature of the 1D nanostructure with a lattice spacing of 0.23 nm, which is assigned to (111) planes between the bulk Pt (JCPDS: 04-0802) and Ag (JCPDS: 04-0783) (0.227 nm and 0.235 nm, respectively). The similar interplanar space of 0.23 nm is observed from Ag_1Pt_1 NR/C (Figure 4.5a), showing the lattice orientation, which confirms the anisotropic growth of 1D nanostructure along the <111> direction. The results of scanning electrode microscopy-EDX (STEM-EDX) mapping analysis of both Ag_1Pt_4 NR/C (Figure 4.4b-e) and Ag_1Pt_1 NR/C (Figure 4.5b-e) show the distribution of Ag and Pt along NRs. The good overlapping of both maps without a high content of Ag at the boundary confirms the alloy structure of the AgPt NR/C catalysts [166].

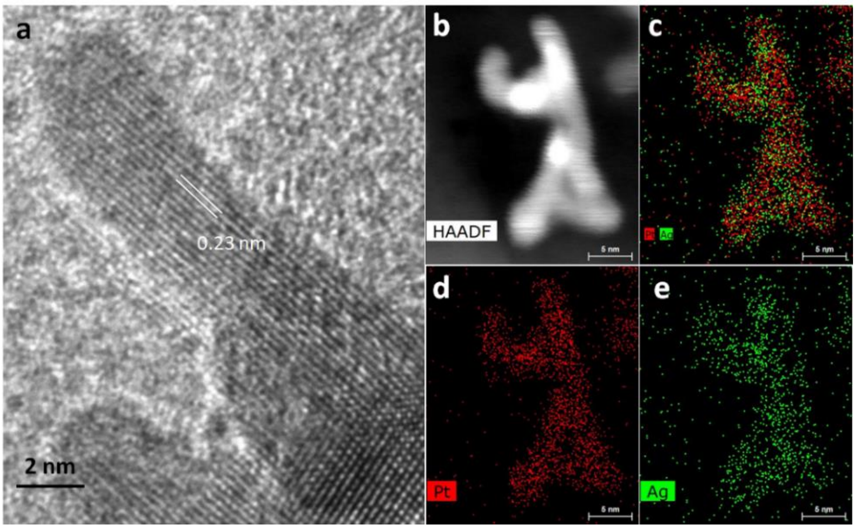

Figure 4.4 (a) HR-TEM image of Ag_1Pt_4 NR/C (atomic ratio of Ag:Pt = 1:4), **(b-e)** show the element mapping by STEM-EDX analysis.

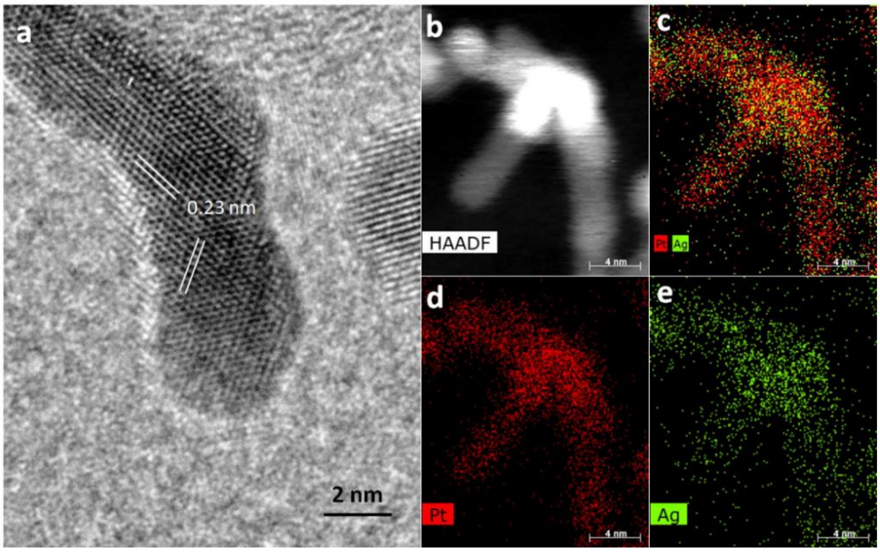

Figure 4.5 (a) HR-TEM image of Ag_1Pt_1 NR/C (atomic ratio of Ag:Pt = 1:1), **(b-e)** show the element mapping by STEM-EDX analysis.

Figure 4.6 displays the X-ray diffraction (XRD) patterns of the Pt NR/C and AgPt NR/C catalysts with varied atomic ratios. The main peaks are indexed to (111), (200), (220) and (311) facets, appointed to the face-centred cubic (FCC) crystal structure. The measured lattice space of Pt NR/C at (111) is 0.225 nm, which is close but smaller than the bulk Pt (JCPDS: 04-0802) (0.227 nm), indicating the change of lattice space because of the 1D NR structure. The high-intensity peaks of Pt NR/C are related to the good crystallinity of 1D nanostructures [143]. These peaks decrease after the introduction of Ag, which can be attributed to the lattice contraction between Ag and Pt atoms. Similar behaviour of XRD pattern transformation because of the changed Ag and Pt ratio is also reported in the literature [190], which further indicates the significant effect of Ag alloying to modify the structure and properties of Pt nanostructures. In agreement, the increasing of Ag ratio to Pt renders the broader width of XRD peaks, confirming an enhanced lattice effect which agrees with the change to shorter NRs observed in the TEM analysis in Figure 4.2.

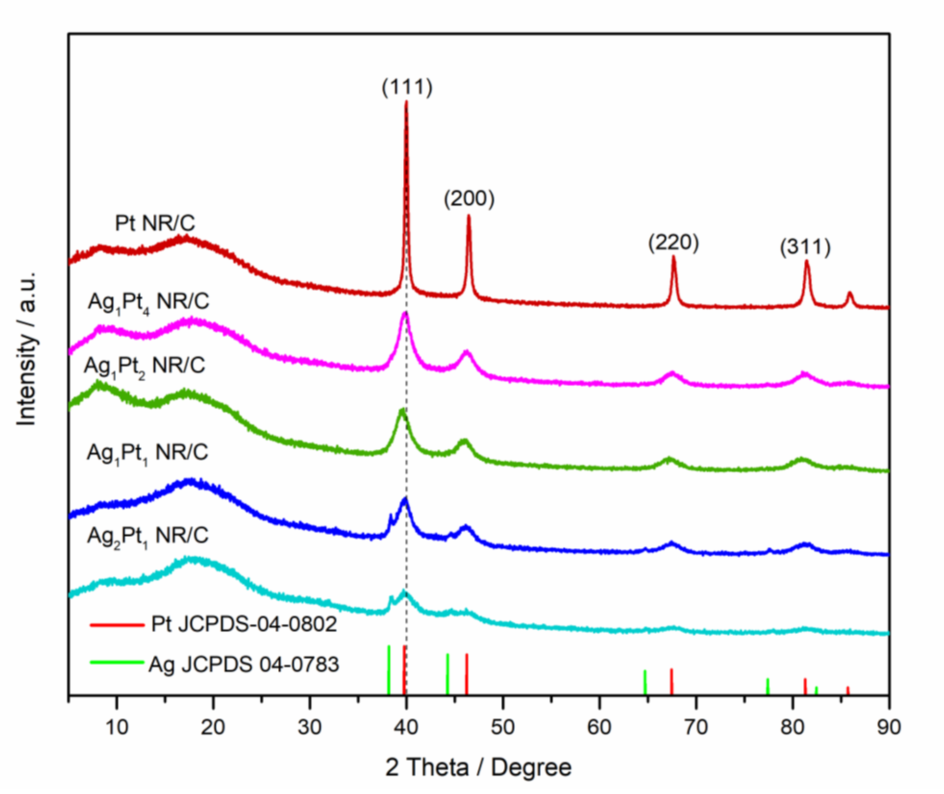

Figure 4.6 XRD patterns of the Pt NR/C and AgPt NR/C catalysts with varied atomic ratio.

A small peak shift is observed due to alloying with Ag, indicating the change of the interplanar space. For instance, the (111) peak of the Ag_1Pt_2 NR/C catalyst shows a shift of 0.47 degree at two theta compared to the Pt NR/C catalyst, which corresponds to an expanded lattice spacing of 0.228 nm. Further increase of the Ag content (Ag_1Pt_1 NR/C) shows less shift, while, the main peaks are in alignment with Ag_1Pt_4 NR/C catalyst, indicating a similar lattice constant which is in agreement with the HR-TEM analysis results in Figure 4.4a and 4.5a. Moreover, the formation of a separate extra peak referencing to the Ag metal phase is observed from Ag_1Pt_1 NR/C and Ag_2Pt_1 NR/C. The significant increase of Ag metal phase peaks in Ag_2Pt_1 NR/C catalysts is formed from the excess of Ag ions, which is rationally related to the higher Ag ratio. Furthermore, a broader (111) peak is obtained with the increase Ag content, intensifying the smaller size of alloy catalysts referencing to the domination of NPs formation as shown by TEM image in Figure 4.2d. These results further indicate the complexity of the formic acid reduction method for the preparation of 1D AgPt nanostructures. Nevertheless, it concludes the dependency on the whole reaction rate to derive 1D nanostructures.

Doubling the concentration of the Ag and Pt precursors toward formic acid and keeping the metal ratio of Ag:Pt = 2:1 (Ag_2Pt_1 NR/C -ii catalyst) shows an effective approach to slow down the kinetic reaction. The growth of relatively longer NRs on the carbon support is shown in the TEM image in the inset of Figure 4.7. However, it also leads to a higher degree of agglomerated NRs rendered by a very slow kinetic reaction, which is similar to our previous observation [142]. Although the Ag metal phase peak is not observed in the XRD pattern (Figure 4.7), an extra pattern of peaks referencing to AgCl (JCPDS: 31-1238) is exhibited. The formation of AgCl is potentially ascribed to the excess concentration of metal ions. It further discloses the limitation of the parameter employed in this work. Thus, the same atomic ratio (Ag:Pt = 1:1) is considered as the optimal alloy composition to obtain 1D AgPt alloy nanostructures. Otherwise, acid leaching and high-temperature treatment (e.g. 250 °C) are required to remove

Cl formed in the high Ag content [191,192]. However, high-temperature treatment of above 150 °C potentially leads to the morphology change of the NR structure [154], which will be further discussed in section 4.5.

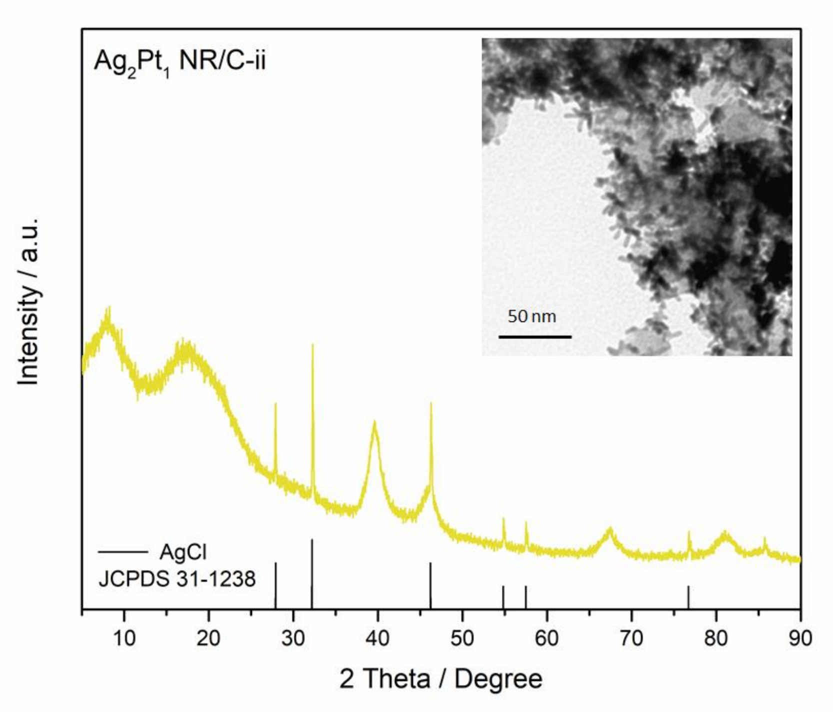

Figure 4.7 TEM image and the corresponding XRD pattern of AgPt NR/C-ii.

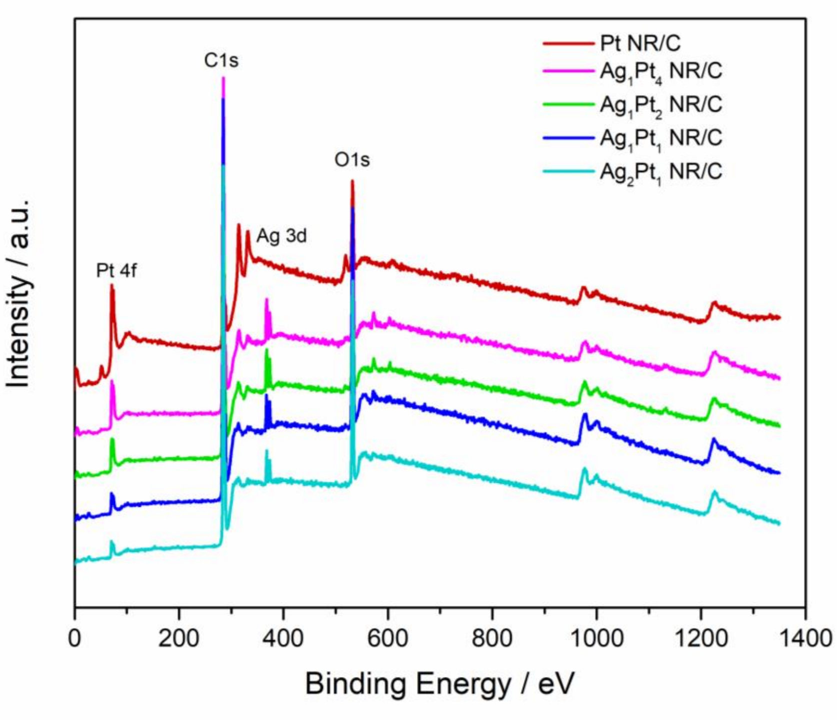

Figure 4.8 XPS survey of the Pt NR/C and AgPt NR/C catalysts with different Ag contents.

The X-ray photoelectron spectroscopy (XPS) survey scan of the AgPt NR catalysts (Figure 4.8) distinguishes the strong signal of Pt 4f and Ag 3d confirming the surface composition of the alloy catalysts. The high-resolution Pt 4f region of the AgPt NR/C catalysts shows a negative shift in binding energy compared to that of Pt NR/C (Figure 4.9a), following a similar trend to the change of the XRD peaks (Figure 4.6). The Ag_1Pt_2 NR/C catalyst exhibits the largest negative shift of 0.41 eV recorded at Pt $4f_{7/2}$ peak relative to the pure 1D Pt NR catalyst (70.84 eV). And then the peak slightly shifts back with the increasing Ag content to 70.56 and 70.64 eV for Ag_1Pt_1 NR/C and Ag_2Pt_1 NR/C, respectively. The same trend is also demonstrated for the high-resolution Ag 3d spectrum with the largest shift observed at the atomic ratio of Ag to Pt = 1:2 (Figure 4.9b). These negative shifts signify the change of the electronic structure after alloying Pt and Ag [159,193].

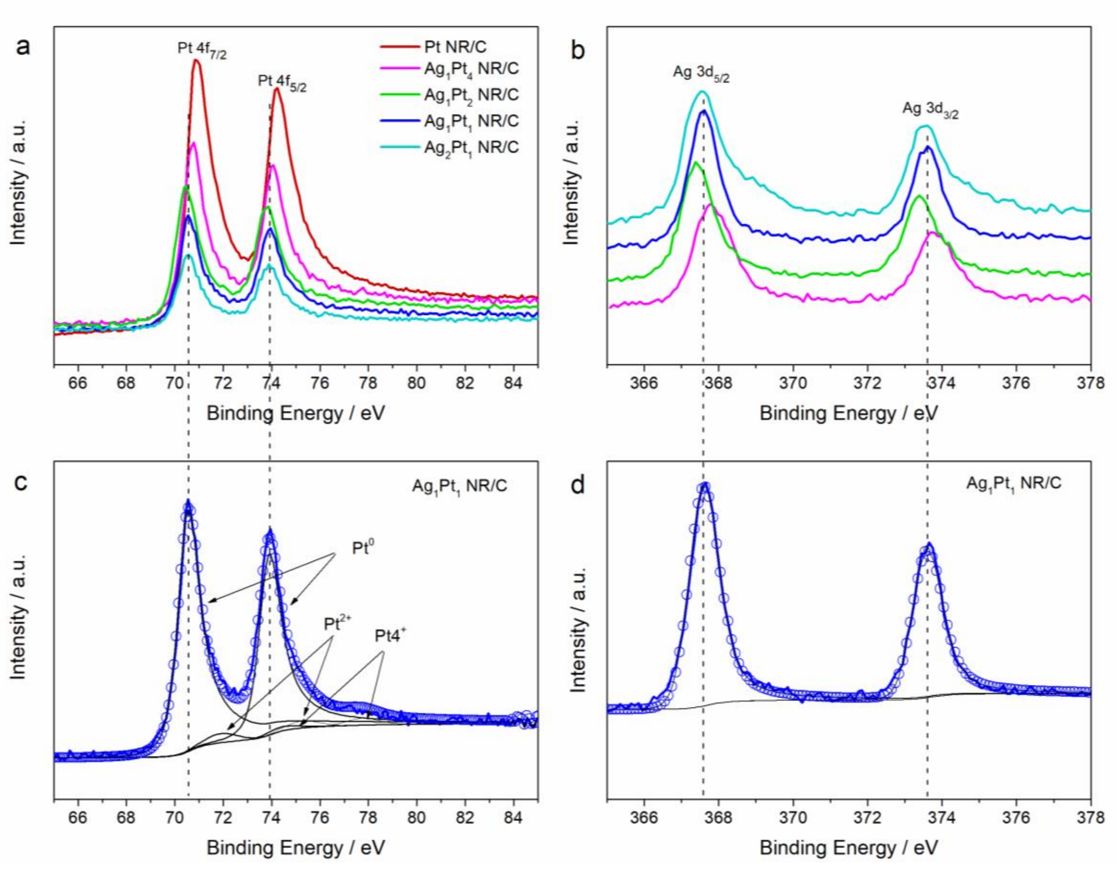

Figure 4.9 XPS spectra of the high-resolution **(a)** Pt 4f and **(b)** Ag 3d region of the Pt NR/C and AgPt NR/C catalysts. The band deconvolution for Ag_1Pt_1 NR/C given in the specific high-resolution XPS regions: **(c)** Pt 4f and **(d)** Ag 3d.

Fitting of Pt 4f peaks for the Ag_1Pt_1 NR/C catalyst (Figure 4.9c) shows the domination of Pt^0 with a percentage of 94.08% ascribing to the metallic state of Pt and meaning that the low oxidation state contribution (Pt^{2+} and Pt $^{4+}$) is less than 6%. The high-resolution Ag 3d spectra locating at 367.66 and 373.70 eV for Ag $3d_{5/2}$ and Ag $3d_{3/2}$ peaks, respectively, (Figure 4.9d) are composed entirely of Ag^0, which indicates that the alloyed Ag ions are completely reduced to its metallic state. Table 4.2 summarises the Pt 4f and Ag 3d fitting results for the Pt NR/C and all AgPt NR/C catalysts, presenting the domination of Pt^0 for all NR catalysts (> 94%) and Ag^0 for all AgPt catalysts (> 97%). These results further demonstrate the high effectiveness of the formic acid reduction method applied in this work to prepare 1D Pt hybrid catalysts.

Table 4.2 Composition of Pt and Ag elements obtained from the Pt 4f and Ag 3d XPS region

Catalysts	Pt 4f / %			Ag 3d / %	
	Pt^0	Pt^{2+}	Pt^{4+}	Ag^0	Ag^+
Pt NR/C	100	0	0	0	0
Ag_1Pt_4 NR/C	96.23	2.19	1.58	100	0
Ag_1Pt_2 NR/C	94.48	2.82	2.7	100	0
Ag_1Pt_1 NR/C	94.08	3.50	2.42	100	0
Ag_2Pt_1 NR/C	94.03	3.08	2.86	97.99	2.01

4.3 MEA Testing

The catalytic performance of the as-prepared 1D AgPt alloy catalysts is evaluated in PEMFCs through the test of MEAs with an active area of 16 cm^2. Benchmarking to the as-made Pt NR/C and commercial Pt/C catalyst (TEC10E50E, TKK), the varied atomic ratio of AgPt NR/C catalysts were employed as cathode catalysts to fabricate gas diffusion electrodes (GDEs) with the same Pt loading applied (0.2 mg_{Pt} cm^{-2}). The polarisation and power density curves for all MEAs are shown in Figure 4.10, and they exhibit a similar open-circuit voltage (OCVs) above

0.9 V. The power densities at 0.6 V are similar (0.42 W cm^{-2}) for the GDE made of the Pt/C, Pt NR/C and AgPt NR/C catalysts with the Ag:Pt ratio of up to 1:2. The attachment of the Ag content of ~50 at% (Ag_1Pt_1 NR/C) shows a higher power density of 0.48 W cm^{-2} at 0.6 V and a maximum power density output of 0.55 W cm^{-2}, which is 1.14 fold higher than that of Pt/C. The enhanced power density with the increasing Ag content indicates a positive effect of the Ag integration toward the ORR activity. However, a further increase of the Ag content (Ag_2Pt_1 NR/C) results in a lower peak power density of 0.43 W cm^{-2}.

The electrochemical impedance spectroscopy (EIS) analysis was conducted at the low current density of 30 mA cm^{-2} to understand the catalytic behaviour of the AgPt NR/C GDEs (Figure 4.10d). The charge transfer resistance shown by the diameter of the semi-circle is comparable for the Pt NR/C GDE and AgPt NR/C GDEs. It indicates a similar kinetic reaction, which is in agreement with the polarisation curve in Figure 4.10a. The unexpected larger impedance is observed from Pt/C GDE due to an unknown error. In this case, the polarisation curve is more reliable to determine the ORR performance of the GDE.

EIS analysis results at the lower potentials of 0.65 and 0.5 V (Figure 4.10e-f) support the trend of polarisation curves in Figure 4.10a. The smallest impedance at a large current density dominated by mass transfer resistance was generated from the GDE made of Ag_1Pt_1 NR/C catalyst (Figure 4.10f). The less aggregated shorter NRs (Figure 4.2c) provide an improved porosity in the catalyst layer structure to enhance gas transport [35]. Additionally, the feasible amount of Ag facilitates good electron transfer advantaging of its high conductivity [157]. However, too high the Ag content (Ag_2Pt_1 NR/C) results in the formation of Ag metal phase (Figure 4.3). It is less advantageous for the ORR kinetic activity because of the limited two-electron reduction pathway on the Ag surface in acidic media [163]. Hence, a larger charge transfer resistance is observed for the Ag_2Pt_1 NR/C GDE, indicating its lower ORR activity.

Furthermore, the NP morphology is more dominant for the Ag_2Pt_1 NR/C catalyst, leading to poorer mass transport behaviour cf. the NR GDEs, which is shown by the EIS spectra at 0.5 V (Figure 4.10f).

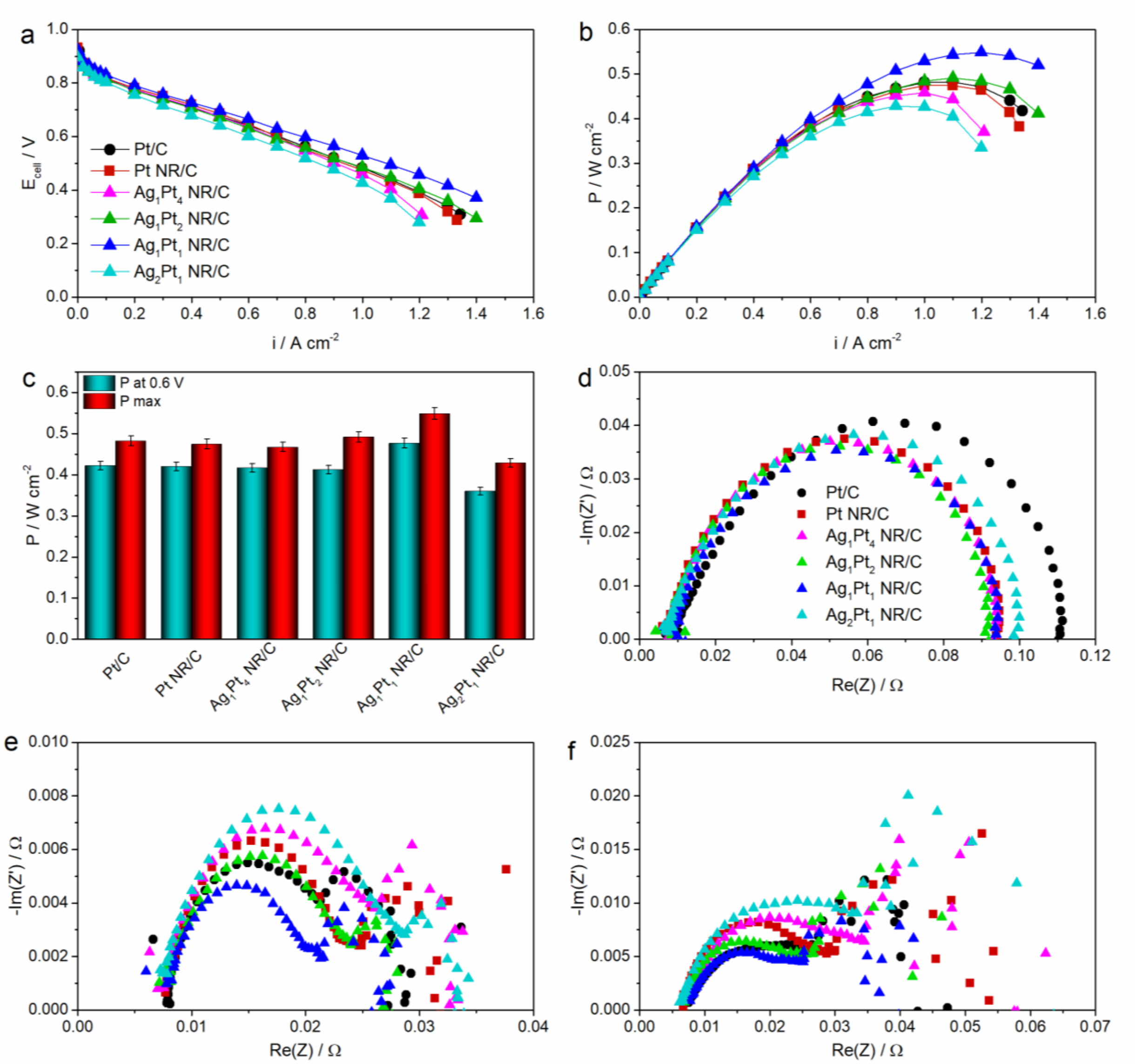

Figure 4.10 MEA testing results of the as-prepared Pt NR/C and AgPt NR/C GDEs in comparison to Pt/C GDE with the same Pt loading of 0.2 mg_{Pt} cm^{-2}: **(a)** polarisation curves, **(b)** power density curves and **(c)** the corresponding power densities recorded at 0.6 V and the peak power densities. The corresponding EIS spectra measured at **(d)** 30 mA cm^{-2} (e) 0.65 V and (f) 0.5 V.

The cyclic voltammetry (CV) plots of the tested MEAs are shown in Figure 4.11a. The GDE made of the 1D NR/C catalysts show lower hydrogen desorption (H_{des}, below 0.4 V) peaks compared to 0D Pt/C. The large aspect ratio and bulk size of 1D nanostructures result in the decreased surface area, thus lower ECSA values. The measured ECSA for the Pt NR/C GDE is 14.68 m^2 g_{Pt}^{-1}, which is very close to the data reported in the previous study [142]. The number of active sites increases with the Ag content obtaining the largest ECSA of 24.26 m^2 g_{Pt}^{-1} for Ag_1Pt_1 NR/C GDE. It is related to the morphology change following the higher Ag content. It further confirms the contributing factor in upgrading the power performance obtained in Figure 4.10. However, a higher atomic ratio of Ag (e.g. Ag:Pt = 2:1) induces much less exposure of Pt active sites, leading to a slightly reduced ECSA of 23.66 m^2 g_{Pt}^{-1}. These results suggest that the same atomic ratio of Ag and Pt (Ag_1Pt_1 NR/C) can be considered as the ideal composition to optimise the ECSA of the 1D AgPt catalyst surface and enhance the AgPt alloy catalytic activity towards the ORR.

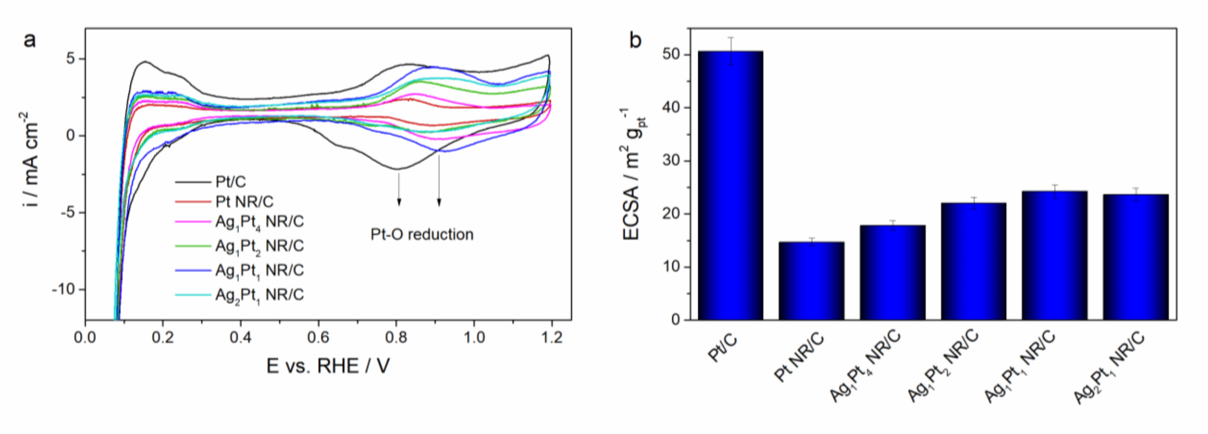

Figure 4.11 (a) CV plots of the Pt/C, Pt NR/C and AgPt NR/C GDEs with different Ag and Pt ratios and **(b)** the corresponding ECSA values measured from the CVs.

The ORR mass activity of the GDE made of the Ag_1Pt_1 NR/C catalyst was further evaluated under H_2/O_2 following the U.S. Department of Energy (DoE) protocol to minimise the influence of mass transport, with the benchmarking to Pt/C and Pt NR/C. The recorded polarisation curves and the ones after the corrections of the ohmic resistance losses and H_2-crossover are presented in Figure 4.12. A mass activity of 0.098 A mg_{Pt}^{-1} at 0.9 V is obtained from the Ag_1Pt_1 NR/C GDE, which is 1.22 and 1.51 fold higher than the Pt NR/C and Pt/C GDEs, respectively, demonstrating the activity enhancement effect towards ORR by alloying

Pt with Ag. At the high current density region above 0.3 A cm^{-2}, because of the reduced mass transport resistance resulting from the longer NRs [194], better power performance is achieved for Pt NR/C compared to Ag_1Pt_1 NR/C. The activity values are summarised in Table 4.3. A larger specific activity (SA) from the NR catalysts further confirms the benefit of 1D nanostructure catalysts to improve the ORR activity. Finally, considering the relatively low cost of Ag (2% of Pt), the mass activity normalised to Pt remains highly sensible in practical application, with which Ag_1Pt_1 NR/C exhibits strong superiority.

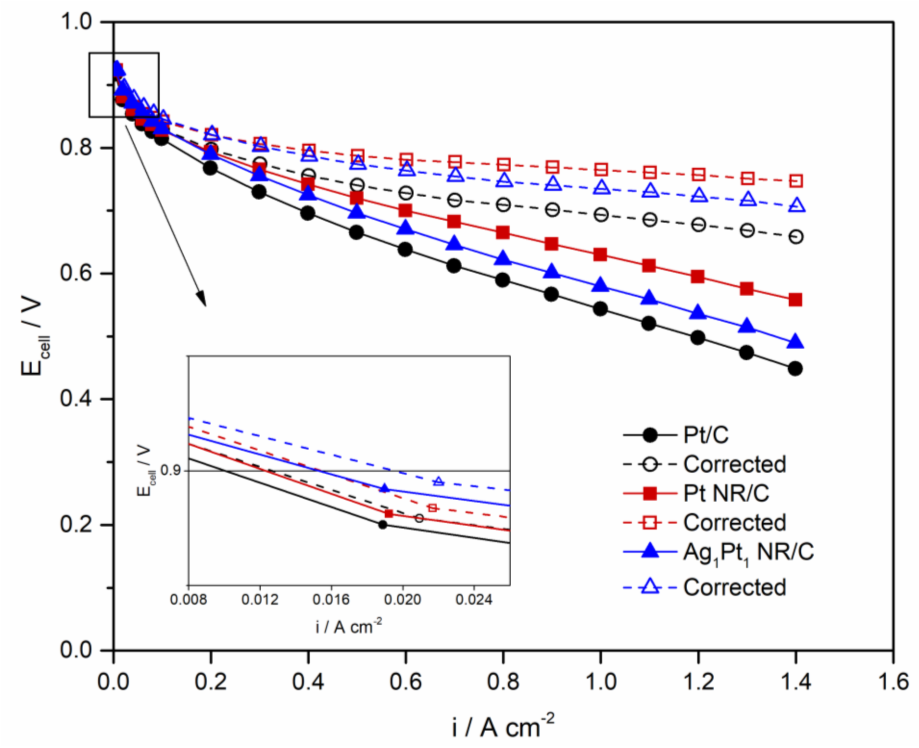

Figure 4.12 Recorded and corrected polarisation curves obtained under H_2/O_2 testing.

Table 4.3 Comparison of catalytic activities for the tested catalysts in the MEA test

Catalysts	I_k (@0.9 V) / A	I_m / A mg$_{Pt}^{-1}$	I_s / μA cm^{-2}
Pt/C	0.21	0.065	130.29
Pt NR/C	0.26	0.080	544.91
Ag_1Pt_1 NR/C	0.30	0.098	391.63

The nature of 1D structures and the involvement of Ag as the alloyed metal has successfully modified the intrinsic Pt catalyst to enhance its catalytic activity towards ORR. The formation of single-crystal along the <111> direction facilitates the preferential exposure of highly active crystal facets with improved ORR activities [195]. A positive shift of the Pt-O reduction peak in the CV plots is observed for the GDEs made of 1D catalysts compared to Pt/C (shown by arrows in Figure 4.11a). The Pt NR/C GDE exhibits a Pt-O reduction peak at 0.889 V vs RHE as compared to 0.805 V vs RHE for the Pt/C GDE. This shift indicates the weakening bond between O-containing species and the catalyst surface caused by the smooth atomic surface of 1D NRs, which is expected to contribute to an improved ORR activity [127]. This improvement is boosted by the synergistic effect between Ag and Pt in the alloy form. The introduction of Ag induces more positive shift as observed from the Ag_1Pt_1 NR/C GDE, for which the Pt-O reduction peak is at 0.913 V (with a shift of 0.108 V), indicating a higher ORR catalytic performance compared to the Pt NR/C GDE. The alloy causes tensile strain on the Pt lattice because of the different lattice constants of Pt and Ag (3.92 and 4.09 Å, respectively), hence, changing the Pt d-band centre and modifying the electronic structure, which is confirmed by the XPS analysis (Figure 4.5) [196,197]. These changes lead to weaker binding of Pt surface with O-containing species formed in the ORR process, thus facilitating the desorption of oxygen for increased ORR kinetics [193]. Furthermore, fewer surface defects of the NRs (cf. NPs) also contributes to less interaction with O-contained species. Therefore, a good balance of Ag and Pt in the alloyed NR catalysts (i.e. Ag_1Pt_1 NR/C) provides a harmony of O-H bonding formation and O-O bonding cleavage, finally leading to enhanced catalytic activities.

4.4 Accelerated degradation test (ADT)

The superiority of the Ag_1Pt_1 NR/C cathode is further examined against durability testing to evaluate the stability of the alloy catalyst in the fuel cell environment. After 5000 potential cycles of ADT under H_2/N_2, a significant performance drop of the tested catalysts is observed (Figure 4.13a). The maximum performance loss follows the trend of Pt NR/C < Pt/C < Ag_1Pt_1 NR/C with the percentage degradation of 41.41%, 44.19% and 46.32%, respectively, as shown in Figure 4.13b.

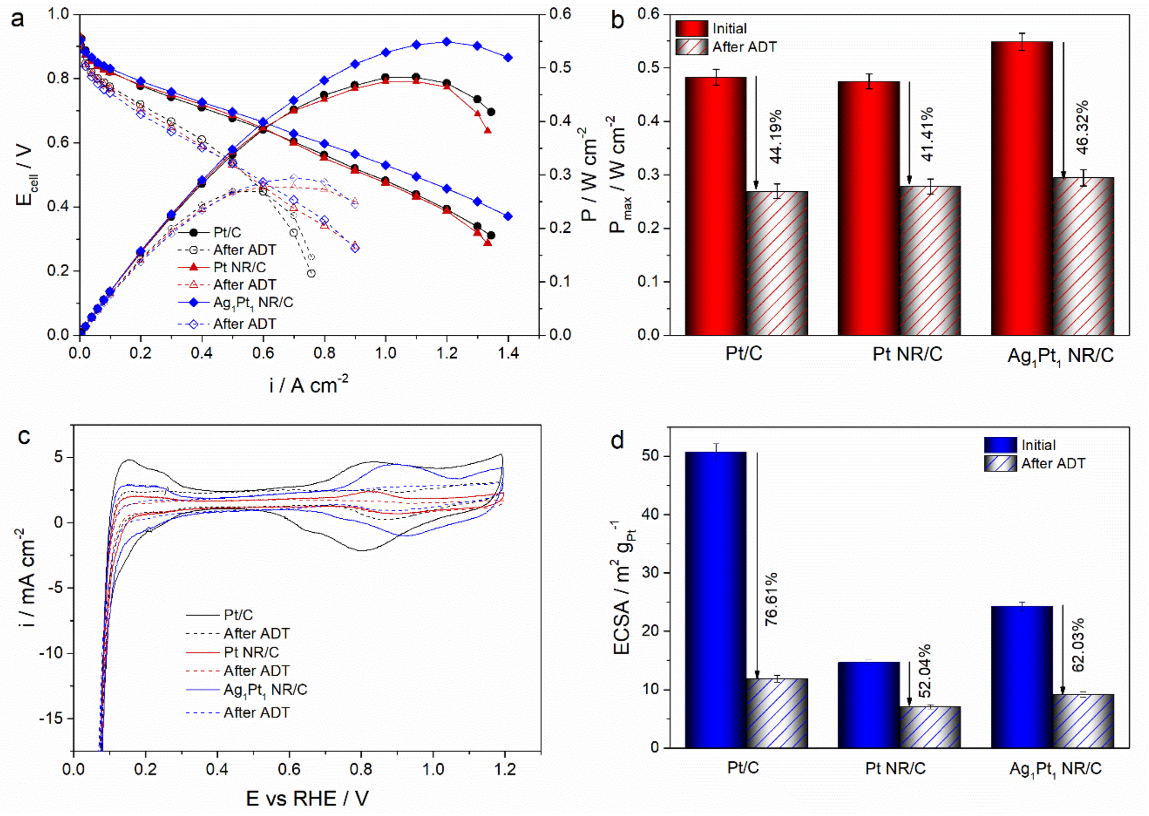

Figure 4.13 Comparison of the Pt/C, Pt NR/C and Ag_1Pt_1 NR/C GDEs after using 5000 potential sweeping cycles of ADT in the MEA test: **(a)** polarisation and power density curves, **(b)** peak power density showing the declines ratios after the ADT, **(c)** CVs and **(d)** the corresponding ECSA declines ratios after the ADT.

To understand the reasons of the power performance decline during the ADT, e.g. by the degradation of the electrode structure or from the catalyst itself, or even both, CV analysis was conducted after the ADT, and the corresponding ECSA change is shown in Figure 4.13c-d. Although with the highest power density drop, the Ag_1Pt_1 NR/C GDE suffers a less ECSA decline of 62.03% compared to the Pt/C GDE of 76.61%. However still larger than the Pt NR/C GDE (52.04%). Immense power and ECSA loss of the Ag_1Pt_1 NR/C GDE after the ADT is attributed to the dissolution of Ag, as shown in Figure 4.14. Regardless of the close lattice constant of Ag and Pt, the segregation of Ag cannot be fully avoided in the severe acidic environment in the PEMFC operation condition. Finally, it leads to the redeposition of Ag at the interface between the cathode and electrolyte membrane inducing the large performance drop after the ADT. The higher ECSA loss because of the alloy with Ag is unavoidable considering the poor stability of Ag in the acidic environment [198], although the final power performance is still reasonable for application in practical devices taking the advantages of the hybrid 1D AgPt nanostructure.

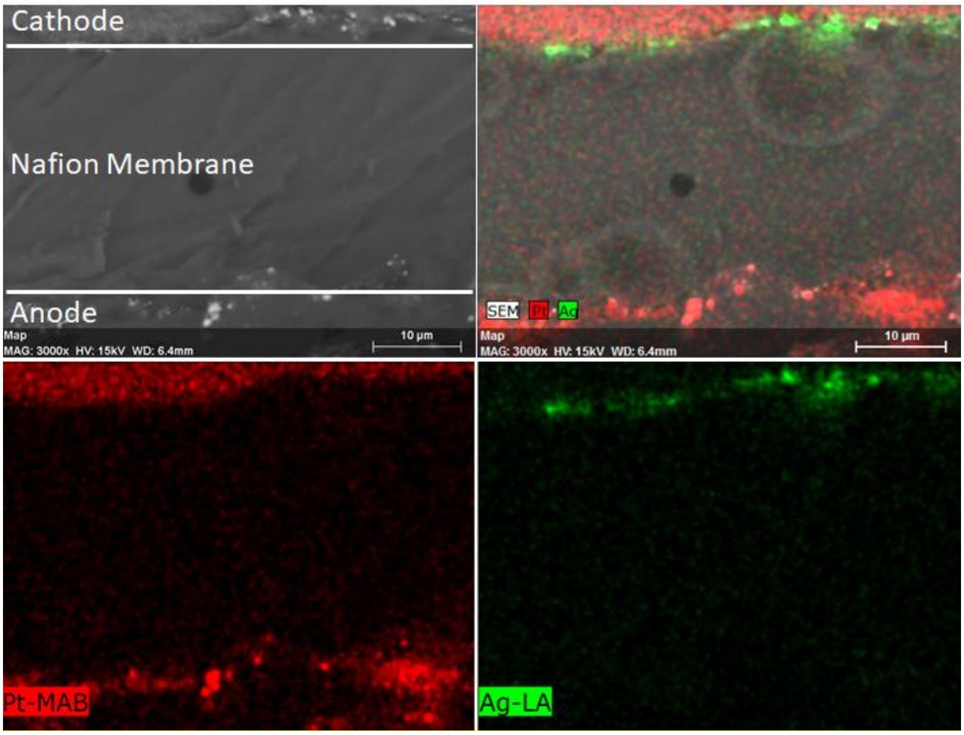

Figure 4.14 Cross-sectional SEM-EDX mapping of the Ag_1Pt_1 NR/C MEA after the ADT

4.5 Impact of the heat treatment on the catalytic performance of AgPt NR/C

The tested AgPt NR/C catalysts in this chapter have been heat-treated at 120 °C for 2 hours under 60 mL min^{-1} of 4% H_2/Ar prior the MEA testing. The heat treatment has been reported as a necessary step to remove the impurities after the synthesis processes, maximising the dispersion of catalysts on the support material to optimise catalytic activities [199,200]. It has also been revealed as an effective step to achieve a good Pt alloying degree and optimise the catalyst surface properties to improve the ORR activity and stability [201]. However, the optimisation of treatment temperature is limited in this work due to the susceptibility of the ultrafine 1D Pt nanostructure toward the heat treatment of above 200 °C [154]. TEM images in Figure 4.15 show the morphology change of the NR structures after the heat treatment. Even a treatment temperature of 150 ^{o}C induces sintering of the 1D nanostructures to form large particles.

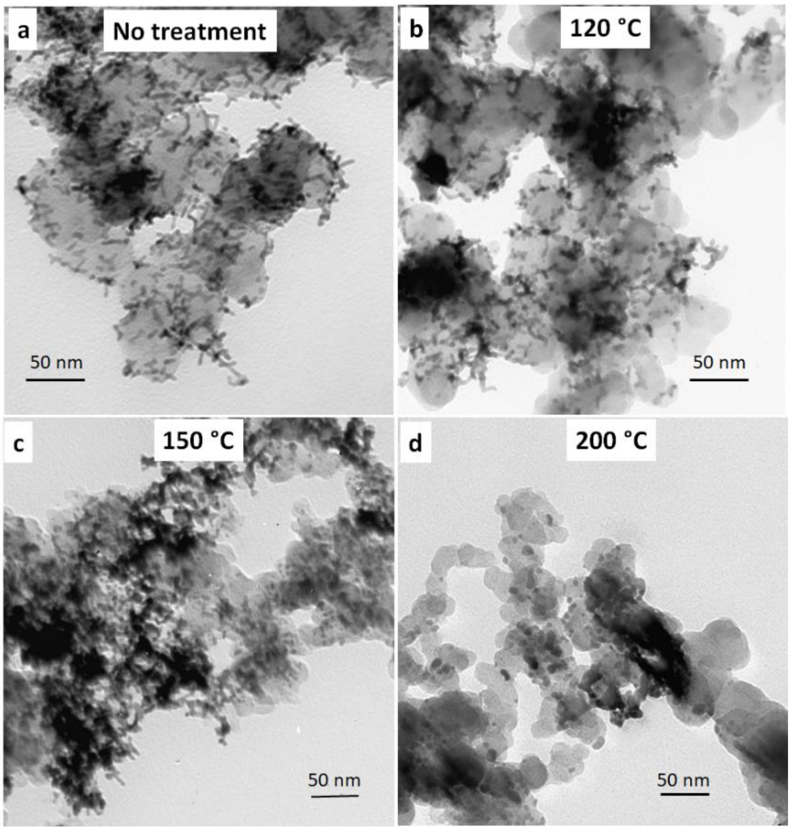

Figure 4.15 TEM images of Ag_1Pt_1 NR/C treated at a different temperature under 60 mL min^{-1} of 4% H_2/Ar.

The TEM images in Figure 4.15a-b exhibit the same structure of Ag_1Pt_1 NR/C before and after the heat treatment at 120 °C, which is in agreement with the XRD patterns presented in Figure 4.16a. The identical XRD peaks suggest little influence of the heat treatment effect toward the crystallinity and lattice constant of the AgPt alloy catalyst. However, the high-resolution XPS peaks at the Ag 3d region exhibits a tremendous negative shift of ca. 0.3 eV prior the heat treatment (Figure 4.16f), confirming a significant heating effect toward the Ag properties compared to that Pt. A positive shift is commonly ascribed to the higher oxidation state of Ag. Here, the peak position for both catalysts is more negative than the pure Ag $3d_{5/2}$ reference (368.3 eV), emphasising charge transfer phenomena of the bimetallic structure [202,203]. Close values were obtained for the Pt^0 and Ag^0 state prior (93.28% and 100%, respectively) and after the heat treatment (the data present in Table 4.2), indicating also the subtle effect of this heating step to minimise the impurities and oxidation species, further confirming the effectiveness of ion reduction method with formic acid.

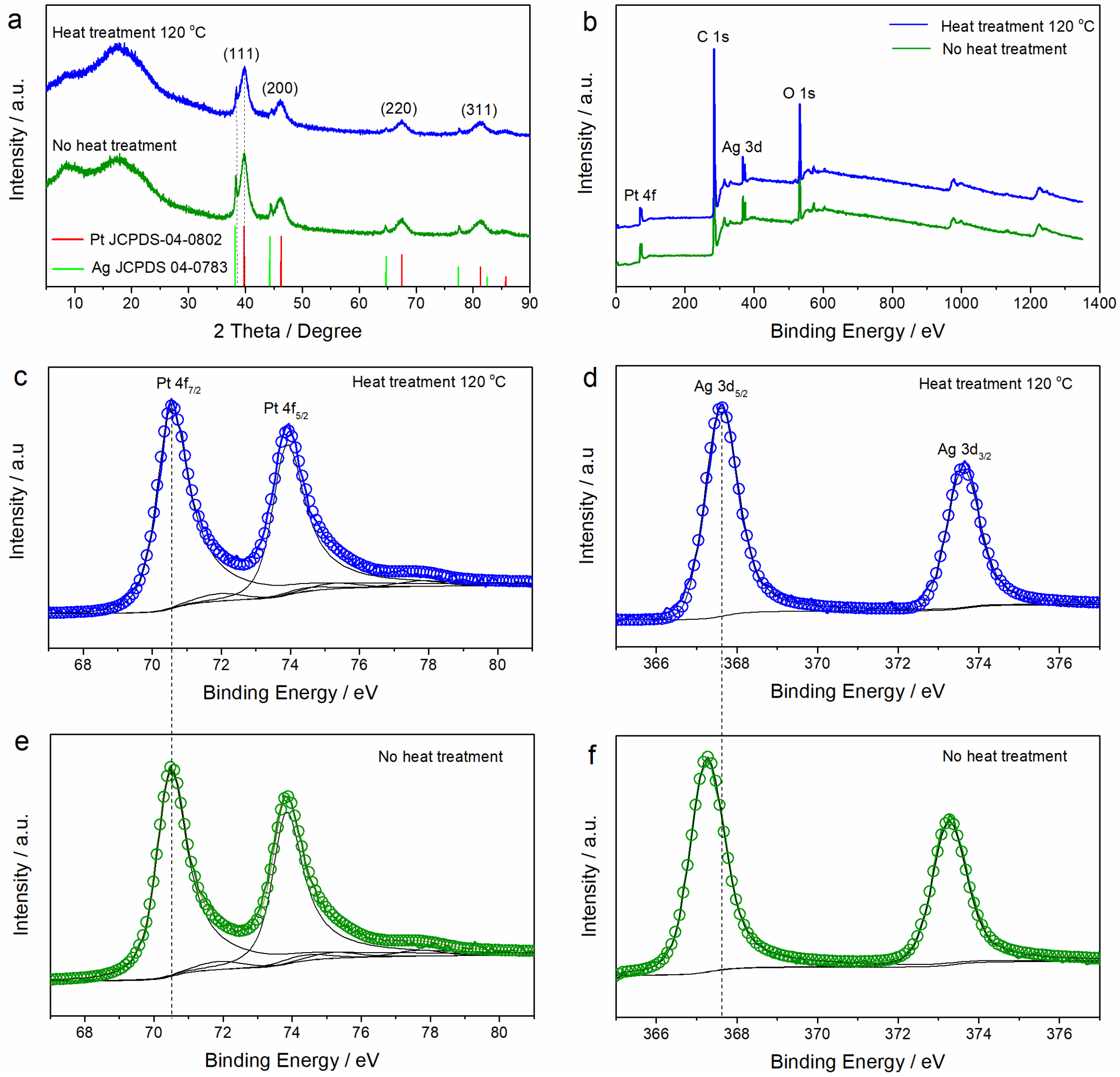

Figure 4.16 (a) Comparison of XRD patterns and **(b)** XPS survey of the pristine and heat-treated Ag_1Pt_1 NR/C at 120 °C with **(c-f)** the high-resolution XPS spectra at the Pt 4f and Ag 3d region.

The heat treatment exhibits an obvious improvement in minimising the potential loss, especially at a higher Ag loading, as shown in Figure 4.17. A noticeable power density increase is observed for the GDEs with a high Ag loading of above 50 at% after the heat treatment at 120 °C, upgrading 6.6% and 23% of the peak power density of the Ag_1Pt_1 NR/C and Ag_2Pt_1 NR/C GDEs, respectively. Meanwhile, only a very small increase is exhibited for the Ag_1Pt_4 NR/C and Ag_1Pt_2 NR/C GDEs, suggesting a reduced effect of the heat treatment on the catalytic performance for the catalysts with a low Ag content.

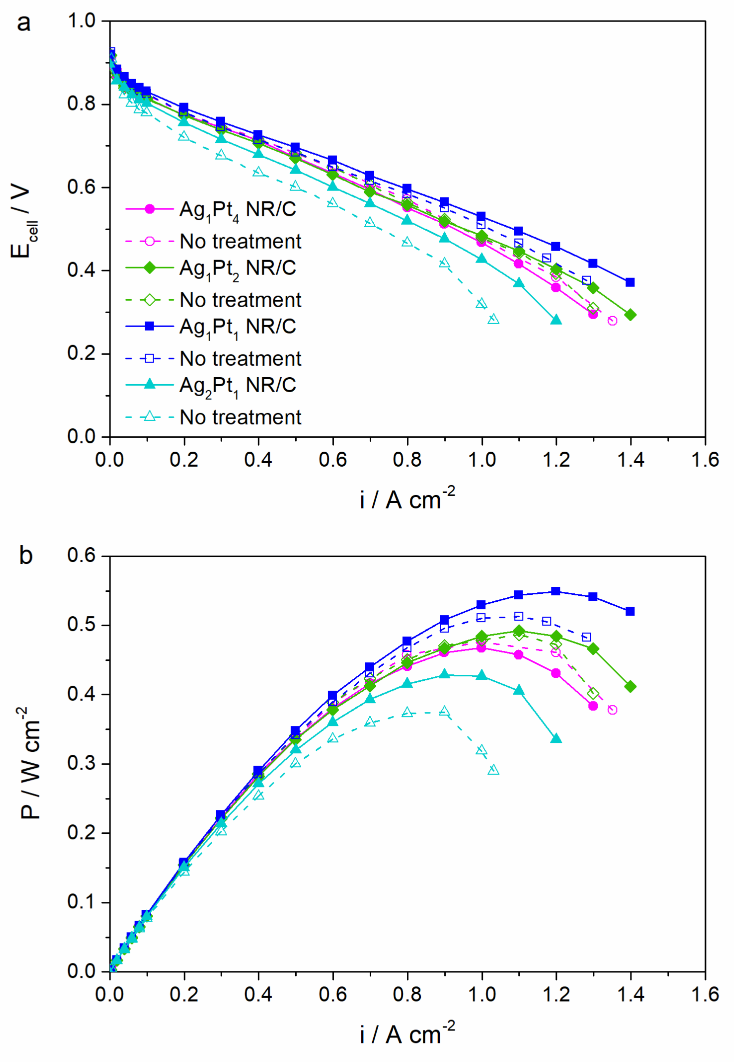

Figure 4.17 MEA testing results of the GDEs made of the AgPt NR/C catalysts in comparison to those of the same catalysts prior heat treatment: **(a)** polarisation and **(b)** power density curves.

A comparative analysis of the EIS spectra for the Ag_1Pt_2 NR/C and Ag_1Pt_1 NR/C GDEs are shown in Figure 4.18. The EIS at a low current density (30 mA cm^{-2}) shows a similar reduction of the semi-circle diameter for both GDEs after the heat treatment. At the lower potentials of 0.65 and 0.5 V (Figure 4.18b-c) the decreased charge transfer resistance because of the heating process is more significant for the catalyst with the higher Ag loading (Ag_1Pt_1 NR/C), asserting the better improvement of the ORR kinetic. Similarly, the decrease of the mass transfer resistance is more prominent for the Ag_1Pt_1 NR/C GDE, which further confirms the notable performance increase in Figure 4.18 after the heat treatment.

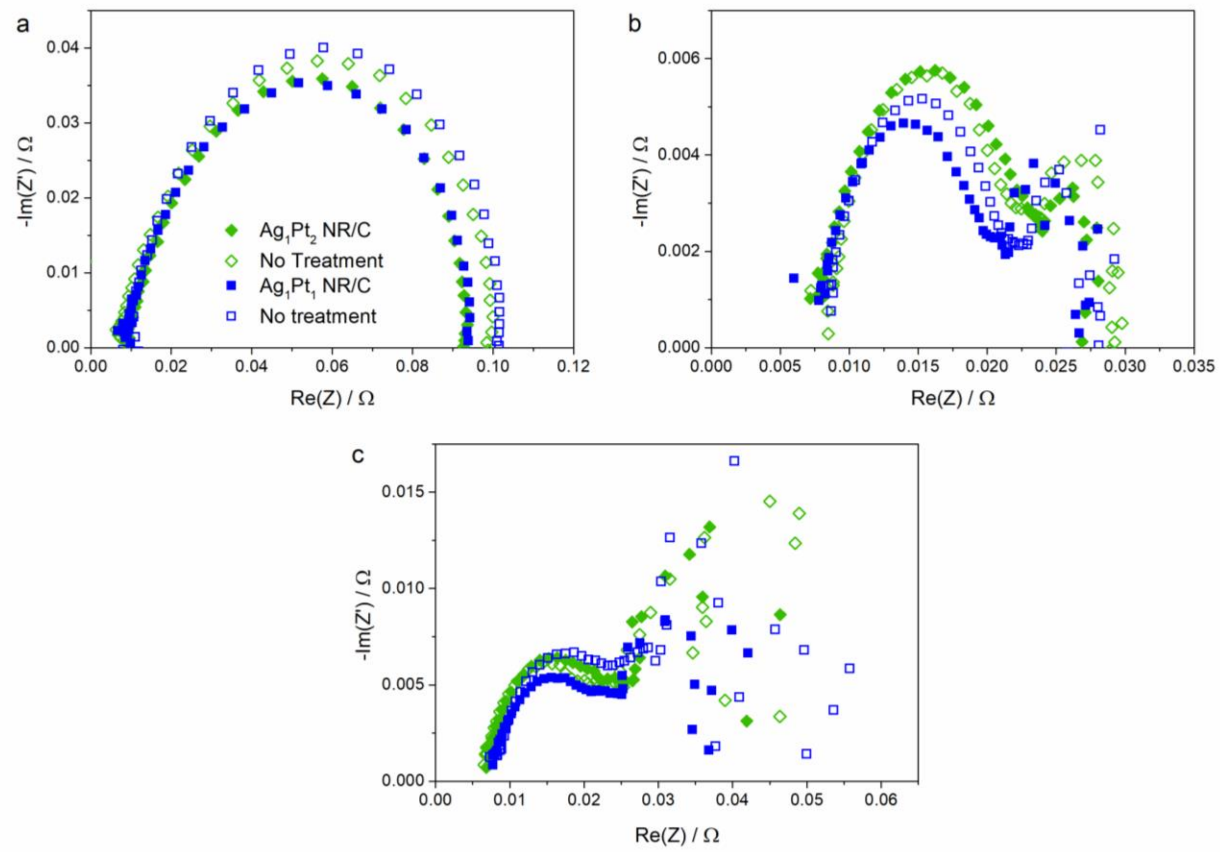

Figure 4.18 EIS plots of the Ag_1Pt_2 NR/C and Ag_1Pt_1 NR/C GDEs recorded at **(a)** 30 mA cm^{-2} **(b)** 0.65 V and **(c)** 0.5 V.

The effects of the heat treatment on the catalyst stability are presented in Figure 4.19. The CVs show a very close ECSA for Ag_1Pt_1 NR/C before and after the heat treatment, as well as a similar ECSA drop after the ADT. These indicate a small influence of the heat treatment effect in preventing the surface area loss. However, the heat-treated catalyst is able to slightly reduce the power performance loss (by ca. 3.4% after 5000 cycles of durability testing) (Figure 4.19b). The stability of Pt alloy catalysts has been long reviewed as the major issue in PEMFCs, which mainly related to the segregation and dissolution of the alloyed metals [204]. The heat treatment can partially improve the Ag and Pt alloy contributing to prohibiting the segregation.

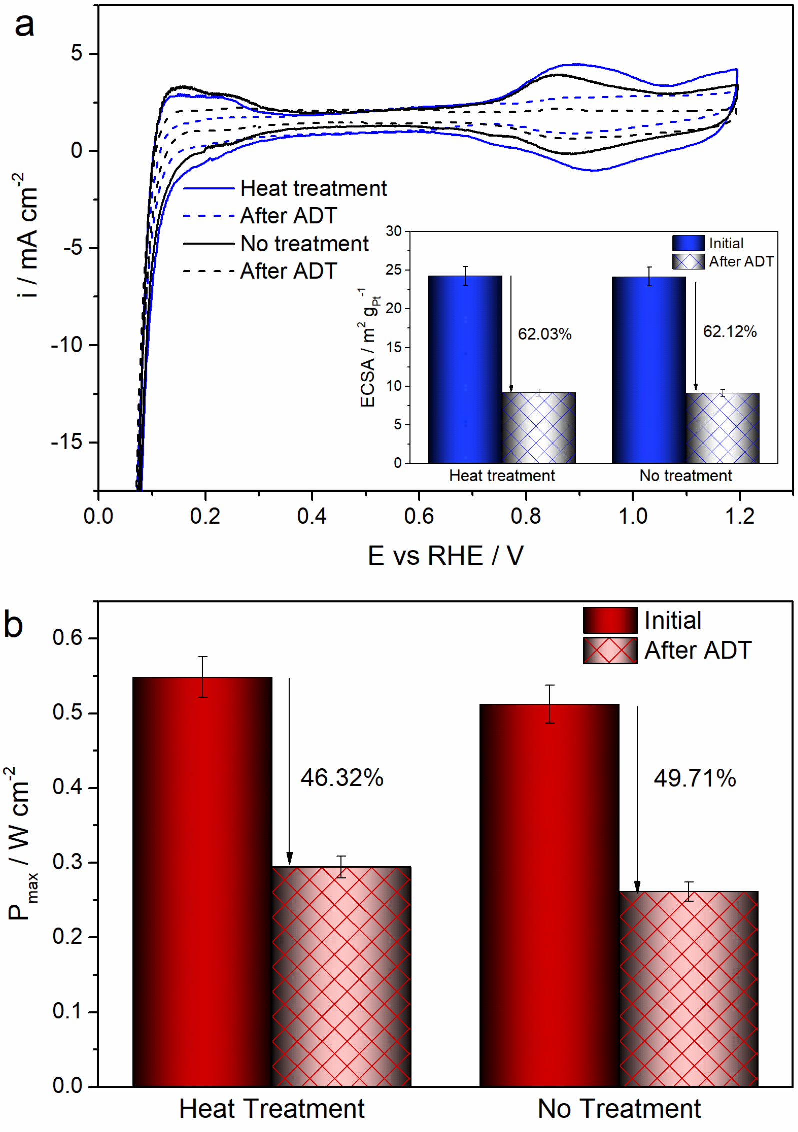

Figure 4.19 (a) CVs of Ag_1Pt_1 NR/C (with and without the heat treatment) including the corresponding ECSA loss (inset) and **(b)** the peak power density decline after the ADT.

4.6 Conclusions

The formic acid reduction method for growing AgPt alloy NRs on carbon support was demonstrated in this chapter. The physical characterisation results showed that the time interval (i.e. 5 hours) of mixing both metal precursors was a crucial step to achieve uniform 1D nanostructures. In the formic acid reduction process, Pt works not only as a size control role in the Ag reduction, but also providing a shape inducing effect leading the growth of AgPt alloy to form single-crystal NRs along the <111> direction. The atomic ratio of Ag to Pt (from 1:4 to 2:1) plays a significant role in determining the morphology and distribution of the AgPt NRs on the carbon support, which also shows a large impact on their catalytic activities.

The MEA test in PEMFCs shows an enhanced power density of 0.549 W cm^{-2} for the Ag_1Pt_1 NR/C GDE, which is 1.14- and 1.16-fold higher than that of the GDEs made of Pt/C and Pt NR/C catalysts, respectively. The improved catalytic performance of the AgPt NR alloy catalyst is attributed to the superiority of the 1D metal nanostructure and the high electrical conductivity of Ag, which is boosted after the heat treatment. A larger ECSA measured from Ag_1Pt_1 NR/C is a contributing factor to the catalytic performance induced by the uniformly less aggregated NRs, which provides enhanced access of reactants throughout the catalyst layers. The ADT test shows its slightly poorer stability compared to the 1D Pt NR, but still much better than the 0D Pt NP. The dissolution and redeposition of Ag is observed at the interface of electrolyte and electrode during the ADT test, and a further approach is required to resolve this issue to really improve the electrode durability.

Chapter 5

Carbon Supported Au Integrated 1-D AgPt Nanostructures as Electrocatalysts for Oxygen Reduction Reaction

The work presented in this chapter is unpublished at the time of writing

In this chapter, Au is introduced to form one-dimensional (1D) Au-AgPt nanorod (NR) structures to improve the stability of the AgPt NR/C catalyst, as well as enhancing their catalytic activities. The formic acid reduction method is deployed and further explored to adjust the Au deposition along with the growth of 1D AgPt alloy structures on the carbon support. The metal ion reduction procedure is precisely controlled to optimise the atomic arrangement. The influence mechanisms of Au on the morphology, structure and catalytic performance are investigated based on the physical characterisation and proton exchange membrane fuel cell (PEMFC) test results. Finally, the accelerated degradation test (ADT) is performed to evaluate the stabilisation effect of Au on the 1D AgPt alloy catalyst in the PEMFC operating conditions.

5.1 Introduction

Following the atomic segregation of AgPt NR catalysts inducing power and surface area loss during the ADT, the surface modification to prevent Ag depletion and dissolution should be further implemented to maintain stability. The integration of the third metal such as Au [170], Rh [205], Mo [206] and Ga [207] has been demonstrated as a promising approach to improve the stability of the Pt-based hybrid catalysts. Therefore, the introduction of Au cluster into AgPt NR/C catalysts is explored in this chapter, considering the nature of metal stability and a closer lattice match to Pt and Ag. Au has been known as an effective doping metal to improve the stability of alloy catalysts [69,169–171]. In Chapter 2, the utilisation of the Au cluster was widely reviewed, which generally provides the stabilisation effect through the electronic structure modification of Pt-based catalysts. It weakens the binding of oxygen species on the catalyst surface, thus suppressing the segregation of the alloyed metal such as Pd, Co and Ni [75,76,170]. Hence, the integration of Au with the AgPt NR catalysts can be a promising strategy to minimise the atomic segregation and upgrade its stability for practical application in PEMFCs.

The introduction of Au forming multimetallic hybrid catalysts has been demonstrated as an effective stabilisation approach [69,179]. However, most of the studies focused on the ex-situ half-cell measurement in liquid electrolytes, and the Au stabilisation effect based on the MEA test in PEMFCs is hardly reported. To meet the practical and commercial application purpose, rational design and scalable synthesis manner is the main consideration factor. In this chapter, we further explore the self-growth formic acid reduction method to control the formation and deposition of Au onto the 1D AgPt alloy structure. The alloying of Au as the third metal is a challenge because of its different standard reduction potential (SRP) compared to two other involved metal ions of Pt and Ag. Hence, it is essential to find the mechanisms to adjust the integration of Au into the growth of the 1D AgPt alloy nanostructure.

5.2 Synthesis of Au integrated AgPt NR/C

The synthesis of the Au-AgPt NR/C catalysts via the formic acid reduction method adapts the growth of the AgPt NRs on the carbon described in Chapter 4. The reduction potential of the metal ions was carefully considered in controlling the whole reaction rate to obtain the 1D nanostructures. For the stabilisation content, the placement of Au along the AgPt NR is crucial, which potentially influences catalytic activities of the catalyst. According to Zhang et al., the attachment of Au on the surface interferes with the catalytic activity as it potentially blocks the active site of the catalyst (e.g. the ORR active sites on Pt) [30]. Meanwhile, the Au stabilising effect is not prevented by displacing it beneath the surface atomic layer [75]. Therefore, to achieve highly active and stable electrocatalysts, the deposition of Au is investigated through controlling the interval time of adding Au precursors along with the growth of the 1D AgPt alloy NRs, which is schematically shown in Figure 5.1.

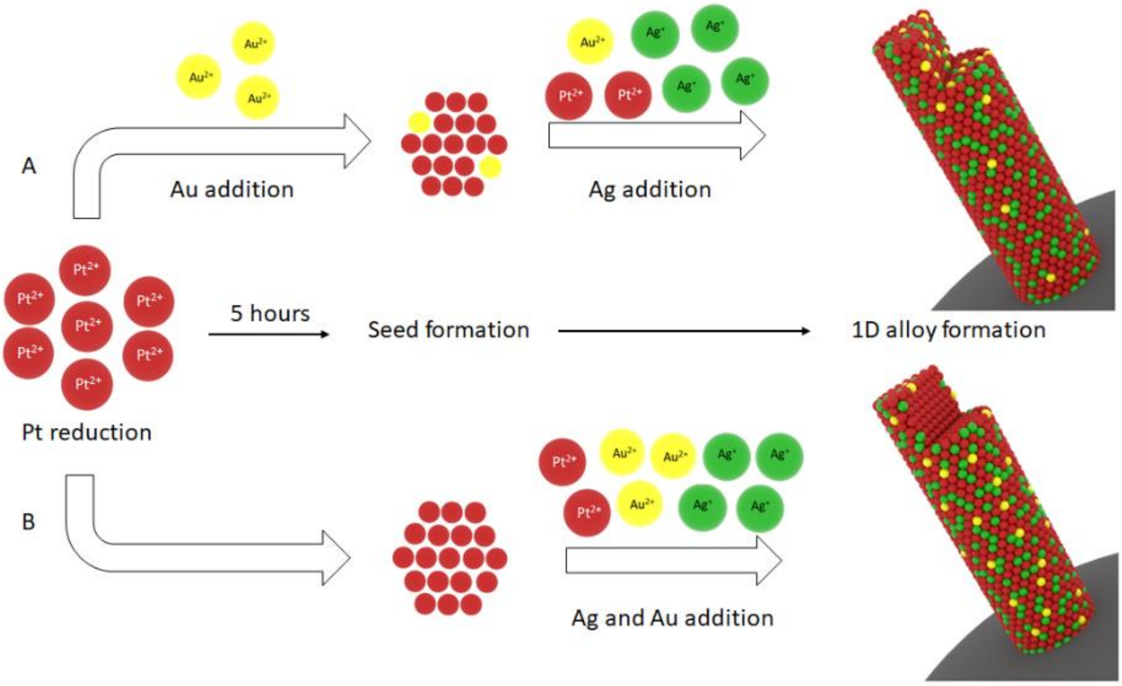

Figure 5.1 The growth scheme of Au integrated AgPt NRs on the carbon via the formic acid reduction method.

The introduction of Au ions at the early reactions stage (Figure 5.1-A) leads to the formation of harmonised ultrafine alloy NRs with an average diameter of 3-4 nm and length of ~20 nm on the carbon support, which is shown by the transmission electron microscope (TEM) and scanning electron microscope – energy-dispersive electron microscopy (STEM-EDX) analysis results in Figure 5.2. A high-resolution-TEM (HR-TEM) image captures a single NR with an interplanar spacing of 0.23 nm (Figure 5.2c), which is close to the lattice space of (111) planes of the bulk Pt-JCPDS: 04-0802 (0.227 nm), Ag-JCPDS: 04-0783 (0.235 nm) and Au-JCPDS: 04-0784 (0.235 nm), indicating the growth along the <111> crystal direction. Uniform lattice orientation shown in the image is expected due to the close lattice constant of Ag, Pt and Au, which also signifies the harmonised alloy structure of these metals. The STEM-EDX mapping results show the distribution of Pt, Ag and Au within the NRs (Figure 5.2d-g). The overlay element map exhibits a homogenous distribution of the three elements without any boundary, representing well alloying behaviour within the NRs. Meanwhile, by delaying the Au addition together with the introduction of the Ag precursors (Figure 5.1-B), more Au and Ag atoms deposit on the outer of the NRs, as shown in Figure 5.3c. This morphology partially blocks the Pt active sites [30]. These results thus confirm the importance of controlling the metal ions reduction process in deriving 1D multimetallic alloy nanostructures using the formic acid reduction method.

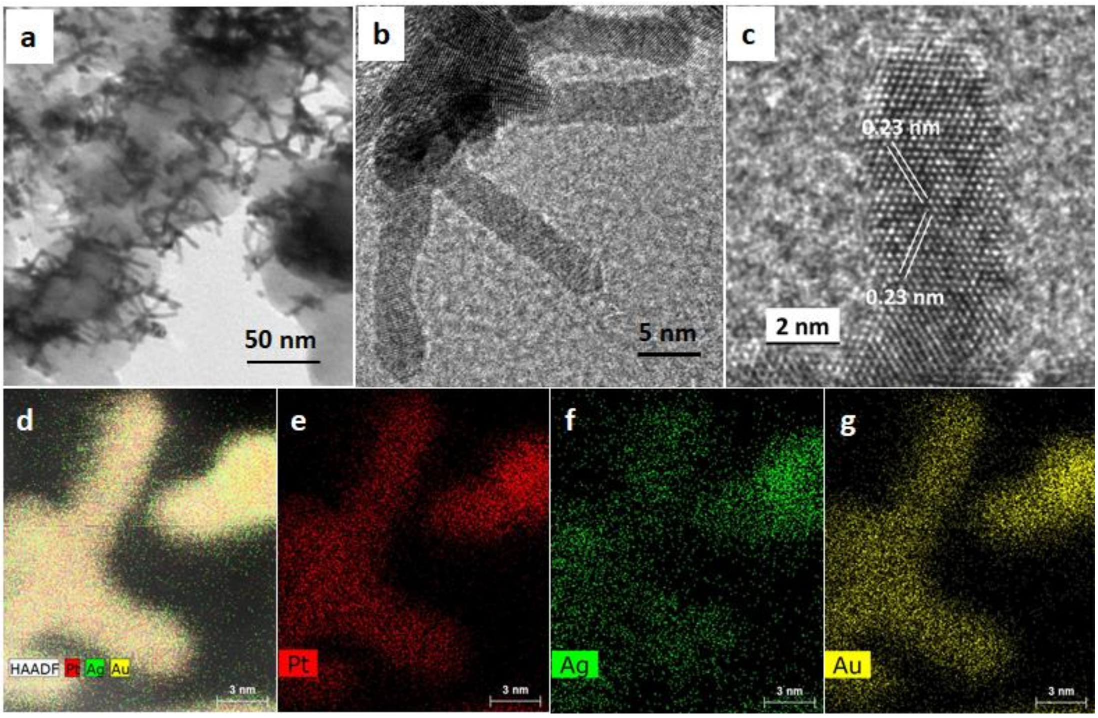

Figure 5.2 TEM images and EDX element maps of the Au-AgPt NR/C A catalyst (synthesised following the reaction scheme A).

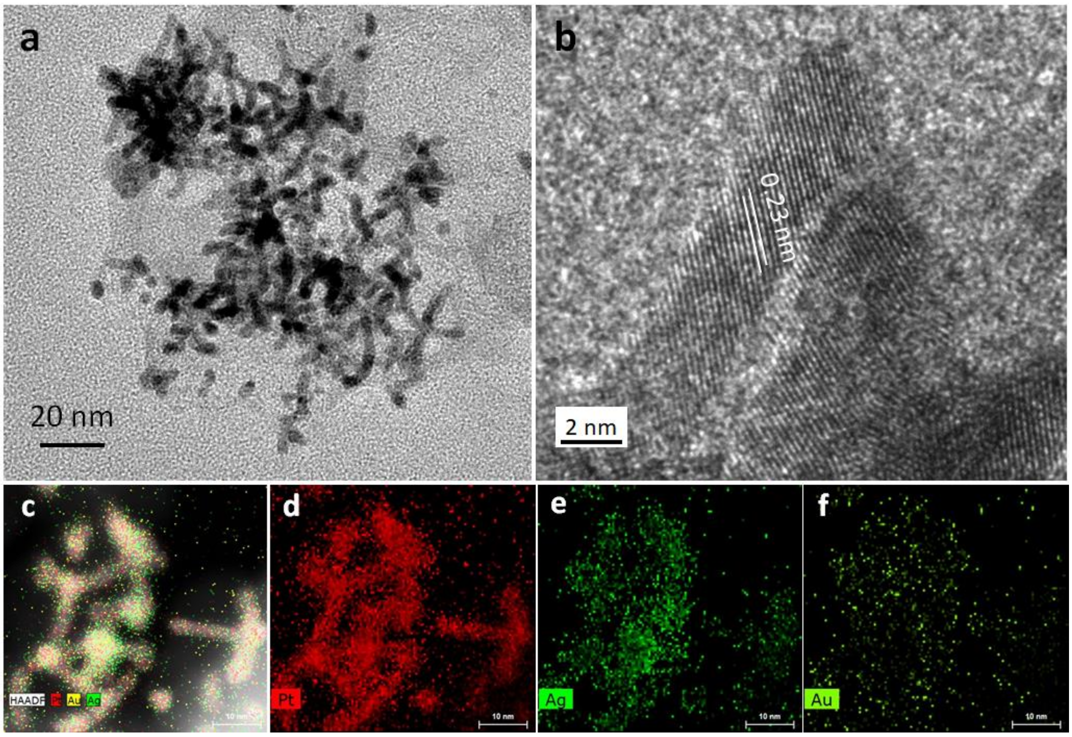

Figure 5.3 TEM images and EDX element maps of the Au-AgPt NR/C B catalyst (synthesised following the reaction scheme B).

With the formic acid reduction process, the growth of 1D Pt nanostructures is based on a slow reaction rate and selectively weaker adsorption of formic acid species products on Pt (111) surface [187–189]. It has been shown in Chapter 4 that the replacement of 50 at% Pt with Ag resulted in the formation of dominated shorter NRs of ca. 15 nm. This outcome is caused by the change of the reaction rate due to the different reduction potential of the Pt and Ag ions. Comparing with the Pt and Ag ions, the higher redox potential of Au ($[AuCl_4^-/Au^0] = 0.93$ V) (cf. Pt and Ag ions) implies a much faster chemical reduction rate under the same environmental condition. Thus, the introduction of the Au precursors with the Pt ions results in dominating Au reduction at the early reaction period (Figure 5.1-A) and thus the slowing down of the Pt reduction step [208]. It induces the sluggish kinetic reaction in the system, leading to longer NRs of ca. 20 nm (Figure 5.2 and 5.3) and more Pt deposition on the NR surface. On the other hand, if Pt ions are left for the reaction for 5 hours at first, (Figure 5.1-B), most of them have been reduced and form Pt seeds [127]. The introduction of Au ions at this point induces a slower Ag reduction and prevents the embedding of Ag in the inner side of NRs. Consequently, most Au and Ag are attached at the outer atomic layers of NRs, as shown in Figure 5.3. Although the ratio of Au is much smaller than that of Pt and Ag, the reaction kinetic is slow enough in the reduction reaction using a weak reducing agent, such as formic acid here. Therefore, a small amount of Au (i.e. ca. 5 at%) plays a significant role in changing the chemical reaction rate for the formation of longer NRs.

Peaks with the X-ray diffraction (XRD) patterns of the AgPt NR/C and 5 at% Au integrated AgPt NR/C catalysts are indexed to (111), (200), (220) and (311) planes (Figure 5.4a). These are the typical face-centred cubic (FCC) structure of Pt, Ag and Au based on the references of Pt (JCPDS: 04-0802), Ag (JCPDS: 04-0783) and Au (JCPDS: 04-0784), respectively. The increased peak intensity and reduced width after the introduction of Au (cf. AgPt NR/C) can be ascribed to the improved crystallinity resulting from the longer NRs, which is in agreement with the TEM analysis results. The introduction of Au also leads to a reduced Ag metal phase peak intensity observed at 38.35° for the (111) plane, indicating an improved alloying degree. Such peaks barely observed from Au-AgPt NR/C B tuned by reducing together of more Au with Ag and remained Pt ions during the second reduction step (Figure 5.1-B).

Comparing surface composition (Table 5.1) measured from the X-ray photoelectron spectroscopy (XPS) survey scan in Figure 5.4b confirms the higher ratio of Pt deposition rendered by the introduction of Au. A very small amount of Au (0.26 %) was detected on the surface of Au-AgPt NR/C A, whereas a high Au composition of 4.34 at% is obtained from Au-AgPt NR/C B. Hence, strong Au $4f_{7/2}$ and $4f_{5/2}$ peaks are observed at 83.46 and 87.12 eV, respectively, close to the high-resolution Pt 4f region (Figure 5.4c). This further confirms the higher Au content on the surface of the NRs synthesised according to scheme B, which agrees well with the TEM analysis results (Figure 5.2 and 5.3). The fitting of the two Pt 4f peaks shows the domination of Pt^0 with the characteristic Pt $4f_{7/2}$ and Pt $4f_{5/2}$ peaks, which are recorded at 70.60 and 73.88 eV for Au-AgPt NR/C A and 70.42 and 73.72 eV for Au-AgPt

NR/C B, respectively (Figure 5.4c). Similarly, the two Ag 3d peaks are completely fitted with the metallic state of Ag^0, and a positive shift is recorded for Au-AgPt NR/C A with Ag $3d_{5/2}$ at 367.58 eV compared to 367.34 eV for Au-AgPt NR/C B (Figure 5.4d). Generally, the binding energy of the main elements with both Au-AgPt NR/C catalysts shifts negatively compared to the monometallic Pt, Ag and Au. However, the shifting degree is varied depending on the Au deposition, which is related to the charge transfer phenomena because of the interaction of the multimetallic structure [203]. The electronic interaction such as electron transfer from the metal atoms results in the change of the binding energy, which further confirms the modified electronic properties of the AgPt alloy catalyst because of the integration with Au [165].

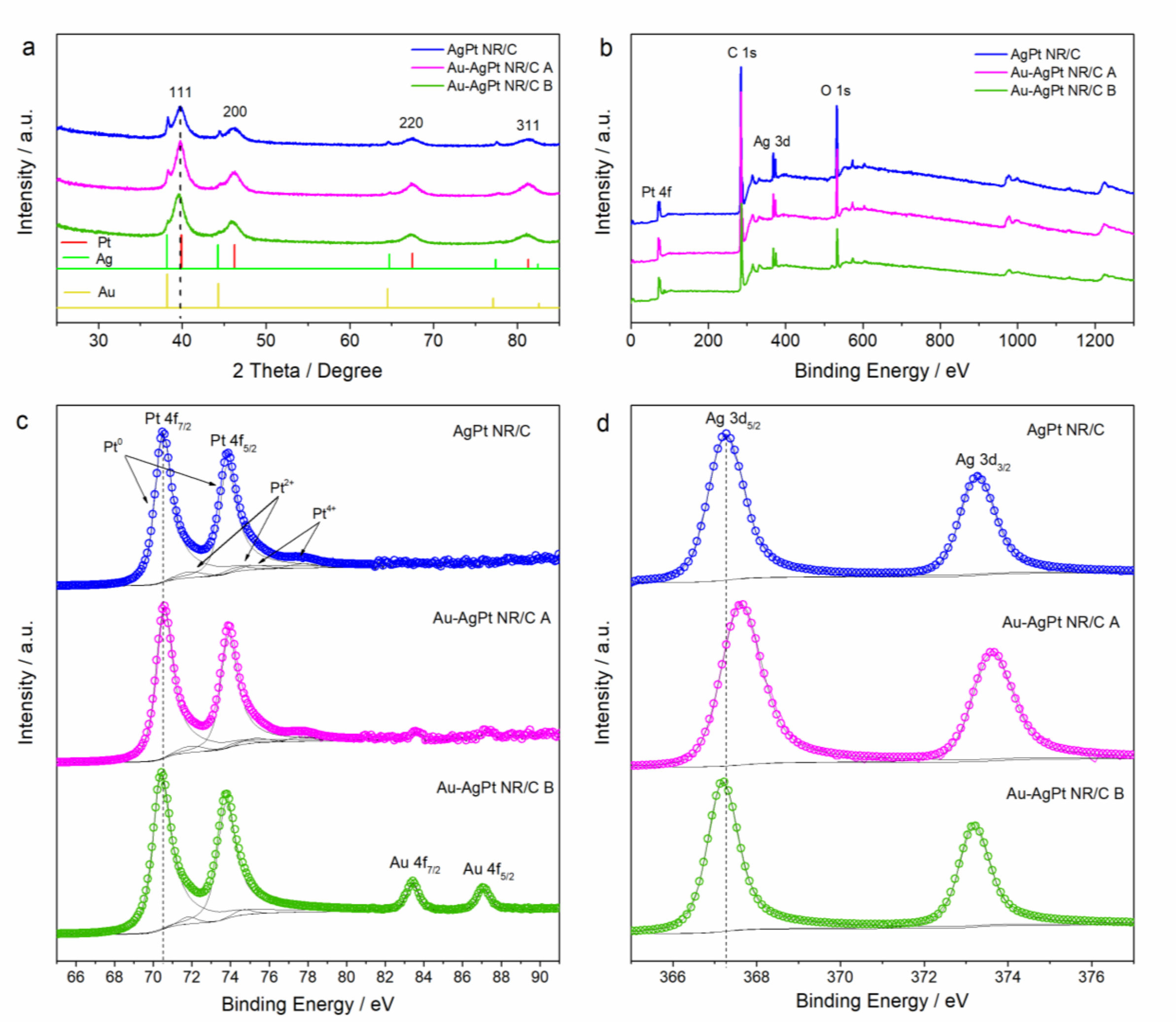

Figure 5.4 (a) XRD pattern and **(b)** XPS survey of AgPt NR/C and Au-AgPt NR/C. The corresponding high-resolution XPS spectra of the **(c)** Pt 4f and **(d)** Ag 3d region.

Table 5.1. Catalysts surface composition measured by XPS

Catalysts	Au / at%	Ag / at%	Pt / at%
AgPt NR	0	49.75	50.25
Au-AgPt NR 5% A	0.26	41.68	58.06
Au-AgPt NR 5% B	4.34	43.17	52.49

5.3 Influence of the Au content

The effect of the Au content on the morphology and structure of Au-AgPt NR/C A is evaluated following the reaction scheme A. The Pt ratio and total metal loading were fixed, while Ag is reduced with the increasing Au. Figure 5.5 shows that longer NRs are formed from the catalyst with a higher Au content. However, increasing the Au loading of up to 12 at% renders serious agglomeration, and the TEM images (Figure 5.5e-f) show a similar NR length as of Au-AgPt NR/C with a lower Au content of 5 at%. This finding suggests that the presence of a high amount of Au induces higher surface energy of Pt nuclei, thus leading to the aggregation because of the trend for minimising the interfacial energy [125]. Else, a slower reduction step tends to induce heavy agglomeration of 1D nanostructures as reported in the previous study [142]. Quantitatively, the metal contents of the catalysts were determined by inductively coupled plasma-mass spectroscopy (ICP-MS) along with thermogravimetric analysis (TGA). The results are presented in Table 5.2, which are in a close agreement with the theoretical values.

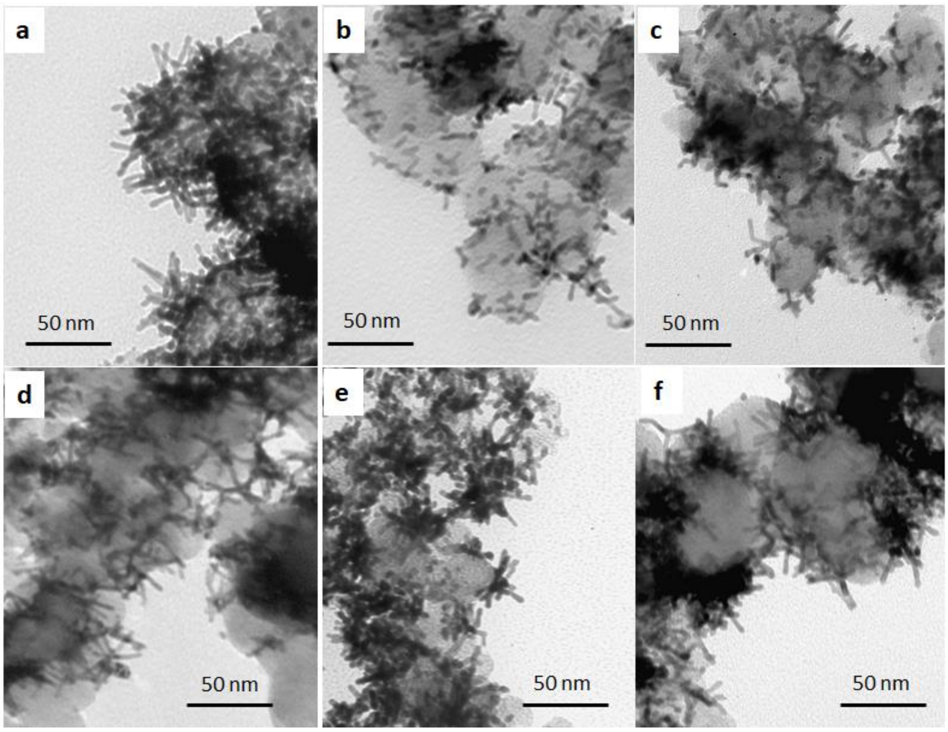

Figure 5.5 TEM images of **(a)** Pt NR/C, **(b)** AgPt NR/C, **(c)** Au-AgPt NR/C 2%, **(d)** Au-AgPt NR/C 5%, **(e)** Au-AgPt NR/C 8% and **(f)** Au-AgPt NR/C 12% synthesised following the reaction scheme A.

Table 5.2. Metal contents of the Au-AgPt NR/C catalysts measured by TGA & ICP-MS

Catalysts	TGA-Residue / wt%	ICP-MS / wt%			ICP-MS / at%		
		Au	Ag	Pt	Au	Ag	Pt
AgPt NR/C	60.98	0	32.23	67.77	0	46.23	53.77
Au-AgPt NR/C 2%	61.27	2.30	30.07	62.53	1.92	45.63	52.45
Au-AgPt NR/C 5%	60.52	6.77	28.56	64.67	5.45	41.97	52.58
Au-AgPt NR/C 8%	62.08	9.92	25.46	62.08	8.16	38.22	53.62
Au-AgPt NR/C 12%	60.66	13.84	24.00	63.06	11.56	35.25	53.19

XRD patterns of the Pt NR/C (as the reference), AgPt NR/C and various Au integrated AgPt NR/C catalysts are shown in Figure 5.6. The (111) peak of the 1D alloy catalysts shows a negative shift of ~0.1 degrees at 2-theta compared to the Pt NR/C catalyst, implying an expanded lattice spacing resulted from the alloying with Ag / Au. These peaks are in a close alignment regardless of the different Au contents, indicating an identical interplanar space.

Increasing the Au loading leads to a weaker Ag metal phase (111) peak at 38.35°, indicating an improved alloying degree. These findings confirm that the alloying degree of Au-AgPt NR/C can be adjusted by both controlling the interval time of introducing Au ions and changing the atomic ratio of Au in the reduction process.

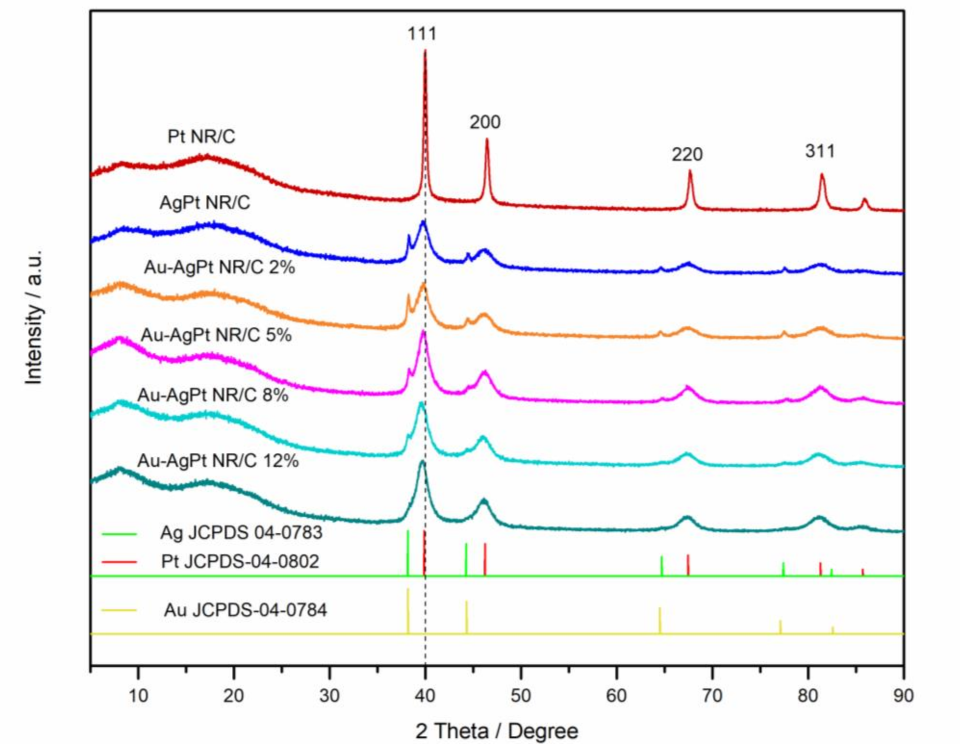

Figure 5.6 XRD patterns of the Pt NR/C, AgPt NR/C and various at% Au integrated AgPt NR/C catalysts synthesised following the reaction scheme A.

The XPS analysis in Pt 4f region (Figure 5.7) shows that the Au signal is hardly distinguished with a very low Au content of 2 at%. The two Au 4f peaks are detected from the background of the high-resolution Pt 4f region with Au content of 5 at% and above. Stronger Au 4f signals are recorded for the catalyst with Au content of 12 at%, suggesting a higher Au loading derives a higher Au deposition on the catalyst surface. The Pt $4f_{7/2}$ peaks of the 1D alloy catalysts shift negatively compared to the Pt NR catalyst (Figure 5.7), indicating the changed Pt electronic properties because of the alloying [193]. The small amount of Au below 8 at% renders a small positive shift of up to 0.14 eV. For instance, the Pt $4f_{7/2}$ peak of 5% Au doped AgPt NR/C locates at 70.60 eV, which is more positive than AgPt NR/C at 70.50 eV. The catalyst with 12 at% Au shows a more negative shift of the Pt $4f_{7/2}$ peak, suggesting the dependency of the Au loading toward the electronic properties of the Au-AgPt NR/C catalysts.

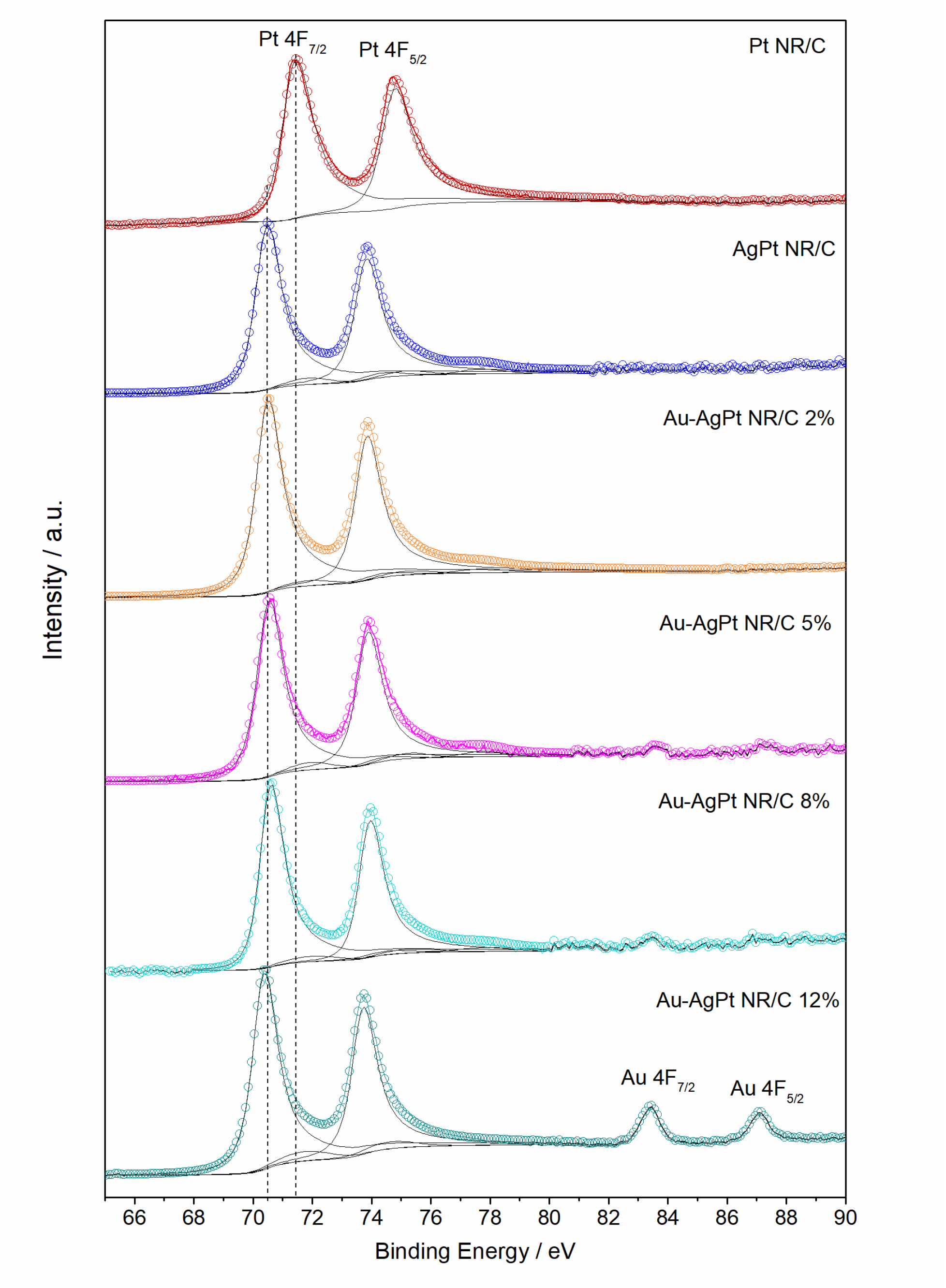

Figure 5.7 High-resolution XPS spectra of the Pt 4f region for the Pt NR/C, AgPt NR/C and various at% Au integrated AgPt NR/C catalysts synthesised following the reaction scheme A.

Similarly, the Ag $3d_{5/2}$ peaks of the Au integrated AgPt catalysts gradually shift in a positive direction with the increasing Au content of up to 8 at% (Figure 5.8). It indicates that the Ag chemical property is also comprehensively influenced by the Au attachment. The Ag $3d_{5/2}$ peaks of the Au-AgPt NR/C catalysts with the Au loading of 5 and 8 at% are in close alignment and show the largest shift of ca. 0.3 eV from AgPt NR/C. The fitting of Pt 4f peaks exhibits the domination of Pt^0 of above 92% for all catalysts (Table 5.3) confirming the domination of the Pt metallic state. Similarly, Ag 3d peaks region is completely fitted with Ag^0, implying 100% reduction of Ag ions into the metallic state.

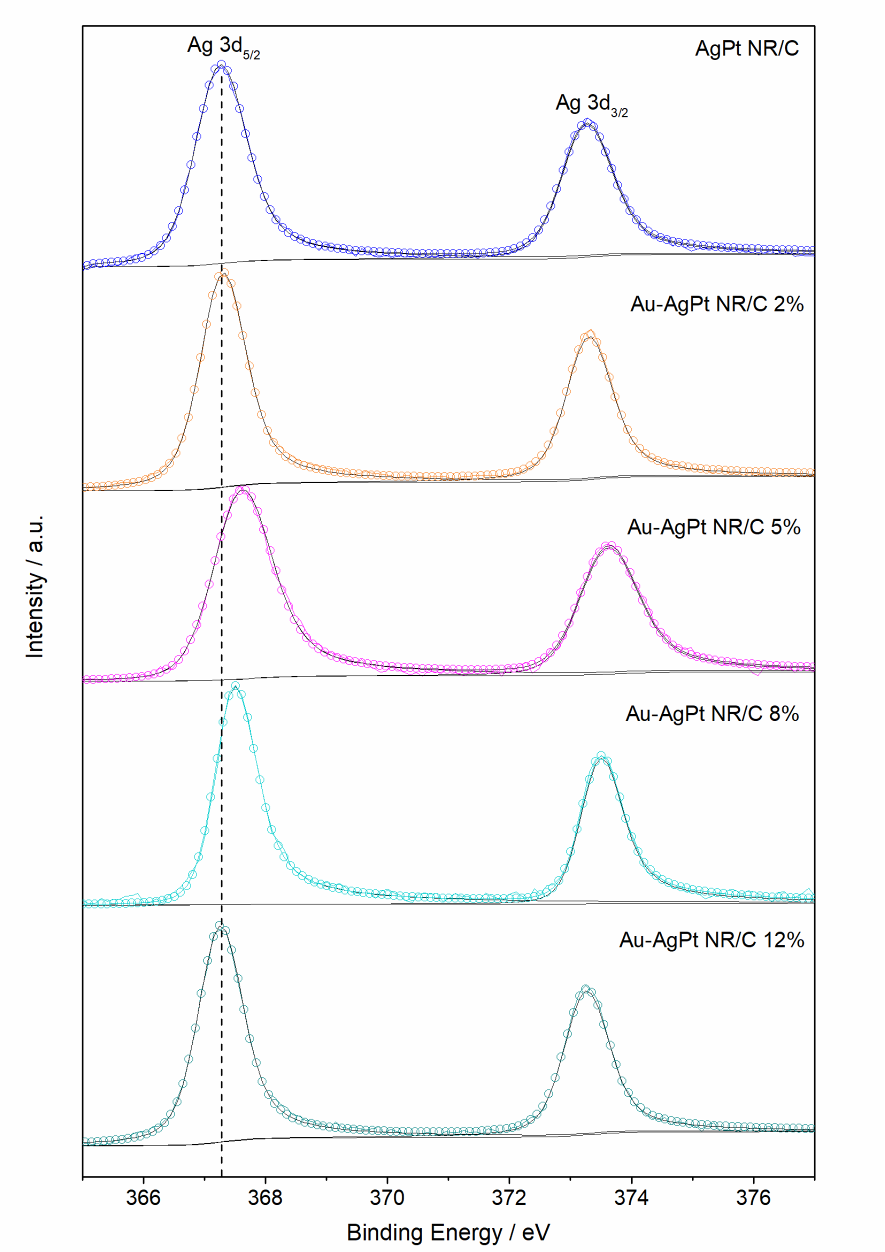

Figure 5.8 High-resolution XPS spectra of the Ag 3d region generated from the AgPt NR/C and various at% Au integrated AgPt NR/C catalysts synthesised following the reaction scheme A.

Table 5.3. Composition of Pt and Ag states obtained from the Pt 4f and Ag 3d XPS region

Catalysts	Pt / %			Ag / %	
	Pt^0	Pt^{2+}	Pt^{4+}	Ag^0	Ag^+
Pt NR/C	100	0	0	0	0
AgPt NR/C	93.28	3.66	3.05	100	0
Au-AgPt NR/C 2%	94.56	2.94	2.50	100	0
Au-AgPt NR/C 5%	93.01	4.02	2.97	100	0
Au-AgPt NR/C 8%	92.86	3.92	3.23	100	0
Au-AgPt NR/C 12%	93.88	6.12	0	100	0

5.4 MEA testing

The membrane electrode assemblies (MEAs) fabricated from Au-AgPt NR/C A and B as the cathode catalyst are evaluated in single fuel cells to understand the effects of the atomic structure and arrangement of the 1D Pt hybrid catalysts on the practical catalytic performance. The commercial Pt/C catalyst is employed as the benchmark together with Pt NR/C and AgPt NR/C (Ag:Pt =1:1). Furthermore, the influence of the Au content towards the catalytic performance and durability of the electrodes is also examined.

5.4.1 MEA testing of Au integrated AgPt NR/C

The MEA test is conducted to evaluate the performance of the as-prepared catalysts toward ORR in the cathode in PEMFCs. Figure 5.9a shows the polarisation and power density curves of the MEAs tested in H_2/Air with the cathode catalyst made of the Pt/C, AgPt NR/C and 5 at% Au integrated AgPt NR/C gas diffusion electrodes (GDEs) with a Pt loading of 0.2 mg_{Pt} cm^{-2}. The performance follows an order of Au-AgPt NR/C B < Pt/C < AgPt NR/C < Au-AgPt

NR/C A with a peak power density of 0.41, 0.48, 0.52 and 0.58 W cm^{-2}, respectively. The enhanced power performance for Au-AgPt NR/C A indicates a positive effect of the Au integration for the AgPt alloy NR catalyst towards ORR, which also depends on the arrangement of Pt, Ag and Au atoms within the NR. For instance, Au-AgPt NR/C B containing the same composition as Au-AgPt NR/C A exhibits the lowest power density because of the higher percentage of Au and Ag on the NR surface.

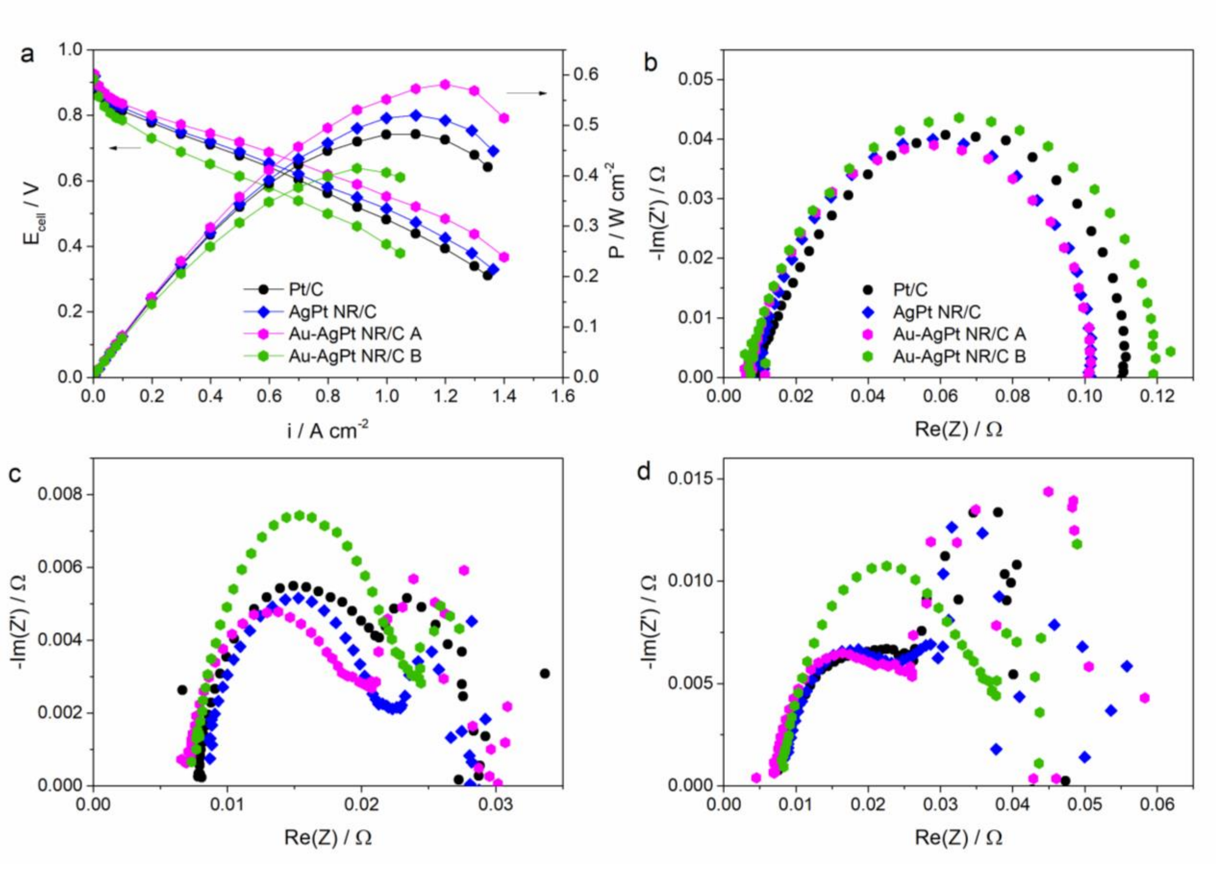

Figure 5.9 Power performance comparison of the MEAs with the cathode GDE made of the Pt/C, AgPt NR/C and 5 at% Au integrated AgPt NR/C catalysts: **(a)** polarisation and power density curves. The corresponding EIS spectra at **(b)** 30 mA cm^{-2}, **(c)** 0.65 V and **(d)** 0.5 V.

The electrochemical impedance spectroscopy (EIS) analysis results at a low current density of 30 mA cm^{-2} are present in Figure 5.9b. The MEA made of the AgPt NR/C, and Au-AgPt NR/C A GDEs show a very similar diameter of the semi-circles, confirming a similar charge transfer resistance, which is smaller than that of the Pt/C GDE. The largest impedance recorded for the

Au-AgPt NR/C B GDE indicates its poor kinetic activity. At a medium current density/potential of 0.65 V (Figure 5.9c), the charge transfer loss is more significant following the trend of polarisation curves in Figure 5.9a. This output confirms that the enhanced ORR performance in operating fuel cells is mainly derived from the superior intrinsic properties of the catalyst induced by the single-crystal 1D structure and alloy composition. The EIS at a low potential of 0.5 V (Figure 5.9d) dominated by mass transfer resistance is inconclusive due to high fluctuation in the low-frequency range. The improved power performance at the large current density region for the MEA made of the Au-AgPt NR/C A GDE is potentially related to the longer and less aggregated NRs, providing a higher porosity to facilitate mass transport in the fuel cell operation [35].

The CV of the GDEs are shown in Figure 5.10, and the calculated ECSA values are listed in Table 5.4. The smaller ECSA of the NR GDEs is ascribed to the anisotropic morphology of the 1D nanostructures, which is in agreement with our previous study [142]. The enlarged ECSA of Au-AgPt NR/C A is attributed to the higher Pt distribution on the NR surface (by 8%) compared to AgPt NR/C (Table 5.1). Meanwhile, a lower ECSA of Au-AgPt NR/C B is related to the higher distribution of Au on the NR surface blocking the active sites, which was also reported in the other studies [30]. These results demonstrate that a large ECSA is responsible for the NR catalyst minimising potential losses and achieve enhanced power performance.

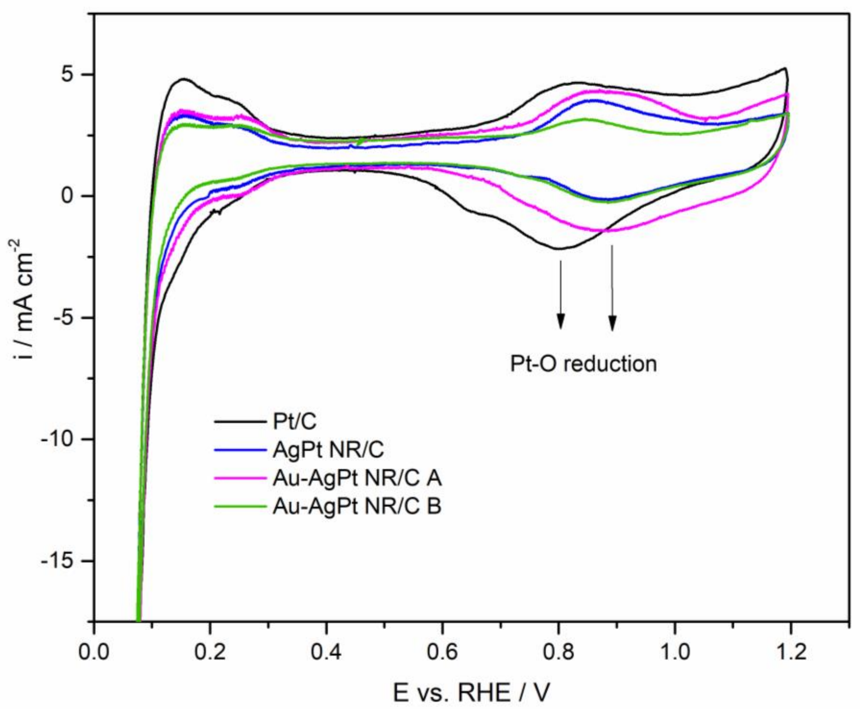

Figure 5.10 CVs of GDE made of the Pt/C, AgPt NR/C and 5 at% Au integrated AgPt NR/C catalysts.

Table 5.4. Catalytic activities of the catalysts determined in the MEA test.

Catalysts	ECSA / m^2 g_{Pt}^{-1}	I_m / A mg_{Pt}^{-1}	I_s / µA cm^{-2}
Pt/C	50.67	0.065	130.29
AgPt NR/C	24.17	0.095	378.57
Au-AgPt NR/C A	25.98	0.110	425.22
Au-AgPt NR/C B	21.73	0.050	204.76

Figure 5.11 shows the polarisation curves obtained under H_2/O_2, and they were corrected with the H_2-crossover and ohmic resistance losses based on the method described by Gasteiger et al. [184]. The measured current densities and mass activities at 0.9 V are summarised in Table 5.4. The highest mass activity is 0.110 A mg_{Pt}^{-1} at 0.9 V for Au-AgPt NR/C A, which is 1.15 and 1.70-fold higher than that of AgPt NR/C and Pt/C, respectively. The enhanced catalytic

activity of Au-AgPt NR/C A is firstly related to the increased ECSA after the integration of Au, providing a larger area for ORR activities. Secondly, the presence of Au renders the tensile strain of Pt and Ag lattice, resulting in a modified electronic structure as shown by the XPS analysis results (Figure 5.4c-d). It has been a strategy to optimise the binding affinity of O-containing species on Pt at a certain degree to improve the kinetic activity [47,193]. This is reflected with the CV (Figure 5.10), where a positive shift of the Pt oxygen reduction peak is recorded than that of Pt/C (0.805 V vs RHE), linking to a weakening bond between the O-containing species and Au-AgPt NRs for the enhanced ORR performance. More specifically, the Pt-O reduction peaks of AgPt NR/C and Au-AgPt NR/C A are at 0.894 V and 0.901 V vs RHE, respectively, revealing the positive effect of the Au integration towards ORR. Apart from the enhancement provided by the Au deposition, the architecture of 1D morphology is also contributed to the improved catalytic activity. It offers the preferential exposure of less low-coordination surface atoms facilitating faster ORR kinetics [127].

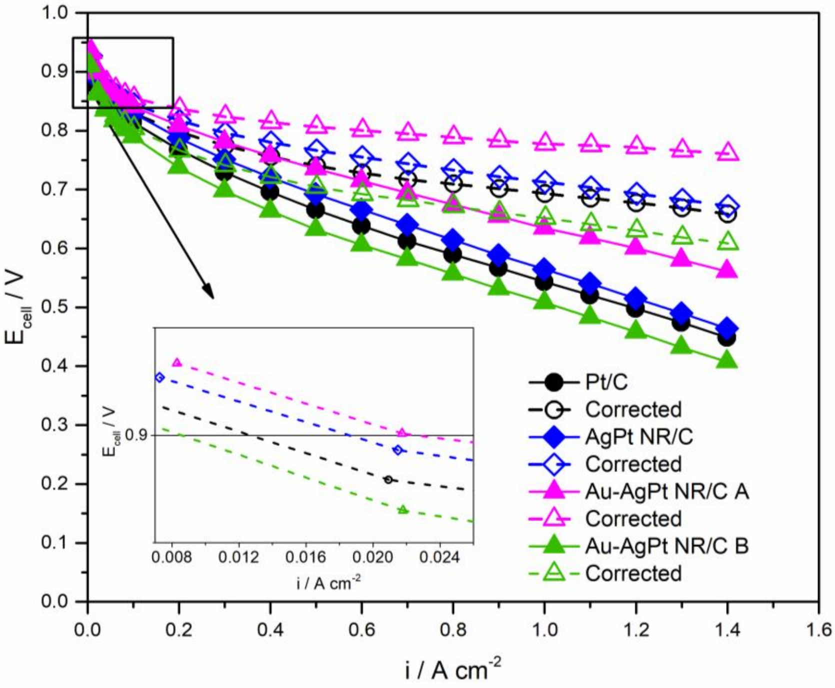

Figure 5.11 Recorded and corrected polarisation curves GDE made of the Pt/C, AgPt NR/C and 5 at% Au integrated AgPt NR/C catalysts obtained under H_2/O_2.

5.4.2 MEA test of varied at% Au integrated AgPt NR/C

To understand the influences of the Au content, the polarisation and power density curves of the GDEs made of the Au-AgPt NR/C A catalyst with various Au contents were recorded and are shown in Figure 5.12a-b. Enhanced power performance is shown with the integration of Au, reaching the highest power output at 5 at% Au. The power densities at the operational voltage of 0.6 V are 0.48 and 0.52 W cm^{-2} for the catalysts containing 2 and 5 at% Au, respectively. Further increasing the Au content results in a decreased power density, and this drops to 0.41 W cm^{-2} at 12 at%, which is even lower than 0.42 W cm^{-2} of the Pt NR/C GDE. Despite the alloying degree is influenced by the contents of Au and Ag, their effect on the catalytic activity is less apparent compared to the arrangement of the metal atoms along with the NR catalyst.

EIS recorded at the low current density of 30 mA cm^{-2} show very similar semi-circles for the Au-AgPt NR/C GDEs with various Au contents and the benchmark GDEs made of Pt NR/C and AgPt NR/C catalysts (Figure 5.12d), signifying their similar charge transfer resistance. At the low potentials of 0.65 and 0.5 V (Figure 5.12e and 5.12f), the transition of the EIS spectra follows the same trend as shown in the polarisation curves. This further signifies the negative effect of applying the high Au content to the 1D Pt alloy catalyst.

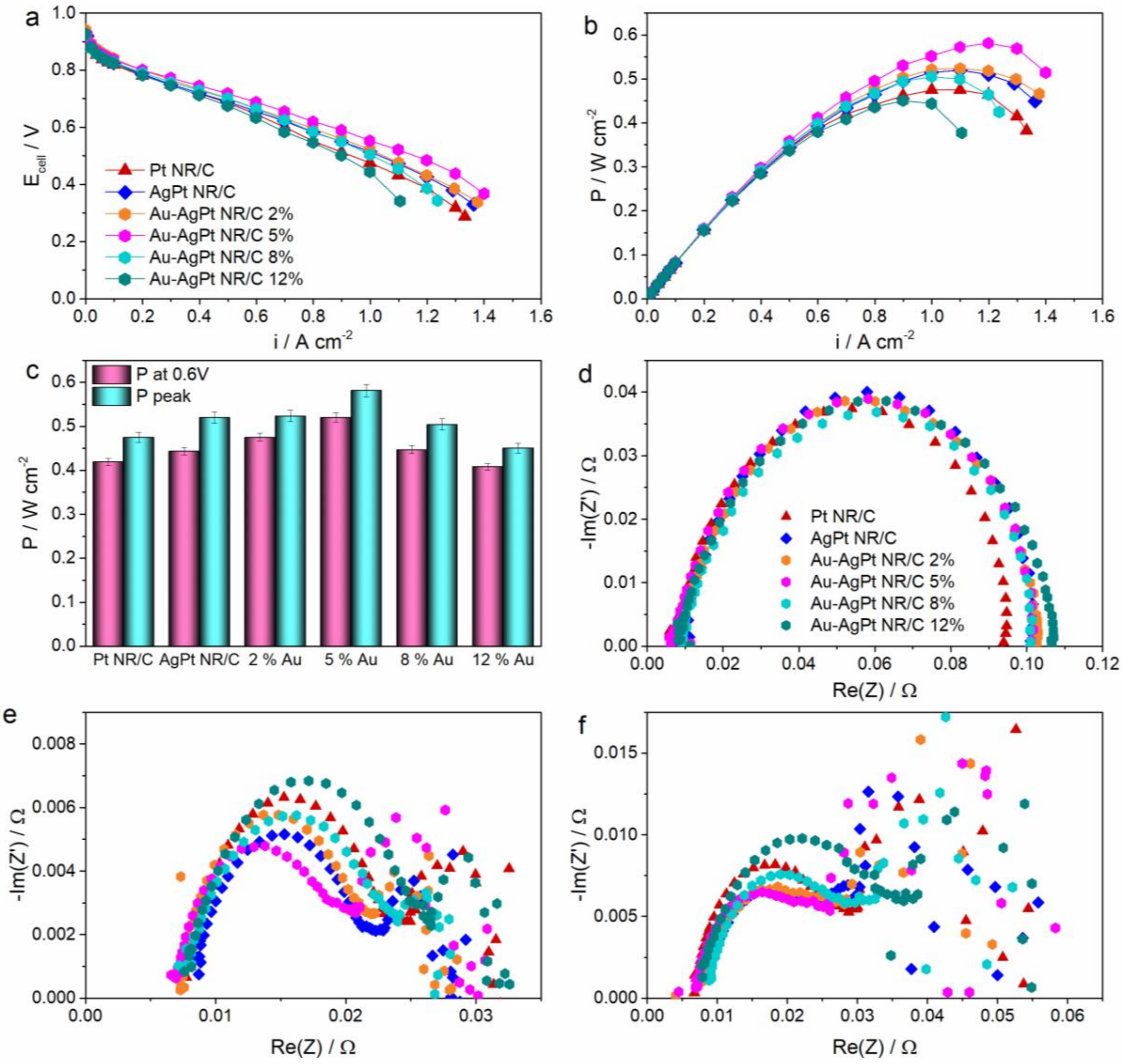

Figure 5.12 Power performance comparison of the MEAs with the cathode GDEs made of Au-AgPt NR/C catalysts with various Au contents synthesised following reaction scheme A, benchmarking to the Pt NR/C and AgPt NR/C GDEs: **(a)** polarisation and **(b)** power density curves, and **(c)** comparison of the power densities at 0.6 V and peak power density. The corresponding EIS spectra at **(d)** 30 mA cm^{-2}, **(e)** 0.65 V and **(f)** 0.5 V.

CVs of the cathode GDEs made of Au-AgPt NR/C catalysts with various Au contents are presented in Figure 5.13a. The measured ECSA normalised to the Pt loading determined from the H_2 desorption peak are compared in Figure 5.13b, and it shows the effectiveness of the 5 at% Au attachment to expand the surface area. A higher Au content of above 5 at% results in decreased ECSA values of 21.37 and 18.34 m^2 g_{Pt}^{-1} for Au-AgPt NR/C 8% and 12%, respectively. Apparently, the lower surface area with the higher Au insertion is caused by the higher deposition of Au on the surface, as shown by the XPS analysis results (Figure 5.7). This outcome is coherent with the obtained results for the Au-AgPt NR/C B catalyst that a high Au deposition on the NR surface renders a negative effect on the catalytic activity as it may block the active sites, finally leading to a lower ECSA. Additionally, the severe agglomeration observed at the high Au content partially blocks gas transport with the catalyst layer, thus leading to a lower catalyst utilisation ratio and poor ORR performance. These results further suggest the limitation of applying a high quantity of Au to continually improve the catalytic performance for the 1D Au-AgPt alloy catalysts.

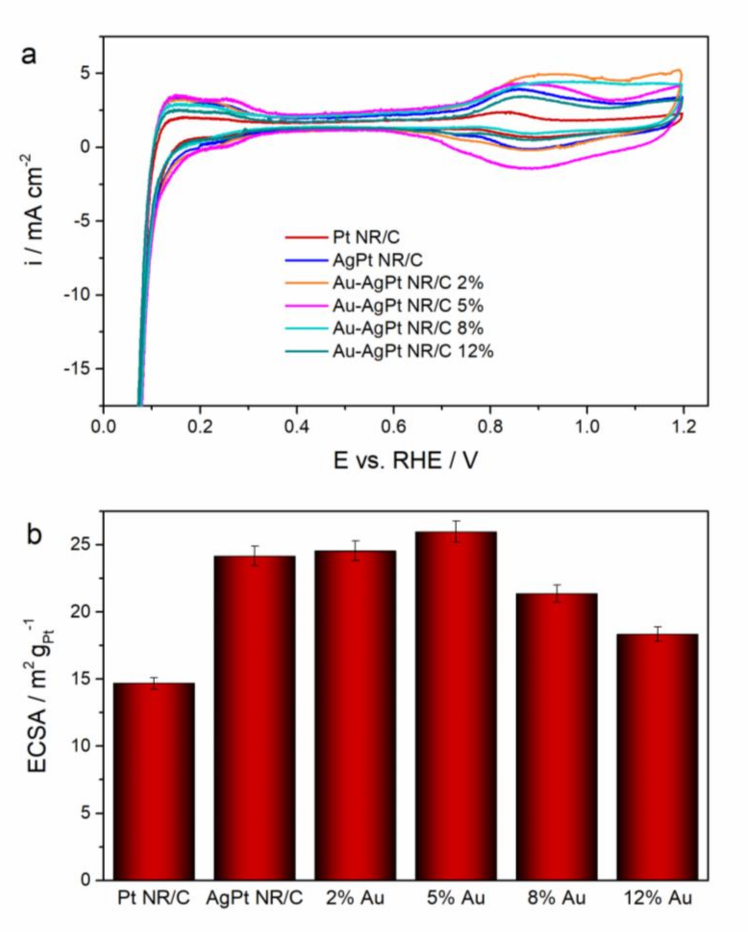

Figure 5.13 (a) CVs of the Pt NR/C, AgPt NR/C and Au-AgPt NR/C GDEs with various Au contents synthesised following the reaction scheme A, and **(b)** the corresponding ECSA normalised to the total Pt loading.

5.4.3 Accelerated degradation test (ADT)

The main enhancement of the Au-AgPt NR/C GDE is more significant on its stability in fuel cell operation. This was evaluated using the ADT in MEAs by potential sweeping between 0.6-1.2 V at a scan rate of 100 mV s^{-1} for 5000 cycles. Comparison between the polarisation curves before and after the ADT is shown in Figure 5.14. The recorded peak power densities after the ADT are 0.28, 0.26 and 0.35 W cm^{-2} for the MEAs with the cathode catalyst made of Pt/C, AgPt NR/C and 5 at% Au-AgPt NR/C A, respectively, indicating the positive effect of the Au deposition toward the electrode durability. The degradation decreases with the increase of the Au content, and the power density decline compared to the initial value is only 39.17% at 8 at% Au after the ADT, which is much lower than that of Pt NR/C (41.41%).

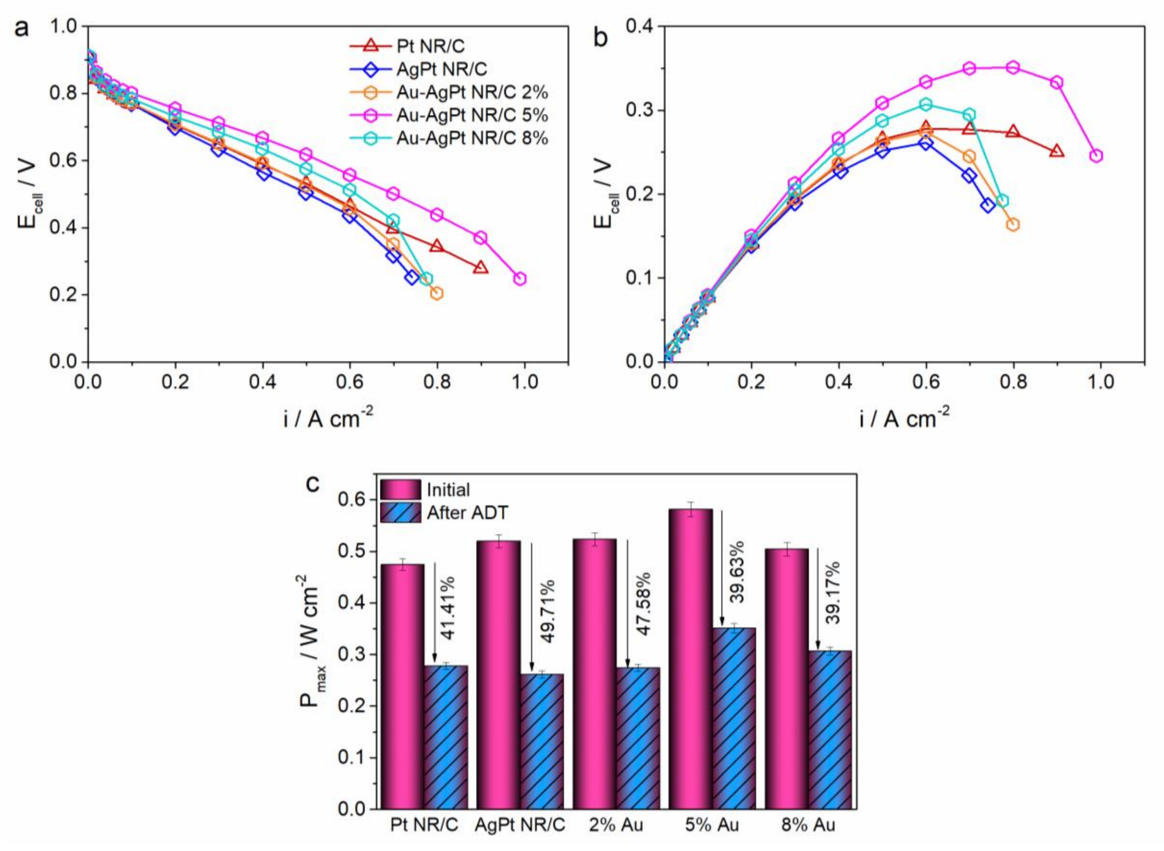

Figure 5.14 (a) Polarisation and **(b)** power density curves recorded after the ADT and **(c)** the corresponding peak power density declines for the MEAs with the cathode GDEs made of the Pt NR/C, AgPt NR/C and Au-AgPt NR/C catalysts with various Au contents synthesised following reaction scheme A.

To further understand the degradation of the as-prepared catalysts, comparison of the CV plots recorded before and after the ADT and the ECSA decline is shown in Figure 5.15. The GDE made of the NR alloy catalysts show a smaller ECSA decline than that of the Pt/C GDE, intensifying the higher stability of the 1D nanostructures. The ECSA loss is improved to 51.20% at 5 at% Au from 62.12% of AgPt NR/C, and this is further minimised to 47.59% at 8 at% Au. This finding explains the role of Au in preventing the surface area loss, which contributes to minimise the power performance drop during the ADT in the MEA test. However, balancing the catalytic activities and stability should be considered to define a good catalyst, thereby, 5 at% is suggested as the optimum Au insertion content for the Au-AgPt NR/C catalyst.

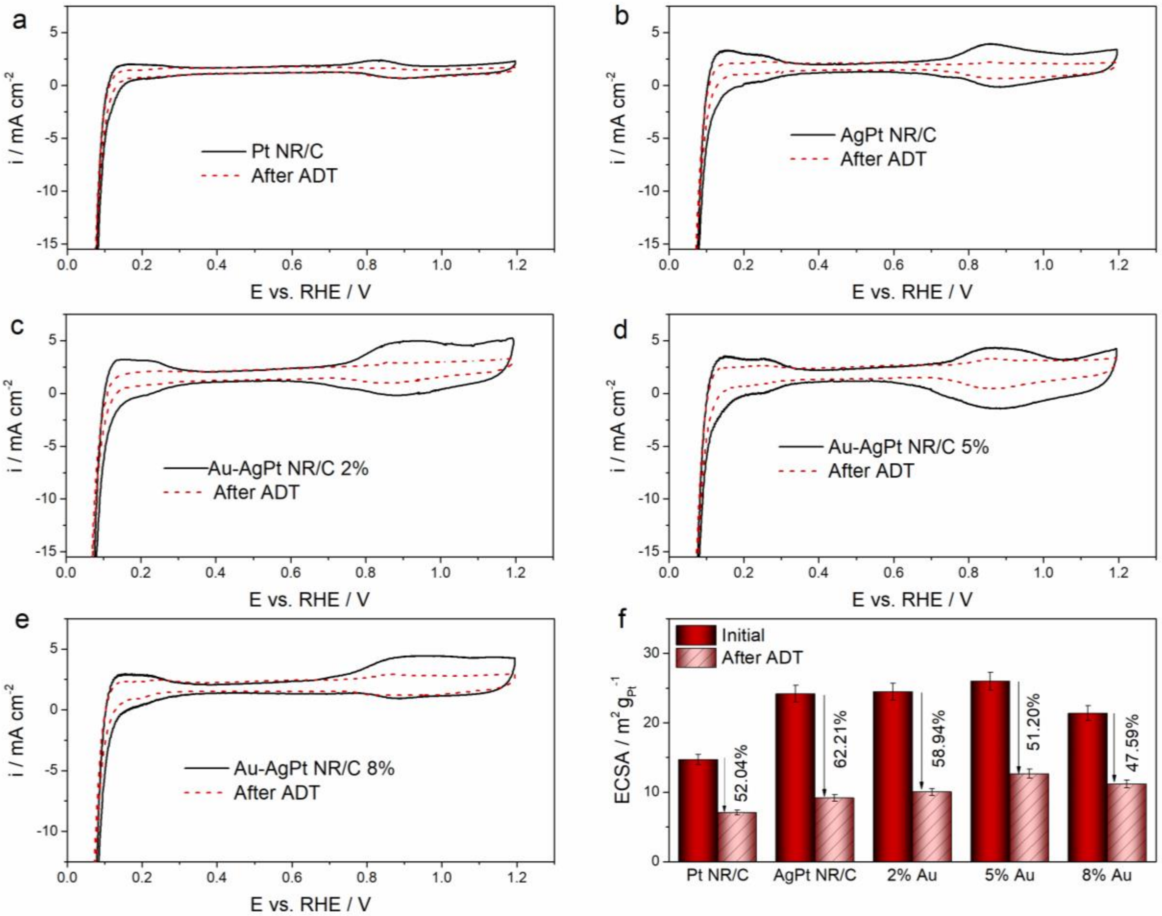

Figure 5.15 Comparison of CVs and the corresponding ECSA decline after the ADT of the MEAs with the cathode GDE made of the Pt NR/C, AgPt NR/C and Au-AgPt NR/C catalysts with various Au contents synthesised following the reaction scheme A.

The introduction of Au clusters changes the chemical and electrical properties of the 1D AgPt NR/C catalyst as shown by the XPS analysis results (Figure 5.4c-d), which contributes not only to the catalytic activity but also stability. A positive shift of the Pt binding energy after combining with 5 at% Au can be an indication of the increased Pt interaction (i.e. Pt-Pt, Pt-Ag and Pt-O) [209]. Consequently, it decreases the instability of the high-energy of Pt and Ag sites, which promotes the immunity to surface area loss during the ADT in the fuel cell environment. Therefore, the NR structure of Au-AgPt NRs is more retained compared to AgPt NRs after the ADT (Figure 5.16). Meanwhile, the destruction of the 1D AgPt nanostructures and aggregation are highly distinguished in the absence of Au, resulting in a larger surface area loss and power performance drop after the ADT, which further confirms the stability issue of the alloy catalysts. Despite that catalyst degradation and power performance decline cannot be fully avoided in the PEMFC operation, Au integration has successfully improved the ECSA loss, which has been a major contribution to minimise the durability issue. Furthermore, the effectiveness of combining Au with the AgPt alloy catalyst to upgrade its catalytic activity and stability highly depends on the atomic arrangement and quantity of the Au content, and a good strategy is necessary to balance the enhancement in both the activity and stability.

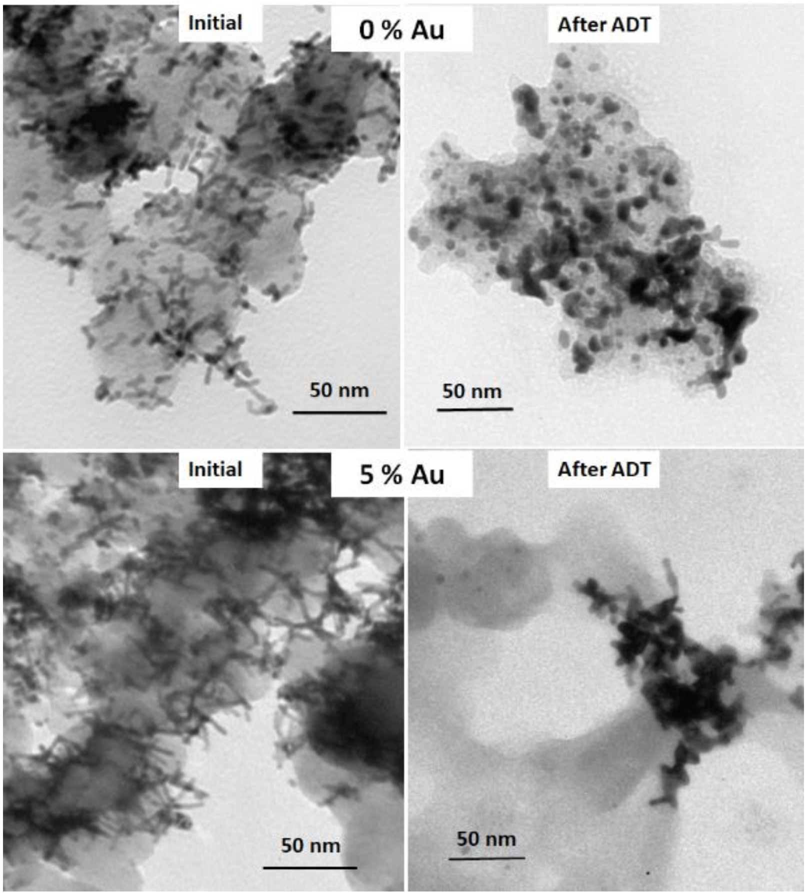

Figure 5.16 TEM images of AgPt NR/C and Au-AgPt NR/C A before and after the ADT.

5.5 Conclusion

A promising strategy for the development of 1D Pt alloy catalysts with high catalytic activities and stability in operating PEMFCs has been demonstrated via Au integration by expanding the formic acid reduction method for 1D AgPt alloys. The adjustment of Au adding period is crucial to control the metal atom arrangement along with the 1D structure. Hence, the addition of Au ions at the early reaction stage is preferred to optimise the Pt deposition on the NR surface. The inclusion of the Au ions tunes the reduction process during the growth of 1D AgPt alloy, leading to longer NRs and thus enhanced mass transport performance for an improved power density. The Au-AgPt NR/C A GDE with 5 at% Au generates 1.12- and 1.20-fold power density compared to the GDEs made of the AgPt NR/C and Pt/C catalysts. The introduction of Au ions derives a slower kinetic reaction rate, which potentially adjusts the placement of more

Pt atoms to the surface, leading to a large ECSA. Testing under H_2/O_2, a mass activity of 0.110 A mg_{Pt}^{-1} is achieved for 5% Au-AgPt NR/C A, which is 1.15- and 1.70-fold higher than AgPt NR/C and Pt/C, respectively. A significantly enhanced effect for the Au integration is observed with the catalyst stability in PEMFCs. 5 at% Au-AgPt NR/C A GDE exhibits a power density and ECSA decline of 39.63% and 51.20% after the ADT, respectively, which are much less compared to 49.71% and 62.12% of the AgPt NR/C GDE and 44.19% and 76.61% of the Pt/C GDE. The increasing of the Au content can effectively reduce the ECSA decline during the ADT, but a content higher than 5 at% reduces the number of catalyst active sites due to a higher Au deposited on the surface of the NRs and their severe aggregation, which finally induces the lower power performance.

The understanding obtained with the Au integration for the NR catalysts can help the design and development of practical shape-controlled Pt alloy catalysts for PEMFCs. It also highlights the importance of controlling the reaction rate and alloying behaviour by alloying with Au. The development of GDEs with 1D Au-AgPt catalyst arrays grown on GDLs will be further explored in the next chapter to optimise the catalytic activities and stability of the ORR electrode.

Chapter 6

Gas Diffusion Electrodes from 1-Dimensional AgPt-based Nanorods Grown on Gas Diffusion Layers

The work presented in this chapter is unpublished at the time of writing

This chapter demonstrates the preparation of gas diffusion electrodes (GDEs) with one-dimensional (1D) AgPt-based nanorods (NRs) grown directly on gas diffusion layers (GDLs), adapting the methods developed in Chapter 4 and 5. The parameters controlling the growth of AgPt NRs on the GDL such as temperature, time interval and the atomic ratio of Ag and Pt are explored considering the electrode power performance towards oxygen reduction reaction (ORR) in PEMFCs. Additionally, the integration of Au to construct Au-AgPt NR GDEs is also investigated, which is intended to tune the atomic arrangement and minimise the atomic segregation for enhanced stability. Finally, the catalytic performance is evaluated in PEMFCs condition along with the ADT.

6.1 Introduction

Support-free GDEs constructed from single-crystal 1D Pt nanostructure arrays have been intensively studied in our group, and demonstrated as an advanced design for highly active and durable electrodes, outperforming the conventional electrodes made of Pt/C nanoparticles in PEMFCs [130,139,140,143]. The extended active site exposure and thin catalyst layer with improved mass transfer performance are the privileges of the open structure within the three-dimensional (3D) ordered electrodes made from 1D nanostructure arrays. The superiority of the 1D nanostructures and elimination of the supported carbon minimise the degradation mechanism, which has been long studied as a major challenge contributing to the performance loss especially at the high potential region [210,211]. Such an attractive feature motivates this PhD research to advance the fabrication of 1D Pt hybrid NRs, by translating the method applied from the previous two chapters to directly grow the alloy catalysts directly on the GDL surface constructing AgPt or even Au-AgPt NR GDEs.

It is a challenge to achieve a good 1D nanostructure distribution with little agglomeration on the GDL surface. Throughout the study in our group, it was revealed that a uniform distribution of 1D Pt nanostructures is prominent to fabricate a high power performance GDE in PEMFCs, which has been optimised by conducting Pt nanowire (NW) growth at 40 °C rather than in room temperature to achieve Pt NW array GDEs [142]. A high reaction temperature at 40 °C can increase the wettability of the GDL surface, which is superhydrophobic because of the polytetrafluoroethylene (PTFE) treatment in manufacture for preventing water flooding in fuel cell operation. Additionally, a high reaction temperature also induces a faster kinetic reaction rate and reduces the Pt nanowire length for a smaller aspect ratio to increase the specific surface area. In this chapter, the moderate temperature of 40 °C is therefore applied to grow AgPt and Au-AgPt NRs on the GDL surface.

6.2 Time interval-controlled growth of 1D AgPt NRs on GDLs

Since the reaction is conducted at a moderate temperature of 40 °C, it potentially changes the reduction rate of both metal ions. Therefore, adjusting time interval (i.e. 1, 3 and 5 hours) of mixing Pt and Ag precursors is evaluated to optimise the properties of 1D AgPt alloy morphology. In this section, a constant concentration of formic acid (1.2 M) and metal loading of 0.4 mg cm^{-2} at an atomic ratio of Ag:Pt = 3:7 are deployed for all GDEs.

The structure of AgPt grown on the GDL surface with different intervals of 1, 3 and 5 hours, for adding the Ag precursor is presented in Figure 6.1. The reduction of Ag is presumed more spontaneously at 40 °C. Hence, the inclusion of Ag ions after 1 hour reaction results in the formation of agglomerated particles observed by transmission electron microscope (TEM) image (Figure 6.1a-b) due to less Pt seeds formed at this stage. After 3 hours, the reduction Pt ions is sufficiently configured Pt seeds, and the introduction of Ag ions at this stage induces a slower reaction rate generating longer 1D AgPt NRs (Figure 6.1c-d), as the consequence of an optimum balance of the Pt and Ag ions. After 5-hours, the enormous amount of Pt seeds have been formed, and the involvement of Ag results to only the construction of shorter NRs (Figure 6.1e-f).

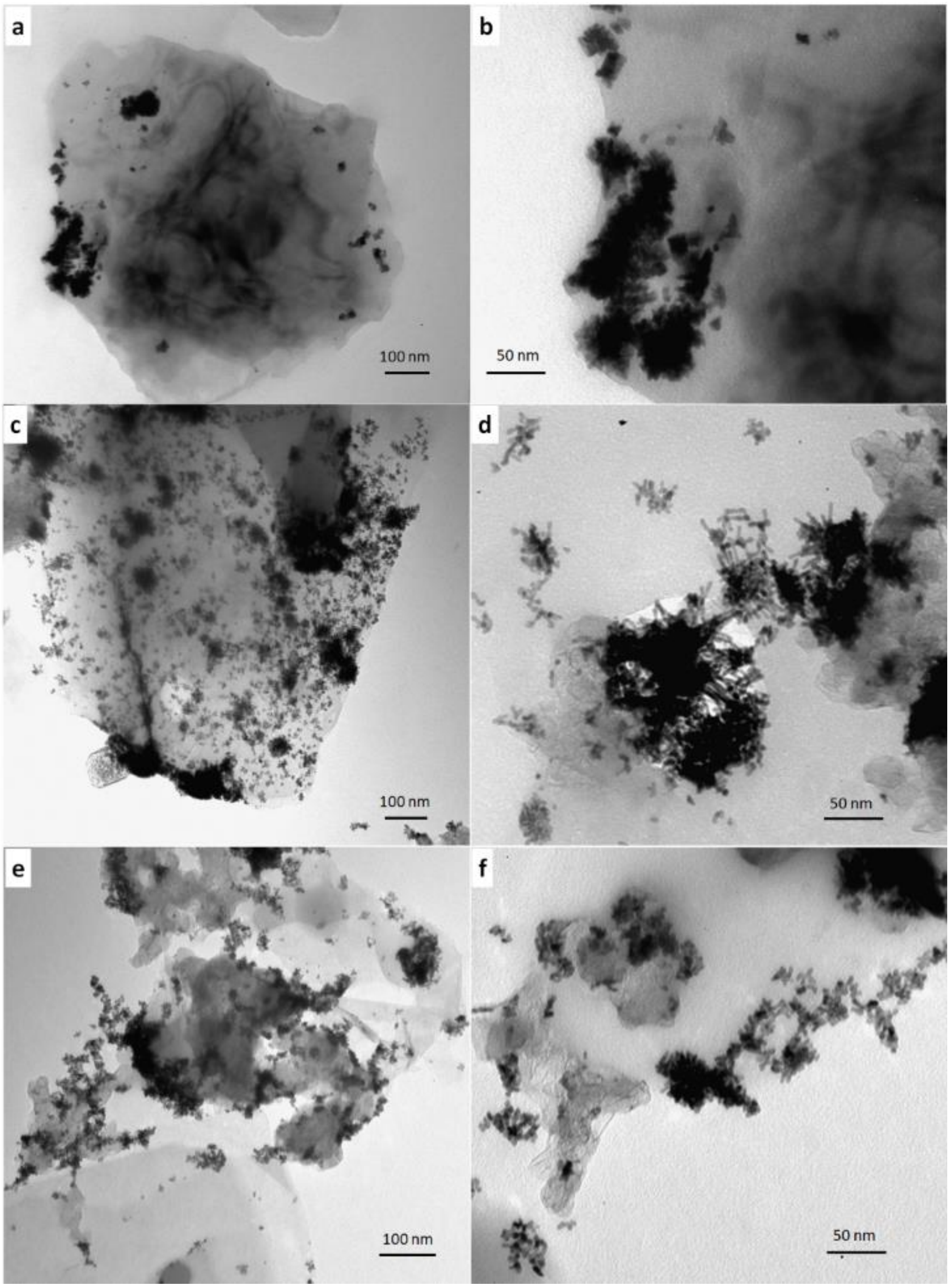

Figure 6.1 TEM images of the AgPt GDEs grown at 40 °C with different intervals of introducing the Ag precursor at **(a-b)** 1 hour, **(c-d)** 3 hours and **(e-f)** 5 hours after the beginning of the reaction.

X-ray diffraction (XRD) patterns of the AgPt GDEs are shown in Figure 6.2. The peaks are indexed to (111), (200), (220) and (311) plane, appointed to the face-centred cubic (FCC) crystal structure of bulk Ag (JCPDS-04-0783) and Pt (JCPDS-04-0802). The main (111) peaks are in alignment indicating the similar lattice space. The peaks are representing the Ag metal phase decline with the shorter interval time of adding the Ag precursor. Within 1 hour interval applied, there is a larger chance for the remaining Pt ions to collaborate with the introduced Ag ions to form an alloy. Hence, the Ag metal phase amount is the lowest. With a longer reaction interval, less amount of Pt ions remained to interact with the Ag ions results in the formation of a higher amount of the Ag metallic state. Both TEM and XRD analysis result further suggest to shortening interval time of 3 hours to generate a fine structure of AgPt NR GDE.

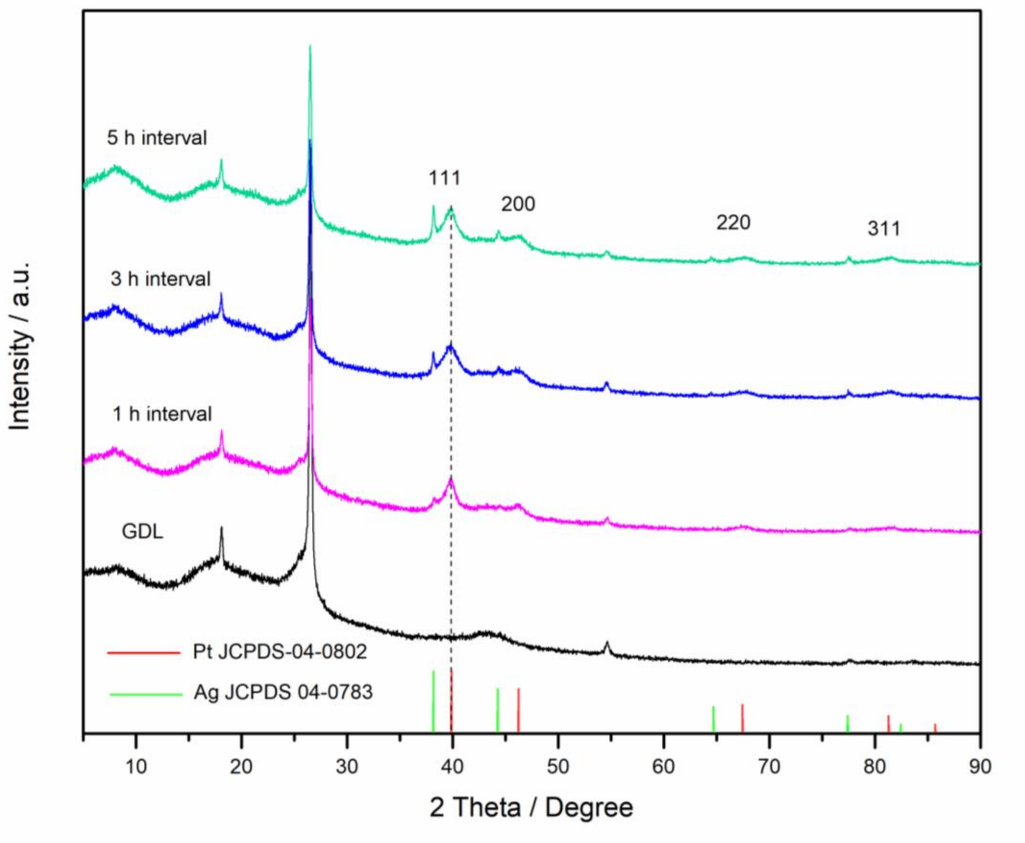

Figure 6.2 XRD patterns of the AgPt GDEs grown at 40 °C with different intervals for the introduction of the Ag precursor.

6.3 GDEs from 1D AgPt NRs with various metal atomic ratios

With an optimal reaction temperature at 40 °C and interval time of ca. 3 hours for adding Ag precursor after the beginning of the reaction, the atomic ratio of Ag and Pt are further investigated to determine an ideal alloy metal composition, keeping the total metal loading constant at 0.4 mg cm^{-2} for the AgPt NR GDE.

6.3.1 Physical characterisation

Figures 6.3a-b display the TEM images of Pt NRs (0% Ag) grown on the GDL surface at 40 °C. The agglomerated NRs in a 3D cubic like structure with an average size of ca. 80-100 nm agrees with our previous work [142]. The average NR diameter is ~ 4 nm with a length of ca. 15-25 nm, which is also comparable to the size of the Pt NRs grown on the carbon support in the previous chapter (Figure 4.1b). The alloy catalyst with 10 at% of Ag exhibits a similar morphology, but with some areas showing huge cubic shape agglomerates of NRs of ca.120 nm (Figure 6.3c-f). A high-resolution TEM (HR-TEM) image of a single NR (Figure 6.3f) shows an ordered plane into the same orientation ascribed as a single crystal with the FCC structure. The crystallinity of the 1D nanostructure with a measured d-spacing of 0.23 nm is assigned to the [111] facets aligned along the NR.

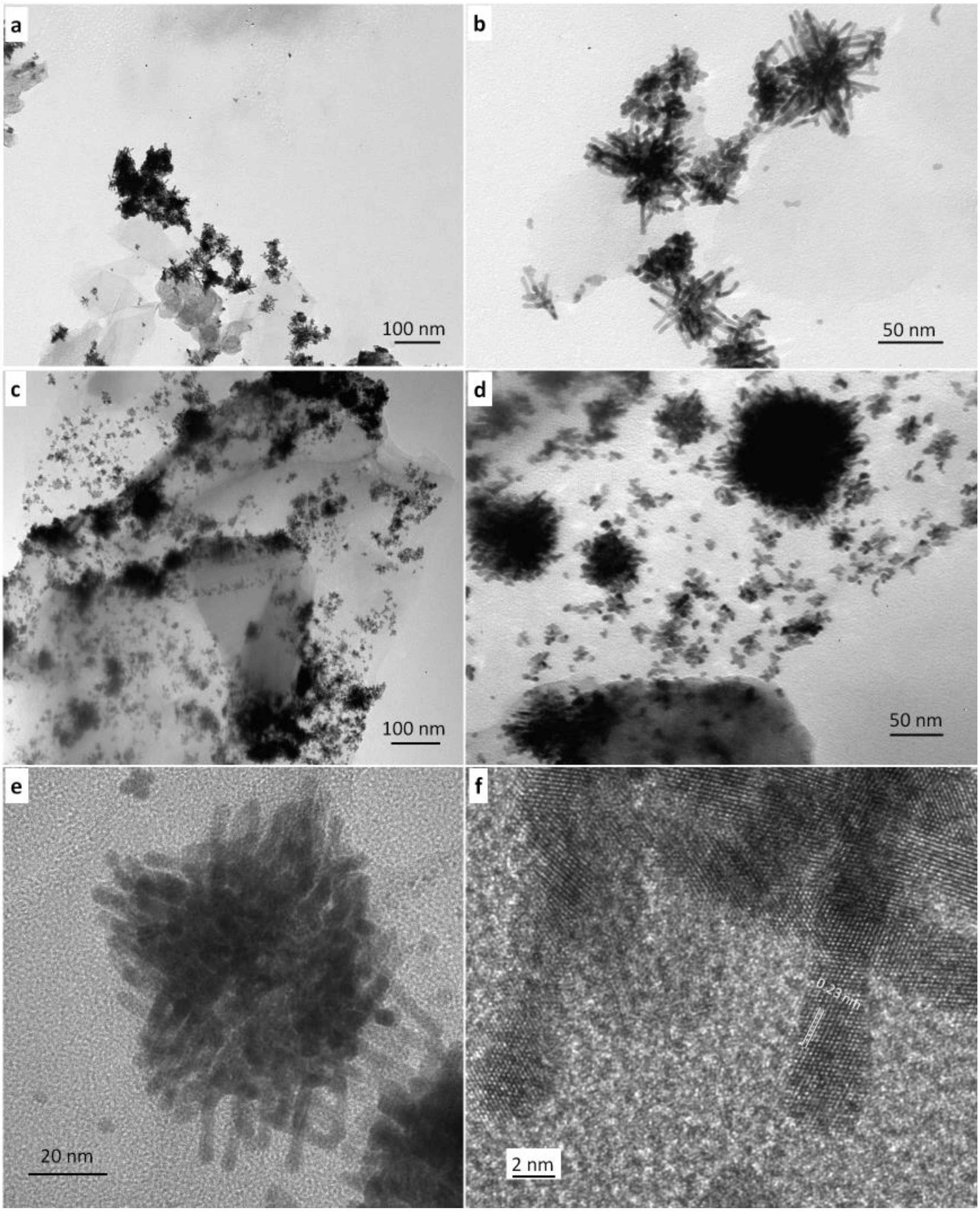

Figure 6.3 TEM images of **(a-b)** Pt NRs and **(c-f)** Ag_1Pt_9 NRs grown on the GDL surface at 40 °C and 3 hours of interval for adding the Ag precursor.

Generally, AgPt NR GDEs with a similar catalyst structure and morphology are observed with the varied Ag content of up to 30 at% (Figure 6.4). At this point, it is agreed that the physical structure of the 1D NRs is less affected by alloying Ag of up to ~30 at%.

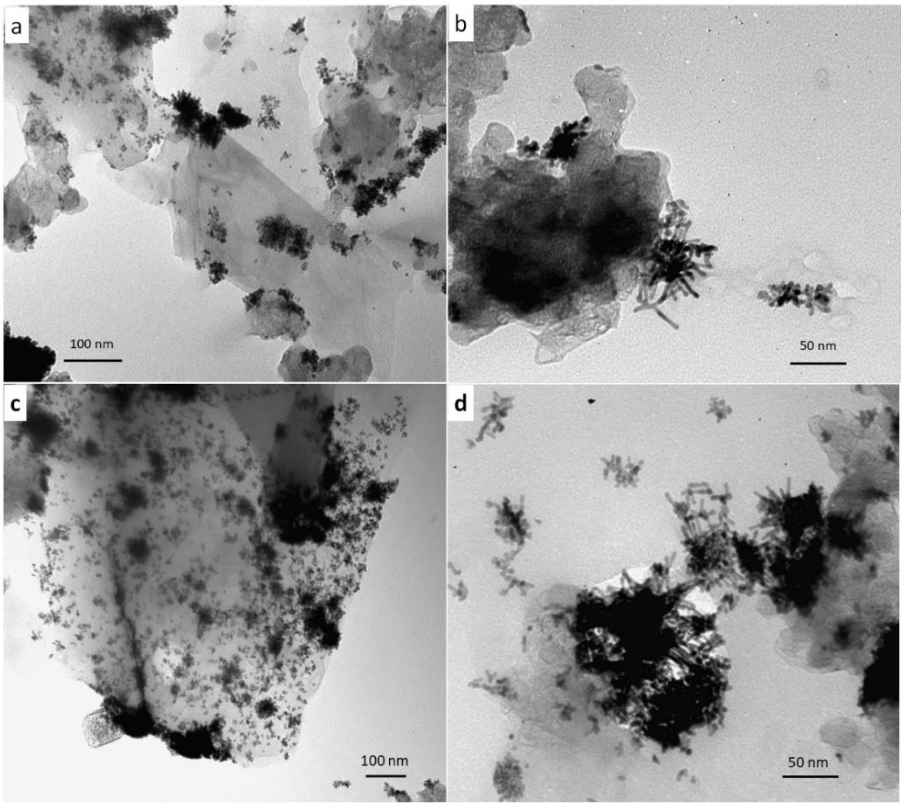

Figure 6.4 TEM images of **(a-b)** Ag_1Pt_4 NRs, **(c-d)** Ag_3Pt_7 NRs grown on the GDL surface at 40 °C and 3 hours interval for adding the Ag precursor.

The increase of the Ag content up to 50 at% (Ag_1Pt_1 NR) leads to the formation of dominated short NRs with a length of ca. 10-15 nm as shown in TEM images (Figure 6.5). It is attributed to the low Pt content inducing a high reduction rate at the first stage of the reaction. Such behaviour has been previously observed with the high Ag content for preparing the AgPt NR/C catalyst in Chapter 4. However, lots of unstructured agglomerates are observed (Figure 6.5b-c). It is potentially formed from the limited Pt seeds and also Ag particles rendered by the faster reduction rate at 40 °C, as well as the limited remaining Pt ions to assist the growth into <111> direction. This finding is supported by the XRD analysis results (Figure 6.6) showing broader Pt peaks with the increasing Ag content at 30 at% and above, which is attributed to the domination of the short NRs. The significantly high and narrow Ag peaks of the Ag_1Pt_1 NR GDE suggest the excessive presence of Ag grains.

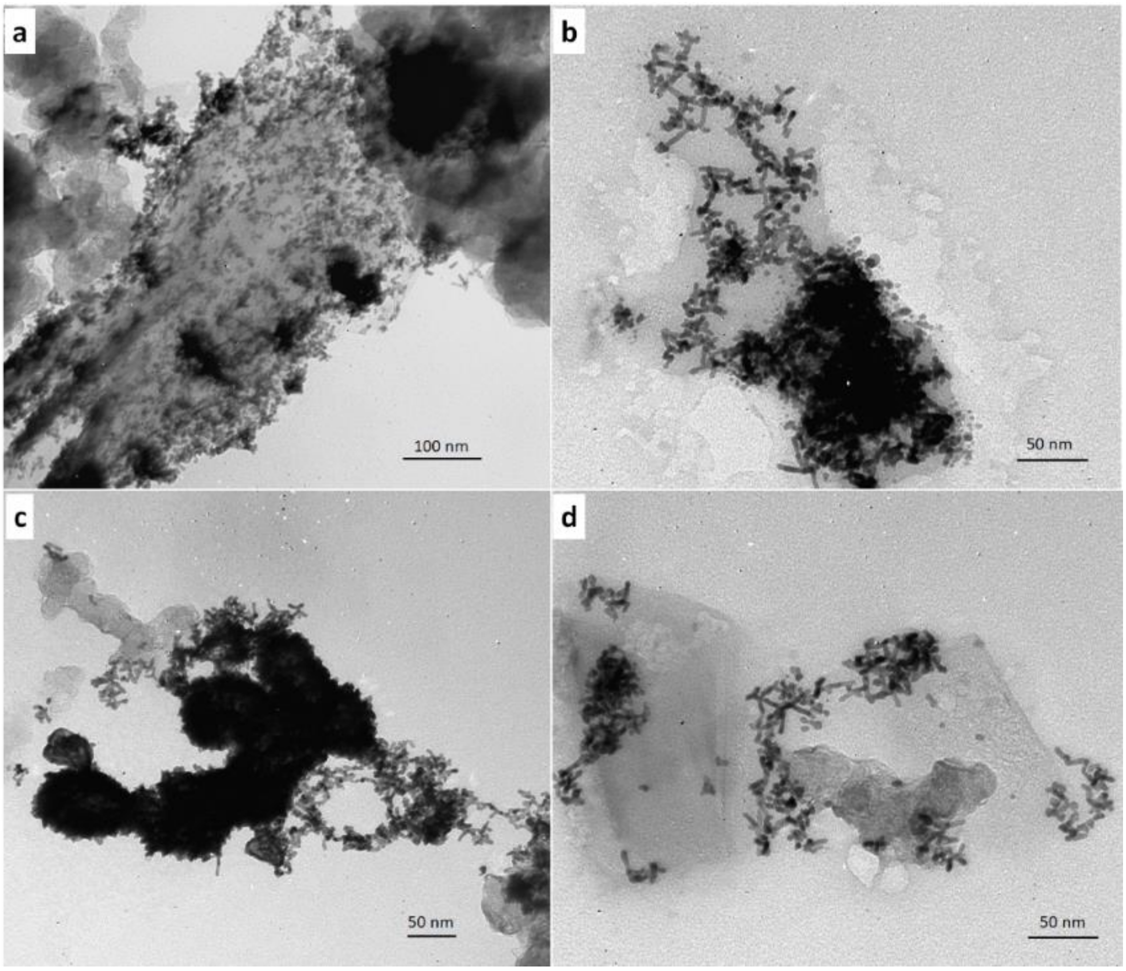

Figure 6.5 TEM images of Ag_1Pt_1 NR grown on the GDL surface at 40 °C and 3 hours interval for adding the Ag precursor.

For the AgPt GDEs with various metal ratios, the main peaks on the XRD patterns (Figure 6.6), except those from the GDL, are well indexed to the FCC crystal structure of bulk Pt (JCPDS: 04-0802) and Ag (JCPDS: 04-0783). With the alloying of Ag, even at 10 at%, the peaks are shifted negatively indicating a larger interplanar space compared to the Pt NRs, but this shift is kept at the same two theta position with the increasing Ag content. The peaks referencing to the Ag metal phase are detected from 20 at% Ag, and the intensity increases with the increasing Ag ratio to Pt, exhibiting the highest intensity at 50 at% Ag. This finding suggests that an optimum lattice contraction is achieved at 10 at% Ag, and more Ag leads to the formation of the Ag metal phase instead of alloying with Pt. The quantitative measurement of the metal contents was performed by the inductively coupled plasma-mass spectroscopy (ICP-MS) analysis along with the thermogravimetric analysis (TGA), and the results are presented in Table 6.1.

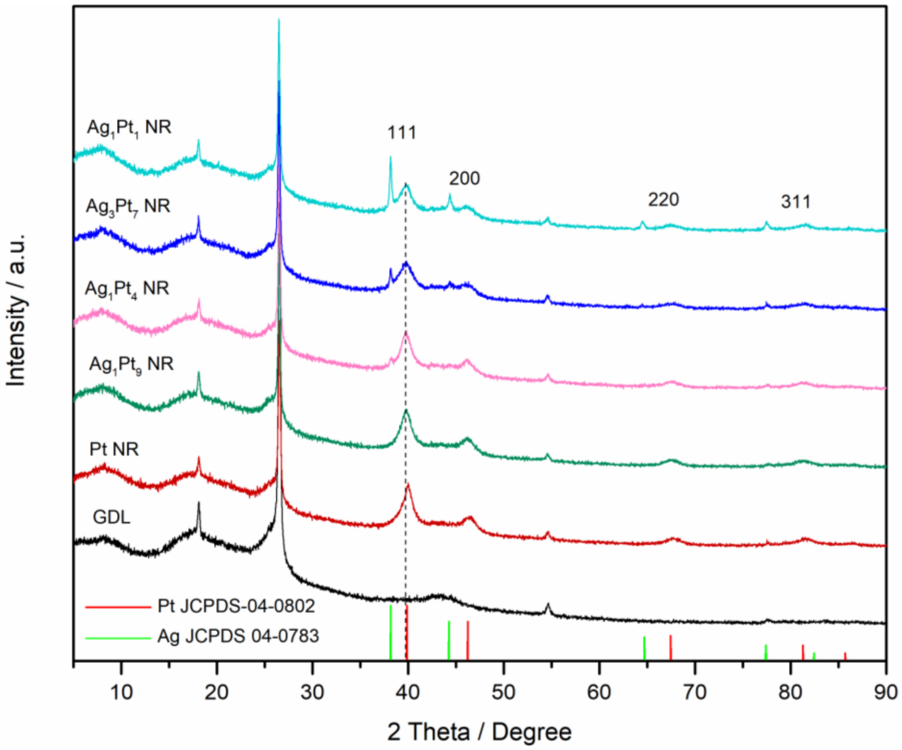

Figure 6.6 XRD patterns of the Pt NR and AgPt NR GDEs with different atomic ratios of Ag and Pt in comparison to the GDL and the reference of bulk Pt and Ag.

Table 6.1 Metal contents for the NR GDEs measured by TGA & ICP-MS

GDE	TGA / mg cm^{-2}	ICP-MS / wt%		ICP-MS / at%	
		Ag	Pt	Ag	Pt
Pt NR	0.41	0	100	0	100
Ag_1Pt_9 NR	0.38	5.44	94.56	9.42	90.58
Ag_1Pt_4 NR	0.42	12.83	87.17	21.03	78.97
Ag_3Pt_7 NR	0.41	21.05	78.95	32.54	67.46
Ag_1Pt_1 NR	0.39	35.79	64.21	50.20	49.80

Apparently, the alloying behaviour of AgPt NRs grown on the GDL is different to those on the carbon presented in Chapter 4. At a moderate reaction temperature of 40 °C, the reduction of Ag and Pt occurs less simultaneously. Proposing that the reduced Ag tends to pile up on the top of Pt, limiting the formation of harmonised alloy structure, especially at the higher Ag atomic ratio of more than 10 at%.

6.3.2 MEA testing

The Pt NR and AgPt NR GDEs with various atomic ratios of Ag and Pt were tested as cathodes in H_2/Air single cells along with the Pt/C GDE as the benchmark. The metal loading was the same for all the GDEs of 0.4 mg cm^{-2}. Polarisation and power density curves recorded are shown in Figure 6.7a. At 0.6V, the power densities for the AgPt NR GDEs with various Ag contents of 0-30 at% are comparable to the Pt/C GDE of 0.49 W cm^{-2}. However, a higher potential loss at the larger current density region is observed with the increasing Ag content, showing a dropping peak power density. The significant performance drop is observed at 50 at% Ag (the Ag_1Pt_1 NR GDE). The Pt NR GDE exhibits the highest power density of 0.54 W cm^{-2} at 0.6 V (Figure 6.7b), demonstrating the superiority of support-free Pt NR GDE compared to that of the Pt/C GDE which agrees with the previous studies in our group. Meanwhile, Ag_3Pt_7 NR GDE shows the highest power output at 0.6 V normalised to Pt loading (Figure 6.7c).

Electrochemical impedance spectroscopy (EIS) analysis at the low current density of 30 mA cm^{-2} is presented in Figure 6.7d. The charge transfer resistance shown by the diameter of the semi-circle is comparable for most of the GDEs. The larger EIS spectra of Ag_1Pt_1 GDE is ascribed to the lower Pt loading in the cathode. It is identical to the obtained results for the pure Pt nanowire GDEs reported in the literature [145]. It also indicates the less significant influence of the Ag alloying on the charge transfer performance of AgPt NR array GDE.

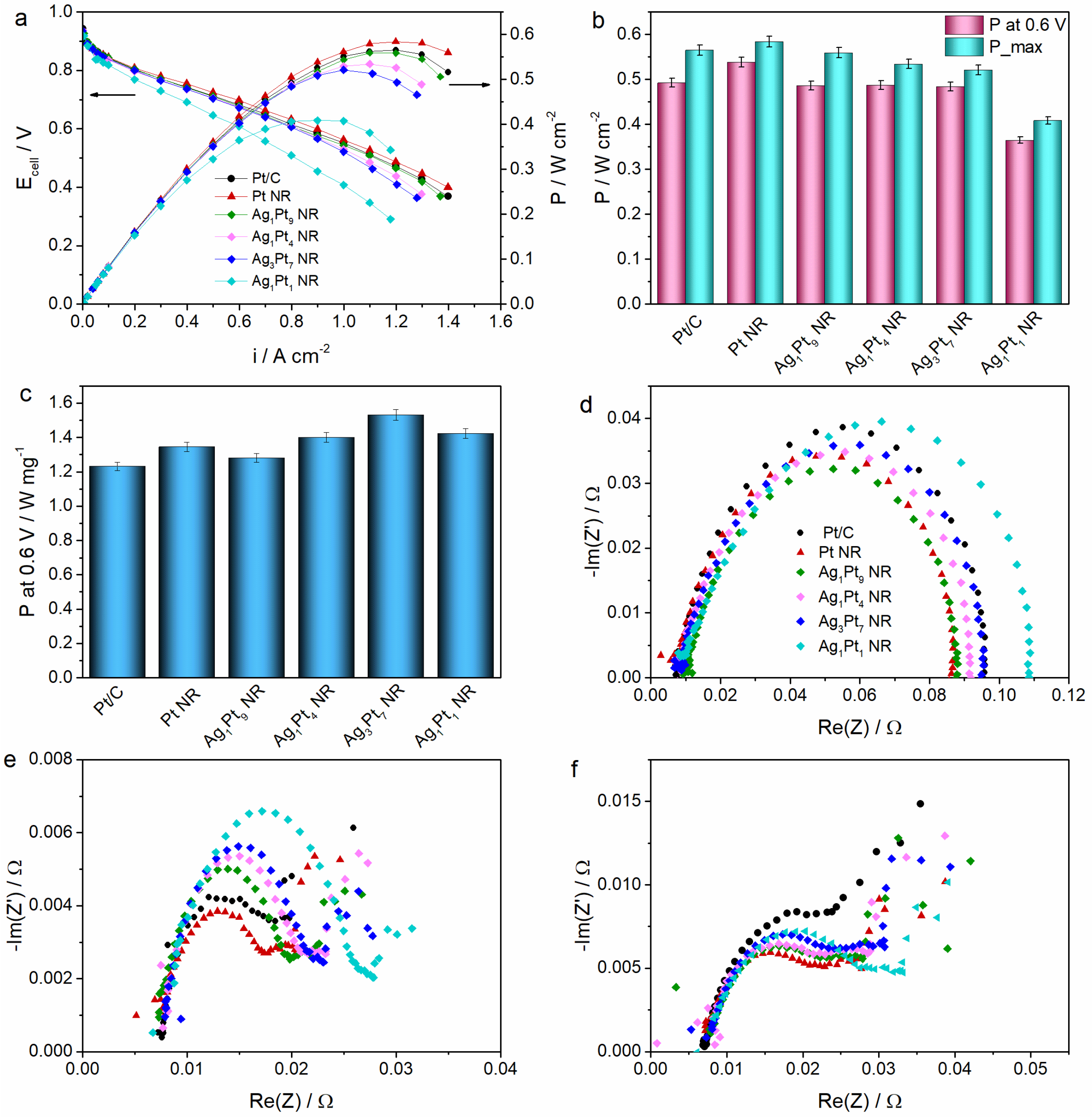

Figure 6.7 (a) Polarisation and power density curves of the Pt/C, Pt NR and AgPt NR GDEs with different metal ratios. **(b)** Comparison of the corresponding peak and power density at 0.6 V, **(c)** comparison of the corresponding power output at 0.6 normalised to Pt loading. The corresponding EIS spectra recorded at **(d)** 30 mA cm^{-2} **(e)** 0.65 V and **(f)** 0.5 V.

At the medium and low potential of 0.65 and 0.5 V (Figure 6.7e and 6.7f), the first arc impedance for the NR GDE increases with the Ag loading. It means the charge transfer resistance is more dominant to affect the potential loss. At the low potential of 0.5 V, all NR GDEs display a smaller impedance than that of the Pt/C GDE. In this case, the polarisation curve (Figure 6.7a) provide a more reliable parameter to determine the voltage loss caused by limited mass transport. The smaller performance loss of Pt NR GDE than of Pt/C GDE can be ascribed to the superiority of the 1D nanostructures and the reduced mass transfer resistance of the NR GDEs because of the smaller thickness and larger porosity, which facilitate the gas transport within the catalyst layer.

The cyclic voltammetry (CV) plots are shown in Figure 6.8, and as in previous chapters, much smaller hydrogen desorption (H_{des}) peaks are recorded for the NR GDEs compared to the Pt/C GDE. The electrochemical surface area (ECSA) measured for the Pt NR GDE is 22.73 m_{Pt}^2 g^{-1} (Table 6.2), which is close to the data reported from the previous studies [142,143]. A lower ECSA value is obtained for the AgPt NR GDEs compared to the Pt NR GDE due to the reduced number of the active sites with the lower Pt content. Similar to the previous observation in Chapter 4 and 5, a large positive shift is observed with the Pt-O reduction peak for the NR GDEs. This shift is also more positive for the AgPt GDEs, indicating a better ORR activity in PEMFCs.

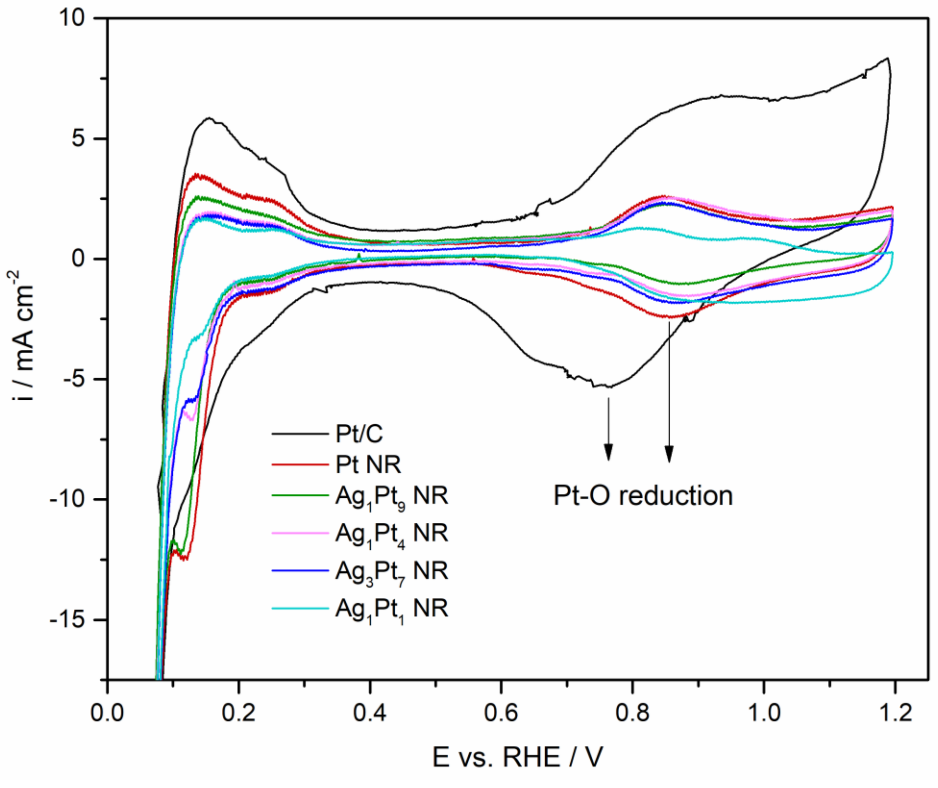

Figure 6.8 CVs of the Pt/C, Pt NR and AgPt NR GDEs with different metal ratios.

The catalytic activity of the AgPt GDEs is further explored in the MEA test under H_2/O_2 following the DoE protocol and the method described by Gasteiger et, al. [184]. Figure 6.9 presents the initial and corrected polarisation curves for the Pt NR and two AgPt NR GDEs. With minimised mass transfer polarisation, the Pt NR and Ag_1Pt_9 NR GDEs exhibit a similar behaviour because of the identical crystallinity and morphology of the 1D catalyst nanostructures. With a high Ag content, the Ag_1Pt_1 NR GDE exhibits a much lower current density. Normalised to the Pt loading (Table 6.2), the ORR activity of the NR GDEs decreases with the increasing Ag content (decreasing Pt loading). The mass activity obtained for the Ag_1Pt_1 NR GDE is 0.066 A mg_{Pt}^{-1}, which is slightly lower than that of the Pt NR GDE of 0.072 A mg_{Pt}^{-1}, but still higher than 0.064 A mg_{Pt}^{-1} of the Pt/C GDE.

Table 6.2 Catalytic activities of the GDEs determined in the MEA test.

GDE	ECSA / $m^2\ g_{pt}^{-1}$	I_m / A mg_{Pt}^{-2}	I_s / µA cm^{-2}
Pt/C	51.71	0.064	122.83
Pt NR	26.64	0.072	316.59
Ag_1Pt_9 NR	19.32	0.070	361.13
Ag_1Pt_4 NR	16.52	0.066	397.65
Ag_3Pt_7 NR	17.20	0.064	372.69
Ag_1Pt_1 NR	19.12	0.066	346.02

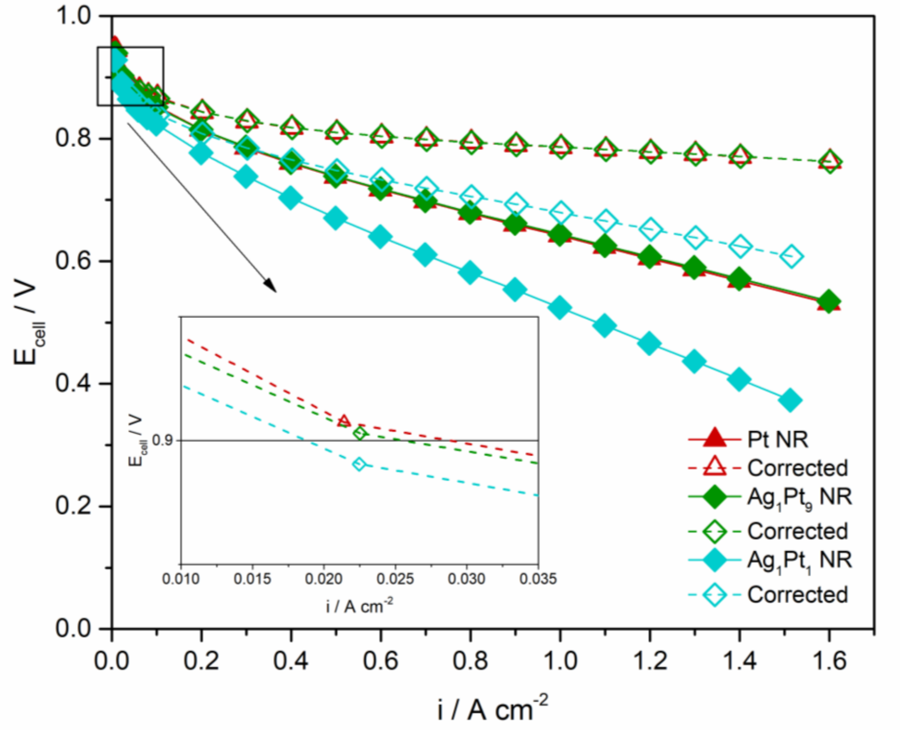

Figure 6.9 Original and corrected polarisation curves of the GDEs made of Pt NR, Ag_1Pt_9 NR and Ag_1Pt_1 NR.

Compared to the results of the AgPt NR/C catalysts obtained in Chapter 4 (Table 4.3), the catalytic activities of the AgPt NR GDEs are much lower in the MEA test. The measured mass and specific activities of the Ag_1Pt_1 NR/C catalyst GDE are 1.5 and 1.13-fold higher than of support-free Ag_1Pt_1 NR GDE with the same ratio of Ag and Pt. A similar trend is also observed for the Pt NR/C GDE, which also shows a higher mass and specific activity than the Pt NR GDE. These findings suggest a better ORR activity with the support of carbon. The inert GDL surface usually leads to the formation of large catalyst agglomerates which reduce the catalyst utilisation ratio. The lower ORR activity of the AgPt GDE is also potentially ascribed to the less harmonised alloying behaviour of Ag and Pt, as shown by the XRD analysis results in Figure 6.6. It is induced by the faster reduction rate of Pt and Ag at 40 °C compared to the room temperature for growing the AgPt NRs on the carbon support. Hence the reduced Ag^0 tends to pile up on the top of Pt, partially blocking the active sites on the catalyst surface resulting in low catalytic activity.

6.4 Au-AgPt NR GDEs

Observed in Chapter 5 is that the including of Au affected the reduction of Pt ions and rendered the placement of Pt on the NR surface. In this section, such method is adjusted to control the arrangement of Pt and Ag on the GDL surface. The influence of the Au addition on the morphology, structure and catalytic performance are investigated based on the physical characterisation and PEMFC test results.

6.4.1 Physical characterisation

The preliminary study of the Au integrated Ag_3Pt_7 NR GDE is conducted at 40 °C with a metal loading of 0.4 mg cm^{-2}. 2 at% Au is introduced together with the Pt precursor at the early reaction stage, followed by adding Ag ions after 3 hours of the reaction. The structure and morphology of the Au-AgPt NRs from the GDE are presented in TEM images in Figure 6.10, showing a fine distribution of the catalysts with some agglomerates on the GDL surface. The HR-TEM image displays an ordered plane with an interplanar space of 0.23 nm referring to the growth of the NR along the <111> direction. Such presentation is similar to the Pt NR GDE and AgPt NR GDE with a low Ag loading.

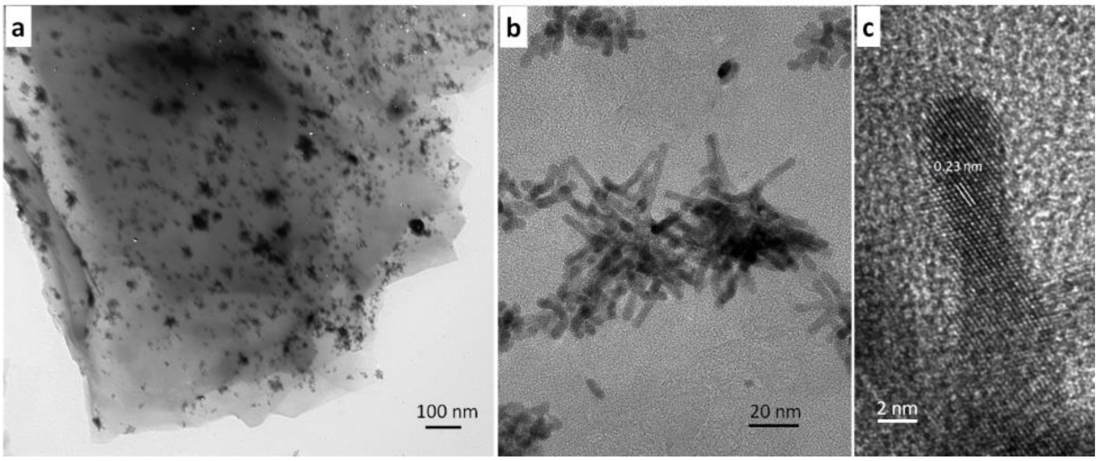

Figure 6.10 TEM images of the Au-AgPt NRs scraped from the GDE with 2 at% Au.

The XRD pattern of the Au-AgPt GDE is shown in Figure 6.11. Compared to the Ag_3Pt_7 NR GDE, the Au-AgPt GDE shows peaks at the same two theta position with a slightly higher intensity because of the longer NRs. The main difference is that the Ag metal phase peaks are disappeared on the pattern of the Au-AgPt NR GDE. This indicates the replacement of 2 at% Ag with Au significantly improves the alloying degree of Ag with Pt.

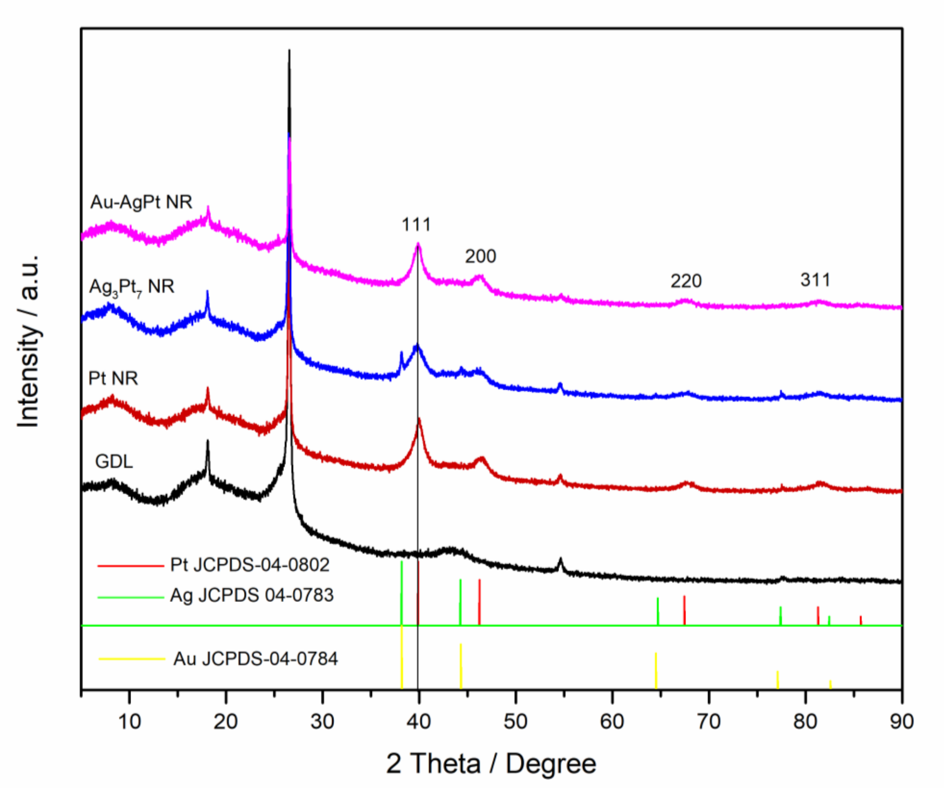

Figure 6.11 XRD patterns of the Au-AgPt NR GDE in comparison to the Pt NR and Ag_3Pt_7 NR GDEs, GDL and the references of bulk Pt, Ag and Au.

Further evaluation with the X-ray photoelectron spectroscopy (XPS) analysis exhibits a significant change of the surface composition (Table 6.3) with ~2 at% of Au, measured from the XPS survey scan in Figure 6.12. XPS detects 57.24 at% of Ag and 42.76 at% of Pt on the surface from the Ag_3Pt_7 NR GDE. After alloying with ~2 at% of Au, Pt dominates the surface composition of 65.46 at%. This changes further confirms the effectiveness of Au alloying to control the arrangement of Pt and Ag along with the NR catalysts, resulting in a high Pt deposition on the surface. While, a very low Au concentration of 0.3 at% is measured, suggesting that most of Au are deposited beneath the surface of the NRs.

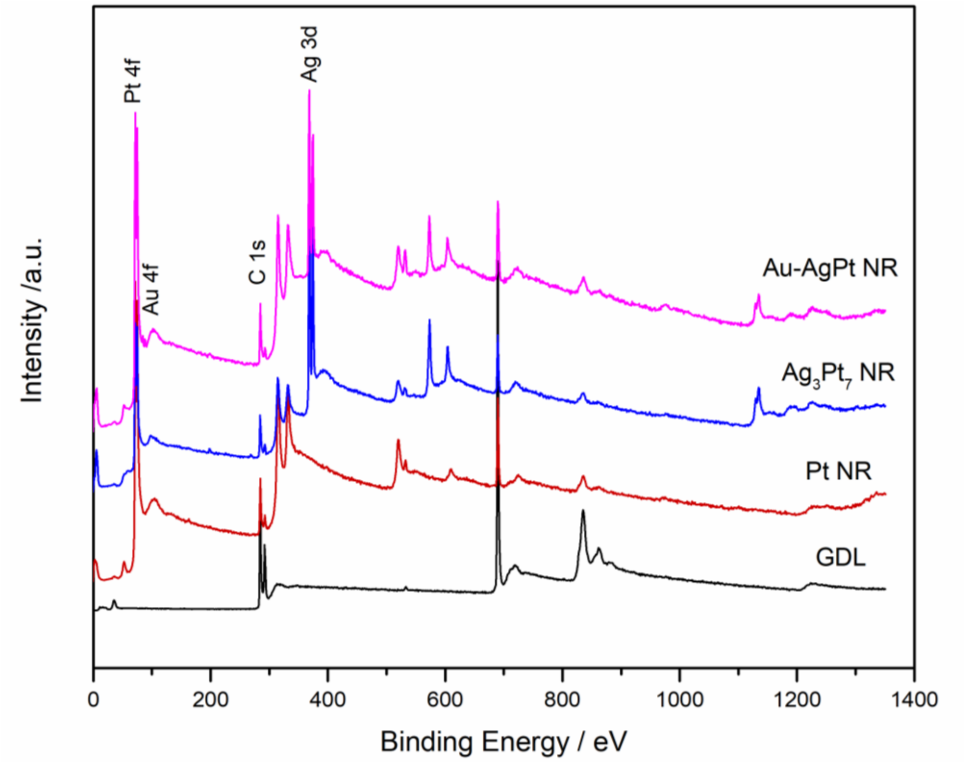

Figure 6.12 XPS survey of the GDL, Pt NR, Ag$_3$Pt$_7$ NR and Au-AgPt NR GDEs.

Table 6.3 Comparison of the quantitative measurement results for the Ag$_3$Pt$_7$ and Au-AgPt NR GDEs by ICP-MS and XPS.

GDE	ICP-MS / at%			XPS / at%		
	Au	Ag	Pt	Au	Ag	Pt
Ag$_3$Pt$_7$ NR GDE	0	32.54	67.46	0	57.24	42.76
Au-AgPt NR GDE	2.48	26.27	71.25	0.30	34.28	65.42

The corresponding high-resolution XPS spectra of the Pt 4f and Ag 3d regions are shown in Figure 6.13. Small Au 4f peaks are detected for the Au-AgPt NR GDE within the high-resolution Pt 4f region (Figure 6.13c). Compared to Pt 4f spectra of the Pt NR GDE (Figure 6.13a), the Pt 4f peaks of the Ag$_3$Pt$_7$ NR and Au-AgPt NR GDEs (Figure 6.13c and e) shift more negatively (~ 0.2 eV), referring to the change of the Pt binding energy. This confirms a similar change as before of the electronic structure of Pt because of the interaction with Ag/Au, inducing modification of the Pt surface after the formation of 1D Pt alloy structures [78]. A closer observation of the Pt 4f region of the Au-AgPt NR GDE shows a very small positive shift of ~0.04 eV compared to the Ag_3Pt_7 NR GDE, indicating the change of the electronic property due to alloying with a small amount of Au. Similarly, Ag 3d peaks of the Ag_3Pt_7 NR and Au-AgPt NR GDEs are shifted negatively of ~0.1 eV from the referenced Ag/GDL (Figure 6.13b), indicating charge transfer phenomena due to formation of the bimetallic Ag and Pt alloy, causing the change of the binding energy of Ag^0 [165]. Nevertheless, both Ag 3d peaks of the Ag_1Pt_4 NR and Au-AgPt NR GDEs are in alignment, indicating a similar Ag binding energy and less influence of the Au alloying on Ag properties. Furthermore, the Pt 4f and Ag 3d peaks are completely fitted to Pt^0 and Ag^0 for both the Ag_1Pt_4 NR and Au-AgPt NR GDEs (Figure 6.13c-f), implying domination of the metallic state composition.

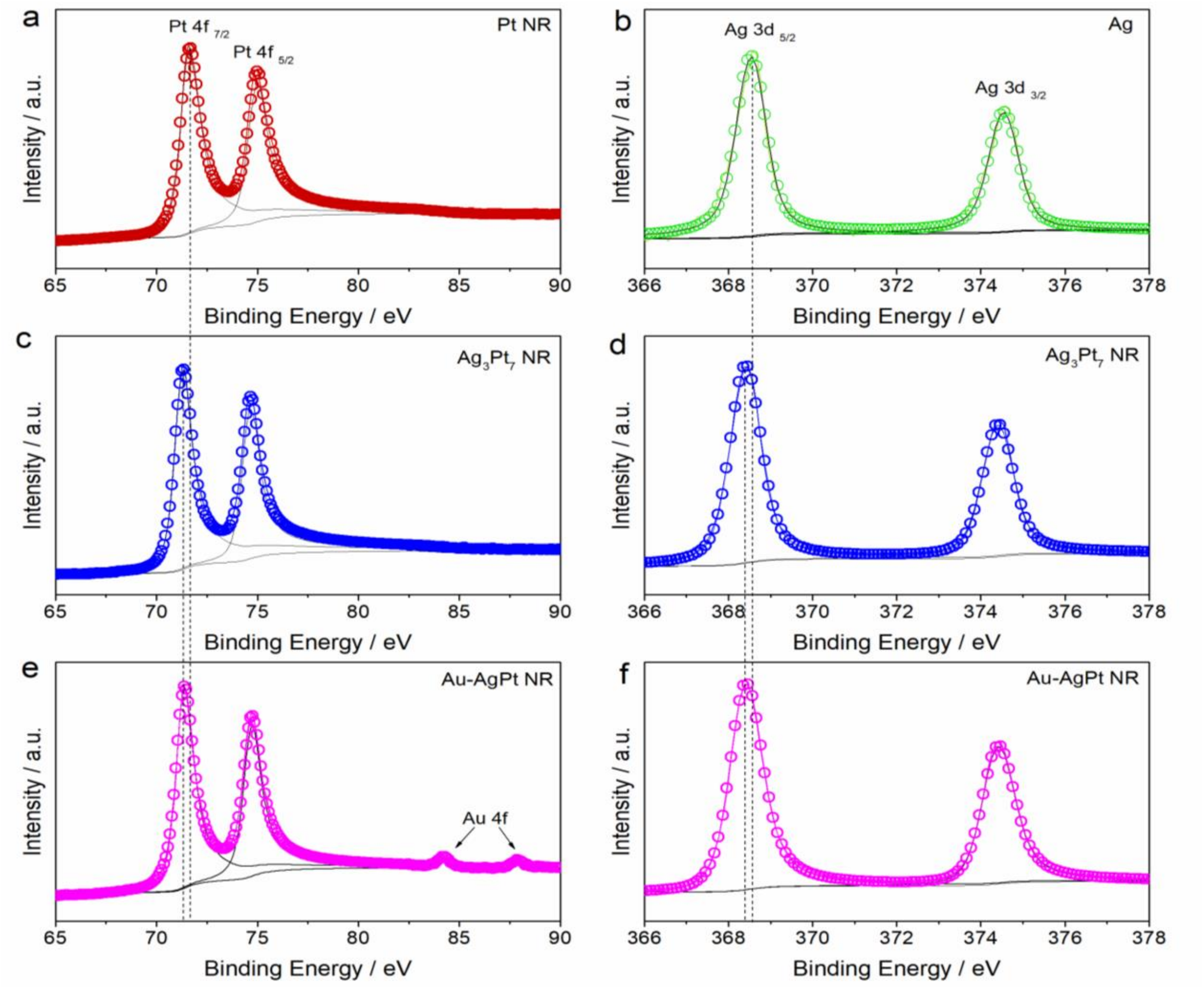

Figure 6.13 High-resolution XPS spectra of Pt 4f region for **(a)** the Pt NR GDE and **(b)** Ag 3d region of Ag grown on the GDL. Pt 4f and Ag 3d region of **(c-d)** the Ag_3Pt_7 NR GDE and **(e-f)** the Au-AgPt GDE.

6.4.2 MEA testing

The polarisation and power density curves recorded under H_2/Air are shown in Figure 6.14a. The power density trend of the GDEs at 0.6 V follows Au-AgPt NR > Pt NR > Ag_3Pt_7 NR. The peak power density of the Au-AgPt NR GDE reaches 0.61 W cm^{-2}, which is higher than that of the Pt NR GDE (0.58 W cm^{-2}) which contains ~20 wt% more of Pt loading. A relatively close charge transfer resistance obtained for all GDEs from EIS spectra recorded at the low current density (Figure 6.14b) agrees with the comparable OCV. However, the more significant reduced charge transfer resistance is observed for the Au-AgPt NR GDE at the medium voltage of 0.65 V compared to Ag_3Pt_7 NR (Figure 6.14c). It follows the polarisation curve trend showing a larger voltage drop for Ag_3Pt_7 NR GDE with the increasing current density (Figure 6.14a), which also confirms the improved intrinsic catalytic activity towards ORR because of the Au alloying effect. The positive impact becomes more pronounced at the low potential. The EIS recorded at 0.5 V shows the lowest impedance of the Au-AgPt NR GDE as a consequence of the much reduced mass transfer resistance, resulting from the good distribution and less aggregation of the NR catalysts formed on the GDL surface (Figure 6.10).

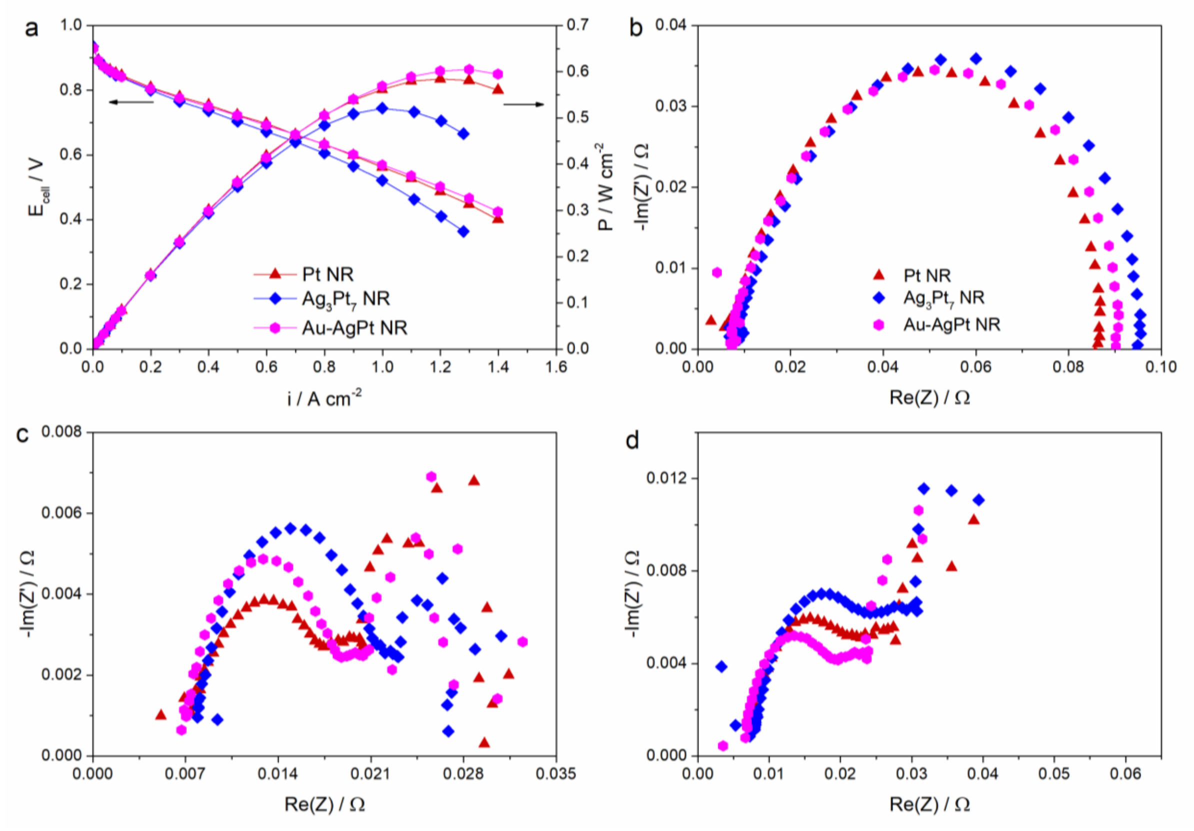

Figure 6.14 (a) MEA testing results of the Pt NR, Ag_3Pt_7 NR and Au-AgPt GDEs. The corresponding EIS spectra recorded at **(b)** 30 mA cm^{-2} **(c)** 0.65 V and **(d)** 0.5 V.

A very similar CV plot is recorded for the Au-AgPt NR GDE as compared to the Ag_3Pt_7 NR GDE (Figure 6.15). Normalised to the Pt loading the ECSA measured are 26.64, 17.20 and 17.35 m_{Pt}^2 g^{-1} for the Pt NR, Ag_3Pt_7 NR and Au-AgPt NR GDEs, respectively. A comparable ECSA of the AgPt NR GDE before and after the Au alloying indicates a similar number of active sites regardless the higher Pt deposition on the catalyst surface with the Au-AgPt NR GDE as presented by the XPS analysis results in Table 6.3. It is potentially related to the larger bulk size with the longer Au-AgPt NRs (cf. AgPt NRs). The effectiveness of replacing ~2 at% Ag with Au to tune the atomic arrangement rendering an increased current density at 0.9 V (Figure 6.16). It results in higher Pt mass and specific activities than those without Au (Table 6.4).

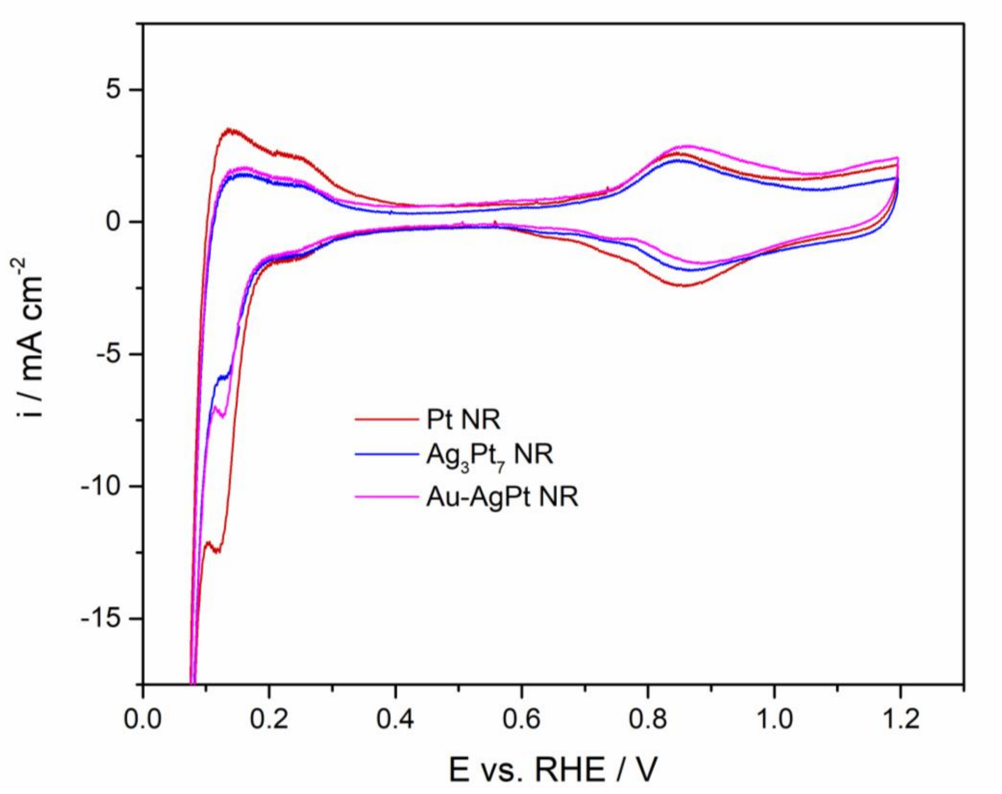

Figure 6.15 CVs of the Pt NR, Ag_1Pt_4 NR and Au-AgPt NR GDEs.

Table 6.4 Catalytic activities of the GDEs in the MEA test.

GDE	ECSA / m g_{pt}^{-1}	I_m / A mg_{Pt}^{-1}	I_s / µA cm^{-2}
Pt NR	26.64	0.072	316.59
Ag_3Pt_7 NR	17.20	0.064	372.69
Au-AgPt NR	17.35	0.080	460.97

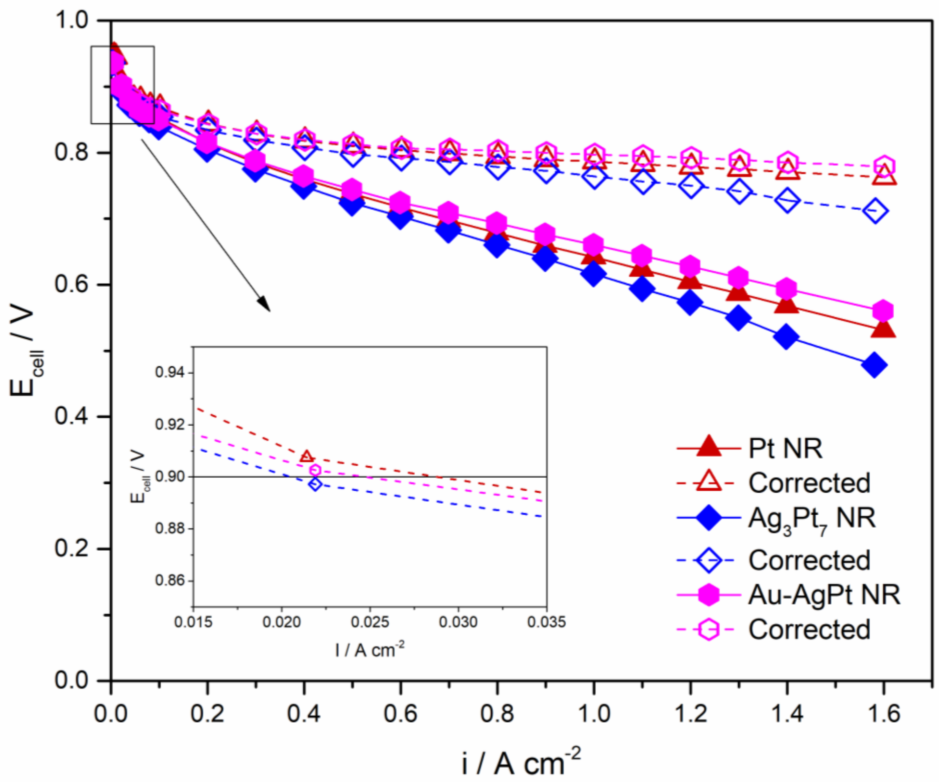

Figure 6.16 Original and corrected polarisation curves of Pt NR, Ag_3Pt_7 NR and Au-AgPt NR GDEs.

These achievements demonstrate a promising attempt of a preliminary study on the Au integration to optimise the atomic arrangement of Pt and its alloy for growing NR GDEs. The Au content may be adjusted depending on the atomic ratio of Ag and Pt. For instance, for the Ag-AgPt NR/C catalysts in Chapter 5, a higher Au content of 5 at% showed more significant improvement than 2 at% Au, which rationally ascribed to the higher Ag ratio of above 40 at%. In this section, the lower Ag ratio of ~30 at% is applied, thus with a lower Au content of 2 at%, it provides a large positive impact on the catalytic performance. Further evaluation on influences of the Au content towards the catalytic activity of the AgPt NR GDE with various atomic ratios can be conducted in future to obtain the optimum composition (i.e. minimise Pt and maximise the Ag loading), which is reasonable for the economic perspective.

6.5 Accelerated degradation test (ADT)

To evaluate the durability of the GDEs made of the 1D Pt and Pt hybrid NRs, the ADT was performed in single-cell PEMFCs benchmarking to the Pt/C NP catalyst. The ADT was conducted with 5000 potential cycles between 0.6 – 1.2 V at a sweep rate of 100 mV s^{-1} under the N_2-saturated cathode. As shown in Figure 6.17, the performance loss of the support-free GDEs is lower than that of the Pt/C GDE, assigning to the better resistance towards the degradation in PEMFC operating conditions. The power decline of the 1D Pt-based GDE becomes larger with the higher Ag content following a trend of Ag_3Pt_7 > Ag_1Pt_9 NR > Pt NR. This suggests a higher degree of dissolution with the higher Ag content, which is potentially related to the segregation of Ag as previously observed in Chapter 4. Nevertheless, such loss is prevented with the integration of 2 at% Au leading to the highest power output and lowest decline of 37.09% after the ADT. It is much lower than that of the monometallic Pt NR GDE (43.62%), which further signifies the positive contribution of the Au alloying towards the electrode durability.

The minimum power density decline of the Au-AgPt NR GDE is related to the least ECSA loss, as presented in Figure 6.18. The trend of decreased H_{des} area from the CVs is in agreement with the decline of the power performance output (Figure 6.17), suggesting the surface area loss as the main contributing factor to the poor ORR activity after the ADT. The larger ECSA decline with the higher Ag loading is related to the stability of Ag in acidic media [198]. The ECSA loss of the Ag_3Pt_7 NR GDE after the ADT is minimised of up to ~14% with the presence of Au. This finding further suggests the stabilisation effect of Au in minimising the atomic segregation and surface oxidation during the potential cycling.

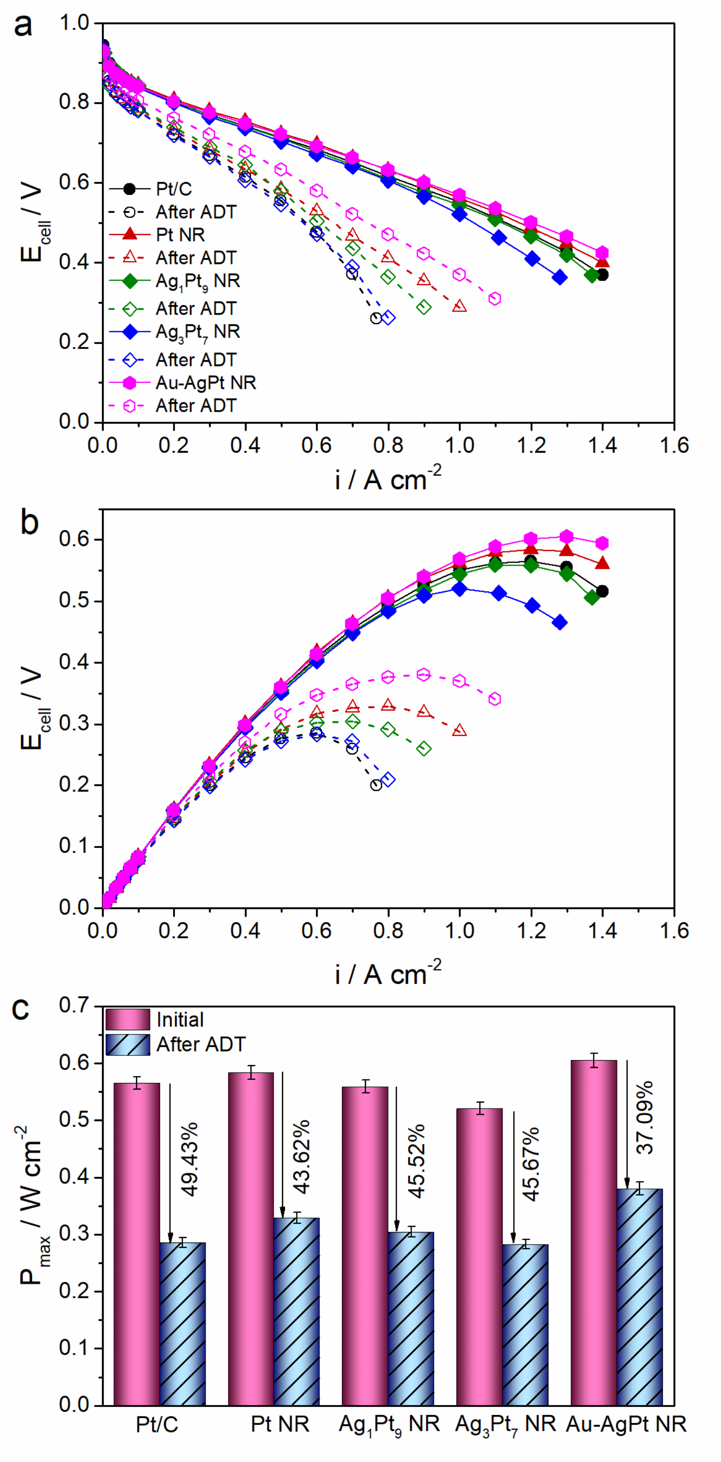

Figure 6.17 Comparison of **(a)** polarisation and **(b)** power density curves, and **(c)** the corresponding power density declines after the ADT recorded for the MEAs made from different catalysts.

The ECSA loss of Pt NR GDE is 47.14% compared to 78.99% of Pt/C (Figure 6.18), which is mainly ascribed to the anisotropic 1D nanostructure and carbon support-free GDE feature. The better stability of 1D Pt NR/C over 0D Pt/C has been evaluated in the previous chapters, confirming the superiority of 1D nanostructure to maintain durability in fuel cell operation. Furthermore, after the elimination of the carbon support, the ECSA loss is better suppressed, reducing the ECSA loss by ~5% for the Pt NR GDE compared to Pt NR/C (Figure 4.16, Chapter 4). Similarly, with the same Au loading, the decline of the Au-AgPt NR GDE is much lower compared to 2 at% Au-AgPt NR/C (Chapter 5), exhibiting less power performance and ECSA decrease by 10.49% and 8.85%, respectively. The lower Ag content may also contribute to the better durability of the Au-AgPt NR GDE. Nevertheless, these findings indicate a successful approach to combine the advances of 1D Pt hybrid nanostructures and eliminating carbon support at the same time.

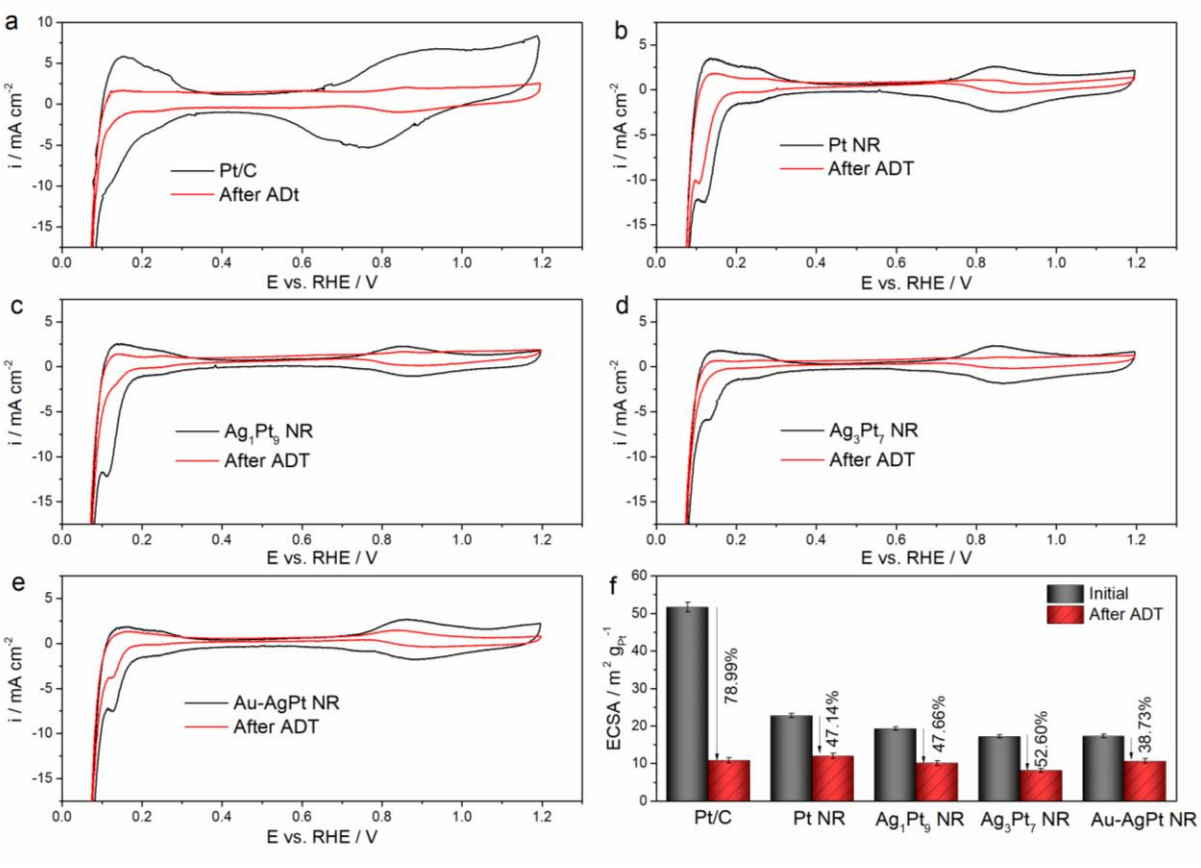

Figure 6.18 Comparison of CVs and the corresponding ECSA decline after the ADT for the Pt/C, Pt NR, a varied ratio of AgPt NR and Au-AgPt NR GDEs.

Although a successful approach to improve the durability of ORR electrodes has been achieved through the development of the 1D NR GDEs, the power performance is compromised in the absence of the carbon support, partially with the integration of Ag. The hydrophobicity of the GDL requires high-temperature reaction (i.e. 40 °C) to facilitate better catalyst nucleation and distribution of the catalysts. However, it leads to a faster kinetic reaction changing the alloying behaviour of Ag and Pt as observed by the XRD analysis results in Figure 6.6. This phenomenon affects the catalytic performance of the AgPt alloy GDE towards ORR, which is also induced by the decreased ECSA. The alloying of Au has successfully controlled the kinetic reaction and adjusted a better atomic arrangement and alloying degree to optimise the active site number of the catalyst. This approach has demonstrated an efficient strategy to control the atomic arrangement via a facile route of one-step wet-chemical reduction method. Although the ORR activity has successfully improved with the presence of Au, the optimum mass activity achieved for the Au-AgPt NR GDE is still lower than that of 5 at% Au-AgPt NR/C (Chapter 5). Therefore, further efforts to adjust the Au content toward the Ag and Pt ratio are required to optimise the ECSA. The integration of 50 at% Ag (Ag_1Pt_1 NR GDE) has shown effectively minimising the aggregated 3D cubic like structures and expanding the ECSA. If the formation of the Ag metal phase can be suppressed, i.e. through a higher Au content, a further enhanced ORR activity may be achieved.

6.6 Conclusions

In this chapter, the development of the AgPt NR GDE has been briefly demonstrated via the formic acid reduction method. The reaction temperature of 40 °C is considered as an ideal parameter to optimise the growth of the AgPt NRs on the GDL surface. Shortening the interval time (ca. 3 hours) of mixing the metal precursors has been shown as an effective method to improve the 1D morphology and increase the alloying degree of the AgPt NR. However, the formation of Ag and Pt alloy structure occurs less harmonious at the high temperature of 40

°C, limiting the formation of a uniform alloy structure, especially at the higher Ag ratio. Increasing the Ag content of up to 50 at% results in the higher Ag metallic phase, suggesting the formation of Ag grains dominating the catalyst surface. This is supported by the decreasing ECSA in the presence of Ag, leading to a poorer catalytic performance at the higher Ag content. The alloying of 2 at% Au has successfully controlled the kinetic reaction rate and led to a better atomic arrangement to optimise the number of active sites on the catalyst surface. As a result, an improved mass activity of 0.080 A mg_{Pt}^{-2} is achieved, which is 1.12 and 1.26-fold higher than that of the Pt NR GDE and Ag_3Pt_7 NR GDE (containing a similar atomic ratio of Ag and Pt), respectively. The durability improvement is also observed for the Au-AgPt NR GDE, which is contributed from the lower ECSA loss (by up to 14%) with the presence of 2 at% Au. These outcomes demonstrate a successful approach to combine the advanced 1D nanostructures and eliminating the carbon support to develop high power performance and durable GDEs.

Chapter 7

Conclusions and Perspective

This thesis focuses on the development of high performance and durable catalyst electrodes for proton exchange membrane fuel cells (PEMFCs) through the hybridisation of one-dimensional (1D) Pt nanostructures. The approach involved the alloying with Ag and Au owning a close lattice constant to Pt, minimising the metal segregation issues for achieving high stability. The fundamental concepts to construct 1D Pt hybrid nanostructures via the formic acid reduction method were comprehensively investigated to understand the reduction of the metal ions and 1D nanorod (NR) growth. This approach provided a highly scalable synthesis solution and translated to fabricating gas diffusion electrodes (GDEs) through directly growing NR arrays on the gas diffusion layer (GDL) surface.

The growth mechanism of AgPt NRs on carbon support - The process for growing 1D AgPt NRs on carbon support using the formic acid reduction method was explored in Chapter 4. The method utilised a slow kinetic reaction at room temperature and preferential adsorption of formic acid species on certain Pt crystal facets leading to the growth of NRs along the <111> direction. TEM analysis revealed the importance of applying interval time of ca. 5 hours in introducing Ag ions to achieve uniform 1D AgPt nanostructures. In the formic acid reduction process, Pt works not only as a size control role in Ag reduction, but also providing shape inducing effect leading the growth to form single-crystal AgPt alloy NRs. The atomic ratio of Ag to Pt (from 1:4 to 2:1) affected both the morphology and distribution of AgPt NRs on the carbon support. A higher Ag content induced a faster reduction reaction yielding shorter and less agglomerated NRs, which also delivered an enormous impact on their catalytic performance as cathode catalysts toward oxygen reduction reaction (ORR) in fuel cell operation.

Catalytic performance of AgPt NR/C in the MEA test - The optimum power performance was obtained in the membrane electrode assembly (MEA) test for the GDE made of the Ag_1Pt_1 NR/C catalyst. A peak power density of 0.55 W cm^{-2} was achieved, which was 1.14- and 1.16-

fold over that of the GDE made of the Pt/C and Pt NR/C catalysts, respectively, with the same Pt loading of 0.2 mg_{Pt} cm^{-2}. This was mainly ascribed to the large electrochemical surface area (ECSA) of Ag_1Pt_1 NR/C resulting from the uniform and less aggregated shorter NRs. Moreover, the high electrical conductivity of Ag also contributed to the power performance improvement, which was boosted after 2 hours of heat treatment at 120 °C. The untreated Ag_1Pt_1 NR/C catalyst possessed a similar structure and catalytic activity as of Ag_1Pt_1 NR/C. However, mass transfer resistance was slightly decreased after the heat treatment improving the power output at a high current density region.

Durability issue - Despite the close lattice constant between Ag and Pt, the atomic segregation and dissolution of Ag were unavoidable in the severe acidic environment in PEMFC operation. After the ADT, the GDE made of the Ag_1Pt_1 NR/C catalyst showed a large ECSA drop. Severe redeposition of Ag is also observed at the interface between the cathode and polymer electrolyte membrane. These degradation mechanisms finally resulted in a huge power performance decline rate.

Au integration effect toward AgPt NR/C - Au was then introduced for the growth of Au-AgPt NRs on carbon support to suppress the metal segregation with AgPt NRs. As presented in Chapter 5, the introduction of Au ions at the early reaction stage, together with Pt is preferred to minimise Au deposition on the surface. With 5 at% Au included, longer NRs were formed with a high ratio of Pt deposition on the catalyst surface, and the ECSA was increased by 7% compared to AgPt NR/C determined by cathode cyclic voltammetry (CV) scan in the MEA test. The GDE made of 5 at% Au-AgPt NR/C catalyst showed 1.15- and 1.70-fold higher ORR mass activity than that of AgPt NR/C and Pt/C, respectively. 1.12-fold power density versus that of AgPt NR/C as the cathode catalyst was demonstrated in the MEA test in H_2/Air PEMFCs. The enhanced ORR performance is mainly derived from the superior intrinsic properties of the catalyst induced by the architect of the single-crystal 1D nanostructure and alloy composition. Applying a higher Au content (8-12 at%) resulted in a decreased ECSA, caused by the severer agglomeration of the NRs and the higher Au deposition on the catalyst surface blocking the number of the active sites. Consequently, it leads to decreased power performance.

The enhancement of the Au-AgPt NR/C catalyst is more significant toward its stability in fuel cell operation. The degradation decreases with the increasing Au content, and the power density decline is only 39.17% at 8 at% Au after the ADT, which is lower than that of monometallic Pt NR/C (41.41%) and Pt/C (44.19%). Such achievement is related to the less surface area loss prevented by the alloying with Au. Considering a good balance between the catalytic activities and stability, the optimum Au content was determined at 5 at%.

Transferring the growth of 1D Pt hybrid NRs on the GDL - Finally, the growth of Pt and Ag was transferred directly onto the GDL substrate to develop the advanced support-free 1D AgPt-based NR array GDE. This approach was firstly attempted to eliminate the degradation mechanism contributed by the carbon support. Secondly, the direct growth of AgPt NRs on GDLs offers a thinner, highly porous catalyst layer, which facilitates an efficient gas transfer for a reduced mass transport resistance. A moderate reaction temperature of 40 °C was applied to grow AgPt NRs on the GDL surface. While shortening the interval time (ca. 3 hours) of adding Ag ions was adjusted to improve the alloying degree of AgPt NRs and their distribution on the GDL surface. A comparable power density at 0.6 V was recorded for the Ag_3Pt_7 NR GDE as that of the Pt/C GDE. However, the high reaction temperature at 40 °C results in a poor alloying degree between Ag and Pt, thus a large ratio of the Ag metallic phase is detected at 50 at% Ag content (Ag_1Pt_1 NR GDE). As a consequence, a low ORR activity was recorded under the MEA test.

The introduction of ~2 at% Au into Ag_3Pt_7 NRs GDE to develop Au-AgPt NR GDE is a game-changing approach. It led to harmonised alloying of all metals and inducing a high degree deposition of Pt by 22 at% on the NR catalyst surface of Au-AgPt NR GDE than that of the Ag_3Pt_7 NR GDE. Hence, 1.25-fold improved ORR activity was generated. The MEA test in H_2/Air recorded an enhanced peak power density of 0.61 W cm^{-2}, surpassing the Pt NR and Pt/C GDEs containing a higher Pt loading (20 wt% more). Furthermore, the MEA with the Au-AgPt NR GDE demonstrated significantly improved durability, losing only 37.09% of the peak power density after 5000 potential cycles, which is the least power decline recorded in this work after the ADT. It is attributed to the effectiveness of the Au alloying to prevent the ECSA loss, which is ~8 and ~14% less than that of the monometallic Pt NR and Ag_3Pt_7 NR GDE, respectively.

Limitations of the support-free Pt hybrid NRs array GDE feature – The optimum catalyst density on the GDL surface is a key to achieve a high power performance electrode, which limits the Pt NRs loading of 0.4 - 0.5 mg cm^{-2} [140]. Reducing Pt amount is possible via hybridisation with the other metal. However, reaching the DoE target of 0.125 mg_{pt} for both anode and cathode is a huge challenge, considering the optimum Pt reduction achieved in this work was only ~35 wt% by replacing it with Ag and Au. Generally, the Pt hybrid NR/C GDEs with a lower Pt content possessed a better ORR activity than of support-free Pt hybrid NR array GDEs (Table 7.1), which can be ascribed to the larger surface area provided by carbon support. Thus, the limitation of support-free Pt hybrid NR array GDE should further be addressed either by modification of GDL surface or employing an alternative support material owning high surface area and good stability.

Perspective - Compared to the GDEs made of the 1D NR/C catalysts, the ECSA losses during the ADT is significantly improved for the support-free 1D NR array GDEs with the Au alloyed NRs (Table 7.1). These results demonstrate an efficient strategy for the fabrication of highly active and durable electrodes by developing 1D Pt hybrid NR array GDEs. There are a few propositions to advance the development of 1D Pt hybrid NR array GDEs for the future:

1. The effect of Au alloying may vary depending on the ratio of Ag and Pt with the Au-AgPt NRs. Demonstrated in Chapter 5 that the optimum activity enhancement was achieved with 5 at% Au-AgPt NR/C, reaching a 1.34 fold higher mass activity than the 2 at% Au-AgPt NR GDE. Therefore, further effort to tuning the Au content based on various Ag and Pt ratios is important to extend the ECSA and ORR activities of the 1D Pt hybrid NR array GDE.
2. The Au-AgPt NR GDE has effectively reduced the usage of Pt by 20 wt% compared to the Pt NR GDE (0.4 mg_{pt} cm^{-2}). However, it is still considered too high in regard to the-state-of-the-art catalyst loading to meet the DoE target of 0.125 mg_{pt} cm^{-2} in PEMFCs. Surface functionalisation step should further be conducted to the GDL substrate, e.g. acid treatment or plasma nitriding [143] to increase the catalyst utilisation ratio and further reduce the catalyst loading.
3. The alloying of Au has been shown as an effective approach to improve the stability of 1D AgPt nanostructures, further Au integration with other catalysts in 1D Pt hybrid GDEs (e.g. PtNi) potentially induce a stabilisation effect and minimise segregation as of observed from the 1D PtNi GDE in operating PEMFCs [212].
4. The growing method applied in this thesis has shown transferable to be adapted in different media (e.g. from the carbon support to the GDL). Employing other support material such as carbon nanotubes can be a promising future work according to our previous study [194].

This thesis has shown a comprehensive study to establish a scalable method to fabricate 1D AgPt NRs. Such an approach is adaptable to integrate other potential alloyed metals, e.g. Ni and Co, into 1D Pt hybrid nanostructures, followed by fully leaching the transitional metals to prepare ultrafine jagged Pt nanorods [31]. This will be a highly scalable approach for preparing extremely active and stable catalysts for practical applications in next-generation PEMFCs.

Table 7.1 Resume of catalytic activities and stability of the GDEs in the MEA test

Catalyst - GDE	Pt loading / mg_{Pt} cm^{-2}	ECSA / m^2 g_{Pt}^{-1}	ORR Performance / W cm^{-2}		ORR activities		Stability (loss) / %	
			P at 0.6 V	P maximum	I_m / A mg_{Pt}^{-1}	I_s / μA cm^{-2}	P maximum	ECSA
Pt/C (TKK)	0.20	50.67	0.42	0.48	0.065	130.29	44.19	76.61
Pt NR/C	0.20	14.68	0.42	0.47	0.080	544.91	41.41	52.04
Ag_1Pt_1 NR/C	0.20	24.26	0.48	0.55	0.098	391.63	46.32	62.03
Ag_1Pt_1 NR/C (no treatment)	0.20	24.17	0.44	0.52	0.095	378.57	49.71	62.12
Au-AgPt NR/C A 2%	0.20	24.47	0.48	0.53	0.098	402.25	47.58	58.94
Au-AgPt NR/C A 5%	0.20	25.98	0.52	0.58	0.110	425.22	39.63	51.2
Au-AgPt NR/C A 8%	0.20	21.37	0.45	0.5	0.090	420.80	39.17	47.59
Au-AgPt NR/C B 5%	0.20	21.73	0.34	0.41	0.050	204.76	-	-
Pt/C (TKK)	0.40	51.71	0.49	0.57	0.064	122.83	49.43	78.99
Pt NR	0.40	26.64	0.54	0.58	0.072	316.59	43.62	47.14
Ag_1Pt_9 NR	0.37	19.32	0.49	0.56	0.070	361.13	45.52	47.66
Ag_1Pt_4 NR	0.34	16.52	0.49	0.53	0.066	397.65	-	-
Ag_3Pt_7 NR	0.32	17.20	0.49	0.52	0.064	372.69	45.67	52.60
Ag_1Pt_1 NR	0.25	19.12	0.36	0.41	0.066	346.02	45.90	51.14
Au-AgPt NR	0.32	17.35	0.54	0.61	0.080	460.97	37.09	38.73

References

[1] B.A. Jafino, P. Soltani, E. Pruyt, Saving Lives and Time: Tackling Transportation Induced Air Pollution in Jakarta, in: Conf. 34th Int. Conf. Syst. Dyn. Soc., 2016.

[2] B. Michael Greenstone, Q. Fan, Indonesia's Worsening Air Quality and its Impact on Life Expectancy, 2019. https://aqli.epic.uchicago.edu/wp-content/uploads/2019/03/Indonesia-Report.pdf.

[3] K. Donaldson, A. Hunter, C. Poland, S. Smith, Toxicology, Survival and Health Hazards of Combustion Products, Royal Society of Chemistry, Cambridge, 2015. https://doi.org/10.1039/9781849737487.

[4] IQAir, Jakarta Air Quality Index (AQI) and Indonesia Air Pollution | AirVisual, (2020). https://www.iqair.com/us/indonesia/jakarta.

[5] The Paris Agreement | UNFCCC, (2015). https://unfccc.int/process-and-meetings/the-paris-agreement/the-paris-agreement.

[6] J. Larminie, A. Dicks, Fuel cell systems explained, 2003.

[7] Y. Wang, K.S. Chen, J. Mishler, S.C. Cho, X.C. Adroher, A review of polymer electrolyte membrane fuel cells: Technology, applications, and needs on fundamental research, Appl. Energy. 88 (2011) 981–1007. https://doi.org/10.1016/j.apenergy.2010.09.030.

[8] L. Andaloro, A. Arista, G. Agnello, G. Napoli, F. Sergi, V. Antonucci, Study and design of a hybrid electric vehicle (Lithium Batteries-PEM FC), Int. J. Hydrogen

Energy. 42 (2017) 3166–3184. https://doi.org/10.1016/j.ijhydene.2016.12.082.

[9] T. Hua, R. Ahluwalia, L. Eudy, G. Singer, B. Jermer, N. Asselin-Miller, S. Wessel, T. Patterson, J. Marcinkoski, Status of hydrogen fuel cell electric buses worldwide, J. Power Sources. 269 (2014) 975–993. https://doi.org/10.1016/j.jpowsour.2014.06.055.

[10] N. Pocard, Fuel Cell Price to Drop 70-80% as Production Volume Scales, (2020). https://blog.ballard.com/fuel-cell-price-drop.

[11] P. Mardle, S. Du, Materials for PEMFC Electrodes, in: Ref. Modul. Mater. Sci. Mater. Eng., Elsevier, 2017. https://doi.org/10.1016/b978-0-12-803581-8.09260-2.

[12] DoE, Fuel cell technologies office multiyear research, development and demonstration plan, 2016. https://doi.org/Department of Energy.

[13] M.A. Khan, B. Sundén, J. Yuan, Analysis of multi-phase transport phenomena with catalyst reactions in polymer electrolyte membrane fuel cells - A review, J. Power Sources. 196 (2011) 7899–7916. https://doi.org/10.1016/j.jpowsour.2011.04.040.

[14] T. Yoshida, K. Kojima, Toyota MIRAI fuel cell vehicle and progress toward a future hydrogen society, Electrochem. Soc. Interface. 24 (2015) 45–49. https://doi.org/10.1149/2.F03152if.

[15] F. Barbir, PEM Fuel Cells : Theory and Practice, Elsevier, 2013.

[16] S.A. Vilekar, R. Datta, The effect of hydrogen crossover on open-circuit voltage in polymer electrolyte membrane fuel cells, J. Power Sources. 195 (2010) 2241–2247. https://doi.org/10.1016/j.jpowsour.2009.10.023.

[17] DoE, Fuel Cell Technologies Market Report 2016, (2016). https://www.energy.gov/sites/prod/files/2017/10/f37/fcto_2016_market_report.pdf.

[18] DoE, Compare Fuel Cell Vehicles, (2020). https://www.fueleconomy.gov/feg/fcv_sbs.shtml.

[19] Europe’s Largest Hybrid Fuel Cell Bus Fleet and First Hydrogen Infrastructure for Public Transport Unveiled - FuelCellsWorks, (2020). https://fuelcellsworks.com/news/europes-largest-hybrid-fuel-cell-bus-fleet-and-first-hydrogen-infrastructure-for-public-transport-unveiled/.

[20] Japan expected to have 80 hydrogen buses | News | gasworld, (2020). https://www.gasworld.com/japan-expected-to-have-80-hydrogen-buses-/2018319.article.

[21] I. Staffell, D. Scamman, A. Velazquez Abad, P. Balcombe, P.E. Dodds, P. Ekins, N. Shah, K.R. Ward, The role of hydrogen and fuel cells in the global energy system, Energy Environ. Sci. 12 (2019) 463–491. https://doi.org/10.1039/c8ee01157e.

[22] A. Kongkanand, M.F. Mathias, The Priority and Challenge of High-Power Performance of Low-Platinum Proton-Exchange Membrane Fuel Cells, J. Phys. Chem. Lett. 7 (2016) 1127–1137. https://doi.org/10.1021/acs.jpclett.6b00216.

[23] A. Wilson, G. Kleen, D. Papageorgopoulos, R. Ahluwalia, B. James, C. Houchins, J. Huya-Kouadio, DOE Hydrogen and Fuel Cells Program Record Title: Fuel Cell System Cost-2017 Originator, 2017.

[24] J.C. Meier, C. Galeano, I. Katsounaros, J. Witte, H.J. Bongard, A.A. Topalov, C. Baldizzone, S. Mezzavilla, F. Schüth, K.J.J. Mayrhofer, Design criteria for stable Pt/C fuel cell catalysts, Beilstein J. Nanotechnol. 5 (2014) 44–67. https://doi.org/10.3762/bjnano.5.5.

[25] D. Banham, S. Ye, K. Pei, J.I. Ozaki, T. Kishimoto, Y. Imashiro, A review of the

stability and durability of non-precious metal catalysts for the oxygen reduction reaction in proton exchange membrane fuel cells, J. Power Sources. 285 (2015) 334–348. https://doi.org/10.1016/j.jpowsour.2015.03.047.

[26] S. Chen, H.A. Gasteiger, K. Hayakawa, T. Tada, Y. Shao-Horn, Platinum-Alloy Cathode Catalyst Degradation in Proton Exchange Membrane Fuel Cells: Nanometer-Scale Compositional and Morphological Changes, J. Electrochem. Soc. 157 (2010) A82. https://doi.org/10.1149/1.3258275.

[27] L. Dubau, M. Lopez-Haro, L. Castanheira, J. Durst, M. Chatenet, P. Bayle-Guillemaud, L. Guétaz, N. Caqué, E. Rossinot, F. Maillard, Probing the structure, the composition and the ORR activity of Pt3Co/C nanocrystallites during a 3422h PEMFC ageing test, Appl. Catal. B Environ. 142–143 (2013) 801–808. https://doi.org/10.1016/j.apcatb.2013.06.011.

[28] C. Chen, Y. Kang, Z. Huo, Z. Zhu, W. Huang, H.L. Xin, J.D. Snyder, D. Li, J.A. Herron, M. Mavrikakis, M. Chi, K.L. More, Y. Li, N.M. Markovic, G.A. Somorjai, P. Yang, V.R. Stamenkovic, Highly crystalline multimetallic nanoframes with three-dimensional electrocatalytic surfaces, Science (80-.). 343 (2014) 1339–1343. https://doi.org/10.1126/science.1249061.

[29] X. Huang, Z. Zhao, L. Cao, Y. Chen, E. Zhu, Z. Lin, M. Li, A. Yan, A. Zettl, Y.M. Wang, X. Duan, T. Mueller, Y. Huang, High-performance transition metal-doped Pt3Ni octahedra for oxygen reduction reaction, Science (80-.). 348 (2015) 1230–1234. https://doi.org/10.1126/science.aaa8765.

[30] J. Zhang, K. Sasaki, E. Sutter, R.R. Adzic, Stabilization of platinum oxygen-reduction electrocatalysts using gold clusters, Science (80-.). 315 (2007) 220–222.

https://doi.org/10.1126/science.1134569.

[31] M. Li, Z. Zhao, T. Cheng, A. Fortunelli, C.Y. Chen, R. Yu, Q. Zhang, L. Gu, B. V. Merinov, Z. Lin, E. Zhu, T. Yu, Q. Jia, J. Guo, L. Zhang, W.A. Goddard, Y. Huang, X. Duan, Ultrafine jagged platinum nanowires enable ultrahigh mass activity for the oxygen reduction reaction, Science (80-.). 354 (2016) 1414–1419. https://doi.org/10.1126/science.aaf9050.

[32] L. Chong, J. Wen, J. Kubal, F.G. Sen, J. Zou, J. Greeley, M. Chan, H. Barkholtz, W. Ding, D.J. Liu, Ultralow-loading platinum-cobalt fuel cell catalysts derived from imidazolate frameworks, Science (80-.). 362 (2018) 1276–1281. https://doi.org/10.1126/science.aau0630.

[33] Y. Xia, P. Yang, Y. Sun, Y. Wu, B. Mayers, B. Gates, Y. Yin, F. Kim, H. Yan, One-dimensional nanostructures: Synthesis, characterization, and applications, Adv. Mater. 15 (2003) 353–389. https://doi.org/10.1002/adma.200390087.

[34] L. Cademartiri, G.A. Ozin, Ultrathin Nanowires—A Materials Chemistry Perspective, Adv. Mater. 21 (2009) 1013–1020. https://doi.org/10.1002/adma.200801836.

[35] Y. Lu, S. Du, R. Steinberger-Wilckens, One-dimensional nanostructured electrocatalysts for polymer electrolyte membrane fuel cells—A review, Appl. Catal. B Environ. 199 (2016) 292–314. https://doi.org/10.1016/j.apcatb.2016.06.022.

[36] G.E. Ramírez-Caballero, Y. Ma, R. Callejas-Tovar, P.B. Balbuena, Surface segregation and stability of core-shell alloy catalysts for oxygen reduction in acid medium, Phys. Chem. Chem. Phys. 12 (2010) 2209–2218. https://doi.org/10.1039/b917899f.

[37] C. Song, J. Zhang, Electrocatalytic oxygen reduction reaction, PEM Fuel Cell

Electrocatal. Catal. Layers. (2008).

[38] M. Shao, P. Liu, R.R. Adzic, Superoxide Anion is the Intermediate in the Oxygen Reduction Reaction on Platinum Electrodes, J. Am. Chem. Soc. 128 (2006) 7408–7409. https://doi.org/10.1021/ja061246s.

[39] H.S. Wroblowa, Yen-Chi-Pan, G. Razumney, Electroreduction of oxygen. A new mechanistic criterion, J. Electroanal. Chem. 69 (1976) 195–201. https://doi.org/10.1016/S0022-0728(76)80250-1.

[40] I. Katsounaros, S. Cherevko, A.R. Zeradjanin, K.J.J. Mayrhofer, Oxygen Electrochemistry as a Cornerstone for Sustainable Energy Conversion, Angew. Chemie Int. Ed. 53 (2014) 102–121. https://doi.org/10.1002/anie.201306588.

[41] R. Borup, J. Meyers, B. Pivovar, Y.S. Kim, R. Mukundan, N. Garland, D. Myers, M. Wilson, F. Garzon, D. Wood, P. Zelenay, K. More, K. Stroh, T. Zawodzinski, J. Boncella, J.E. McGrath, M. Inaba, K. Miyatake, M. Hori, K. Ota, Z. Ogumi, S. Miyata, A. Nishikata, Z. Siroma, Y. Uchimoto, K. Yasuda, K.I. Kimijima, N. Iwashita, Scientific aspects of polymer electrolyte fuel cell durability and degradation, Chem. Rev. 107 (2007) 3904–3951. https://doi.org/10.1021/cr050182l.

[42] I. Morcos, E. Yeager, Kinetic studies of the oxygen-peroxide couple on pyrolytic graphite, Electrochim. Acta. 15 (1970) 953–975. https://doi.org/10.1016/0013-4686(70)80037-8.

[43] J.K. Nørskov, J. Rossmeisl, A. Logadottir, L. Lindqvist, J.R. Kitchin, T. Bligaard, H. Jónsson, Origin of the overpotential for oxygen reduction at a fuel-cell cathode, J. Phys. Chem. B. 108 (2004) 17886–17892. https://doi.org/10.1021/jp047349j.

[44] N. Jung, D.Y. Chung, J. Ryu, S.J. Yoo, Y.E. Sung, Pt-based nanoarchitecture and

catalyst design for fuel cell applications, Nano Today. 9 (2014) 433–456. https://doi.org/10.1016/j.nantod.2014.06.006.

[45] N.M. Marković, T.J. Schmidt, V. Stamenković, P.N. Ross, Oxygen Reduction Reaction on Pt and Pt Bimetallic Surfaces: A Selective Review, Fuel Cells. 1 (2001) 105–116. https://doi.org/10.1002/1615-6854(200107)1:2<105::AID-FUCE105>3.0.CO;2-9.

[46] V. Viswanathan, H.A. Hansen, J. Rossmeisl, J.K. Nørskov, Universality in oxygen reduction electrocatalysis on metal surfaces, ACS Catal. 2 (2012) 1654–1660. https://doi.org/10.1021/cs300227s.

[47] V. Stamenkovic, B.S. Mun, K.J.J. Mayrhofer, P.N. Ross, N.M. Markovic, J. Rossmeisl, J. Greeley, J.K. Nørskov, Changing the activity of electrocatalysts for oxygen reduction by tuning the surface electronic structure., Angew. Chem. Int. Ed. Engl. 45 (2006) 2897–901. https://doi.org/10.1002/anie.200504386.

[48] Y.J. Wang, N. Zhao, B. Fang, H. Li, X.T. Bi, H. Wang, Carbon-Supported Pt-Based Alloy Electrocatalysts for the Oxygen Reduction Reaction in Polymer Electrolyte Membrane Fuel Cells: Particle Size, Shape, and Composition Manipulation and Their Impact to Activity, Chem. Rev. 115 (2015) 3433–3467. https://doi.org/10.1021/cr500519c.

[49] M. Shao, Q. Chang, J.P. Dodelet, R. Chenitz, Recent Advances in Electrocatalysts for Oxygen Reduction Reaction, Chem. Rev. 116 (2016) 3594–3657. https://doi.org/10.1021/acs.chemrev.5b00462.

[50] I.E.L. Stephens, A.S. Bondarenko, U. Grønbjerg, J. Rossmeisl, I. Chorkendorff, Understanding the electrocatalysis of oxygen reduction on platinum and its alloys,

Energy Environ. Sci. 5 (2012) 6744–6762. https://doi.org/10.1039/c2ee03590a.

[51] Q. Jia, W. Liang, M.K. Bates, P. Mani, W. Lee, S. Mukerjee, Activity descriptor identification for oxygen reduction on platinum-based bimetallic nanoparticles: In situ observation of the linear composition-strain-activity relationship, ACS Nano. 9 (2015) 387–400. https://doi.org/10.1021/nn506721f.

[52] J.R. Kitchin, J.K. Nørskov, M.A. Barteau, J.G. Chen, Role of strain and ligand effects in the modification of the electronic and chemical Properties of bimetallic surfaces, Phys. Rev. Lett. 93 (2004) 156801. https://doi.org/10.1103/PhysRevLett.93.156801.

[53] A. Ruban, B. Hammer, P. Stoltze, H.L. Skriver, J.K. Nørskov, Surface electronic structure and reactivity of transition and noble metals, in: J. Mol. Catal. A Chem., Elsevier, 1997: pp. 421–429. https://doi.org/10.1016/S1381-1169(96)00348-2.

[54] M.T. Gorzkowski, A. Lewera, Probing the Limits of d-Band Center Theory: Electronic and Electrocatalytic Properties of Pd-Shell-Pt-Core Nanoparticles, J. Phys. Chem. C. 119 (2015) 18389–18395. https://doi.org/10.1021/acs.jpcc.5b05302.

[55] K. Kinoshita, Particle Size Effects for Oxygen Reduction on Highly Dispersed Platinum in Acid Electrolytes, J. Electrochem. Soc. 137 (1990) 845. https://doi.org/10.1149/1.2086566.

[56] M. Shao, A. Peles, K. Shoemaker, Electrocatalysis on platinum nanoparticles: Particle size effect on oxygen reduction reaction activity, Nano Lett. 11 (2011) 3714–3719. https://doi.org/10.1021/nl2017459.

[57] F.J. Perez-Alonso, D.N. McCarthy, A. Nierhoff, P. Hernandez-Fernandez, C. Strebel, I.E.L. Stephens, J.H. Nielsen, I. Chorkendorff, The effect of size on the oxygen electroreduction activity of mass-selected platinum nanoparticles, Angew. Chemie -

Int. Ed. 51 (2012) 4641–4643. https://doi.org/10.1002/anie.201200586.

[58] S.S. and N.M.M. Dongguo Li, Chao Wang, Dusan S. Strmcnik, Dusan V. Tripkovic, Xiaolian Sun, Yijin Kang, Miaofang Chi, Joshua, Snyder Dennis van der Vliet, Yifen Tsai, Vojislav R. Stamenkovic, Functional links between Pt single crystal morphology and nanoparticles with different size and shape: the oxygen reduction reaction case, Energy Environ. Sci. 7 (2014) 4061–4069. https://doi.org/10.1039/C4EE01564A.

[59] F. Calle-Vallejo, J. Tymoczko, V. Colic, Q.H. Vu, M.D. Pohl, K. Morgenstern, D. Loffreda, P. Sautet, W. Schuhmann, A.S. Bandarenka, Finding optimal surface sites on heterogeneous catalysts by counting nearest neighbors, Science (80-.). 350 (2015) 185–189. https://doi.org/10.1126/science.aab3501.

[60] M.K. Debe, Electrocatalyst approaches and challenges for automotive fuel cells, Nature. 486 (2012) 43–51. https://doi.org/10.1038/nature11115.

[61] D. Wang, H. ordered intermetallic platinum-cobalt core-shell nanoparticles with enhanced activity and stability as oxygen reduction electrocatalystsn L. Xin, R. Hovden, H. Wang, Y. Yu, D.A. Muller, F.J. Disalvo, H.D. Abruña, Structurally ordered intermetallic platinum-cobalt core-shell nanoparticles with enhanced activity and stability as oxygen reduction electrocatalysts, Nat. Mater. 12 (2013) 81–87. https://doi.org/10.1038/nmat3458.

[62] J. Greeley, I.E.L. Stephens, A.S. Bondarenko, T.P. Johansson, H.A. Hansen, T.F. Jaramillo, J. Rossmeisl, I. Chorkendorff, J.K. Nørskov, Alloys of platinum and early transition metals as oxygen reduction electrocatalysts, Nat. Chem. 1 (2009) 552–556. https://doi.org/10.1038/nchem.367.

[63] L. Bu, S. Guo, X. Zhang, X. Shen, D. Su, G. Lu, X. Zhu, J. Yao, J. Guo, X. Huang,

Surface engineering of hierarchical platinum-cobalt nanowires for efficient electrocatalysis, Nat. Commun. 7 (2016) 1–10. https://doi.org/10.1038/ncomms11850.

[64] X. Huang, E. Zhu, Y. Chen, Y. Li, C.Y. Chiu, Y. Xu, Z. Lin, X. Duan, Y. Huang, A facile strategy to Pt3Ni nanocrystals with highly porous features as an enhanced oxygen reduction reaction catalyst, Adv. Mater. 25 (2013) 2974–2979. https://doi.org/10.1002/adma.201205315.

[65] V.R. Stamenkovic, B. Fowler, B.S. Mun, G. Wang, P.N. Ross, C.A. Lucas, N.M. Markovic, Improved oxygen reduction activity on Pt3Ni(111) via increased surface site availability, Science (80-.). 315 (2007) 493–497. https://doi.org/10.1126/science.1135941.

[66] L. Bu, J. Ding, S. Guo, X. Zhang, D. Su, X. Zhu, J. Yao, J. Guo, G. Lu, X. Huang, A General Method for Multimetallic Platinum Alloy Nanowires as Highly Active and Stable Oxygen Reduction Catalysts, Adv. Mater. 27 (2015) 7204–7212. https://doi.org/10.1002/adma.201502725.

[67] Y.H. Chung, D.Y. Chung, N. Jung, H.Y. Park, Y.E. Sung, S.J. Yoo, Effect of surface composition of Pt-Fe nanoparticles for oxygen reduction reactions, Int. J. Hydrogen Energy. 39 (2014) 14751–14759. https://doi.org/10.1016/j.ijhydene.2014.07.097.

[68] D.Y. Chung, S.W. Jun, G. Yoon, S.G. Kwon, D.Y. Shin, P. Seo, J.M. Yoo, H. Shin, Y.H. Chung, H. Kim, B.S. Mun, K.S. Lee, N.S. Lee, S.J. Yoo, D.H. Lim, K. Kang, Y.E. Sung, T. Hyeon, Highly Durable and Active PtFe Nanocatalyst for Electrochemical Oxygen Reduction Reaction, J. Am. Chem. Soc. 137 (2015) 15478–15485. https://doi.org/10.1021/jacs.5b09653.

[69] C. Wang, D. Van Der Vliet, K.L. More, N.J. Zaluzec, S. Peng, S. Sun, H. Daimon, G.

Wang, J. Greeley, J. Pearson, A.P. Paulikas, G. Karapetrov, D. Strmcnik, N.M. Markovic, V.R. Stamenkovic, Multimetallic Au/FePt3 nanoparticles as highly durable electrocatalyst, Nano Lett. 11 (2011) 919–926. https://doi.org/10.1021/nl102369k.

[70] Y. Lu, S. Du, R. Steinberger-Wilckens, Three-dimensional catalyst electrodes based on PtPd nanodendrites for oxygen reduction reaction in PEFC applications, Appl. Catal. B Environ. 187 (2016) 108–114. https://doi.org/10.1016/j.apcatb.2016.01.019.

[71] B. Lim, M. Jiang, P.H.C. Camargo, E.C. Cho, J. Tao, X. Lu, Y. Zhu, Y. Xia, Pd-Pt bimetallic nanodendrites with high activity for oxygen reduction, Science (80-.). 324 (2009) 1302–1305. https://doi.org/10.1126/science.1170377.

[72] Z. Peng, H. Yang, Synthesis and oxygen reduction electrocatalytic property of Pt-on-Pd bimetallic heteronanostructures, J. Am. Chem. Soc. 131 (2009) 7542–7543. https://doi.org/10.1021/ja902256a.

[73] S. Il Choi, M. Shao, N. Lu, A. Ruditskiy, H.C. Peng, J. Park, S. Guerrero, J. Wang, M.J. Kim, Y. Xia, Synthesis and characterization of Pd@Pt-Ni core-shell octahedra with high activity toward oxygen reduction, ACS Nano. 8 (2014) 10363–10371. https://doi.org/10.1021/nn5036894.

[74] Y. Liang, S. Lin, C. Liu, S. Chung, T. Chen, J.-H. Wang, K. Wang, The performance and stability of the oxygen reduction reaction on Pt–M (M = Pd, Ag and Au) nanorods: an experimental and computational study, Chem. Commun. 51 (2015) 6605–6608. https://doi.org/10.1039/C5CC01629K.

[75] Y. Kang, J. Snyder, M. Chi, D. Li, K.L. More, N.M. Markovic, V.R. Stamenkovic, Multimetallic core/interlayer/shell nanostructures as advanced electrocatalysts, Nano Lett. 14 (2014) 6361–6367. https://doi.org/10.1021/nl5028205.

[76] K. Sasaki, H. Naohara, Y. Choi, Y. Cai, W.F. Chen, P. Liu, R.R. Adzic, Highly stable Pt monolayer on PdAu nanoparticle electrocatalysts for the oxygen reduction reaction, Nat. Commun. 3 (2012). https://doi.org/10.1038/ncomms2124.

[77] A. Esfandiari, M. Kazemeini, D. Bastani, Synthesis, characterization and performance determination of an Ag@Pt/C electrocatalyst for the ORR in a PEM fuel cell, Int. J. Hydrogen Energy. 41 (2016) 20720–20730. https://doi.org/10.1016/j.ijhydene.2016.09.097.

[78] H. Liu, F. Ye, Q. Yao, H. Cao, J. Xie, J.Y. Lee, J. Yang, Stellated Ag-Pt bimetallic nanoparticles: An effective platform for catalytic activity tuning, Sci. Rep. 4 (2014) 1–7. https://doi.org/10.1038/srep03969.

[79] T. Fu, J. Fang, C. Wang, J. Zhao, Hollow porous nanoparticles with Pt skin on a Ag-Pt alloy structure as a highly active electrocatalyst for the oxygen reduction reaction, J. Mater. Chem. A. 4 (2016) 8803–8811. https://doi.org/10.1039/c6ta02202b.

[80] Y. Zhou, D. Zhang, Nano PtCu binary and PtCuAg ternary alloy catalysts for oxygen reduction reaction in proton exchange membrane fuel cells, J. Power Sources. 278 (2015) 396–403. https://doi.org/10.1016/j.jpowsour.2014.12.088.

[81] J. Ryu, J. Choi, D.H. Lim, H.L. Seo, S.Y. Lee, Y. Sohn, J.H. Park, J.H. Jang, H.J. Kim, S.A. Hong, P. Kim, S.J. Yoo, Morphology-controlled synthesis of ternary Pt-Pd-Cu alloy nanoparticles for efficient electrocatalytic oxygen reduction reactions, Appl. Catal. B Environ. 174–175 (2015) 526–532. https://doi.org/10.1016/j.apcatb.2015.03.019.

[82] K. Jayasayee, J.A.R. Van Veen, T.G. Manivasagam, S. Celebi, E.J.M. Hensen, F.A. de Bruijn, Oxygen reduction reaction (ORR) activity and durability of carbon supported

PtM (Co, Ni, Cu) alloys: Influence of particle size and non-noble metals, Appl. Catal. B Environ. 111–112 (2012) 515–526. https://doi.org/10.1016/j.apcatb.2011.11.003.

[83] P. Strasser, S. Koh, T. Anniyev, J. Greeley, K. More, C. Yu, Z. Liu, S. Kaya, D. Nordlund, H. Ogasawara, M.F. Toney, A. Nilsson, Lattice-strain control of the activity in dealloyed core-shell fuel cell catalysts, Nat. Chem. 2 (2010) 454–460. https://doi.org/10.1038/nchem.623.

[84] P. Hernandez-Fernandez, F. Masini, D.N. McCarthy, C.E. Strebel, D. Friebel, D. Deiana, P. Malacrida, A. Nierhoff, A. Bodin, A.M. Wise, J.H. Nielsen, T.W. Hansen, A. Nilsson, I.E.L. Stephens, I. Chorkendorff, Mass-selected nanoparticles of Ptx y as model catalysts for oxygen electroreduction, Nat. Chem. 6 (2014) 732–738. https://doi.org/10.1038/nchem.2001.

[85] J.N. Schwämmlein, G.S. Harzer, P. Pfändner, A. Blankenship, H.A. El-Sayed, H.A. Gasteiger, Activity and Stability of Carbon Supported Pt x Y Alloys for the ORR Determined by RDE and Single-Cell PEMFC Measurements , J. Electrochem. Soc. 165 (2018) J3173–J3185. https://doi.org/10.1149/2.0221815jes.

[86] T. Ghosh, M.B. Vukmirovic, F.J. DiSalvo, R.R. Adzic, Intermetallics as novel supports for Pt monolayer O2 reduction electrocatalysts: Potential for significantly improving properties, J. Am. Chem. Soc. 132 (2010) 906–907. https://doi.org/10.1021/ja905850c.

[87] L. Bu, N. Zhang, S. Guo, X. Zhang, J. Li, J. Yao, T. Wu, G. Lu, J.Y. Ma, D. Su, X. Huang, Biaxially strained PtPb/Pt core/shell nanoplate boosts oxygen reduction catalysis, Science (80-.). 354 (2016) 1410–1414. https://doi.org/10.1126/science.aah6133.

[88] A. Schlapka, M. Lischka, A. Groß, U. Käsberger, P. Jakob, Surface strain versus substrate interaction in heteroepitaxial metal layers: Pt on Ru(0001), Phys. Rev. Lett. 91 (2003) 016101/1-016101/4. https://doi.org/10.1103/PhysRevLett.91.016101.

[89] Q. Jia, C.U. Segre, D. Ramaker, K. Caldwell, M. Trahan, S. Mukerjee, Structure-property-activity correlations of Pt-bimetallic nanoparticles: A theoretical study, Electrochim. Acta. 88 (2013) 604–613. https://doi.org/10.1016/j.electacta.2012.10.124.

[90] V.R. Stamenkovic, B.S. Mun, M. Arenz, K.J.J. Mayrhofer, C.A. Lucas, G. Wang, P.N. Ross, N.M. Markovic, Trends in electrocatalysis on extended and nanoscale Pt-bimetallic alloy surfaces, Nat. Mater. 6 (2007) 241–247. https://doi.org/10.1038/nmat1840.

[91] D. Banham, S. Ye, Current status and future development of catalyst materials and catalyst layers for proton exchange membrane fuel cells: An industrial perspective, ACS Energy Lett. 2 (2017) 629–638. https://doi.org/10.1021/acsenergylett.6b00644.

[92] M. Escudero-Escribano, K.D. Jensen, A.W. Jensen, Recent advances in bimetallic electrocatalysts for oxygen reduction: design principles, structure-function relations and active phase elucidation, Curr. Opin. Electrochem. 8 (2018) 135–146. https://doi.org/10.1016/j.coelec.2018.04.013.

[93] V. Rao, P.A. Simonov, E.R. Savinova, G. V. Plaksin, S. V. Cherepanova, G.N. Kryukova, U. Stimming, The influence of carbon support porosity on the activity of PtRu/Sibunit anode catalysts for methanol oxidation, J. Power Sources. 145 (2005) 178–187. https://doi.org/10.1016/j.jpowsour.2004.12.064.

[94] D. Myers, X. Wang, S. Lee, M. Ferrandon, N. Kariuki, T. Krause, High-Throughput/Combinatorial Optimization of Low-Pt PEMFC Cathode Performance

High-Throughput Synthesis, ORR Activity Modeling, and Testing of non-PGM PEMFC Cathode Catalysts, 2015. https://www.hydrogen.energy.gov/pdfs/review15/fc114_myers_2015_o.pdf.

[95] L. Pan, S. Ott, F. Dionigi, P. Strasser, Current challenges related to the deployment of shape-controlled Pt alloy oxygen reduction reaction nanocatalysts into low Pt-loaded cathode layers of proton exchange membrane fuel cells, Curr. Opin. Electrochem. 18 (2019) 61–71. https://doi.org/10.1016/j.coelec.2019.10.011.

[96] P.J. Ferreira, G.J. la O', Y. Shao-Horn, D. Morgan, R. Makharia, S. Kocha, H.A. Gasteiger, Instability of Pt⁄C Electrocatalysts in Proton Exchange Membrane Fuel Cells, J. Electrochem. Soc. 152 (2005) A2256. https://doi.org/10.1149/1.2050347.

[97] Y. Shao, G. Yin, Y. Gao, Understanding and approaches for the durability issues of Pt-based catalysts for PEM fuel cell, J. Power Sources. 171 (2007) 558–566. https://doi.org/10.1016/j.jpowsour.2007.07.004.

[98] D.Y. Chung, J.M. Yoo, Y.-E. Sung, Highly Durable and Active Pt-Based Nanoscale Design for Fuel-Cell Oxygen-Reduction Electrocatalysts, Adv. Mater. 30 (2018) 1704123. https://doi.org/10.1002/adma.201704123.

[99] N. Macauley, D.D. Papadias, J. Fairweather, D. Spernjak, D. Langlois, R. Ahluwalia, K.L. More, R. Mukundan, R.L. Borup, Carbon corrosion in PEM fuel cells and the development of accelerated stress tests, J. Electrochem. Soc. 165 (2018) F3148–F3160. https://doi.org/10.1149/2.0061806jes.

[100] L. Dubau, L. Castanheira, F. Maillard, M. Chatenet, O. Lottin, G. Maranzana, J. Dillet, A. Lamibrac, J.C. Perrin, E. Moukheiber, A. Elkaddouri, G. De Moor, C. Bas, L. Flandin, N. Caqué, A review of PEM fuel cell durability: Materials degradation, local

heterogeneities of aging and possible mitigation strategies, Wiley Interdiscip. Rev. Energy Environ. 3 (2014) 540–560. https://doi.org/10.1002/wene.113.

[101] F. Maillard, W. O. Silva, L. Castanheira, L. Dubau, F.H.B. Lima, Carbon Corrosion in Proton-Exchange Membrane Fuel Cells: Spectrometric Evidence for Pt-Catalysed Decarboxylation at Anode-Relevant Potentials, ChemPhysChem. 20 (2019) 3106–3111. https://doi.org/10.1002/cphc.201900505.

[102] C. Cui, L. Gan, M. Heggen, S. Rudi, P. Strasser, Compositional segregation in shaped Pt alloy nanoparticles and their structural behaviour during electrocatalysis, Nat. Mater. 12 (2013) 765–771. https://doi.org/10.1038/nmat3668.

[103] C.T. Campbell, S.C. Parker, D.E. Starr, The effect of size-dependent nanoparticle energetics on catalyst sintering, Science (80-.). 298 (2002) 811–814. https://doi.org/10.1126/science.1075094.

[104] E.F. Holby, W. Sheng, Y. Shao-Horn, D. Morgan, Pt nanoparticle stability in PEM fuel cells: Influence of particle size distribution and crossover hydrogen, Energy Environ. Sci. 2 (2009) 865–871. https://doi.org/10.1039/b821622n.

[105] K. Yu, D.J. Groom, X. Wang, Z. Yang, M. Gummalla, S.C. Ball, D.J. Myers, P.J. Ferreira, Degradation mechanisms of platinum nanoparticle catalysts in proton exchange membrane fuel cells: The role of particle size, Chem. Mater. 26 (2014) 5540–5548. https://doi.org/10.1021/cm501867c.

[106] J.A. Gilbert, N.N. Kariuki, R. Subbaraman, A.J. Kropf, M.C. Smith, E.F. Holby, D. Morgan, D.J. Myers, In situ anomalous small-angle x-ray scattering studies of platinum nanoparticle fuel cell electrocatalyst degradation, J. Am. Chem. Soc. 134 (2012) 14823–14833. https://doi.org/10.1021/ja3038257.

[107] Z. Yang, S. Ball, D. Condit, M. Gummalla, Systematic Study on the Impact of Pt Particle Size and Operating Conditions on PEMFC Cathode Catalyst Durability, J. Electrochem. Soc. 158 (2011) B1439. https://doi.org/10.1149/2.081111jes.

[108] M. Gummalla, S. Ball, D. Condit, S. Rasouli, K. Yu, P. Ferreira, D. Myers, Z. Yang, Effect of Particle Size and Operating Conditions on Pt3Co PEMFC Cathode Catalyst Durability, Catalysts. 5 (2015) 926–948. https://doi.org/10.3390/catal5020926.

[109] A.A. Topalov, S. Cherevko, A.R. Zeradjanin, J.C. Meier, I. Katsounaros, K.J.J. Mayrhofer, Towards a comprehensive understanding of platinum dissolution in acidic media, Chem. Sci. 5 (2014) 631–638. https://doi.org/10.1039/c3sc52411f.

[110] P.P. Lopes, D. Strmcnik, D. Tripkovic, J.G. Connell, V. Stamenkovic, N.M. Markovic, Relationships between Atomic Level Surface Structure and Stability/Activity of Platinum Surface Atoms in Aqueous Environments, ACS Catal. 6 (2016) 2536–2544. https://doi.org/10.1021/acscatal.5b02920.

[111] D.Y. Chung, H. Shin, J.M. Yoo, K.S. Lee, N.S. Lee, K. Kang, Y.E. Sung, Functional link between surface low-coordination sites and the electrochemical durability of Pt nanoparticles, J. Power Sources. 334 (2016) 52–57. https://doi.org/10.1016/j.jpowsour.2016.10.007.

[112] J. Wang, H. Gu, Novel metal nanomaterials and their catalytic applications, Molecules. 20 (2015) 17070–17092. https://doi.org/10.3390/molecules200917070.

[113] Y. Song, R.M. Garcia, R.M. Dorin, H. Wang, Y. Qiu, E.N. Coker, W.A. Steen, J.E. Miller, J.A. Shelnut, Synthesis of platinum nanowire networks using a soft template, Nano Lett. 7 (2007) 3650–3655. https://doi.org/10.1021/nl0719123.

[114] C. Koenigsmann, W.P. Zhou, R.R. Adzic, E. Sutter, S.S. Wong, Size-dependent

enhancement of electrocatalytic performance in relatively defect-free, processed ultrathin platinum nanowires, Nano Lett. 10 (2010) 2806–2811. https://doi.org/10.1021/nl100718k.

[115] C. Koenigsmann, M.E. Scofield, H. Liu, S.S. Wong, Designing Enhanced One-Dimensional Electrocatalysts for the Oxygen Reduction Reaction: Probing Size- and Composition-Dependent Electrocatalytic Behavior in Noble Metal Nanowires, J. Phys. Chem. Lett. 3 (2012) 3385–3398. https://doi.org/10.1021/jz301457h.

[116] L. Ruan, E. Zhu, Y. Chen, Z. Lin, X. Huang, X. Duan, Y. Huang, Biomimetic synthesis of an ultrathin platinum nanowire network with a high twin density for enhanced electrocatalytic activity and durability, Angew. Chemie - Int. Ed. 52 (2013) 12577–12581. https://doi.org/10.1002/anie.201304658.

[117] M. Wang, H. Zhang, G. Thirunavukkarasu, I. Salam, J.R. Varcoe, P. Mardle, X. Li, S. Mu, S. Du, Ionic Liquid-Modified Microporous ZnCoNC-Based Electrocatalysts for Polymer Electrolyte Fuel Cells, ACS Energy Lett. 4 (2019) 2104–2110. https://doi.org/10.1021/acsenergylett.9b01407.

[118] Y. Piao, H. Lim, J.Y. Chang, W.Y. Lee, H. Kim, Nanostructured materials prepared by use of ordered porous alumina membranes, in: Electrochim. Acta, Pergamon, 2005: pp. 2997–3013. https://doi.org/10.1016/j.electacta.2004.12.043.

[119] G.Y. Zhao, C.L. Xu, D.J. Guo, H. Li, H.L. Li, Template preparation of Pt nanowire array electrode on Ti/Si substrate for methanol electro-oxidation, Appl. Surf. Sci. 253 (2007) 3242–3246. https://doi.org/10.1016/j.apsusc.2006.07.015.

[120] S.M. Choi, J.H. Kim, J.Y. Jung, E.Y. Yoon, W.B. Kim, Pt nanowires prepared via a polymer template method: Its promise toward high Pt-loaded electrocatalysts for

methanol oxidation, Electrochim. Acta. 53 (2008) 5804–5811. https://doi.org/10.1016/j.electacta.2008.03.041.

[121] I.S. Park, J.H. Choi, Y.E. Sung, Synthesis of 3 nm Pt nanowire using MCM-41 and electrocatalytic activity in methanol electro-oxidation, Electrochem. Solid-State Lett. 11 (2008) B71. https://doi.org/10.1149/1.2888220.

[122] K.M. Koczkur, S. Mourdikoudis, L. Polavarapu, S.E. Skrabalak, Polyvinylpyrrolidone (PVP) in nanoparticle synthesis, Dalt. Trans. 44 (2015) 17883–17905. https://doi.org/10.1039/c5dt02964c.

[123] J. St-Pierre, Y. Zhai, M.S. Angelo, Effect of Selected Airborne Contaminants on PEMFC Performance, J. Electrochem. Soc. 161 (2014) F280–F290. https://doi.org/10.1149/2.057403jes.

[124] J. St-Pierre, Y. Zhai, Impact of the cathode PT loading on PEMFC contamination by several airborne contaminants, Molecules. 25 (2020). https://doi.org/10.3390/molecules25051060.

[125] S. Sun, D. Yang, D. Villers, G. Zhang, E. Sacher, J.P. Dodelet, Template- And surfactant-free room temperature synthesis of self-assembled 3D Pt nanoflowers from single-crystal nanowires, Adv. Mater. 20 (2008) 571–574. https://doi.org/10.1002/adma.200701408.

[126] S. Sun, F. Jaouen, J.P. Dodelet, Controlled growth of Pt nanowires on carbon nanospheres and their enhanced performance as electrocatalysts in PEM fuel cells, Adv. Mater. 20 (2008) 3900–3904. https://doi.org/10.1002/adma.200800491.

[127] S. Sun, G. Zhang, D. Geng, Y. Chen, R. Li, M. Cai, X. Sun, A highly durable platinum nanocatalyst for proton exchange membrane fuel cells: Multiarmed starlike nanowire

single crystal, Angew. Chemie - Int. Ed. 50 (2011) 422–426. https://doi.org/10.1002/anie.201004631.

[128] B. Li, Z. Yan, D.C. Higgins, D. Yang, Z. Chen, J. Ma, Carbon-supported Pt nanowire as novel cathode catalysts for proton exchange membrane fuel cells, J. Power Sources. 262 (2014) 488–493. https://doi.org/10.1016/j.jpowsour.2014.04.004.

[129] B. Li, D.C. Higgins, Q. Xiao, D. Yang, C. Zhng, M. Cai, Z. Chen, J. Ma, The durability of carbon supported Pt nanowire as novel cathode catalyst for a 1.5kW PEMFC stack, Appl. Catal. B Environ. 162 (2015) 133–140. https://doi.org/10.1016/j.apcatb.2014.06.040.

[130] S. Du, B. Millington, B.G. Pollet, The effect of Nafion ionomer loading coated on gas diffusion electrodes with in-situ grown Pt nanowires and their durability in proton exchange membrane fuel cells, Int. J. Hydrogen Energy. 36 (2011) 4386–4393. https://doi.org/10.1016/j.ijhydene.2011.01.014.

[131] Z. Chen, M. Waje, W. Li, Y. Yan, Supportless Pt and PtPd nanotubes as electrocatalysts for oxygen-reduction reactions, Angew. Chemie - Int. Ed. 46 (2007) 4060–4063. https://doi.org/10.1002/anie.200700894.

[132] H.W. Liang, X. Cao, F. Zhou, C.H. Cui, W.J. Zhang, S.H. Yu, A free-standing Pt-nanowire membrane as a highly stable electrocatalyst for the oxygen reduction reaction, Adv. Mater. 23 (2011) 1467–1471. https://doi.org/10.1002/adma.201004377.

[133] Z.L. Zhao, Q. Wang, L.Y. Zhang, H.M. An, Z. Li, C.M. Li, Galvanic exchange-formed ultra-low Pt loading on synthesized unique porous Ag-Pd nanotubes for increased active sites toward oxygen reduction reaction, Electrochim. Acta. 263 (2018) 209–216. https://doi.org/10.1016/j.electacta.2017.12.036.

[134] A.L. Dicks, The role of carbon in fuel cells, J. Power Sources. 156 (2006) 128–141. https://doi.org/10.1016/j.jpowsour.2006.02.054.

[135] H. Tang, Z. Qi, M. Ramani, J.F. Elter, PEM fuel cell cathode carbon corrosion due to the formation of air/fuel boundary at the anode, J. Power Sources. 158 (2006) 1306–1312. https://doi.org/10.1016/j.jpowsour.2005.10.059.

[136] C.A. Reiser, L. Bregoli, T.W. Patterson, J.S. Yi, J.D. Yang, M.L. Perry, T.D. Jarvi, A reverse-current decay mechanism for fuel cells, Electrochem. Solid-State Lett. 8 (2005) A273. https://doi.org/10.1149/1.1896466.

[137] S.C. Ball, S.L. Hudson, D. Thompsett, B. Theobald, An investigation into factors affecting the stability of carbons and carbon supported platinum and platinum/cobalt alloy catalysts during 1.2 V potentiostatic hold regimes at a range of temperatures, J. Power Sources. 171 (2007) 18–25. https://doi.org/10.1016/j.jpowsour.2006.11.004.

[138] T. Asset, N. Job, Y. Busby, A. Crisci, V. Martin, V. Stergiopoulos, C. Bonnaud, A. Serov, P. Atanassov, R. Chattot, L. Dubau, F. Maillard, Porous Hollow PtNi/C Electrocatalysts: Carbon Support Considerations to Meet Performance and Stability Requirements, ACS Catal. 8 (2018) 893–903. https://doi.org/10.1021/acscatal.7b03539.

[139] S. Du, A Facile Route for Polymer Electrolyte Membrane Fuel Cell Electrodes with in situ Grown Pt Nanowires, J. Power Sources. 195 (2010) 289–292. https://doi.org/10.1016/j.jpowsour.2009.06.091.

[140] S. Du, B.G. Pollet, Catalyst loading for Pt-nanowire thin film electrodes in PEFCs, Int. J. Hydrogen Energy. 37 (2012) 17892–17898. https://doi.org/10.1016/j.ijhydene.2012.08.148.

[141] A. El-Kharouf, T.J. Mason, D.J.L. Brett, B.G. Pollet, Ex-situ characterisation of gas diffusion layers for proton exchange membrane fuel cells, J. Power Sources. 218 (2012) 393–404. https://doi.org/10.1016/j.jpowsour.2012.06.099.

[142] Y. Lu, S. Du, R. Steinberger-Wilckens, Temperature-controlled growth of single-crystal Pt nanowire arrays for high performance catalyst electrodes in polymer electrolyte fuel cells, Appl. Catal. B Environ. 164 (2015) 389–395. https://doi.org/10.1016/j.apcatb.2014.09.040.

[143] S. Du, K. Lin, S.K. Malladi, Y. Lu, S. Sun, Q. Xu, R. Steinberger-Wilckens, H. Dong, Plasma nitriding induced growth of Pt-nanowire arrays as high performance electrocatalysts for fuel cells, Sci. Rep. 4 (2014). https://doi.org/10.1038/srep06439.

[144] S. Sui, Z. Wei, K. Su, A. He, X. Wang, Y. Su, X. Hou, S. Raffet, S. Du, Pt nanowire growth induced by Pt nanoparticles in application of the cathodes for Polymer Electrolyte Membrane Fuel Cells (PEMFCs), Int. J. Hydrogen Energy. 43 (2018) 20041–20049. https://doi.org/10.1016/j.ijhydene.2018.09.009.

[145] X. Yao, K. Su, S. Sui, L. Mao, A. He, J. Zhang, S. Du, A novel catalyst layer with carbon matrix for Pt nanowire growth in proton exchange membrane fuel cells (PEMFCs), Int. J. Hydrogen Energy. 38 (2013) 12374–12378. https://doi.org/10.1016/j.ijhydene.2013.07.037.

[146] K. Su, X. Yao, S. Sui, Z. Wei, J. Zhang, S. Du, Matrix Material Study for *in situ* Grown Pt Nanowire Electrocatalyst Layer in Proton Exchange Membrane Fuel Cells (PEMFCs), Fuel Cells. 15 (2015) 449–455. https://doi.org/10.1002/fuce.201400168.

[147] H. Lv, J. Wang, Z. Yan, B. Li, D. Yang, C. Zhang, Carbon-supported Pt-Co Nanowires as a Novel Cathode Catalyst for Proton Exchange Membrane Fuel Cells, Fuel Cells. 17

(2017) 635–642. https://doi.org/10.1002/fuce.201700136.

[148] Y. Hoshi, T. Yoshida, A. Nishikata, T. Tsuru, Dissolution of Pt-M (M: Cu, Co, Ni, Fe) binary alloys in sulfuric acid solution, Electrochim. Acta. 56 (2011) 5302–5309. https://doi.org/10.1016/j.electacta.2011.04.007.

[149] S. Guo, D. Li, H. Zhu, S. Zhang, N.M. Markovic, V.R. Stamenkovic, S. Sun, FePt and CoPt nanowires as efficient catalysts for the oxygen reduction reaction, Angew. Chemie - Int. Ed. 52 (2013) 3465–3468. https://doi.org/10.1002/anie.201209871.

[150] K. Jiang, D. Zhao, S. Guo, X. Zhang, X. Zhu, J. Guo, G. Lu, X. Huang, Efficient oxygen reduction catalysis by subnanometer Pt alloy nanowires, Sci. Adv. 3 (2017) e1601705. https://doi.org/10.1126/sciadv.1601705.

[151] F. Maillard, L. Dubau, J. Durst, M. Chatenet, J. André, E. Rossinot, Durability of Pt3Co/C nanoparticles in a proton-exchange membrane fuel cell: Direct evidence of bulk Co segregation to the surface, Electrochem. Commun. 12 (2010) 1161–1164. https://doi.org/10.1016/j.elecom.2010.06.007.

[152] Y. Ma, P.B. Balbuena, Pt surface segregation in bimetallic Pt3M alloys: A density functional theory study, Surf. Sci. 602 (2008) 107–113. https://doi.org/10.1016/j.susc.2007.09.052.

[153] M. Luo, Y. Sun, L. Wang, S. Guo, Tuning Multimetallic Ordered Intermetallic Nanocrystals for Efficient Energy Electrocatalysis, Adv. Energy Mater. 7 (2017) 1602073. https://doi.org/10.1002/aenm.201602073.

[154] P. Mardle, S. Du, Annealing Behaviour of Pt and PtNi Nanowires for Proton Exchange Membrane Fuel Cells, Materials (Basel). 11 (2018) 1473. https://doi.org/10.3390/ma11081473.

[155] S. Yu, Q. Lou, K. Han, Z. Wang, H. Zhu, Synthesis and electrocatalytic performance of MWCNT-supported Ag@Pt core-shell nanoparticles for ORR, Int. J. Hydrogen Energy. 37 (2012) 13365–13370. https://doi.org/10.1016/j.ijhydene.2012.06.109.

[156] Y.Y. Feng, G.R. Zhang, J.H. Ma, G. Liu, B.Q. Xu, Carbon-supported PtˆAg nanostructures as cathode catalysts for oxygen reduction reaction, Phys. Chem. Chem. Phys. 13 (2011) 3863–3872. https://doi.org/10.1039/c0cp01612h.

[157] D.R. Lide, G. Baysinger, L.I. Berger, R.N. Goldberg, H. V Kehiaian, K. Kuchitsu, D.L. Roth, D. Zwillinger, CRC Handbook of Chemistry and Physics Editor-in-Chief, n.d.

[158] M. Liu, F. Chi, J. Liu, Y. Song, F. Wang, A novel strategy to synthesize bimetallic Pt-Ag particles with tunable nanostructures and their superior electrocatalytic activities toward the oxygen reduction reaction, RSC Adv. 6 (2016) 62327–62335. https://doi.org/10.1039/c6ra05549d.

[159] A.J. Wang, L. Liu, X.X. Lin, J. Yuan, J.J. Feng, One-pot synthesis of 3D freestanding porous PtAg hollow chain-like networks as efficient electrocatalyst for oxygen reduction reaction, Electrochim. Acta. 245 (2017) 883–892. https://doi.org/10.1016/j.electacta.2017.06.013.

[160] Y. Lai, G. Du, Z. Zheng, Y. Dong, H. Li, Q. Kuang, Z. Xie, Facile synthesis of clean PtAg dendritic nanostructures with enhanced electrochemical properties, Inorg. Chem. Front. 7 (2020) 1250–1256. https://doi.org/10.1039/c9qi01460h.

[161] Y.Y. Feng, J.H. Ma, G.R. Zhang, G. Liu, B.Q. Xu, Dealloyed carbon-supported PtAg nanostructures: Enhanced electrocatalytic activity for oxygen reduction reaction, Electrochem. Commun. 12 (2010) 1191–1194.

https://doi.org/10.1016/j.elecom.2010.06.016.

[162] M. Chatenet, L. Genies-Bultel, M. Aurousseau, R. Durand, F. Andolfatto, Oxygen reduction on silver catalysts in solutions containing various concentrations of sodium hydroxide - Comparison with platinum, J. Appl. Electrochem. 32 (2002) 1131–1140. https://doi.org/10.1023/A:1021231503922.

[163] B.B. Blizanac, P.N. Ross, N.M. Markovic, Oxygen electroreduction on Ag(1 1 1): The pH effect, Electrochim. Acta. 52 (2007) 2264–2271. https://doi.org/10.1016/j.electacta.2006.06.047.

[164] E. Zhang, F. Ma, J. Liu, J. Sun, W. Chen, H. Rong, X. Zhu, J. Liu, M. Xu, Z. Zhuang, S. Chen, Z. Wen, J. Zhang, Porous platinum-silver bimetallic alloys: Surface composition and strain tunability toward enhanced electrocatalysis, Nanoscale. 10 (2018) 21703–21711. https://doi.org/10.1039/c8nr06192k.

[165] C. Fang, J. Zhao, G. Zhao, L. Kuai, B. Geng, Simultaneous tunable structure and composition of PtAg alloyed nanocrystals as superior catalysts, Nanoscale. 8 (2016) 14971–14978. https://doi.org/10.1039/c6nr02643e.

[166] F.Q. Shao, X.Y. Zhu, A.J. Wang, K.M. Fang, J. Yuan, J.J. Feng, One-pot synthesis of hollow AgPt alloyed nanocrystals with enhanced electrocatalytic activity for hydrogen evolution and oxygen reduction reactions, J. Colloid Interface Sci. 505 (2017) 307–314. https://doi.org/10.1016/j.jcis.2017.05.088.

[167] Y. Feng, J. Ma, G. Zhang, D. Zhao, B. Xu, An interfacially alloyed Pt^Ag cathode catalyst for the electrochemical reduction of oxygen, Cuihua Xuebao / Chinese J. Catal. 30 (2009) 776–779. https://doi.org/10.1016/s1872-2067(08)60124-2.

[168] Z. Li, Y. Li, C. He, P.K. Shen, Bimetallic PtAg alloyed nanoparticles and 3-D

mesoporous graphene nanosheet hybrid architectures for advanced oxygen reduction reaction electrocatalysts, J. Mater. Chem. A. 5 (2017) 23158–23169. https://doi.org/10.1039/c7ta07525a.

[169] M. Gatalo, P. Jovanovič, G. Polymeros, J.-P. Grote, A. Pavlišič, F. Ruiz- Zepeda, V.S. Šelih, M. Šala, S. Hočevar, M. Bele, K.J.J. Mayrhofer, N. Hodnik, M. Gaberšček, Positive Effect of Surface Doping with Au on the Stability of Pt-Based Electrocatalysts, ACS Catal. 6 (2016) 1630–1634. https://doi.org/10.1021/acscatal.5b02883.

[170] J. Choi, J. Cho, C.W. Roh, B.S. Kim, M.S. Choi, H. Jeong, H.C. Ham, H. Lee, Au-doped PtCo/C catalyst preventing Co leaching for proton exchange membrane fuel cells, Appl. Catal. B Environ. 247 (2019) 142–149. https://doi.org/10.1016/j.apcatb.2019.02.002.

[171] A. Dorjgotov, Y. Jeon, J. Hwang, B. Ulziidelger, H.S. Kim, B. Han, Y.G. Shul, Synthesis of Durable Small-sized Bilayer Au@Pt Nanoparticles for High Performance PEMFC Catalysts, Electrochim. Acta. 228 (2017) 389–397. https://doi.org/10.1016/j.electacta.2017.01.083.

[172] F. Chang, S. Shan, V. Petkov, Z. Skeete, A. Lu, J. Ravid, J. Wu, J. Luo, G. Yu, Y. Ren, C.J. Zhong, Composition Tunability and (111)-Dominant Facets of Ultrathin Platinum-Gold Alloy Nanowires toward Enhanced Electrocatalysis, J. Am. Chem. Soc. 138 (2016) 12166–12175. https://doi.org/10.1021/jacs.6b05187.

[173] C.W. Liu, Y.C. Wei, C.C. Liu, K.W. Wang, Pt-Au core/shell nanorods: Preparation and applications as electrocatalysts for fuel cells, J. Mater. Chem. 22 (2012) 4641–4644. https://doi.org/10.1039/c2jm16407h.

[174] H.Y. Park, T.Y. Jeon, J.H. Jang, S.J. Yoo, K.H. Choi, N. Jung, Y.H. Chung, M. Ahn, Y.H. Cho, K.S. Lee, Y.E. Sung, Enhancement of oxygen reduction reaction on PtAu nanoparticles via CO induced surface Pt enrichment, Appl. Catal. B Environ. 129 (2013) 375–381. https://doi.org/10.1016/j.apcatb.2012.09.041.

[175] K. Gong, D. Su, R.R. Adzic, Platinum-monolayer shell on AuNi0.5Fe nanoparticle core electrocatalyst with high activity and stability for the oxygen reduction reaction, J. Am. Chem. Soc. 132 (2010) 14364–14366. https://doi.org/10.1021/ja1063873.

[176] L. Zhang, R. Iyyamperumal, D.F. Yancey, R.M. Crooks, G. Henkelman, Design of Pt-shell nanoparticles with alloy cores for the oxygen reduction reaction, ACS Nano. 7 (2013) 9168–9172. https://doi.org/10.1021/nn403788a.

[177] L.L. Shen, G.R. Zhang, S. Miao, J. Liu, B.Q. Xu, Core-Shell Nanostructured Au@NimPt2 Electrocatalysts with Enhanced Activity and Durability for Oxygen Reduction Reaction, ACS Catal. 6 (2016) 1680–1690. https://doi.org/10.1021/acscatal.5b02124.

[178] Y. Tan, J. Fan, G. Chen, N. Zheng, Q. Xie, Au/Pt and Au/Pt3Ni nanowires as self-supported electrocatalysts with high activity and durability for oxygen reduction, Chem. Commun. 47 (2011) 11624–11626. https://doi.org/10.1039/c1cc15558j.

[179] S. Guo, S. Zhang, D. Su, S. Sun, Seed-mediated synthesis of core/shell FePtM/FePt (M = Pd, Au) nanowires and their electrocatalysis for oxygen reduction reaction, J. Am. Chem. Soc. 135 (2013) 13879–13884. https://doi.org/10.1021/ja406091p.

[180] V. Mazumder, M. Chi, K.L. More, S. Sun, Core/Shell Pd/FePt nanoparticles as an active and durable catalyst for the oxygen reduction reaction, J. Am. Chem. Soc. 132 (2010) 7848–7849. https://doi.org/10.1021/ja1024436.

[181] T.H. Yeh, C.W. Liu, H.S. Chen, K.W. Wang, Preparation of carbon-supported PtM (M = Au, Pd, or Cu) nanorods and their application in oxygen reduction reaction, Electrochem. Commun. 31 (2013) 125–128. https://doi.org/10.1016/j.elecom.2013.03.025.

[182] G. Tsotridis, A. Pilenga, G. De Marco, T. Malkow, EU Harmonised Test Protocols for PEMFC MEA Testing in Single Cell Configuration for Automotive Applications; JRC Science for Policy report, 2015. https://doi.org/10.2790/54653.

[183] X.Z. Yuan, C. Song, H. Wang, J. Zhang, Electrochemical impedance spectroscopy in PEM fuel cells: Fundamentals and applications, Springer London, 2010. https://doi.org/10.1007/978-1-84882-846-9.

[184] H.A. Gasteiger, S.S. Kocha, B. Sompalli, F.T. Wagner, Activity benchmarks and requirements for Pt, Pt-alloy, and non-Pt oxygen reduction catalysts for PEMFCs, Appl. Catal. B Environ. 56 (2005) 9–35. https://doi.org/10.1016/j.apcatb.2004.06.021.

[185] Y. Garsany, O.A. Baturina, K.E. Swider-Lyons, S.S. Kocha, Experimental methods for quantifying the activity of platinum electrocatalysts for the oxygen reduction reaction, in: Anal. Chem., 2010: pp. 6321–6328. https://doi.org/10.1021/ac100306c.

[186] S. Sui, X. Zhuo, K. Su, X. Yao, J. Zhang, S. Du, K. Kendall, In situ grown nanoscale platinum on carbon powder as catalyst layer in proton exchange membrane fuel cells (PEMFCs), J. Energy Chem. 22 (2013) 477–483. https://doi.org/10.1016/S2095-4956(13)60062-5.

[187] C. Busó-Rogero, A. Ferre-Vilaplana, E. Herrero, J.M. Feliu, The role of formic acid/formate equilibria in the oxidation of formic acid on Pt (111), Electrochem. Commun. 98 (2019) 10–14. https://doi.org/10.1016/j.elecom.2018.11.011.

[188] A. Boronat-González, E. Herrero, J.M. Feliu, Fundamental aspects of HCOOH oxidation at platinum single crystal surfaces with basal orientations and modified by irreversibly adsorbed adatoms, J. Solid State Electrochem. 18 (2014) 1181–1193. https://doi.org/10.1007/s10008-013-2209-x.

[189] H. Meng, Y. Zhan, D. Zeng, X. Zhang, G. Zhang, F. Jaouen, Factors Influencing the Growth of Pt Nanowires via Chemical Self-Assembly and their Fuel Cell Performance, Small. 11 (2015) 3377–3386. https://doi.org/10.1002/smll.201402904.

[190] A. Bin Yousaf, M. Imran, A. Zeb, T. Wen, X. Xie, Y.F. Jiang, C.Z. Yuan, A.W. Xu, Single Phase PtAg Bimetallic Alloy Nanoparticles Highly Dispersed on Reduced Graphene Oxide for Electrocatalytic Application of Methanol Oxidation Reaction, Electrochim. Acta. 197 (2016) 117–125. https://doi.org/10.1016/j.electacta.2016.03.067.

[191] K. Kinoshita, K. Routsis, J.A.S. Bett, The thermal decomposition of platinum(II) and (IV) complexes, Thermochim. Acta. 10 (1974) 109–117. https://doi.org/10.1016/0040-6031(74)85029-X.

[192] C.J. Levy, R.J. Puddephatt, Thermal decomposition of platinum(IV)-silicon, -germanium, and -tin complexes, Organometallics. 16 (1997) 4115–4120. https://doi.org/10.1021/om970204x.

[193] M.P. Hyman, J.W. Medlin, Effects of electronic structure modifications on the adsorption of oxygen reduction reaction intermediates on model Pt(111)-alloy surfaces, J. Phys. Chem. C. 111 (2007) 17052–17060. https://doi.org/10.1021/jp075108g.

[194] P. Mardle, X. Ji, J. Wu, S. Guan, H. Dong, S. Du, Thin film electrodes from Pt

nanorods supported on aligned N-CNTs for proton exchange membrane fuel cells, Appl. Catal. B Environ. 260 (2020) 118031. https://doi.org/10.1016/j.apcatb.2019.118031.

[195] C. Koenigsmann, S.S. Wong, One-dimensional noble metal electrocatalysts: A promising structural paradigm for direct methanol fuel cells, Energy Environ. Sci. 4 (2011) 1161–1176. https://doi.org/10.1039/c0ee00197j.

[196] Z. Peng, H. You, H. Yang, An electrochemical approach to PtAg alloy nanostructures rich in Pt at the surface, in: Adv. Funct. Mater., 2010: pp. 3734–3741. https://doi.org/10.1002/adfm.201001194.

[197] T. Fu, J. Fang, C. Wang, J. Zhao, Hollow porous nanoparticles with Pt skin on a Ag-Pt alloy structure as a highly active electrocatalyst for the oxygen reduction reaction, J. Mater. Chem. A. 4 (2016) 8803–8811. https://doi.org/10.1039/c6ta02202b.

[198] H.A. Hansen, J. Rossmeisl, J.K. Nørskov, Surface Pourbaix diagrams and oxygen reduction activity of Pt, Ag and Ni(111) surfaces studied by DFT, Phys. Chem. Chem. Phys. 10 (2008) 3722–3730. https://doi.org/10.1039/b803956a.

[199] H. Cheng, W. Yuan, K. Scott, The influence of a new fabrication procedure on the catalytic activity of ruthenium-selenium catalysts, Electrochim. Acta. 52 (2006) 466–473. https://doi.org/10.1016/j.electacta.2006.05.028.

[200] G. Hinds, Preparation and characterisation of PEM fuel cell electrocatalysts: a review., (2005).

[201] C.W.B. Bezerra, L. Zhang, H. Liu, K. Lee, A.L.B. Marques, E.P. Marques, H. Wang, J. Zhang, A review of heat-treatment effects on activity and stability of PEM fuel cell catalysts for oxygen reduction reaction, J. Power Sources. 173 (2007) 891–908.

https://doi.org/10.1016/j.jpowsour.2007.08.028.

[202] A.M. Ferraria, A.P. Carapeto, A.M. Botelho Do Rego, X-ray photoelectron spectroscopy: Silver salts revisited, Vacuum. 86 (2012) 1988–1991. https://doi.org/10.1016/j.vacuum.2012.05.031.

[203] X. Xie, G. Gao, S. Kang, T. Shibayama, Y. Lei, D. Gao, L. Cai, Site-Selective Trimetallic Heterogeneous Nanostructures for Enhanced Electrocatalytic Performance, Adv. Mater. 27 (2015) 5573–5577. https://doi.org/10.1002/adma.201501133.

[204] H.R. Colón-Mercado, B.N. Popov, Stability of platinum based alloy cathode catalysts in PEM fuel cells, J. Power Sources. 155 (2006) 253–263. https://doi.org/10.1016/j.jpowsour.2005.05.011.

[205] V. Beermann, M. Gocyla, E. Willinger, S. Rudi, M. Heggen, R.E. Dunin-Borkowski, M.G. Willinger, P. Strasser, Rh-Doped Pt-Ni Octahedral Nanoparticles: Understanding the Correlation between Elemental Distribution, Oxygen Reduction Reaction, and Shape Stability, Nano Lett. 16 (2016) 1719–1725. https://doi.org/10.1021/acs.nanolett.5b04636.

[206] Q. Jia, Z. Zhao, L. Cao, J. Li, S. Ghoshal, V. Davies, E. Stavitski, K. Attenkofer, Z. Liu, M. Li, X. Duan, S. Mukerjee, T. Mueller, Y. Huang, Roles of Mo Surface Dopants in Enhancing the ORR Performance of Octahedral PtNi Nanoparticles, Nano Lett. 18 (2018) 798–804. https://doi.org/10.1021/acs.nanolett.7b04007.

[207] J. Lim, H. Shin, M. Kim, H. Lee, K.S. Lee, Y. Kwon, D. Song, S. Oh, H. Kim, E. Cho, Ga-Doped Pt-Ni Octahedral Nanoparticles as a Highly Active and Durable Electrocatalyst for Oxygen Reduction Reaction, Nano Lett. 18 (2018) 2450–2458. https://doi.org/10.1021/acs.nanolett.8b00028.

[208] C. Tojo, D. Buceta, M.A. López-Quintela, Slowing Down Kinetics in Microemulsions for Nanosegregation Control: A Simulation Study, J. Phys. Chem. C. 122 (2018) 20006–20018. https://doi.org/10.1021/acs.jpcc.8b06057.

[209] W. An, P. Liu, Rationalization of Au Concentration and Distribution in AuNi@Pt Core-Shell Nanoparticles for Oxygen Reduction Reaction, ACS Catal. 5 (2015) 6328–6336. https://doi.org/10.1021/acscatal.5b01656.

[210] C.C. Hung, P.Y. Lim, J.R. Chen, H.C. Shih, Corrosion of carbon support for PEM fuel cells by electrochemical quartz crystal microbalance, J. Power Sources. (2011). https://doi.org/10.1016/j.jpowsour.2010.07.015.

[211] S. Holdcroft, Fuel cell catalyst layers: A polymer science perspective, Chem. Mater. 26 (2014) 381–393. https://doi.org/10.1021/cm401445h.

[212] P. Mardle, G. Thirunavukkarasu, S. Guan, Y.-L. Chiu, S. Du, Comparative study of PtNi nanowire array electrodes toward oxygen reduction reaction by half-cell measurement and PEMFC test, ACS Appl. Mater. Interfaces. (2020) acsami.0c11531. https://doi.org/10.1021/acsami.0c11531.